NASA Technical Memorandum 107380

The Effect of Wake Passing on Turbine Blade Film Cooling

James David Heidmann
Lewis Research Center
Cleveland, Ohio

December 1996

National Aeronautics and
Space Administration

THE EFFECT OF WAKE PASSING ON TURBINE BLADE FILM COOLING

by

JAMES DAVID HEIDMANN

Submitted in partial fulfillment of the requirements

for the degree of Doctor of Philosophy

Thesis Adviser: Dr. Eli Reshotko

Department of Mechanical and Aerospace Engineering

CASE WESTERN RESERVE UNIVERSITY

January, 1997

THE EFFECT OF WAKE PASSING ON
TURBINE BLADE FILM COOLING

Abstract

by

JAMES DAVID HEIDMANN

The effect of upstream blade row wake passing on the showerhead film cooling performance of a downstream turbine blade has been investigated through a combination of experimental and computational studies. The experiments were performed in a steady-flow annular turbine cascade facility equipped with an upstream rotating row of cylindrical rods to produce a periodic wake field similar to that found in an actual turbine. Spanwise, chordwise, and temporal resolution of the blade surface temperature were achieved through the use of an array of nickel thin-film surface gauges covering one unit cell of showerhead film hole pattern. Film effectiveness and Nusselt number values were determined for a test matrix of various injectants, injectant blowing ratios, and wake Strouhal numbers. Results indicated a demonstrable reduction in film effectiveness with increasing Strouhal number, as well as the expected increase in film effectiveness with blowing ratio. An equation was developed to correlate the span-average film effectiveness data. The primary effect of wake unsteadiness was found to be correlated well by a chordwise-constant decrement of $0.094 \cdot St$. Measurable spanwise film effectiveness variations were found near the showerhead region, but meaningful unsteady variations and downstream spanwise variations were not found. Nusselt numbers were less sensitive to wake and injection changes.

Computations were performed using a three-dimensional turbulent Navier-Stokes code which was modified to model wake passing and film cooling. Unsteady computations were found to agree well with steady computations provided the proper time-average blowing ratio and pressure/suction surface flow split are matched. The remaining differences were isolated to be due to the enhanced mixing in the unsteady solution caused by the wake sweeping normally on the pressure surface. Steady computations were found to be in excellent agreement with experimental Nusselt numbers, but to overpredict experimental film effectiveness values. This is likely due to the inability to match actual hole exit velocity profiles and the absence of a credible turbulence model for film cooling.

TABLE OF CONTENTS

LIST OF FIGURES

LIST OF TABLES

NOMENCLATURE

Symbol	Description
B	blowing ratio
c	blade chord
c_v	constant volume specific heat
c_p	constant pressure specific heat
D	cylindrical rod diameter
d	cooling hole diameter
DR	density ratio
f	wake passing frequency
h	heat transfer coefficient
I	momentum ratio
I_h	heater current
k	thermal conductivity
L	cooling hole length
L_h	heater length
M	molecular weight
Ma	Mach number
N	rotor speed in rpm
n	number of rods in rotor
Nu	Nusselt number

p	pressure
q''	heat flux per unit area
r	recovery factor
r_j	jet radius of curvature
r_w	wall radius of curvature
S	effective slot width
s	entropy
St	Strouhal number
T	temperature
U	cascade inlet axial velocity
V_h	heater voltage
W_h	heater width
x	streamwise surface distance from leading edge
x_i	mole fraction of species i
x_j	mole fraction of species j
y	normal distance from wall
y^+	dimensionless normal distance from wall
α	thermal diffusivity
β	angle between free-stream and injection
γ	ratio of specific heats, c_p/c_v
η	film effectiveness
μ	dynamic viscosity

ν	kinematic viscosity
ρ	density
τ	shear stress
Φ	positive value, $0 \leq \Phi \leq 1$
Φ_{ij}	gas mixture weighting coefficient

Subscripts

b	with blowing
c	coolant conditions
f	film conditions
h	with heating
mix	mixture
nb	no blowing
nh	no heating
o	stagnation conditions
r	recovery conditions
w	heated wall conditions
wall	wall conditions
∞	free-stream conditions

1. INTRODUCTION

Turbomachinery unsteady effects

The flow in turbomachinery blade rows is inherently unsteady due to the relative motion of adjacent blade rows. These unsteady flows can generally be divided into two classes: two-dimensional effects associated with wake and shock passing and potential interactions, and effects generated by three-dimensional secondary flows in upstream blade rows. These secondary flows include tip clearance vortices, passage vortices, horseshoe vortices, and the relative eddy. The passing of wakes from the upstream blade row causes periodic fluctuations in both the magnitude and relative direction of the flow velocity in the downstream blade row. In addition, the secondary flows cause fluctuations which vary in the spanwise direction. Therefore to precisely model a turbomachinery flow field either experimentally or computationally requires inclusion of the time-varying quantities.

However, due to the complexity of the unsteady flow field and the difficulty in adequately representing it, the flow field in a single blade row is often considered to be steady. This may be done in several ways. In the simplest case, the blade row is completely isolated from all others such as in an experimental cascade of blades, or computationally by a steady calculation on a single blade row. The next level of modeling involves the simulation of upstream blade rows through the application of

a steady circumferentially-uniform boundary condition upstream of a given blade row. Computationally, this is done through the use of a "mixing plane" model. In this case, the flow through the first blade row is computed, and the flow variables are averaged circumferentially in some way at a plane between the first and second blade rows. The resulting distribution is then used as the upstream boundary condition for the second blade row. This process may be continued for as many blade rows as desired. A similar technique may be employed experimentally. Stationary turbulence grids may be placed upstream of a cascade of blades to model the aerodynamic losses of the upstream blade rows. In recent years, Adamczyk [1] has developed a steady computational method which models inter-blade row effects through the application of body forces throughout the flow field. Unlike the mixing plane approach, this allows for potential flow effects between adjacent blade rows. This approach has gained merit for multi-stage turbomachinery, where the cumulative effect of blade row interactions becomes important.

The most active area of unsteady turbomachinery research involves studies on the influence of the unsteadiness on blade aerodynamic performance. Sharma et al. [2] claim that wake and secondary flow unsteadiness have an adverse effect on turbomachinery efficiency of several points relative to the steady time-mean flow. In turbines, this is likely due in large part to the effect of the flow unsteadiness on turbine blade boundary layer transition [3]. The effect of flow unsteadiness on turbine blade heat transfer has been investigated by Ashworth et al. [4] and on the stagnation

region heat transfer of a cylinder by O'Brien [5]. In both of these studies, the unsteadiness is produced by cylinder wakes. In general, this unsteadiness increases heat transfer in the stagnation region through an increase in turbulence intensity in the wake. Recently, the impact of wake passing on the heat transfer characteristics of a more complex and realistic type of turbine blade - a *film-cooled* blade - has come into question. In the following discussion, the motivation for and use of film cooling in turbine blades will be described.

Turbine cooling

As a result of efforts to improve turbine engine performance, turbine inlet temperatures have increased dramatically over the past 50 years. A useful figure of merit for aircraft turbine engines is the specific fuel consumption, or SFC. This is the rate of fuel consumption per unit thrust of the engine. At a given flight Mach number, the minimum ideal SFC is dependent on turbine inlet temperature. For the turbofan engine which dominates the commercial aviation market today, the goal of minimum SFC drives the engine to higher bypass ratios, higher core pressure ratios, and higher turbine inlet temperatures [6]. As shown in Figure 1, current turbine inlet temperatures are approaching 2000 K, while the best available metallic turbine materials can withstand a maximum temperature of only about 1300 K [7]. The use of metallic turbine blades thus necessitates a method of cooling to prolong turbine life. Although ceramics and other high temperature materials are being investigated, there

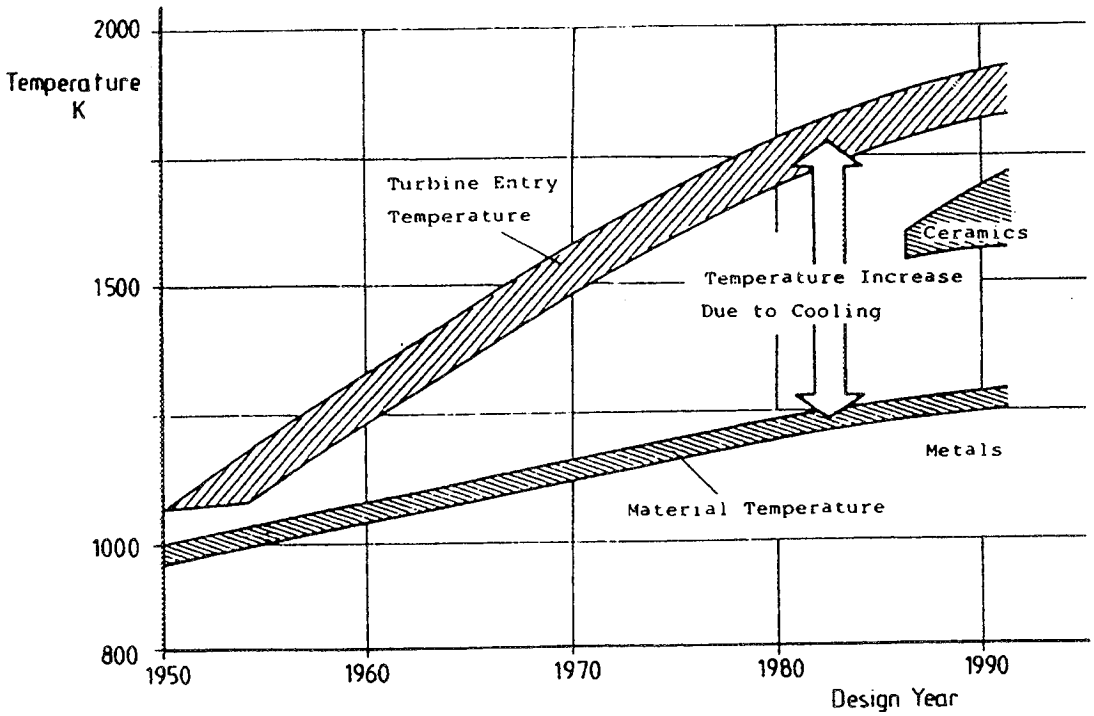

Figure 1: Trends in operational turbine inlet temperature [7].

remain serious limitations to their applicability. One of the most severe of these limitations is the brittle fracture failure mode of many non-metallic materials. Obviously, such a failure mode is unacceptable for a turbine in an aircraft engine. Thus in the short term, metallic turbine blades will be used in most, if not all, aircraft engines. In the long term, non-metallic turbine blades may be developed which can withstand current turbine inlet temperatures without cooling. However, the trend toward higher turbine inlet temperatures would require that even these blades be cooled. Thus it seems that turbine cooling will remain a valid research concern well into the 21st century.

Several different methods of turbine blade cooling exist. All involve the diversion of some of the engine compressor discharge air around the combustor and directly into the turbine blades. Although the compressor discharge gas is warm due to the work of compression, it is cooler than the combustor exit flow. Figure 2 shows the relative effectiveness of several turbine cooling techniques versus coolant flow rate [8]. Since the coolant flow is bled directly from the compressor discharge, it represents a loss in the total engine power output. Thus the designer attempts to cool the blade with a minimum of coolant flow. The simpler cooling methods involve purely internal flow of coolant within the turbine blade. The effectiveness of internal cooling may be improved with enhancements such as impingement, trip strips, and multi-pass arrangements. However, when the external gas temperature exceeds the maximum metal temperature by a significant amount, as it does in most modern aircraft engines,

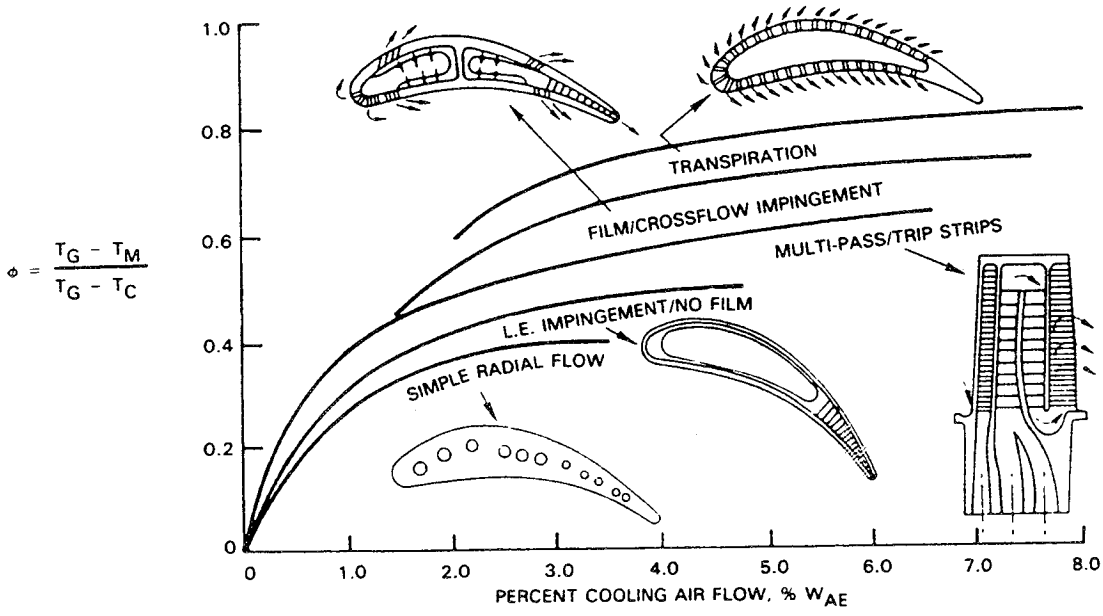

Figure 2: Effectiveness of various turbine cooling schemes [8].

these methods can no longer adequately protect the blade from failure. When internal cooling alone is inadequate, film cooling must be employed. This is typically necessary for the turbine first stage, and sometimes the second. In film cooling, the coolant air is discharged through small holes in the turbine surface to form a protective film between the turbine blade and the hot combustor discharge gas. These holes are usually concentrated on the pressure surface and leading edge region of the blades. Film cooling in the leading edge region is referred to as *showerhead cooling*. To remain effective, the film coolant must remain near the surface and not separate into the free stream. For this reason, pressure and suction surface film cooling holes are typically angled in the streamwise direction. Showerhead holes are usually angled in the spanwise direction due to the large streamwise curvature in the leading edge region. Film holes may also have a compound angle, meaning that neither the streamwise nor the spanwise angle is normal to the surface. However, mechanical constraints prohibit ejection at very small angles (less than about 30°) from the blade surface. Because of the many parameters involved in film cooling (hole angle, hole shape, placement of rows, etc.), the design of turbine film cooling schemes has tended to rely on a trial-and-error approach. Thus it is extremely important to know the trajectory of the film coolant under a variety of flow conditions.

There are three related parameters which are commonly used to describe the flow exiting a film cooling hole: the density ratio (DR), blowing ratio (B), and the momentum ratio (I). The density ratio is simply the ratio of coolant to free-stream

density. The blowing ratio is the ratio of coolant to free-stream mass flux. Finally, the momentum ratio is the ratio of coolant to free-stream momentum flux. Of the three, the blowing ratio is most often referred to in the literature because it has a first order effect on the cooling performance. Since the three parameters are related, only two can be varied independently. For a given blowing ratio, the momentum ratio varies in inverse proportion to the density ratio. The second order effect of these parameters is that at a fixed blowing ratio, a higher density ratio (lower momentum ratio) is associated with less penetration of the coolant into the free-stream, and improved cooling performance.

Transpiration cooling is the logical extension of film cooling. In this case, the coolant flows through the turbine wall, which is made of a porous material. Although this method of cooling is highly effective for a given amount of coolant flow, it has a disruptive effect on the external boundary layer because the coolant tends to emerge from the blade normal to the wall, unlike film cooling. In addition, the very small pores in the porous wall can easily become plugged. For these reasons, transpiration cooling is rarely used in turbine engines.

Literature review

Because of its importance in turbine design, there has been much investigation into the behavior of turbine film cooling flows. These investigations have ranged from

simple flat plate studies to full rotating blade geometries. Goldstein [9] reviewed the early research in the film cooling arena. This review consolidated experiments of various hole geometries and blowing parameters, and summarized analytical solutions for two-dimensional slot injection. It suggests a superposition technique for analyzing discrete hole film cooling applicable for non-interacting jets. However, for most modern applications, the film cooling jets interact to a large degree. Goldstein also gave several definitions for the film cooling effectiveness, η. For incompressible flow:

$$\eta = \frac{T_f - T_\infty}{T_c - T_\infty}$$

In this case, T_f is the film temperature, which is the adiabatic wall temperature in the presence of film cooling, T_∞ is the free-stream temperature, and T_c is the coolant temperature. For compressible flow:

$$\eta = \frac{T_f - T_r}{T_c - T_r}$$

where T_r is the free-stream recovery temperature, and T_c is now the coolant stagnation temperature. The film effectiveness may have values between 0 (no cooling effect) and 1 (maximum cooling effect).

Although they are relatively simple to model analytically, slots are impractical in

turbine blades due to structural limitations. Thus in recent years, more attention has been paid to discrete hole film cooling rather than to slot cooling. The simplest example of discrete hole cooling is for a cooled flat plate. The many early experimental studies on film-cooled flat plates are summarized by Goldstein [9]. These studies typically had long film holes (L/d greater than 10.0). A landmark computational study by Leylek and Zerkle [10] considered a flat plate with a single row of circular film holes angled at 35° to the free-stream direction. This study was the first to consider the plenum chamber, film hole, and mainstream simultaneously. The interactions between these three regions become important for the relatively short film holes (L/d less than 4.0) which are common in gas turbine engines. A three-dimensional turbulent Navier-Stokes method was used, and the results were in good agreement with experiment. The computation showed the familiar pair of counterrotating vortices emerging from the hole and a local jetting effect inside the hole due to the sharp change in flow direction as the coolant enters the hole from the plenum. These effects depend strongly on the blowing ratio, hole angle, and film-hole length-to-diameter ratio. Both effects differ from the common assumption of fully-developed flow which holds for very long holes.

Several researchers have investigated the effect of showerhead film cooling schemes experimentally using a single blunt body in a channel. In these arrangements, the body has a semi-circular leading edge and a flat plate afterbody. This type of experiment has the advantage of allowing a large scale idealized geometry. Mick and

Mayle [11] measured detailed film effectiveness and Nusselt number values downstream of four showerhead rows of holes, two on each symmetric half of the blunt body. Air injection was used, and the holes were angled at 30° to the surface tangent. Blowing ratios of 0.38, 0.64, and 0.97 were studied, and optimum downstream film effectiveness values were found at the 0.64 blowing ratio, suggesting competing effects of increasing coolant flow rate and penetration into the free-stream. In a group of papers, Mehendale and Han [12], Ou et al. [13], and Ou and Han [14] investigated the effects of free-stream turbulence and film hole row location on a showerhead film-cooled blunt body similar to that of Mick and Mayle [11]. High free-stream turbulence was produced using both a passive grid and a jet grid. It was found that the film effectiveness was reduced by the presence of high free-stream turbulence, but that this effect was smaller in the leading edge region for higher blowing ratios. The row location study showed that film injection closer to the stagnation line (±15°) was more adversely affected by the high free-stream turbulence level than injection from the downstream rows (±40°).

A computational study of showerhead cooling on a blunt body was performed by He et al. [15]. Four rows of staggered holes angled at 30° in the spanwise direction were considered. Because of symmetry, only half of the flow field was analyzed. The flow inside the holes and the external flow were computed, but not the plenum flow. Several physical phenomenon were identified. The flow emerging from the row nearest the stagnation point was shown to differ substantially from the downstream

hole due to the pressure variations present in the leading edge region. Also, interactions between the coolant from the two rows of holes depended on the blowing ratio. At the lower blowing ratio of 0.52, the upstream coolant falls between the downstream holes, giving good coverage. At the higher blowing ratio of 0.97, the upstream coolant aligns with the downstream holes, reducing the span-average film effectiveness.

Although blunt body models have the advantages of simplicity and generality, they neglect the curvature of an actual turbine blade which gives rise to the suction and pressure surface pressure gradients. It is well known due to the work of Ito et al. [16] and others that differences in blade curvature have a tremendous effect on film cooling performance. By applying a force balance to a portion of a film cooling jet flowing parallel to a curved wall, Ito et al. [16] were able to show that:

$$\frac{|r_j|}{|r_w|} = 1+\phi(I\cos^2\alpha - 1)$$

where r_j is the jet radius of curvature, r_w is the wall radius of curvature, ϕ is a parameter between 0 and 1, I is the momentum ratio, and α is the angle between the free-stream and injection directions. If $I\cos^2\alpha$ is less than 1, the jet has a smaller radius of curvature than the wall. This means that the jet will tend to move away from a concave surface and toward a convex surface, since the sign of the jet and wall curvature must be the same. Thus for a concave surface such as the pressure surface

of a turbine blade, film cooling performance should be worse than that on a flat plate for $I\cos^2\alpha < 1$ and better for $I\cos^2\alpha > 1$. For a convex surface such as the suction surface of a turbine blade, film cooling performance should be better than that on a flat plate for $I\cos^2\alpha < 1$ and worse for $I\cos^2\alpha > 1$. These results were for non-showerhead cooling, and thus did not account for spanwise injection.

Lander et al. [17] used an actual aircraft engine combustor upstream of a film-cooled cascade to measure film effectiveness and heat transfer coefficient values downstream of suction surface film cooling holes. Film effectiveness values were found to be reduced compared to slot ejection, and heat transfer coefficients were shown to increase in the presence of injection. In this case, the reference temperature used in determining the heat transfer coefficients was the film temperature T_f, which is the adiabatic wall temperature in the presence of film cooling. This is the traditional definition, and yields:

$$h = \frac{q''}{T_f - T_w}$$

T_f is typically determined experimentally by removing the heat source used in determining T_w or by conducting the experiment with the coolant at the same stagnation temperature as the free-stream. An alternate definition favored by Rigby et al. [18] and described in detail by Abhari [19] involves the use of the adiabatic wall

temperature in the absence of film cooling as the reference temperature. For high speed flow, compressibility effects are important, and the recovery temperature must be used:

$$h = \frac{q''}{T_r - T_w}$$

The advantage of the first definition of heat transfer coefficient is that it isolates the effect of the wall heat flux on the wall temperature and correlates data taken for different coolant-to-free-stream temperature ratios. The second definition gives a better picture of the overall heat transfer in the presence of film cooling. Since the present study allows for the independent control of wall heat flux and coolant flow, and the primary goal of the study is to gain insight into the relevant flow physics of film cooling, the first definition of heat transfer coefficient will be used herein.

An additional effect of blade curvature is that of the interaction of wall boundary layers with endwall boundary layers in the presence of blade pressure gradients. These interactions give rise to three-dimensional secondary flows which have an impact on the effectiveness of a film cooling scheme. This impact is particularly pronounced for low aspect ratio blading. Takeishi et al. [20] studied the effect of the three-dimensional flow field on film cooling effectiveness and heat transfer coefficient for an annular cascade of low aspect ratio turbine vanes. The aspect ratio of the

blades was 0.5. It was found that the presence of the passage vortex strongly affected the heat transfer and film cooling on the suction surface of the vane and on the endwall, but had little impact on the pressure surface. Flow visualization techniques showed the familiar migration of low momentum endwall boundary layer fluid from the pressure surface toward the suction surface due to pressure gradients. This migration, along with the leading edge horseshoe vortex, produced a very complex streamline pattern on the endwall and near the endwall on the suction surface.

None of the aforementioned studies have considered the effects of turbine blade curvature on the heat transfer characteristics of a blade with showerhead film cooling. The following recent studies have included the combined effect of realistic blade cascade geometries with showerhead cooling schemes. Nirmalan and Hylton [21] produced a data set of film cooling performance as a function of Mach number, Reynolds number, turbulence, wall-to-gas temperature ratio, coolant-to-gas temperature ratio, and coolant-to-gas pressure ratio for a typical turbine vane with showerhead, pressure surface and suction surface film cooling. The downstream film cooling process was shown to be governed by the competing mechanisms of a temperature dilution effect and a turbulence enhancement effect. The temperature dilution effect reduces the heat transfer to the blade, while the turbulence enhancement effect increases it. The turbulence enhancement is particularly crucial as it relates to the showerhead cooling, since the leading edge injection trips the boundary layer, likely causing the blade boundary layer to be turbulent.

Camci and Arts [22] investigated the effects of blowing ratio, temperature ratio, and free-stream turbulence on film cooling for a realistic turbine cascade geometry. The blade had three rows of showerhead cooling holes, as well as downstream cooling on both the pressure and suction surfaces. Realistic engine conditions were matched. It was found that the presence of showerhead film cooling holes without coolant injection caused an earlier transition of the suction surface boundary layer. Heat transfer rates were found to increase immediately downstream of film holes for the high blowing ratio cases, while the lower blowing ratio cases exhibited a gradually increasing heat transfer rate downstream of the holes. This was considered to be due to separation and reattachment of the film at the higher blowing ratios. Finally, the effect of free-stream turbulence on heat transfer was insignificant compared to experimental uncertainty due to the buffer layer created by the coolant film and the fully turbulent nature of the blade boundary layer.

In an extension of their earlier work, Camci and Arts [23] measured heat transfer rates for the same geometry with blade incidence angles varying from -10° to +15°. The blade heat transfer rates were found to be extremely sensitive to changes in incidence angle. Since the incidence angle determines the blade attachment line, it also fixes the split of the showerhead coolant flow between the suction and pressure surfaces. Variations in the split of coolant flow were reflected by heat rates on the suction side which varied inversely as those on the pressure side.

Abuaf et al. [24] investigated showerhead and suction surface film cooling in a linear cascade. A comparison was made between heat transfer coefficients with coolant injection at a high blowing ratio (between 1.5 and 2.7) and with the film holes plugged, forming a smooth surface. The injection of film was found to increase heat transfer coefficients on both the suction and pressure sides of the blade. This is consistent with the results of Camci and Arts [22], although Abuaf et al. used the traditional definition of heat transfer coefficient, while Camci and Arts used the overall heat transfer definition. In both cases, the act of injection at high blowing ratios causes an increase in mixing immediately downstream of the hole, which in turn enhances heat transfer. The Camci and Arts results additionally show that this mixing is sufficient to overshadow the effect of a larger flux of lower enthalpy injectant.

In a series of papers, Garg and Gaugler have presented computational methodology and results for a film-cooled vane and rotor. The blades included showerhead as well as pressure and suction surface film cooling. Each blade was analyzed in isolation in the steady frame of reference. Garg and Gaugler [25] described the modification of a three-dimensional Navier-Stokes code to predict heat transfer on a film-cooled blade. The film holes were modeled by approximately 20 control volumes per hole at the hole exit plane, but the hole pipes themselves were not discretized. Computational results were in fair agreement with experimental data. Garg and Gaugler [26] used the same numerical procedure with both fully developed laminar (polynomial) and fully developed turbulent (one-seventh power law) velocity boundary

conditions supplied at the hole exit plane. It was found that the choice of hole exit boundary condition could cause as much as a 60% variation in the heat transfer coefficient on the blade near the holes. Results were dependent on geometrical factors, such as the blade profile and film hole shape. Garg and Gaugler [27] showed that reducing the showerhead hole spacing while maintaining the coolant-to-free-stream mass flow ratio resulted in higher film effectiveness values. For the largest spanwise pitch of 7.5 times the hole diameter, increasing the coolant mass flow resulted in a reduction in film effectiveness due to film jet lift-off. This phenomenon was not predicted for smaller spanwise pitches.

To this point, all studies discussed have assumed the free-stream flow to be steady. This has been a reasonable approach, since assessing film cooling performance even in a steady external flow is not trivial, and to a first order approximation can model conditions in an engine. Relatively less work has been done on the impact of wake passing unsteadiness on film cooling in a turbine blade. Rigby et al. [18] used a rotating wheel wake generator with cylindrical bars to model inlet guide vane wakes and shock waves under transonic flow conditions. A linear cascade of 5 turbine blades was located downstream of the wake generator. The middle blade was film-cooled with two injection locations on both the suction and pressure sides of the blade. There was no showerhead cooling. The blades were highly loaded and typical of turbine rotor geometries. An optimum blowing ratio of 1.0 was found on the suction surface, while the film cooling had very little effect on the pressure surface

for all blowing ratios. The main effect of the wake passing was a reduction in effectiveness caused by enhanced film mixing, and the shock passing effect was found to produce large fluctuations in the heat transfer rate. Ou et al. [28] and Mehendale et al. [29] used an experimental approach similar to Rigby et al. [18], except with a different blade profile, and including showerhead cooling. Because the tunnel was low speed, shocks were not present. Both air and CO_2 injection were employed for different density ratios. Ou et al. [28] investigated the effect of wake passing on heat transfer coefficients. It was found that in general, the introduction of film injection increases local Nusselt numbers and is the dominant effect. Likewise, increasing wake passing frequency increases local Nusselt numbers for all blowing ratios, but this effect is reduced at higher blowing ratios. The wake passing frequency is correlated in terms of Strouhal number, which is defined as:

$$St = \frac{2\pi fD}{U}$$

where f is the wake passing frequency in Hz, D is the diameter of the wake-producing body, and U is the average cascade inlet velocity. The comparisons between air and CO_2 are questionable because the fluid properties of air were used for both cases in determining Nusselt number. Mehendale et al. [29] investigated the effect of wake passing on film effectiveness. Again, a blowing ratio near 1.0 was found to provide the highest film effectiveness, although the CO_2 performed better than air at a blowing ratio of 1.2, while the air performed better at lower blowing ratios. This is likely due

to the higher density of CO_2, which gives a lower momentum ratio than air for the same blowing ratio. It is the separation of the film from the blade surface which lowers film effectiveness at very high blowing ratios. This is driven by the injectant momentum, and the lower momentum CO_2 thus performs better at the higher blowing ratios. At low blowing ratios, film separation is not a problem, and the air performs better, perhaps because the additional effect of species diffusion is not present.

Funazaki et al. [30] used a rotating wheel wake generator with cylindrical bars upstream of a showerhead-cooled blunt body. Three different turbulence grids were also employed to independently study the effects of deterministic and indeterministic unsteadiness. Although the holes were not spanwise-angled as in an actual blade and heated air was used as the injectant, resulting in density ratios less than 1.0, several conclusions were drawn. Film effectiveness values were highest at the lowest blowing ratio of 0.4. This is in contrast to other studies which find higher optimum blowing ratios, but can be explained by the injection normal to the surface which encourages film separation at lower blowing ratios. Increasing wake passing frequency (or Strouhal number) was found to reduce film effectiveness, especially at lower blowing ratios where the influence of the wake on the low momentum film is strongest. Finally, the wake effect was reduced as free-stream turbulence increased, as expected.

Several studies have investigated film cooling performance on a turbine blade in an actual rotating turbine stage environment. There are two major differences between

this situation and the previous studies which used cylinder wakes to produce unsteadiness. The first is obviously the use of actual blades to produce the upstream wakes instead of cylindrical bars. The character of the two types of wakes may differ due to the boundary layer development on the blade and the flow turning caused by curved blades. The second major difference is the frame of reference of the film-cooled blade. In the cascade tests, the film-cooled blade is stationary, while the wake-generators rotate. In the stage tests, the film-cooled blade rotates, and the wake-producing blades are stationary. This second difference may be important for cases where the density of the coolant is greater than the free-stream, as in an engine, since centrifugal forces will produce a buoyancy effect.

Dring et al. [31] were the first to study film cooling performance on a large scale model of a high pressure turbine first stage. Coolant was injected from a single hole on both the pressure and suction sides of the rotor blade. Density ratios from 1.0 to 4.0 were investigated and flow visualization studies showed radial migration of the coolant, especially on the pressure side. The migration was found to be relatively insensitive to the coolant properties. Film effectiveness profiles were measured downstream of the holes. The suction surface profiles were found to correlate well with flat plate data, while the pressure surface film effectiveness was significantly reduced. This reduction was likely due to the radial migration of the coolant and the concave curvature.

Takeishi et al. [32] also measured film cooling effectiveness for a rotating turbine blade. In this case, the blade had a realistic cooling geometry with showerhead, pressure, and suction surface rows of cooling holes. The results of Dring et al. [31] were corroborated, as the pressure surface film effectiveness was found to decrease relative to cascade tests due to the radial flow and concave curvature. The suction surface film effectiveness was in good agreement with the stationary blade tests except far downstream where enhanced mixing reduced the film effectiveness. Abhari and Epstein [33] used a short duration turbine test facility to again study a film-cooled rotating blade in a turbine stage environment. The cooling arrangement consisted of three rows of coolant holes on the pressure surface and two on the suction surface, but no showerhead cooling. Unlike Dring et al. [31] and Takeishi et al. [32], this study considered transonic flow. This introduced unsteady shock passing in addition to wake passing as unsteady effects. For these tests, the suction surface had a 12 percent decrease in heat transfer, while the pressure surface had a 5 percent increase relative to cascade tests. The unsteady effects were attributed to coolant flow rate changes caused primarily by shock passing pressure fluctuations. A linear subsonic model for the flow in the film hole using the external pressure computed by an unsteady Navier-Stokes code was presented to account for this effect. Predictions using the model were found to be in good agreement with experimental results.

Numerical simulations for an entire film-cooled turbine stage are scarce due to the large computational time associated with capturing both the small time scales of blade

passing and the small length scales of film cooling and heat transfer. However, Dorney and Davis [34] showed that such a simulation could be achieved using a time-accurate Navier-Stokes solver. The computational constraints limited the simulation to only two grid points per film hole, so local effects due to hole exit profile could not be modeled. However, unlike previous computational simulations such as those by Garg and Gaugler, [25]-[27], the effect of blade endwalls was modeled.

Motivation and purpose

Although recent research has begun to focus on the unsteady flow environment, the majority of research on film coolant flow has considered the turbine free stream flow to be steady, as indicated by Eckert et al. [35]. Studies of film-cooled turbine stages include unsteadiness ([31]-[33]), but lack the ability to vary the unsteady parameter. Cylindrical wake experiments solve this problem, but those in the literature ([18] and [28]-[30]) have not sought to resolve spanwise and time variations to isolate the important physical phenomena associated with film coolant flow. Others have considered spanwise variations under steady conditions, for example with showerhead cooling on a flat body with a blunt leading edge ([11]-[15]). However, detailed experimental results for showerhead film cooling with representative blade geometries, particularly in the unsteady environment, are lacking in the literature. To this end, this study aims to investigate the effect of flow unsteadiness on turbine film cooling in a more detailed and fundamental manner. Showerhead cooling was chosen because

of the more pressing need for film cooling [34] and the larger temporal fluctuations in static pressure [33] in the leading edge region, as well as the demonstrated effect of incidence on showerhead cooling behavior [23].

It is expected that the primary unsteady effect on film coolant flow in subsonic and moderately transonic turbines is due to wake passing, especially near midspan. Further, secondary flows are highly dependent on the turbine geometry, and are not easily generalized to a broad range of problems. Thus this study concentrates on the effect of wake passing on the film coolant flow. This can be accomplished experimentally using a rotating rod arrangement upstream of an annular turbine cascade. Such an arrangement produces a periodic wake pattern which impinges on the turbine blades, and avoids the angular mismatch which occurs with the more common linear cascades ([18], [28], and [29]). The rods are sized to match the trailing edge diameter of an appropriate inlet guide vane for the test turbine. There is some debate as to the similarity of cylinder wakes to blade wakes [36]. However cylinder wakes have been shown [37] to accurately represent the relative velocity vector diagram and mean wake velocity profiles of an actual inlet guide vane.

Computationally, the unsteady flow field in a full turbine stage can be modeled using current three-dimensional viscous unsteady flow codes. Such codes can even model film-cooled blades through flow injection at selected grid points [34]. However, the computational time required for such a computation in sufficient detail for this

problem would be enormous, making it impractical to perform a parametric study of the important variables. In addition, it is not guaranteed that an improved understanding of the flow physics would be obtained from such an effort. Thus the computations of this study focus on the two-dimensional wake passing effect approximated by the rotating rod arrangement of the experimental study. The problem is then studied through a combination of physical and computational experiments. These experiments are flexible enough to allow application to an appropriate matrix of operating conditions and detailed enough to enable accurate interpretation of the underlying flow physics. The goal of this study is to develop a physics-based unsteady film coolant flow model which may be incorporated into steady design codes.

2. EXPERIMENTAL APPARATUS AND PROCEDURE

Test facility

The NASA Lewis Rotor-Wake Heat Transfer Rig (Figure 3) was chosen as an appropriate facility to investigate wake induced unsteadiness effects on a film-cooled turbine blade. This annular-flow open-circuit wind tunnel was described in detail by Simoneau et al. [38]. Air from the test cell is drawn through a bellmouth inlet into the wind tunnel by the opening of downstream valves which lead to a low pressure altitude exhaust system. The maximum flow rate for the facility is about 10 kg/s. An ASME standard sharp-edged orifice located downstream of the test section is used to measure the overall flow rate. The flow annulus has an outer diameter of 0.4064 m. and an inner diameter of 0.2705 m. The facility has a rotor upstream of the test section (Figure 4) which is capable of rotating at speeds up to 7000 rpm. The rotor has 24 equally spaced holes at 15° intervals for the insertion of wake-producing bodies. Although various solid and perforated plates had been employed in the rotor previously, cylindrical rods having a diameter of 3.2 mm were employed for this experiment. The 24 holes allow for maximum flexibility in the number of upstream rods, since 1, 2, 3, 4, 6, 8, 12, or 24 rods may be equally spaced in the available holes. For the purposes of this experiment, all 24 rods were used at all times, except for the cases with the rotor removed. O'Brien and Capp [37] described the two-component phase-average turbulence statistics downstream of the rods. Ashworth et

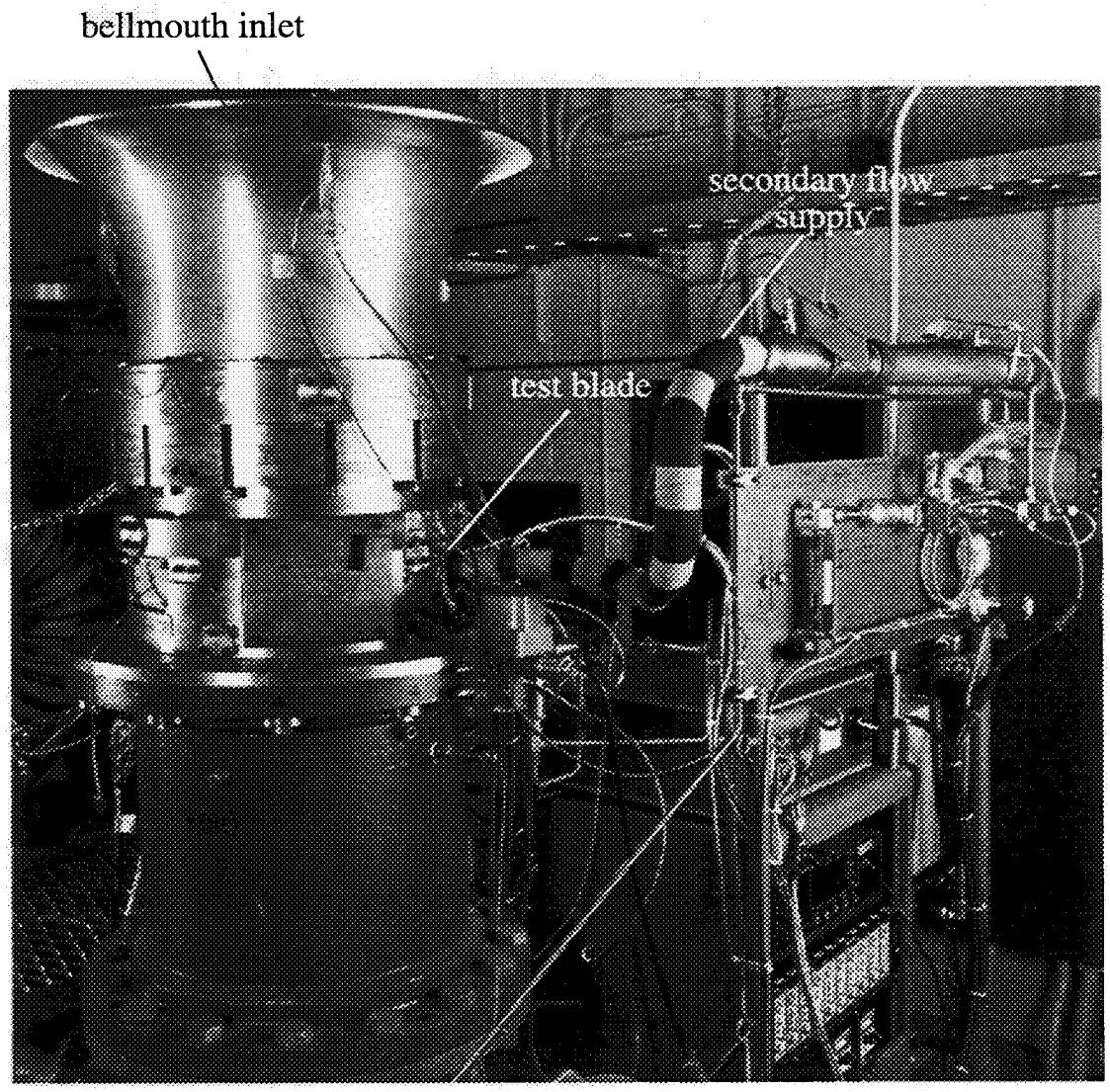

Figure 3: Rotor–wake facility.

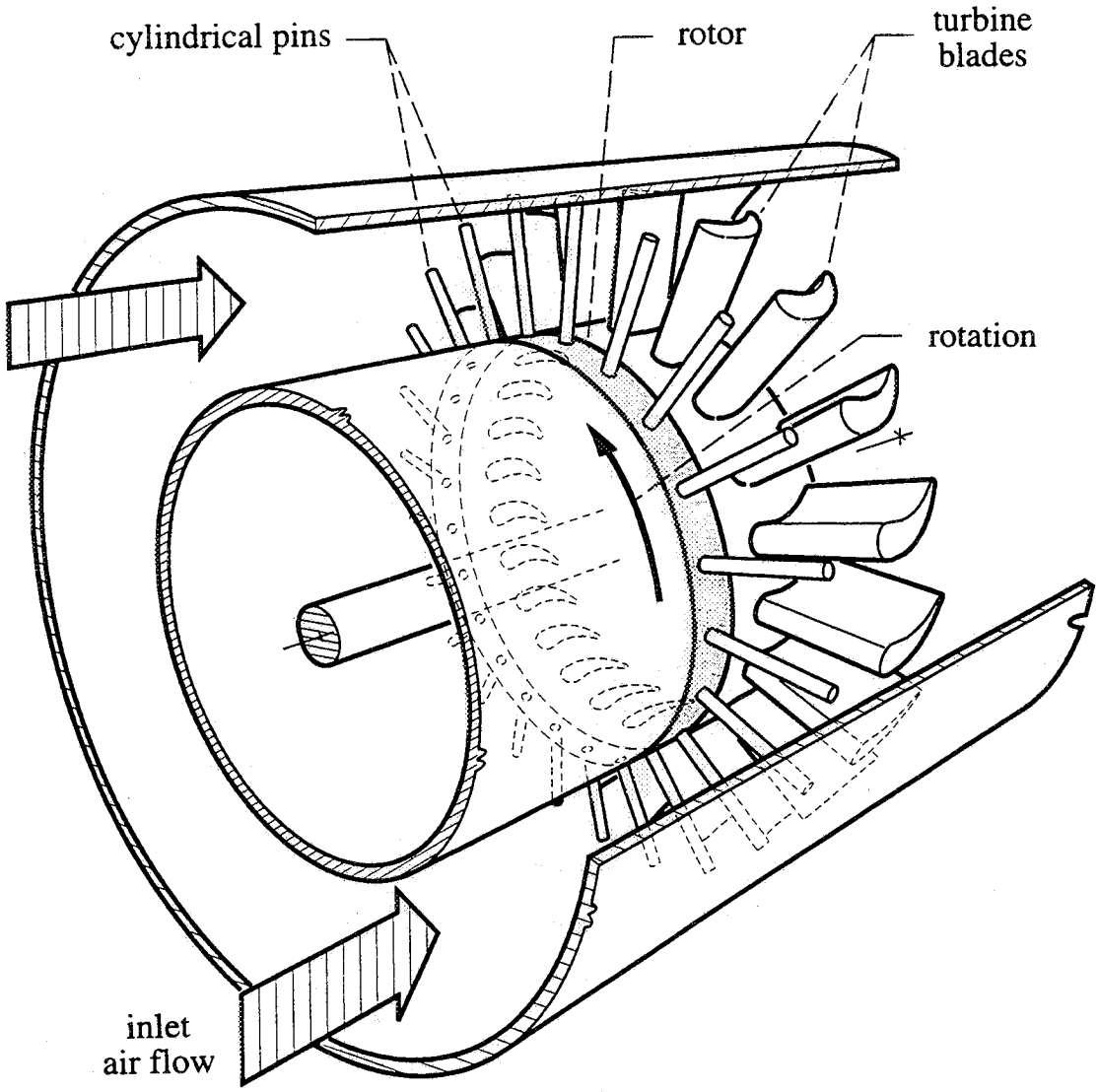

Figure 4: Rotor–wake facility schematic.

al. [4], have also used a cylindrical rod wake generator to simulate the effect of an upstream blade row. While both sets of researchers admit to the differences between cylinder wakes and blade wakes, they agree that much useful information can be gained from experiments using cylinder wakes. Specifically, cylinder wakes cannot model the effects of boundary layer production on an upstream blade. However, the velocity deficit, turbulence increase, and rotative speed are all modeled reasonably well [37].

The exposed tips of the rotor rods were painted black except for the tip of one rod which was painted with silver reflecting paint. A fiber-optic sensor was mounted on the outside annulus of the rig. This sensor detected the passage of the silver rod tip, and yielded a once per revolution signal. The signal was converted to a once per wake signal by an electronic shaft-angle encoder. The once per wake signal was recorded during each test run and used later to allow phase-averaging of the unsteady data.

Downstream of the rotor is an annular turbine cascade consisting of 23 blades. 23 blades were employed to avoid a common multiple with the number of wakes and the associated vibrations and stresses due to simultaneous wake/blade interactions. The first natural vibrational bending mode of the cylindrical rods was computed to be approximately 3100 Hz. The highest rod/blade passing frequency achievable in the facility relative to each rod is 2680 Hz, so no natural bending modes are within the

range of imposed forcing frequencies. The leading edge of the blades are 12.7 mm downstream of the rotor centerline. The blades in the cascade have 67° of turning, and may be viewed as representing embedded stator blades or lightly loaded rotor blades. The blade profile is shown in Figure 5. Since the nominal inlet flow direction is axial, blades in the cascade must have an inlet angle of 0° for optimum incidence. This restriction disqualifies blades with the turning angles of 90° or greater which are typical of rotor blades. However, the blades in this cascade were designed as typical rotor blades with the leading edge portion removed, leaving a blade inlet angle of 0°. The outer annulus of the rig has three ports spaced nearly 120° apart, each of which may be used to insert a test blade into the cascade. In this experiment, two of the ports were filled with metal dummy blades identical to the permanent blades. The third port was used to insert the test blade.

A secondary flow supply system (Figure 6) was developed to allow injection of film cooling flow through the test blade. One of the most important parameters of interest in film cooling studies is the ratio of film coolant density to free-stream density. This parameter is important because of the interrelation of density, mass flux, and momentum flux. For a given mass flux of coolant, a higher density coolant will have a lower momentum flux, and will penetrate less deeply into the free-stream than a lower density coolant [9]. In an actual turbine engine, the ratio of the film coolant temperature to the free-stream temperature may be as low as 0.5. Such temperature ratios produce density ratios of up to 2.0 through simple application of the ideal gas

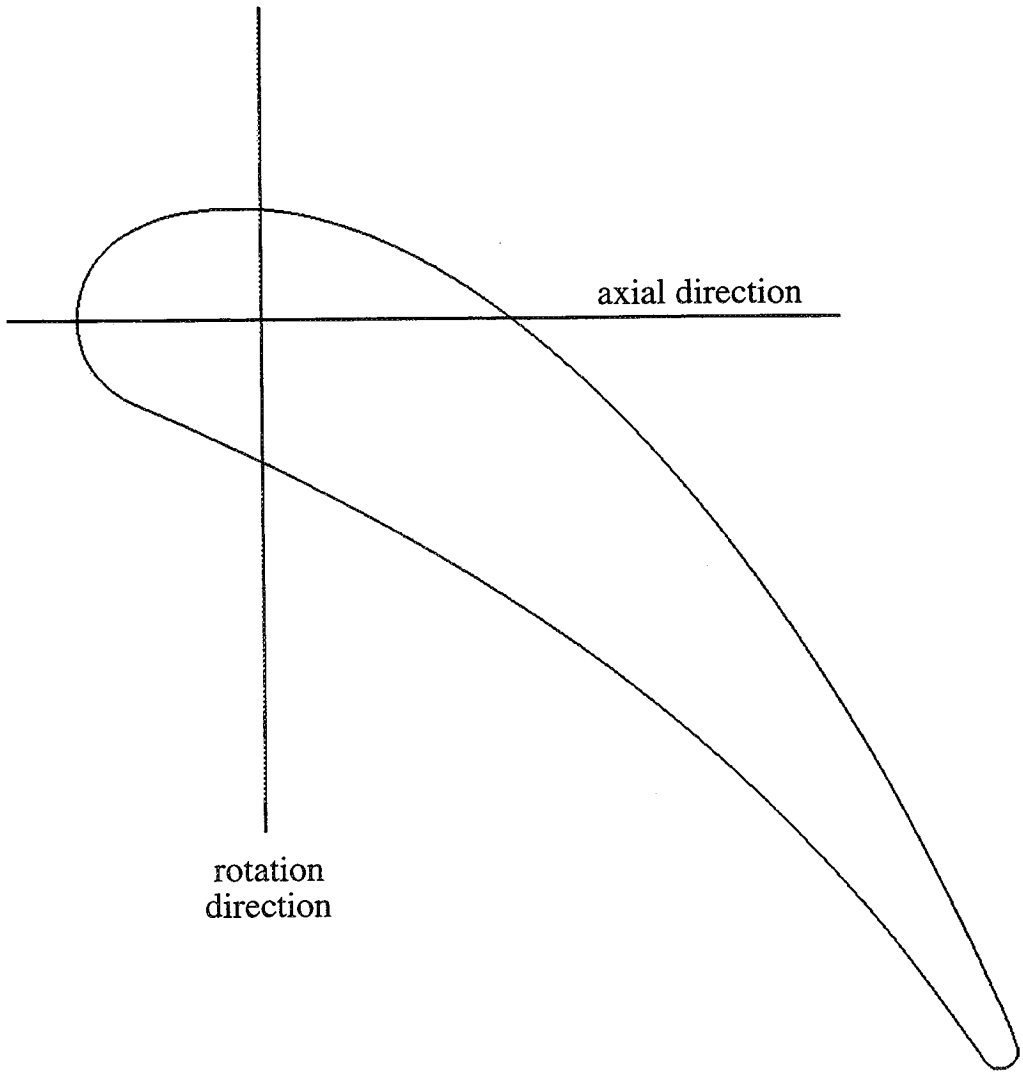

Figure 5: Blade profile.

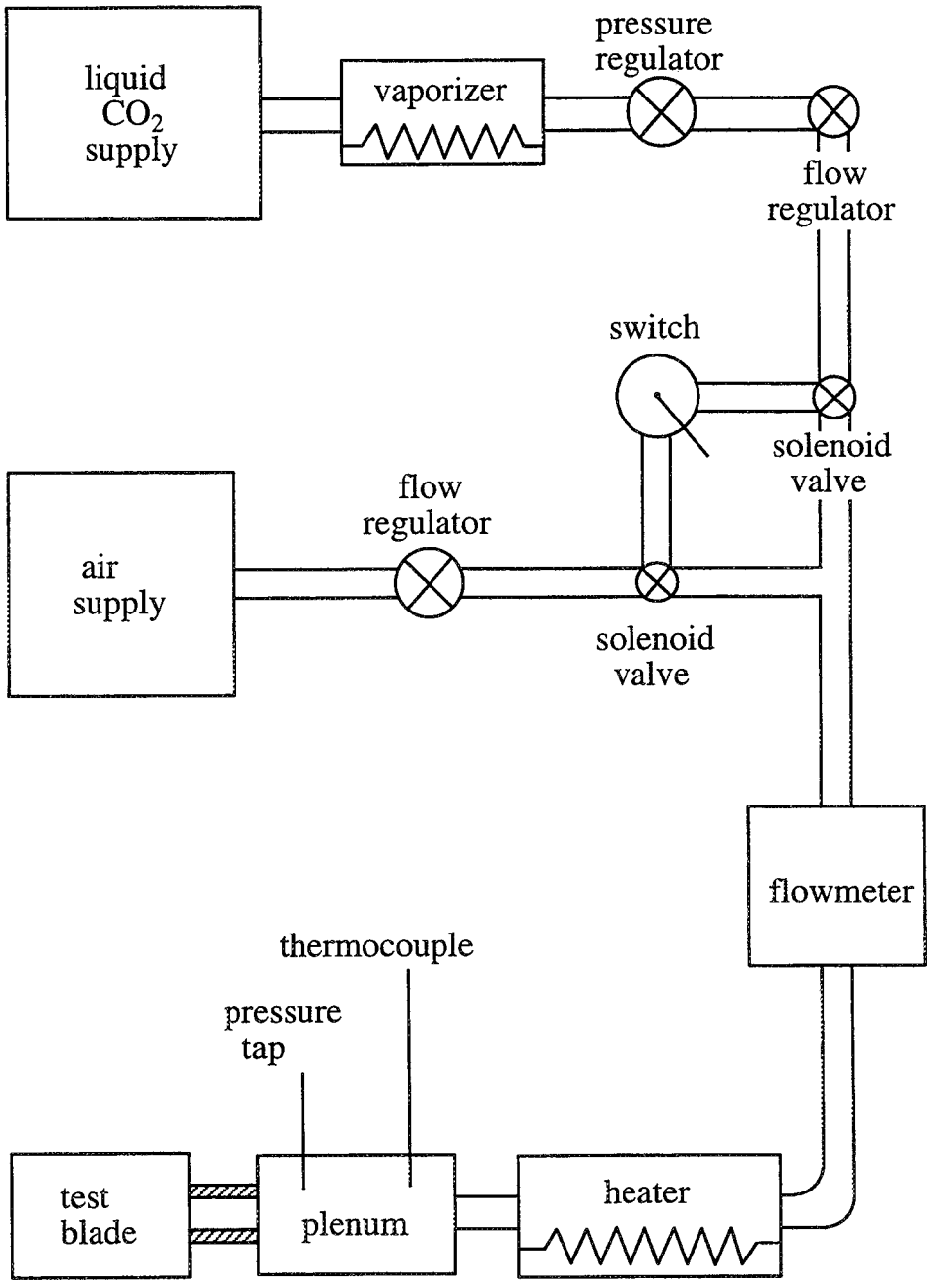

Figure 6: Secondary flow system schematic.

law. It was realized at an early stage in this research that such density ratios would be impossible to achieve with air injection. Because this facility is an open-circuit tunnel which is supplied by test cell air, extremely low temperature injection air would be required to achieve appropriate density ratios. Even if it were practical to produce such low temperature air, the injection of it into the free-stream would result in condensation and freezing of the water vapor in the relatively humid test cell air. To avoid this problem, the secondary flow system was designed to supply both air and CO_2 to the test blade. CO_2 has a molecular weight of 44.01 compared to 28.97 for air, so at atmospheric pressure and temperature, it has a density 1.519 times that of air. This allows more realistic density ratios to be achieved in the experiment. The capability to inject air was retained to allow study of the density ratio effect.

The secondary flow rates required to give blowing ratios of 0.5 and 1.0 (typical of showerhead film cooling) for this facility at nominal primary flow rates were about 0.002 kg/s and 0.004 kg/s, respectively. These values account for the fact that only one blade is film-cooled, but all 23 are exposed to free-stream flow. Although these flow rates are relatively small, over the time scale of a six hour test run nearly 100 kg of secondary flow can be used, although the actual usage was usually less. Because of these high secondary flow requirements, large dewars holding about 70 kg of liquid CO_2 were used. Two dewars were attached in parallel to the 13 mm secondary flow supply line. These dewars were refilled regularly as they became empty. The dewars were designed with a pressure-building regulator and a liquid

outlet valve, which supplied a steady flow of liquid CO_2 at high pressure and room temperature to a vaporizer. Both dewars were used simultaneously to reduce frost formation and to ensure a more constant supply pressure as the dewars emptied. The vaporizer produces CO_2 gas through a throttling process, and contains a heater which raises the temperature of the gas to about 300 K. Downstream of the vaporizer is a pressure regulator which was maintained at a gauge pressure of 276 kPa. Next, the CO_2 flows through a precise flow regulation valve which was used to control the secondary flow rate. The flow then passes through a Hastings HFM-201 mass flowmeter. The flowmeter has a maximum flow rate of 0.011 kg/s, and was calibrated for both air and CO_2 using a linear regression. The accuracy of the flow rate was determined to be within 1.0%.

Immediately upstream of the flowmeter is the convergence of the air and CO_2 supply lines. To allow switching of secondary flow between air and CO_2, electronically-controlled solenoid valves were placed in both the air and CO_2 supply lines, immediately upstream of the convergence point. The solenoid valves are controlled by an external switch which allows either one or neither of the supply lines to be open. Both supply lines may not be open simultaneously. The air is supplied by a 138 kPa shop air system which is standard in NASA Lewis test cells. The air supply is nominally at a stagnation temperature of 293 K and has a water vapor content approximately equal to that of the laboratory air. The air flow rate is controlled by a separate flow regulation valve. The air supply line is 13 mm diameter steel pipe.

In order to measure thermal film effectiveness values, the secondary flow must be at a different temperature than the free-stream. This temperature difference should be as large as possible to improve the accuracy of the film effectiveness measurement. Although the density ratio problem is avoided by using CO_2, the problem of free-stream water vapor condensation is still present for secondary flow temperatures much lower than room temperature. For this reason, it was decided to heat the secondary flow to a temperature greater than that of the free-stream. The wall temperatures are then higher than the uncooled wall recovery temperatures, which is opposite to the situation in an actual engine, but this difference is accounted for by the definition of film effectiveness. To heat the secondary flow in the test facility, an electrical resistance heater was employed. The heater consisted of a series of resistors embedded in a cylindrical tube through which the secondary flow passed. The effective resistance of the heating element was about 60 Ω. The heater was connected to a DC power supply with a maximum voltage setting of 200 V. The maximum power output of the heater was thus about 700 W. For the blowing ratios of this study (0.5 and 1.0), power supply voltages of 70 V and 100 V were used, respectively. For air and CO_2, these voltages resulted in secondary flow temperature rises of about 35 K and 30 K, respectively, owing to differences in specific heat for the two gases. The secondary flow temperature and pressure were measured by a thermocouple and static tap, respectively, centered in a 51 mm diameter plenum pipe. For the secondary flow rates of this test, this diameter tube was sufficient to reduce Mach numbers to less than 0.01, so that the dynamic components of pressure and

temperature are essentially zero. The plenum tube was connected to the test blade by a short length of flexible plastic tubing which was force-fitted over a 30 mm long brass tube. The plastic tubing was wrapped with 25 mm thick foam insulation to minimize any conduction heat loss. The brass tube was cemented into the test blade and mounting plate, as shown in Figure 7.

Test blade

The test blade was assembled in several parts, as shown in Figure 8. The bulk of the blade is wood, which was used because of its low thermal conductivity to reduce thermal conduction in the blade. In order to allow determination of heat transfer coefficients on the blade surface, a heat source is required. For this experiment, a 25.4 μm thick sheet of Inconel foil was used as a resistive heater. This method is well established, and has been discussed in detail by Hippensteele et al. [39]. Inconel is a nickel alloy which has a nearly constant electrical resistivity over a large range of temperatures, which makes it ideal for producing a constant heat flux over time. To achieve a heat flux which is constant over the exposed surface area of the test blade, a rectangular sheet of the foil was used to cover both the suction and pressure surfaces of the blade, leaving the showerhead region exposed. The portion of the blade covered by foil begins immediately downstream of the last row of film holes on both the suction and pressure sides. An alternative method would have been to cover the entire blade and drill holes in the foil at the hole locations so that the

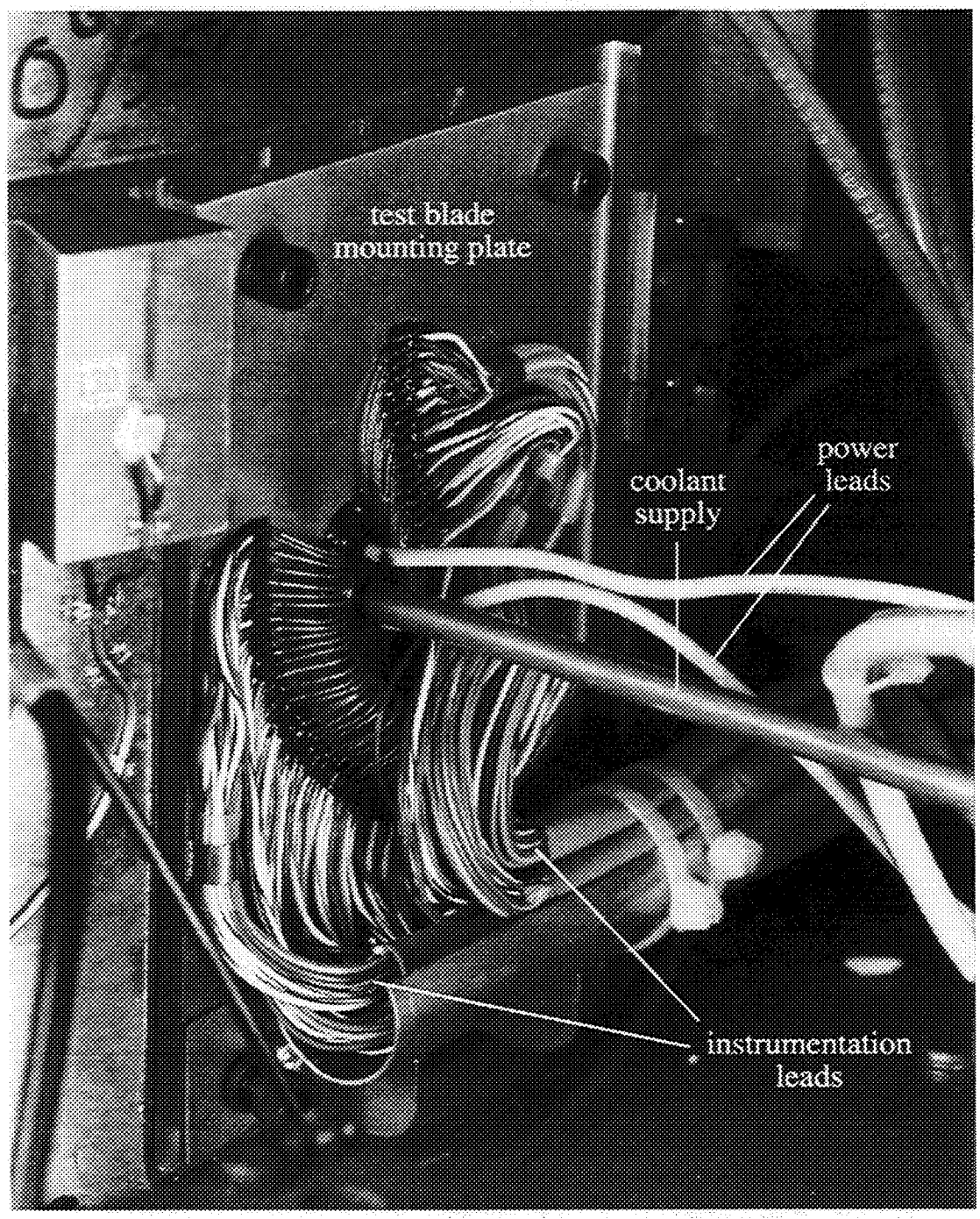

Figure 7: Instrumented blade mounting plate.

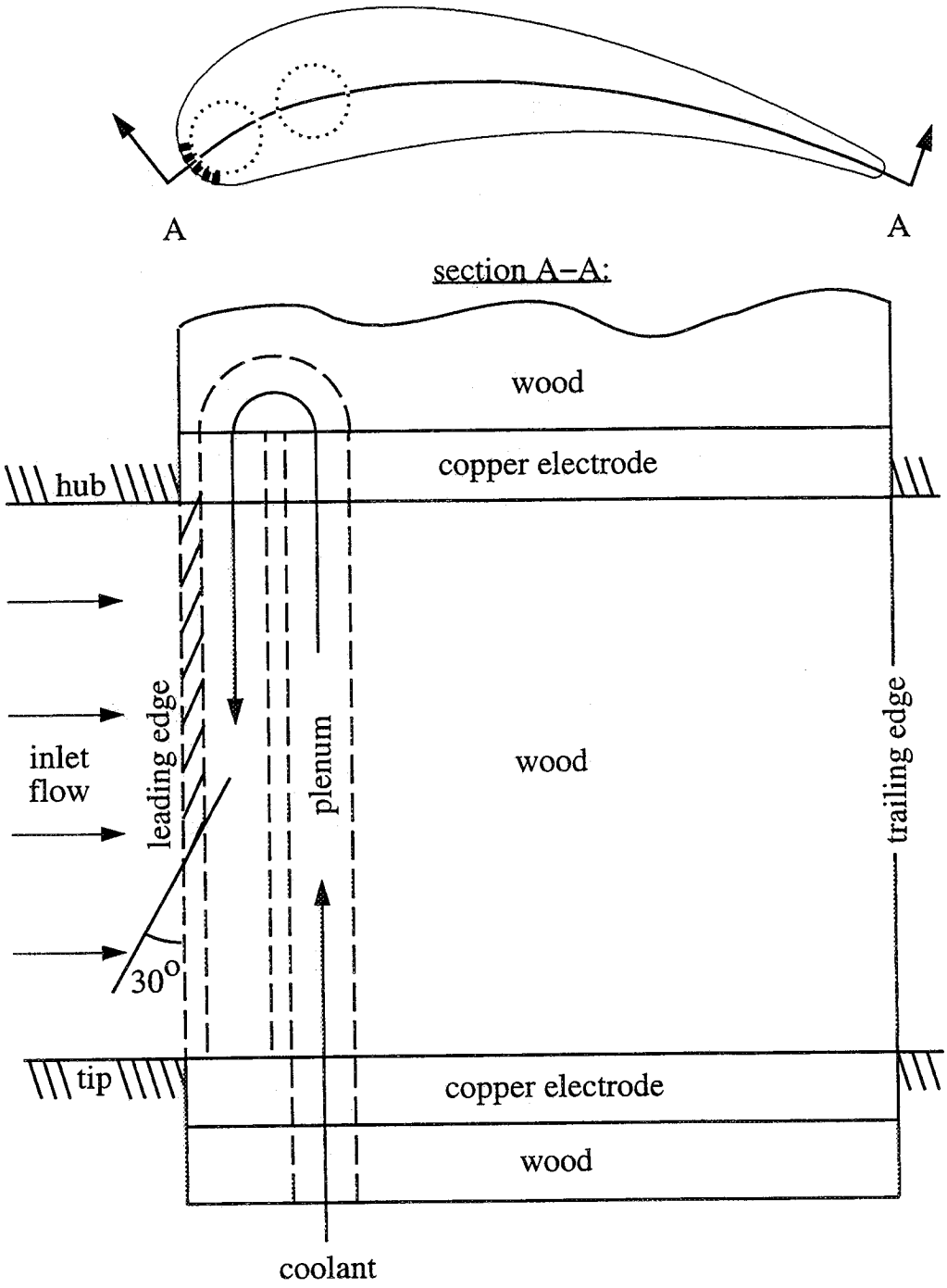

Figure 8: Blade cross–section.

regions between holes would also be heated. However, this method would require estimation of and correction for the non-constant heat flux in the leading edge region, and so was not used. The foil was attached to the wood blade using a double-sided adhesive.

Two copper electrodes were machined having the same profile as the blade, and a thickness of 6.3 mm. These electrodes were glued into the test blade as shown in Figure 8 such that they would lie adjacent to the inner and outer rig endwalls while remaining outside the flow annulus. The foil was attached to both electrodes using a continuous line of very small spot welds to assure a uniform distribution of heat flux over the blade surface. The length L_h of the heater between weld lines is 76.2 mm, and the cumulative width W_h of the pressure and suction surface heaters is 127.0 mm. The heat flux produced by the heaters can be determined from:

$$q'' = \frac{V_h I_h}{L_h W_h}$$

where V_h is the voltage across the heater, and I_h is the current through the heater. The electrodes were connected to a 50 Ampere power supply via heavy gauge wire to minimize heat generation in the leads. Access to the inner diameter electrode was achieved by drilling a 3.2 mm spanwise hole in the center of the blade. Although the heat flux generated in the leads was less than one percent of the total heat generation, the circuit current was limited to 36 Amperes by electrician code restrictions for the

leads. This current was determined to be sufficient to generate a nominal temperature increase of 10 K on the blade surface under standard flow conditions.

The secondary flow passage as shown in Figure 8 is a 6.3 mm diameter hole which extends the length of the rig annulus to the inner diameter, makes a 180° turn, and extends back toward the outer diameter. This serpentine passage was employed because of the angle of the film cooling holes. The holes are angled 30° to the blade surface in the spanwise direction, and are oriented toward the outer diameter of the rig. Bench tests indicated that a more uniform spanwise distribution of flow from the film holes could be achieved by an outward-directed supply flow. Because the supply tube inside the blade is limited in diameter, the velocities in the tube are large. If the supply flow is directed inward, the high flow momentum causes the spanwise velocity distribution to be skewed heavily toward the last (inner diameter) holes. If it is directed outward, the effect is lessened due to the smaller angle which the flow must turn to exit the film hole.

The film cooling hole pattern consists of five staggered rows of showerhead film holes. Figure 9 shows the film hole row placement relative to the leading edge of the blade. Computations using the viscous flow solver rvc3d [42] indicated that the attachment line for the blade was slightly offset from the geometric leading edge toward the pressure side of the blade. Further computations were used to attempt to place the center row of holes such that the flow from this row would evenly split

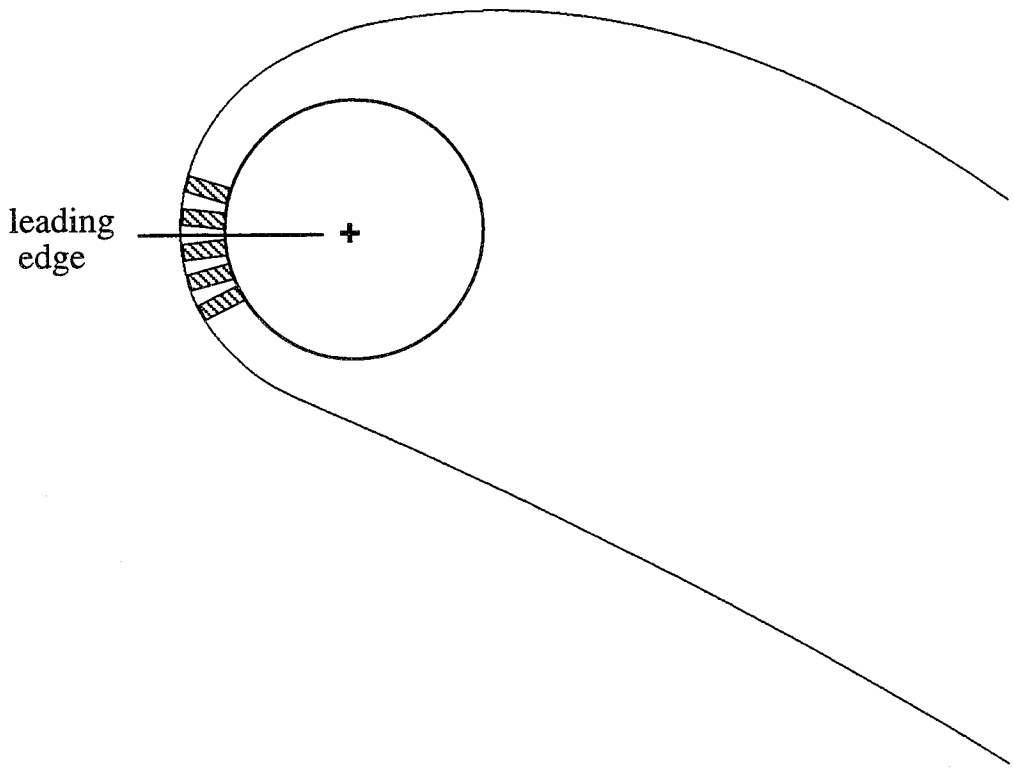

Figure 9: Test blade leading edge.

between the suction and pressure sides. Because the leading edge radius of the blade is 4.9 mm, and the last leg of the 6.3 mm diameter secondary flow passage is concentric with the blade leading edge circle, the radial length of the film holes is 1.75 mm. Since the holes are angled at 30°, their true length is 3.5 mm, resulting in a length-to-diameter ratio (L/d) of 3.5. This parameter is important in film cooling research, since it determines the characteristics of the flow exiting the hole. Much basic research has been done for large L/d values (greater than about 10), for example [9]. However, the small size of gas turbine blades usually causes L/d values to be much smaller, often in the range from 2 to 4. As a result, the flow issuing from the film holes is not fully developed, and depends on the length of the hole. The value of 3.5 in the present study was chosen as representative for highly angled holes.

Figure 10 shows the film cooling hole pattern as viewed on an unwrapped flat surface. As previously indicated, the film cooling holes are angled 30° to the blade surface in the spanwise direction, and 90° in the streamwise direction. This set of angles causes the hole exit shapes to be ellipses with aspect ratios of 2:1. The pitch-to-diameter ratio in both the spanwise and streamwise directions is 4.0, where the pitch is defined as the surface distance from the center of a given hole to the center of the next aligned hole. The diameter used is the true diameter of the holes (1.0 mm). There are 17 holes in rows 1, 3, and 5, and 16 holes in rows 2 and 4.

The test blade is instrumented with an array of 72 nickel thin-film gauges capable of

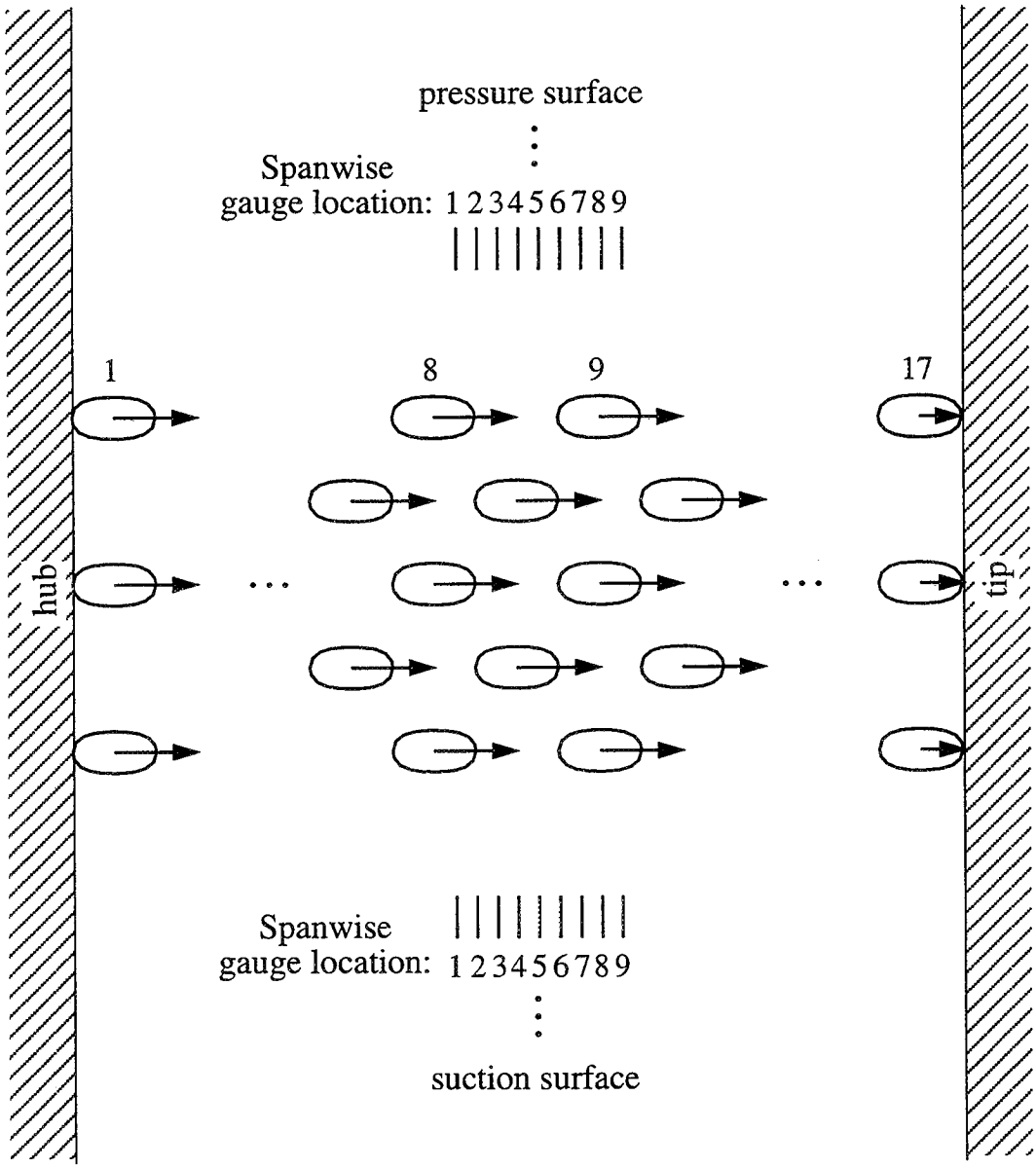

Figure 10: Film hole pattern and gauge spanwise location.

responding to high frequency changes in temperature. The gauges were manufactured by Tao Systems, Inc., and consisted of nickel sensing elements with copper leads. The temperatures measured by these gauges are used to determine film effectiveness and heat transfer coefficient profiles on the blade surface. The entire gauge array is shown in Figure 11. In order to allow spanwise resolution of the temperature profile behind the film cooling hole pattern, eight gauges were placed at each chordwise location. These eight gauges were situated to completely span one unit cell of the hole pattern, as shown in Figure 10. The gauges were deposited on a Kapton polyimide sheet by the manufacturer. This sheet was cemented to the blade surface over the Inconel foil heater. Figure 12 shows a schematic view of the layers on the blade surface. The thicknesses of the polyimide sheet, copper leads, and nickel gauges are 63.5 μm, 5.0 μm, and 0.25 μm, respectively. The test blade had been machined slightly smaller than the cascade blades to allow the layers of instrumentation and adhesive to bring the blade to the proper size. Because the showerhead region is free from instrumentation and adhesive, it was coated with a thin layer of wood putty to allow a smooth surface contour transition from the showerhead region to the instrumented portion of the blade. Covering the film holes was avoided by placing 1.0 mm pins in them during this coating process which were removed after the putty had hardened. Each gauge has a width of 0.3 mm, and the hole pattern has a pitch of 4.0 mm. The gap between adjacent gauges is 0.2 mm. The streamwise length of each gauge is 1.0 mm. There are nine gauge rows in the chordwise direction, four on the pressure surface, and five on the suction surface. The

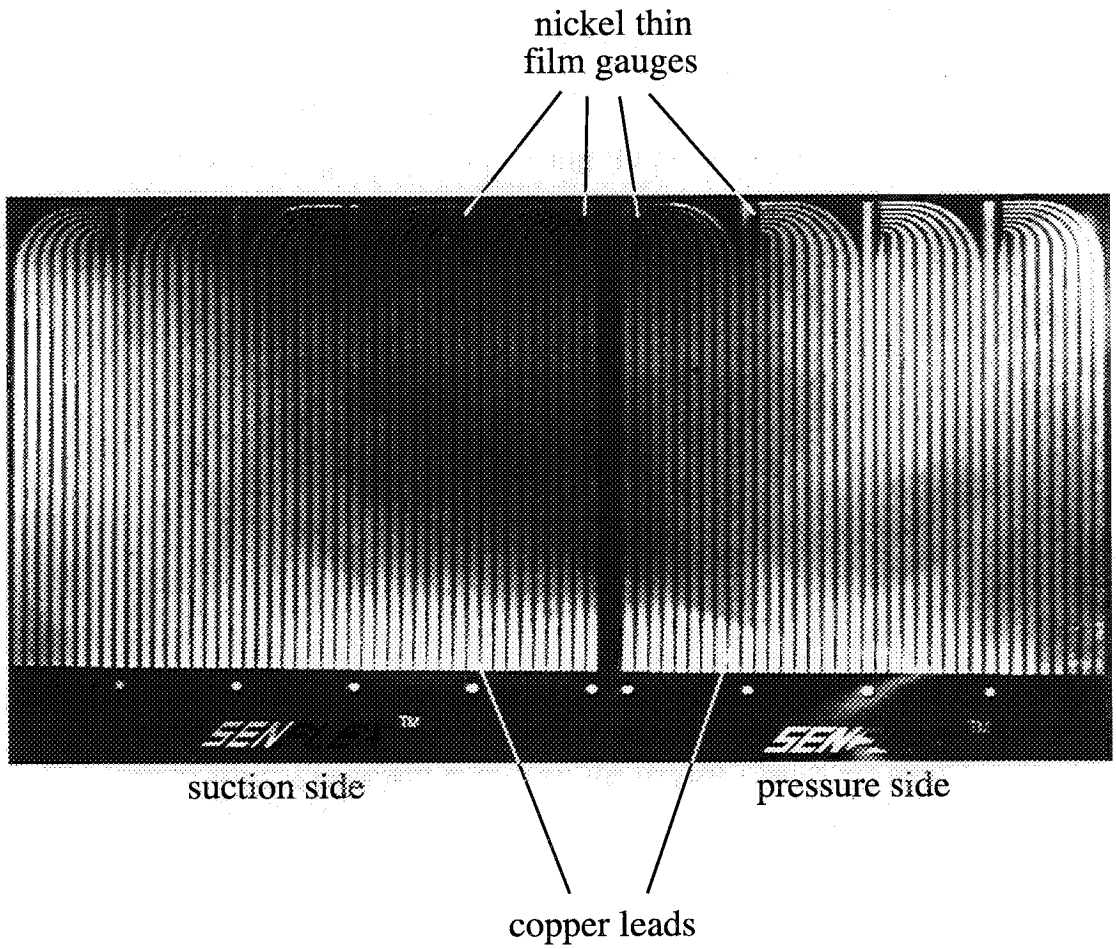

Figure 11: Thin–film gauge array.

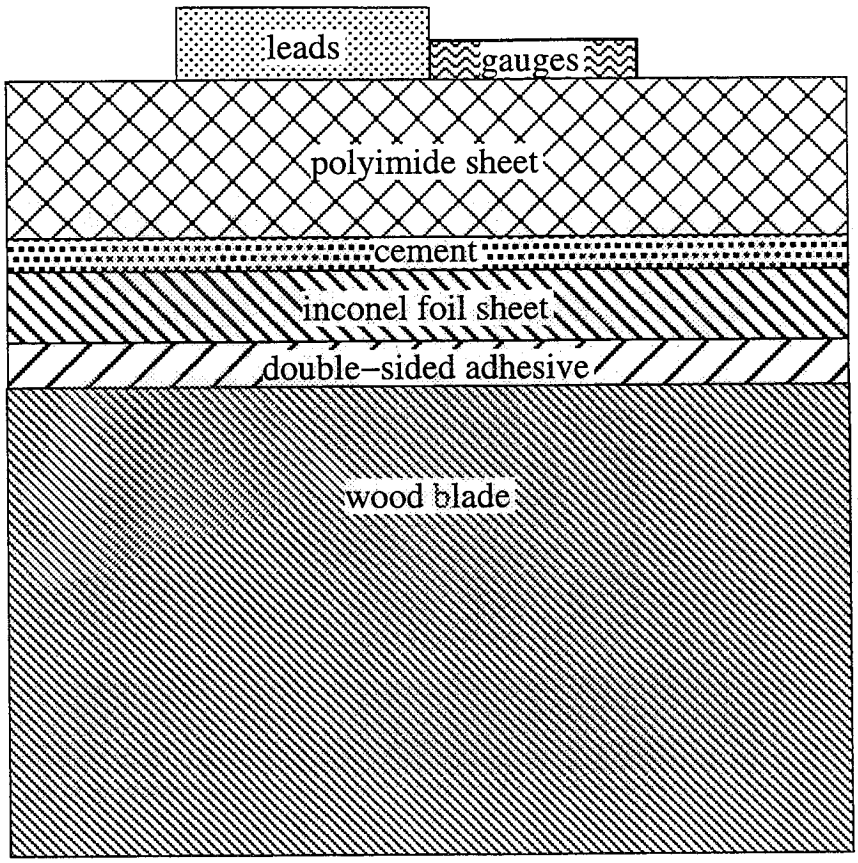

(thicknesses not to scale)

Figure 12: Blade surface layers.

first row on each surface is 8.0 mm downstream of the center row of film holes, and the subsequent rows are spaced at 13.5 mm intervals. This results in chordwise gauge locations summarized in the following table as a function of x/d, the surface distance of the gauge from the leading edge divided by the film hole diameter of 1.0 mm. Gauges are numbered sequentially from suction surface trailing edge to pressure surface trailing edge, and pressure surface distances are considered positive.

chord location	x/d
1	-62.0
2	-48.5
3	-35.0
4	-21.5
5	-8.0
6	8.0
7	21.5
8	35.0
9	48.5

Each individual gauge, as shown in Figure 13, consists of a serpentine pattern of nickel deposited on the polyimide substrate. Eight serpentine passes were required to give the desired electrical resistance of approximately 50 Ω per gauge. It was determined that lower resistances would result in excessive experimental error. In the manufacturing process, the entire gauge pattern including leads was initially deposited

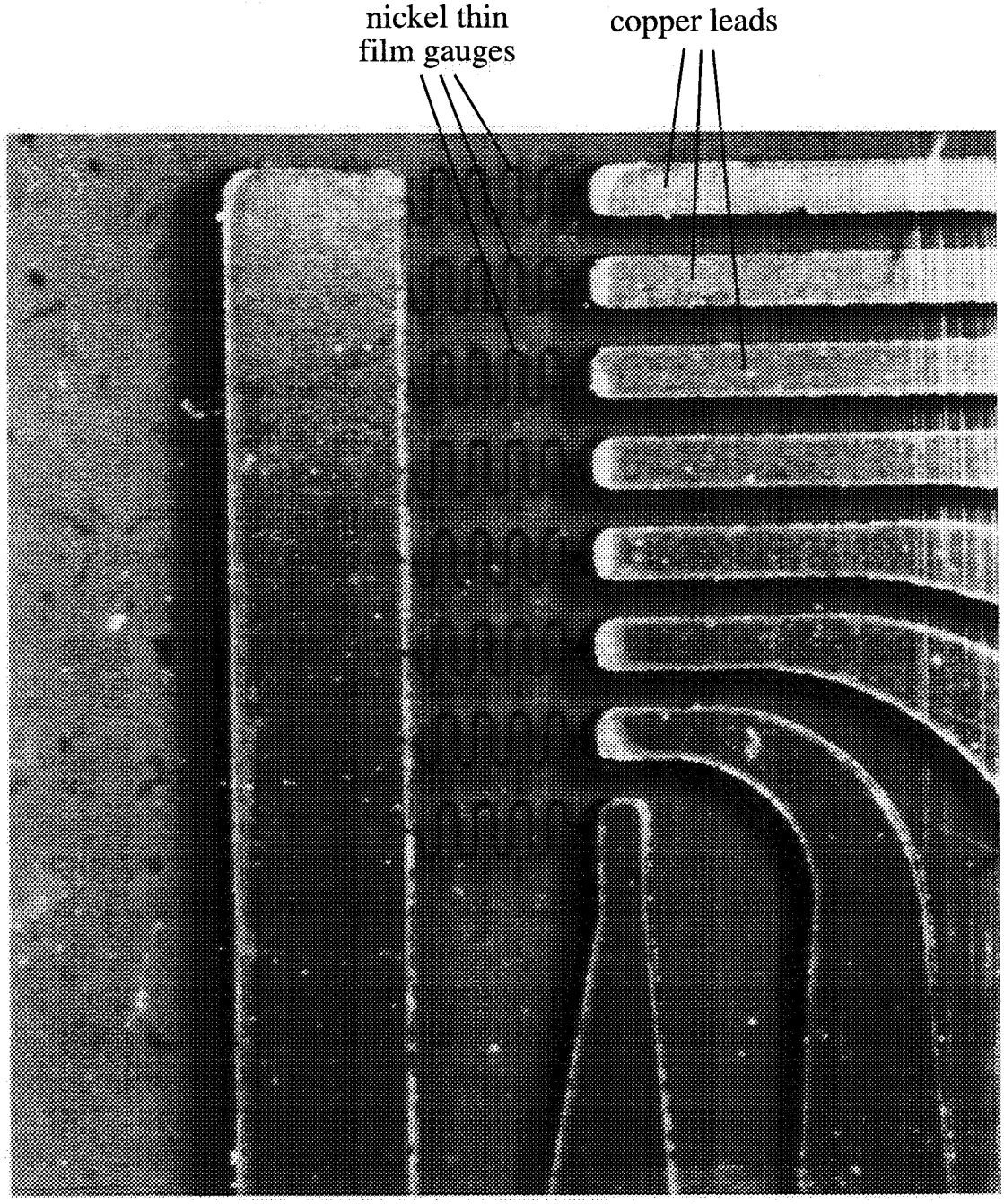

Figure 13: Thin–film gauge enlargement.

using nickel. Subsequently, the leads were covered with copper to decrease their electrical resistance, leaving only the active part of the gauge exposed. Because of the larger current flow area in the leads and the lower electrical resistivity of copper, the leads contributed less than 1.0% of the total circuit resistance.

The thin-film gauges were calibrated by the Cortez III Service Corporation in an isothermal chamber. The resistance of the gauges was measured at 10 °C intervals from 10 °C to 80 °C using the experimental current of 1.0 mA as the reference signal to simulate any resistive heating effect in the experiment. Any such effect was found to be negligible. Resistances were measured for each temperature starting with the lowest, progressing to the highest, then back to the lowest again to account for any hysteresis effect. The two readings for each gauge at each temperature were averaged, although the differences were again found to be negligible. Because of the slight non-linearity of the temperature-resistance curve, a quadratic equation was used to calibrate each gauge. Due to the expected temperature range of the experiment and to achieve a better correlation with the calibration data, a least squares fit to the data was performed using only the 20 °C to 60 °C calibration data. The resulting calibration curves were found to agree with the calibration data to within about 1.0 °C.

Figures 14 and 15 show the fully instrumented test blade suction and pressure sides, respectively. The rectangular plate on one end of the blade is used to mount the blade

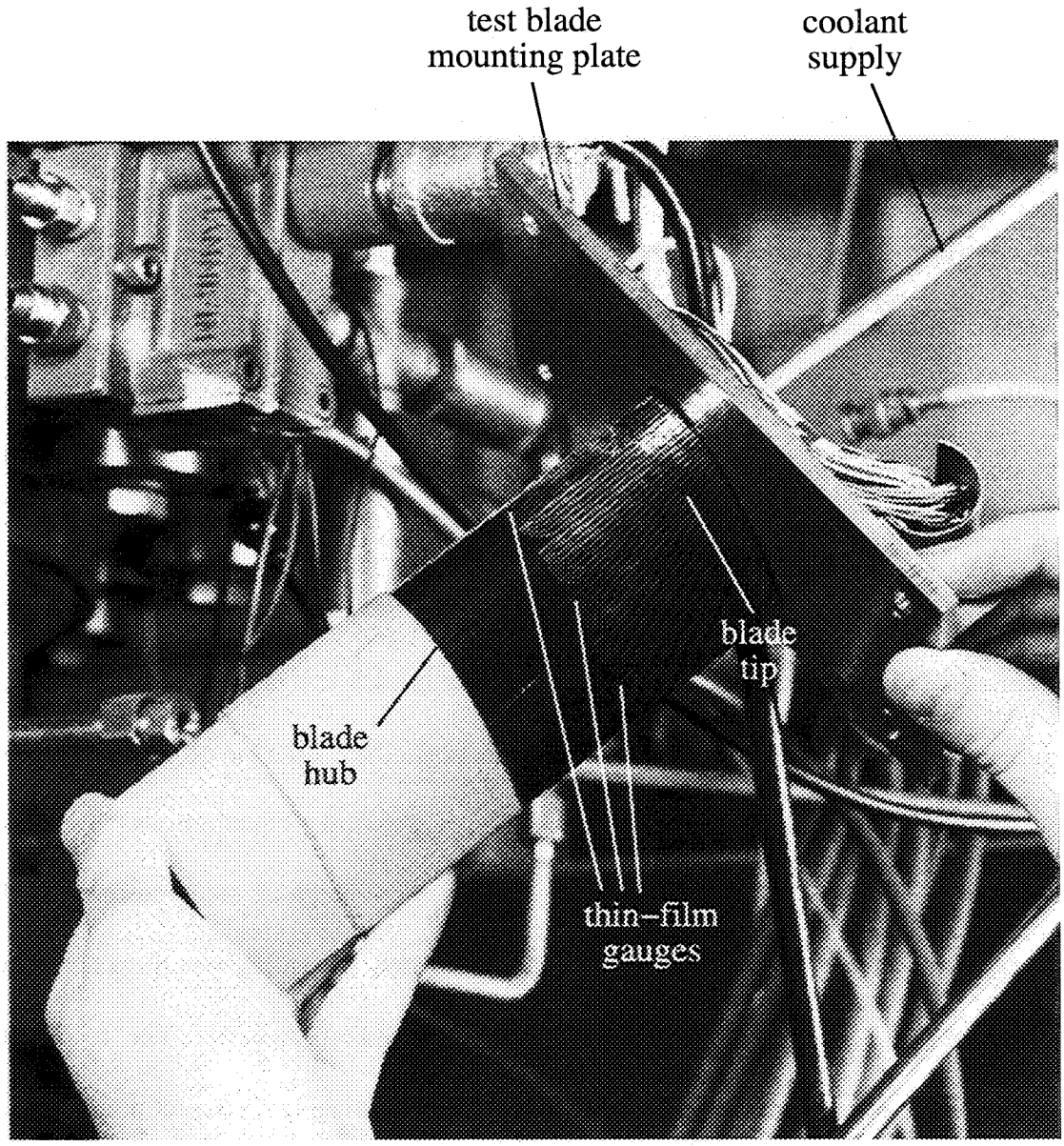

Figure 14: Instrumented blade suction side.

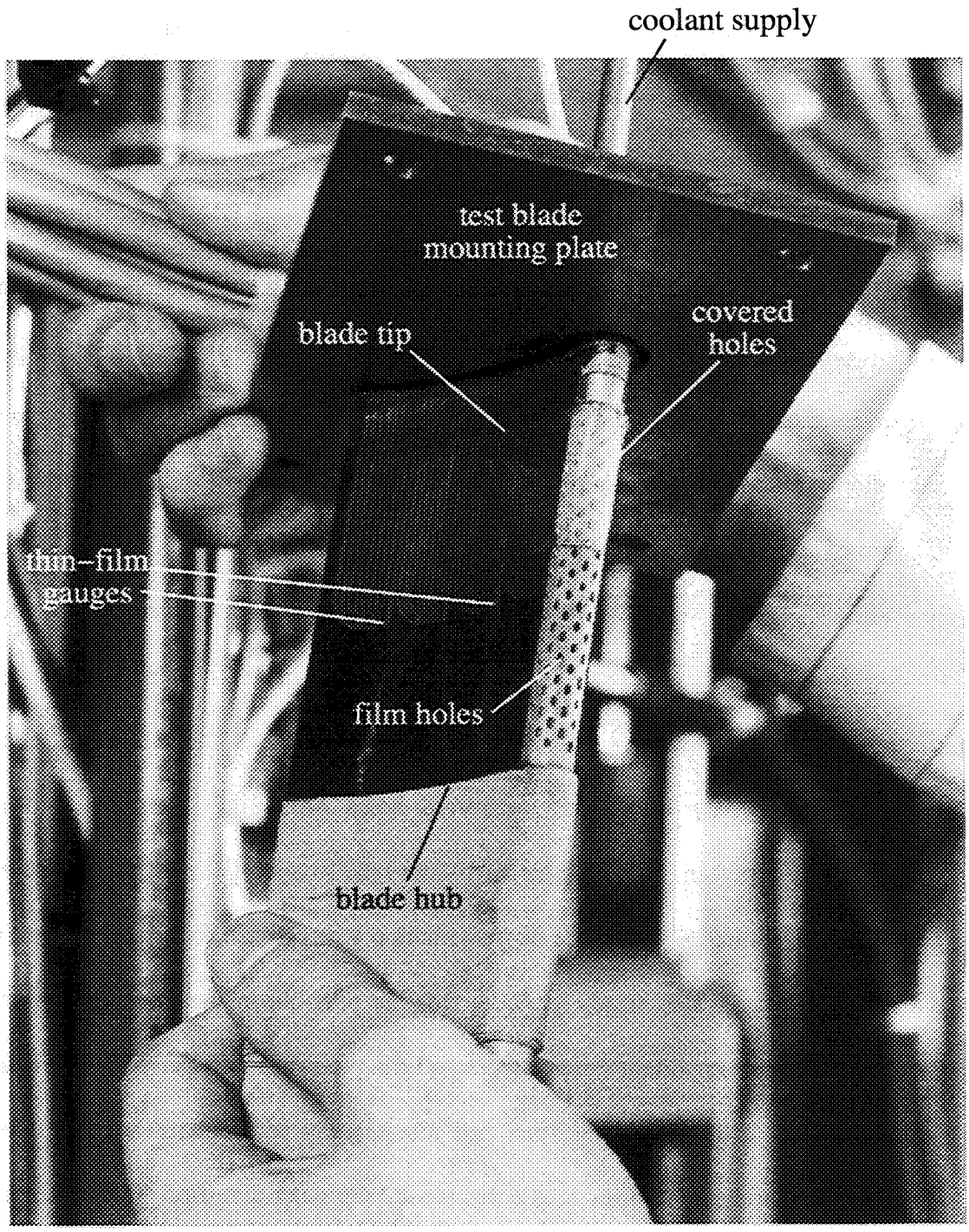

Figure 15: Instrumented blade leading edge and pressure side.

in the test section. The film cooling hole pattern originally was designed to extend the entire length of the flow annulus. However, preliminary bench tests indicated that even with the supply flow directed outward, the spanwise velocity distribution is skewed toward the last (outer diameter) holes. Additional bench tests were performed to measure the stagnation pressure supplying each film hole in the middle row of holes. There are 17 holes in the spanwise direction in the middle row. Hole 1 refers to the innermost hole and hole 17 refers to the outermost hole. With all holes open, and a flow rate corresponding to a blowing ratio of 1.0 with air as the secondary gas, stagnation pressure varied from 0 Pa at hole 1 to 4550 Pa at hole 17. Hole 9 had a pressure of 2516 Pa. However, holes 14 through 17 all had supply pressures within 70 Pa of each other. With this in mind, holes were incrementally covered with tape, starting with the outermost and progressing toward midspan. At each step, the stagnation pressures at each hole were measured. It was found that at each configuration, the five outermost uncovered holes had supply pressures within approximately 5 percent of each other. At inner hole locations, the supply pressures were reduced. Since the test blade instrumentation was planned to be at midspan, it is desired to establish as nearly periodic flow as possible in the midspan region. Clearly, the most important holes for establishing downstream periodicity in the midspan region are those at midspan and immediately adjacent toward the inner diameter, since the coolant flow is injected toward the outer diameter. Computations using the viscous flow solver rvc3d [42] indicated that flow from a given film hole migrates no more than about three hole pattern unit cell pitches in the spanwise

direction by the time it reaches the blade trailing edge. On the basis of this information and the desire to have at least one unit cell beyond the midspan hole uncovered, holes 11 through 17 were permanently covered with smooth tape. All holes in the other rows beyond this point were also covered. The tape covering these holes can be seen in Figure 15.

Test procedure

The following discussion will describe the procedure for a typical experimental session. After all equipment has been prepared and with the rig bellmouth remaining covered, the time-average temperature of all 72 thin-film gauges are recorded along with the rig inlet temperature, which is determined via the average of three thermocouples inside the covered rig, immediately upstream of the test blade. This information is used to calibrate any offset of the gauges relative to the reference inlet thermocouples. There was a slow drift of thin-film gauge readings relative to the inlet thermocouples, particularly on the pressure side of the blade. This drift occurred over a period of months, as the pressure side gauges gradually indicated higher temperatures due to higher resistances. It was suggested by the calibration company to adjust the experimental temperatures by the measured offset at room temperature. However, the increase in gauge resistance may have been due to a gradual erosion of the gauge material by particulates in the laboratory air. This explanation is strengthened by the fact that particles would impact on the pressure side of the blade

because their density is greater than that of air. Indeed, a black film was found on the pressure side of the blade upon inspection. Such an explanation for the gauge drift gives a unique adjusted calibration curve for a given offset at room temperature, assuming the resistivity of the gauge to be constant. This adjustment was used in the data reduction.

After the calibration readings, the rig bellmouth cover is removed, and the secondary flow (either air or CO_2) is initiated. The secondary flow power supply is turned on and set to the proper voltage. A waiting period of up to an hour is required to allow the secondary flow to reach steady state conditions. When this occurs, the valves are opened to allow the primary rig flow to begin. The primary flow is adjusted to reach an inlet Mach number of 0.27. Next, the rotor is spun to the required speed. The pertinent data are then recorded for each row of gauges, allowing about 1 minute between each set of readings for the steady component of the gauge readings to reach a constant value. The Escort data system reads the data once per second for twenty seconds and records the average value of all data.

Simultaneous to every steady data reading, the amplified AC component of the gauge signals are recorded on the Masscomp data system at a frequency necessary to record about 50 time steps per wake passing. For the highest rotor speed, this results in a frequency of about 140 kHz. The signals are recorded for a period of about 50 rotor revolutions, or 1200 wake passings. The AC data are passed through a 5 kHz low-

pass filter to remove very high frequency noise from the data. This was necessary because the phase-average unfiltered data exhibited an unacceptable level of high frequency noise. Phase-averaging was accomplished by placing the AC data into bins based on their occurrence in time relative to the once per revolution signal. The number of bins is slightly less than the number of points measured per wake passing to ensure that all bins receive at least one reading per wake passing. The readings for each bin are then summed and averaged. There was also a problem with a 60 Hz noise signal in the lab. This was remedied by averaging the unsteady data over a sufficiently large number of wake passing periods.

After all data are recorded for a given rotor speed, the procedure is repeated for the other rotor speeds of interest. Next, the power supply to the Inconel foil heater on the blade is turned on, and the voltage is set at the test value. Several minutes are allowed for the blade to reach a steady periodic temperature. The entire test procedure is now repeated for all rotor speeds. The comparison of the data sets with and without the foil heater allows determination of heat transfer coefficients.

The entire test procedure described to this point is repeated for both air and CO_2 at blowing ratios of 0.5 and 1.0. In order to determine recovery temperatures on the blade, the film holes are taped over with thin cellophane tape, and the test procedure is conducted as before, both with and without heating the blade. The heated blade case is used to establish non-film-cooled heat transfer coefficient distributions.

Baseline steady cases for comparison to the rotating data are established by two different methods. In the first method, eight test cases are investigated with the rotor fixed in eight equispaced positions relative to the test blade. The angular rotation between adjacent positions is 1.875°, which is equivalent to a midspan distance 1.75 times the cylindrical rod diameter. The results from these cases were averaged for comparison to the rotating cases. The advantage of this method is that it represents a true limiting case for the rotating data, since the blockage of the cylindrical rods remains present as it is for the rotating cases. Unfortunately, the results must be averaged over many incrementally shifted rotor positions to achieve a true average, and the time required to record such data is prohibitive. Alternatively, the rotor was removed entirely and a baseline case was established with no upstream rotor. This has the advantage of simplicity and short test time, but does not represent a true limiting case, as mentioned previously.

Data reduction procedure

The experiment was conducted for fixed values of Strouhal number. The definition of Strouhal number used to determine the required rotor speed is:

$$St = \frac{2\pi NDn}{60U}$$

where N is the rotor speed in rpm, D is the cylindrical rod diameter, n is the number

of rods in the rotor, and U is the cascade inlet axial velocity. This definition is consistent with that used in the majority of previous rotor-wake experiments.

The definition of film effectiveness as given for compressible flow is:

$$\eta = \frac{T_f - T_r}{T_c - T_r}$$

where T_f is the film temperature, T_r is the recovery temperature, and T_c is the injectant stagnation temperature. The various temperatures are measured under different experimental conditions in separate test runs. The film temperature and injectant stagnation temperature are measured with the film cooling on, and the recovery temperature is measured with the film cooling off. Since laboratory air is used for the primary flow, it is not in general possible to maintain the same inlet temperature for both test runs. Thus the recovery temperature must be corrected to match the film-cooled case. It is known that:

$$T_r = T(1 + \frac{\gamma - 1}{2} r M^2)$$

and

$$T_o = T(1 + \frac{\gamma - 1}{2} M^2)$$

where T_o is the free-stream stagnation temperature, T is the free-stream static temperature, r is the recovery factor, and M is the free-stream Mach number. Taking the ratio of recovery to stagnation temperature:

$$\frac{T_r}{T_o} = \frac{1 + \frac{\gamma - 1}{2} r M^2}{1 + \frac{\gamma - 1}{2} M^2}$$

If γ, r, and M are all invariant with film blowing rate at a particular location on the blade, then so is the temperature ratio:

$$\left(\frac{T_r}{T_o}\right)_b = \left(\frac{T_r}{T_o}\right)_{nb}$$

where the subscripts b and nb indicate blowing and no blowing, respectively. Substituting back into the definition of film effectiveness:

$$\eta = \frac{T_f - (T_{r,nb})\left(\frac{T_{o,b}}{T_{o,nb}}\right)}{T_c - (T_{r,nb})\left(\frac{T_{o,b}}{T_{o,nb}}\right)}$$

The definition of heat transfer coefficient as given previously is:

$$h = \frac{q''}{T_w - T_f}$$

where T_f is the film temperature and T_w is the wall temperature with film cooling and a local heat flux of q". Here the sign of the denominator is defined for a positive heat flux into the flow. Again, the film temperature and wall temperature are measured experimentally in separate test runs, necessitating corrections to account for differences in flow conditions between the two test runs. A correction must be applied not only for differences in inlet stagnation temperature, but also for differences in injectant stagnation temperature, which may also vary slightly between test runs. It is necessary to determine the film temperature which would result if the heat flux were set to zero in the heated wall test run. To do this, the definitions of film effectiveness for both runs are used:

$$\eta_{nh} = \frac{T_{f,nh} - (T_{r,nb,nh})\left(\frac{T_{o,b,nh}}{T_{o,nb,nh}}\right)}{T_{c,nh} - (T_{r,nb,nh})\left(\frac{T_{o,b,nh}}{T_{o,nb,nh}}\right)}$$

and

$$\eta_{h} = \frac{T_{f,h} - (T_{r,nb,nh})\left(\frac{T_{o,b,h}}{T_{o,nb,nh}}\right)}{T_{c,h} - (T_{r,nb,nh})\left(\frac{T_{o,b,h}}{T_{o,nb,nh}}\right)}$$

where subscripts h and nh indicate heating and no heating, respectively. If it is

assumed that the film effectiveness is the same for both wall heat flux conditions, then the film temperature for the heated wall case is:

$$T_{f,h} = (T_{f,nh} - T_{r,nb,nh}(\frac{T_{o,b,nh}}{T_{o,nb,nh}}))(\frac{T_{c,h} - T_{r,nb,nh}(\frac{T_{o,b,h}}{T_{o,nb,nh}})}{T_{c,nh} - T_{r,nb,nh}(\frac{T_{o,b,nh}}{T_{o,nb,nh}})}) + T_{r,nb,nh}(\frac{T_{o,b,h}}{T_{o,nb,nh}})$$

and the heat transfer coefficient may be determined from:

$$h = \frac{q''}{T_w - T_{f,h}}$$

The Nusselt number is typically defined in turbine heat transfer studies as:

$$Nu = \frac{hc}{k}$$

where c is the blade chord length (63.5 mm in this experiment), and k is the thermal conductivity of the film. For air injection, a constant thermal conductivity of 0.0263 W/m·K is used [40] based on a mean temperature of 300 K. For carbon dioxide injection, a mixture of gases is present at the wall, and the procedure of Bird et al. [41] is used to estimate the thermal conductivity at the wall. For this analysis, a constant thermal conductivity of 0.01655 W/m·K is used for pure CO_2 [40], again at 300 K. The analysis also requires knowledge of the dynamic viscosity of both gases. These values at 300 K are 1.846 x 10^{-5} N·s/m^2 and 1.49 x 10^{-5} N·s/m^2 for air and

carbon dioxide, respectively [40]. The flow on the blade may be considered fully turbulent due to the presence of the leading edge injection. The ratio of eddy thermal diffusivity to eddy mass diffusivity may then be assumed to be 1.0 by the analogy between turbulent heat and mass transfer [41]. With this assumption, the local mole fraction of carbon dioxide may be taken to be equal to the local film effectiveness because of the similarity of the thermal and mass boundary layers. The equations for a mixture of gases as given by Bird et al. [41] are:

$$k_{mix} = \sum_{i=1}^{n} \frac{x_i k_i}{\sum_{j=1}^{n} x_j \Phi_{ij}}$$

where k_{mix} is the effective thermal conductivity of the mixture, x_i is the mole fraction of component i, k_i is the thermal conductivity of component i, and Φ_{ij} is given by:

$$\Phi_{ij} = \frac{1}{\sqrt{8}}\left(1 + \frac{M_i}{M_j}\right)^{-1/2}\left[1 + \left(\frac{\mu_i}{\mu_j}\right)^{1/2}\left(\frac{M_j}{M_i}\right)^{1/4}\right]^2$$

where M_i is the molecular weight of component i and μ_i is the dynamic viscosity of component i. Using the previous two equations with the properties of air and carbon dioxide given, the following equation was derived to determine the thermal conductivity of the mixture:

$$k_{mix} = 0.0263 \cdot \left(\frac{1 + 0.258\eta - 0.045\eta^2}{1 + 0.774\eta + 0.150\eta^2}\right) \frac{W}{m \cdot K}$$

3. EXPERIMENTAL RESULTS

Time-resolved results

As indicated in Chapter 1, one of the goals of this study was to obtain time-resolved film effectiveness and Nusselt number distributions for various test conditions. The next several plots graphically show the steps involved in attempting to obtain these quantities. Due to the massive quantities of data recorded, representative cases are presented here.

Figure 16 shows the phase-average voltage trace for a typical single gauge with film injectant. It can be seen that the filtering process and averaging of many wake passing cycles has provided a rather smooth periodic profile. However, the magnitudes of the variations are extremely small. The absolute value of the voltages is irrelevant, since the voltage trace contains only the AC portion of the signal. When the AC and DC voltages are combined and converted to a temperature using the gauge calibration curve, the result is a phase-average temperature trace as shown in Figure 17. The conversion to temperature does not change the character of the curve, since the changes in temperature are small, and the calibration curve is nearly linear. In fact, the temperature variations shown in Figure 17 are only about 0.2% of the difference in temperature between the free-stream and the injectant. Figure 18 shows the phase-average temperature trace for the same gauge with no film injectant. The

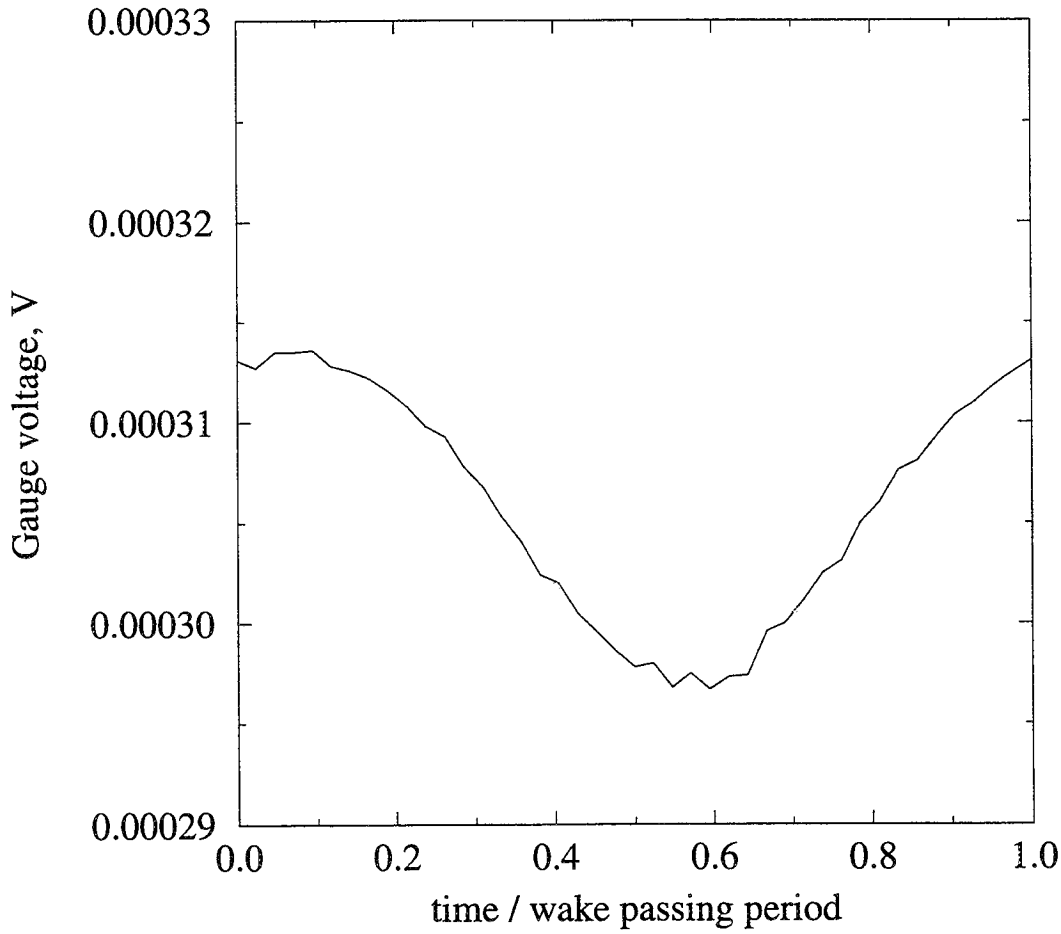

Figure 16: Phase–average voltage for a single gauge.

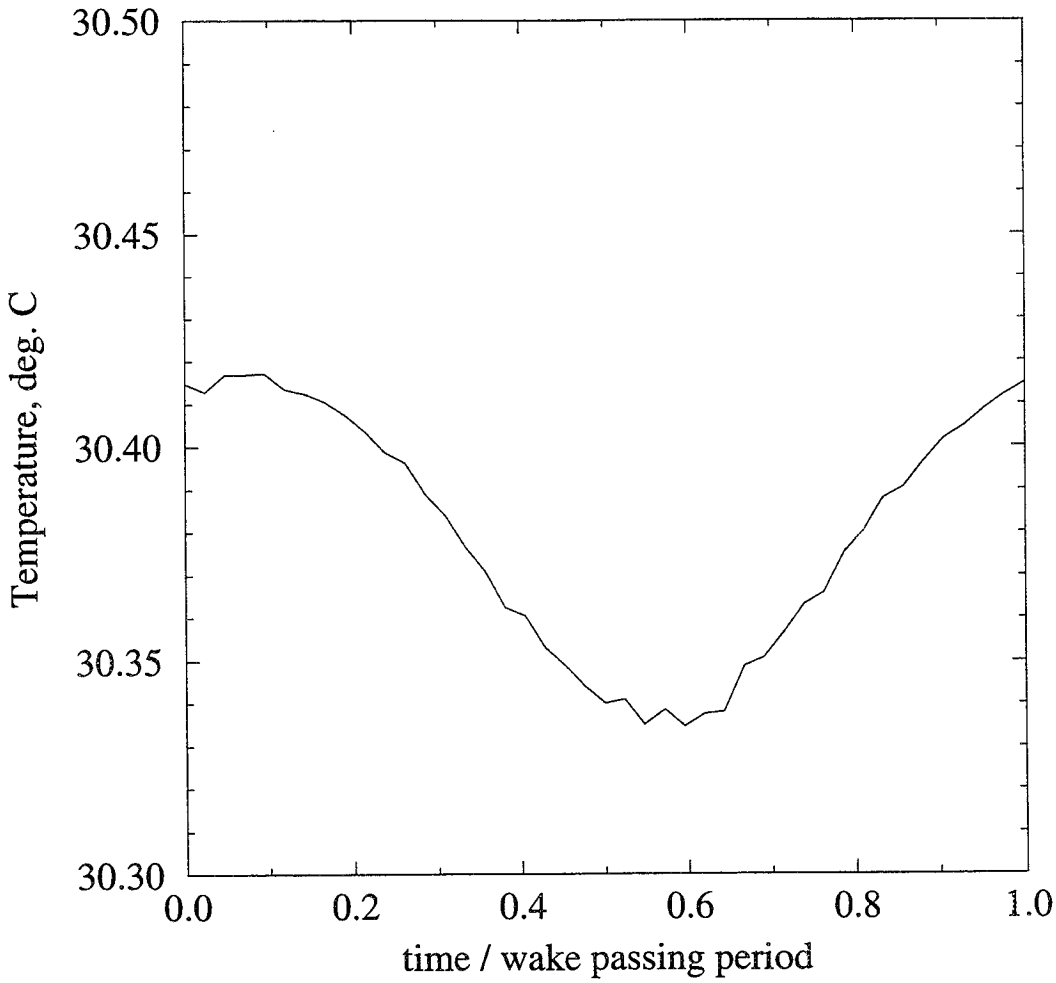

Figure 17: Phase–average temperature for a single gauge with film injection.

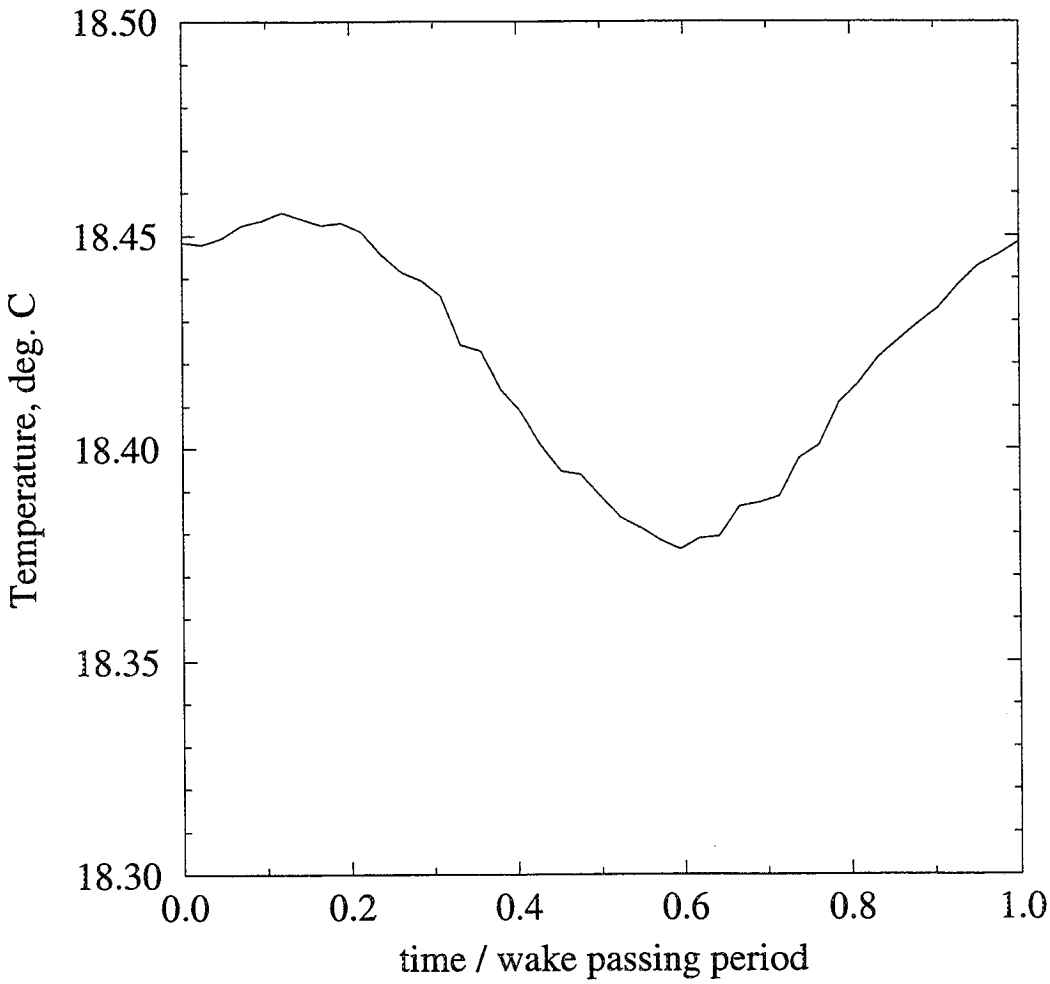

Figure 18: Phase–average temperature for a single gauge without film injection.

temperatures are lower because the injectant is hotter than the free-stream. Surprisingly, the curve shows the same behavior as in Figure 17, with the peak shifted only very slightly to the right, and the magnitude of variation reduced slightly. The difference between the curves in Figures 17 and 18 is essentially the numerator in the film effectiveness definition, and so this difference is proportional to the film effectiveness. Because the curves exhibit similar behavior, the variations cancel out in the difference, and the unsteady film effectiveness is constant in time within experimental accuracy. However, even if the curves were not similar, the very small magnitude of the temperature variations would result in only minor variations in film effectiveness.

The definition of film effectiveness assumes that the heat flux at the wall is zero. A proper definition of unsteady film effectiveness thus requires that the heat flux at the wall be zero at all times. Computationally, this is easily accomplished by setting the temperature gradient to zero at the wall for each time step. This was in fact done for the computational work in this project. An identical experiment would require the use of a substrate material under the gauges having zero thermal conductivity. Obviously, this is impossible, and so transient thermal conduction in the substrate is a problem. The film temperature required by the film effectiveness definition is then not equal to the actual wall temperature, but is rather the temperature the wall would reach if it were adiabatic. The magnitude of this effect depends on the frequency of the free-stream temperature fluctuation and the substrate properties, and is in general high for

the frequencies of this study. A procedure is described in Appendix II which enables estimation of the periodic adiabatic wall temperature from the measured periodic surface temperature. Using this procedure, the corrected film temperature for the data in Figures 17 and 18 is shown in Figure 19. It can be seen that the magnitude of the adiabatic wall temperature variations is much greater than the measured wall temperature variations, by a factor of about 50, and the peak temperature has shifted. However, the procedure described in Appendix II also amplifies any noise in the measured signal, since it involves the derivative of measured temperature with time. This relative increase in the noise is apparent in Figure 19.

Despite the increased variations in the corrected wall temperatures, the periodic temperature profiles with and without injectant are still similar for the gauge shown, and these variations again cancel in the film effectiveness definition. Figure 20 shows the phase-average film effectiveness variation using the corrected temperatures. The variation is small for this particular gauge. Other gauges showed larger time variations of film effectiveness, but these were random and lacked repeatability. Because of the increase in noise caused by the correction procedure, it is difficult to glean much information from the results of individual gauges. The Nusselt number results for individual gauges showed even more noise than the film effectiveness results. For this reason, the unsteady film effectiveness and Nusselt number were span-averaged to determine if any trends would emerge. Figures 21 through 24 present these span-average data for each gauge row with a wake passing Strouhal

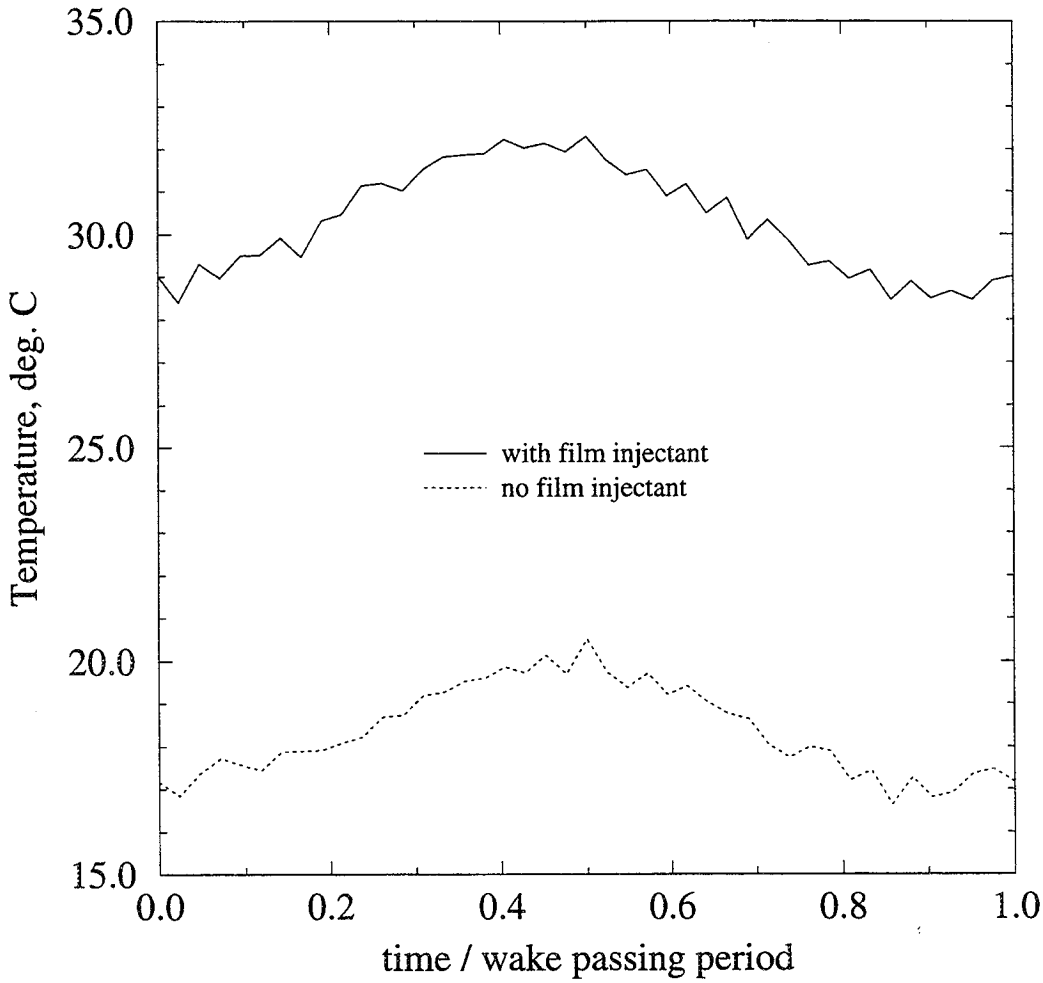

Figure 19: Corrected phase–average temperatures for a single gauge.

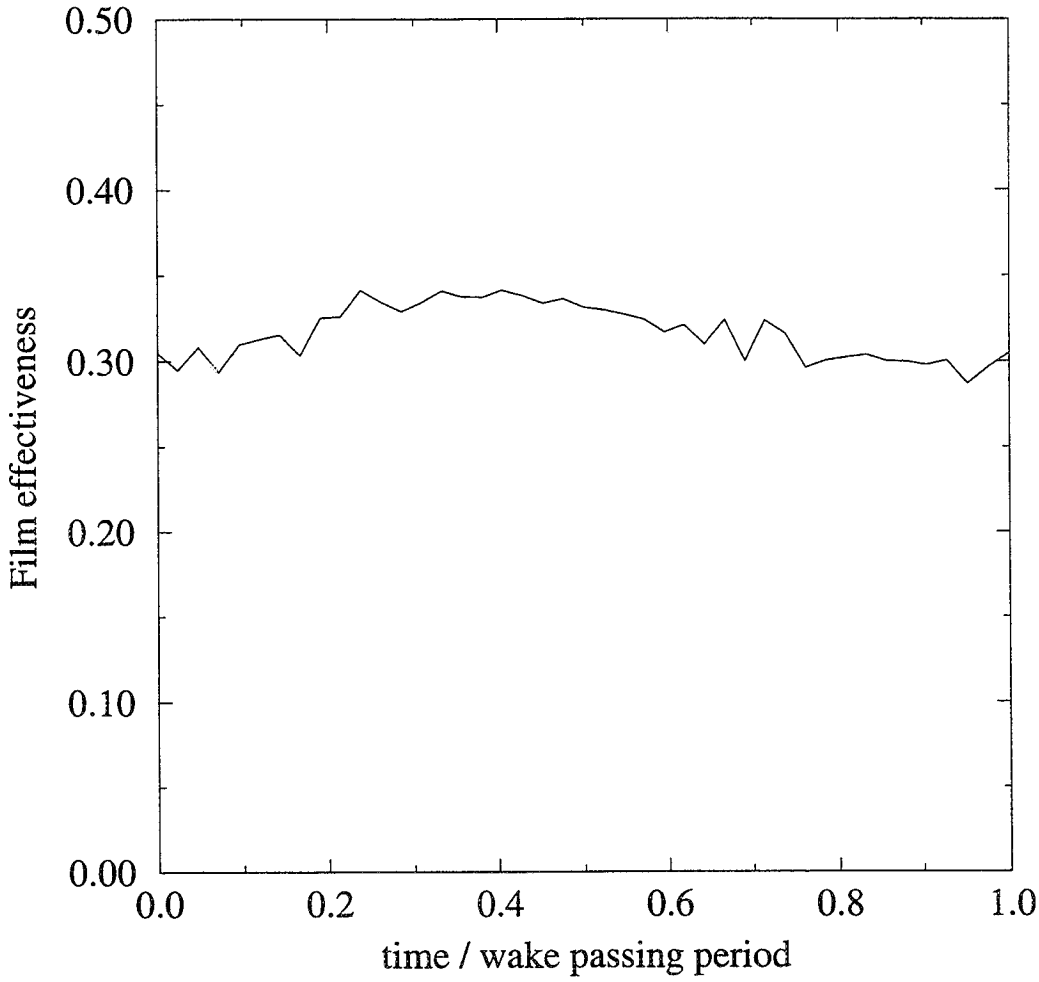

Figure 20: Corrected phase–average film effectiveness for a single gauge.

number of 0.600.

Figures 21 and 22 show film effectiveness values for the suction and pressure surface gauges, respectively. It can be seen that even with span-averaging, the high frequency fluctuations are large relative to the overall trends. Certainly at the downstream locations (chords 1, 2, 3, 8, and 9), the film effectiveness is effectively constant with time. Chord 4 shows a large reduction in film effectiveness, and chord 7 shows a smaller reduction which occurs at the same dimensionless time of 0.6, while chord 6 exhibits a small increase near that time. The uncertainty in the data warrants caution in focusing on small trends, although perhaps a wake effect is travelling down the blade and causing out-of-phase effects at different chordwise locations. It is interesting that chords 4 and 7 seem to have a similar trend, since both are the second gauge row from the film holes, and thus are the same distance from the leading edge.

Figures 23 and 24 show Nusselt number values for the suction and pressure surface gauges, respectively. Again, high frequency fluctuations are present which are now more pronounced at the near-hole locations (chords 5 and 6). The Nusselt number trends seem to follow the film effectiveness trends for each gauge row, with higher Nusselt numbers associated with higher film effectiveness values. Higher Nusselt numbers are seen near a dimensionless time of 0.6 for both chords 5 and 6, which may indicate the mechanism responsible for the known enhancement of Nusselt number in the stagnation region due to wake passing (O'Brien [5]).

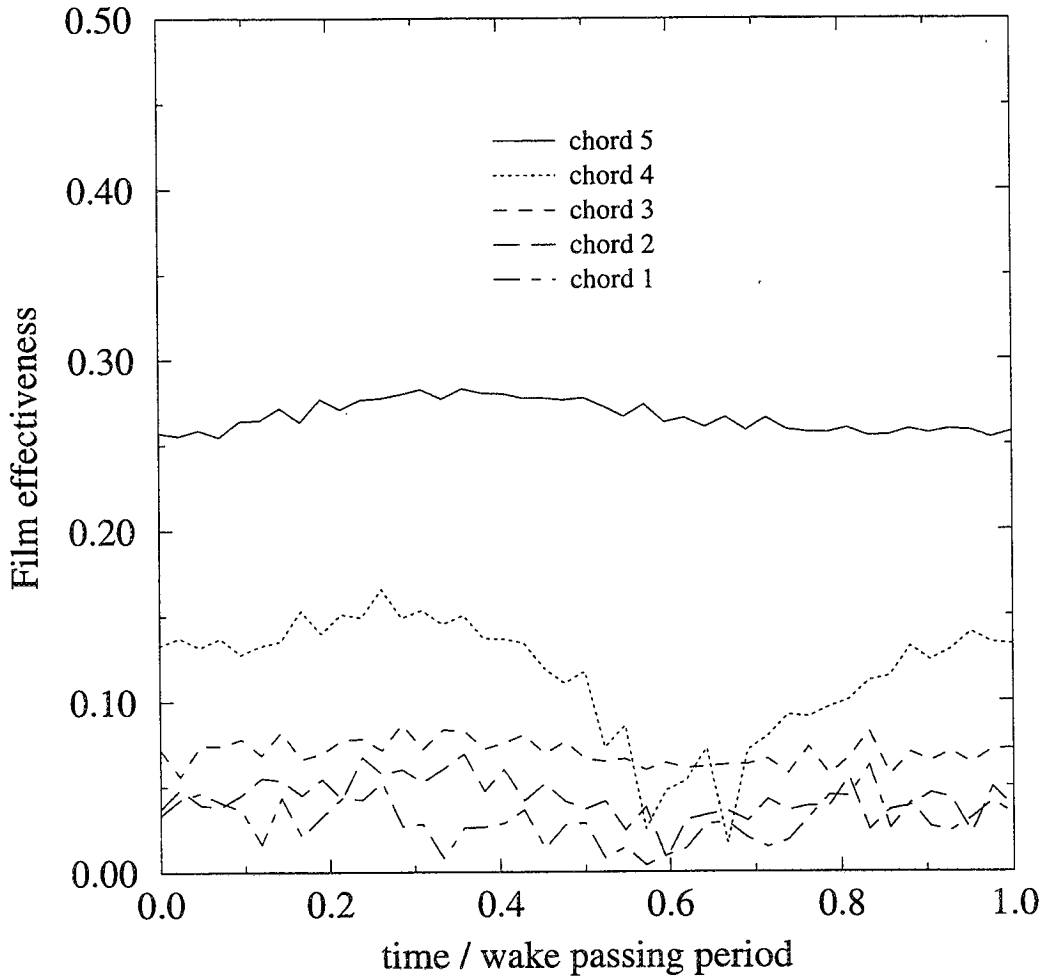

Figure 21: Span–average film effectiveness on suction surface for St=0.600.

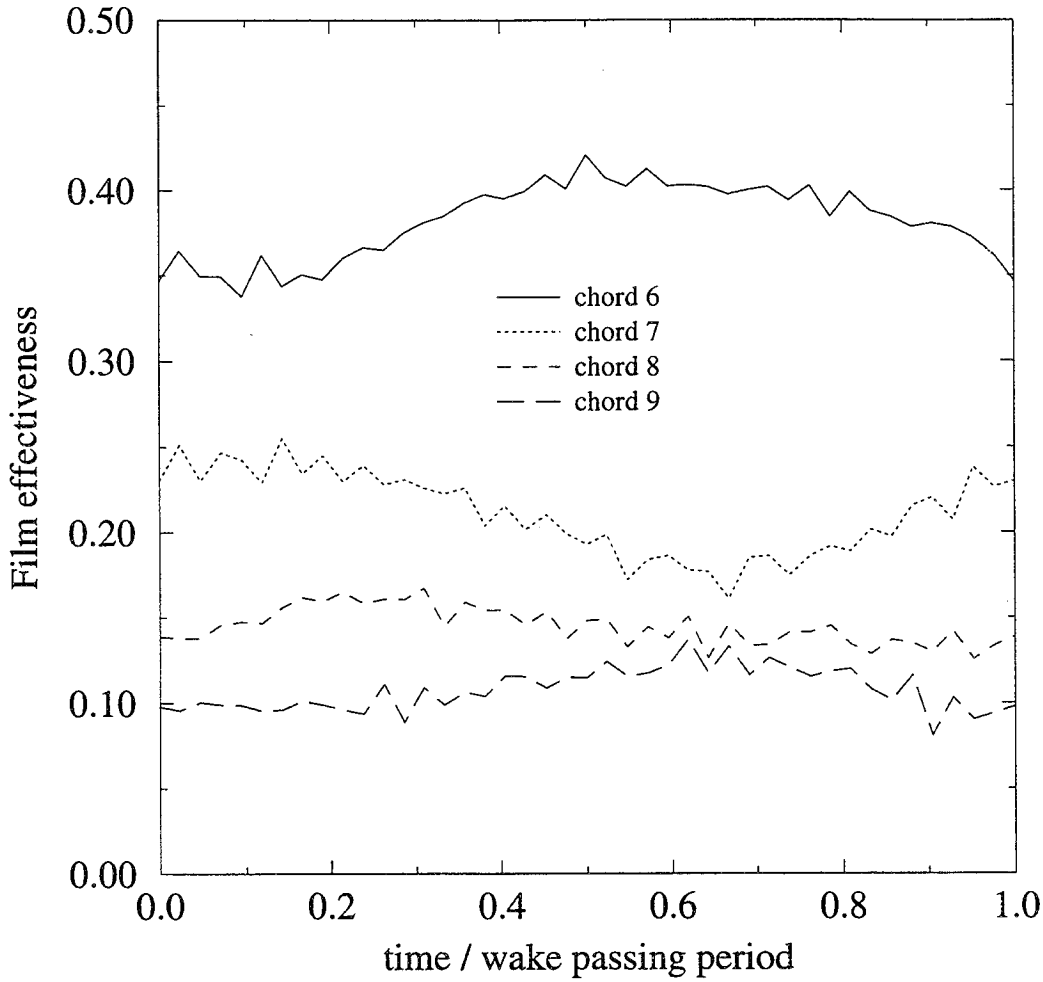

Figure 22: Span–average film effectiveness on pressure surface for St=0.600.

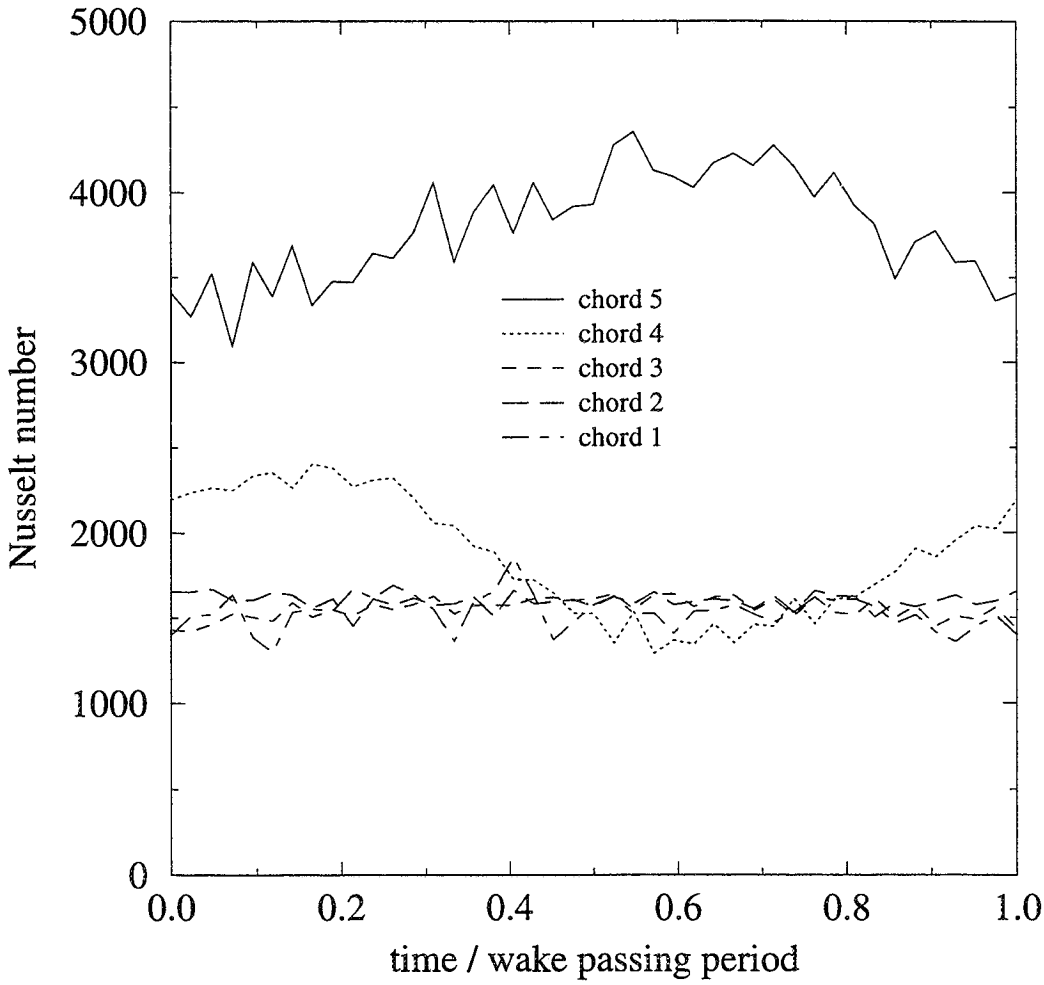

Figure 23: Span–average Nusselt number on suction surface for St=0.600.

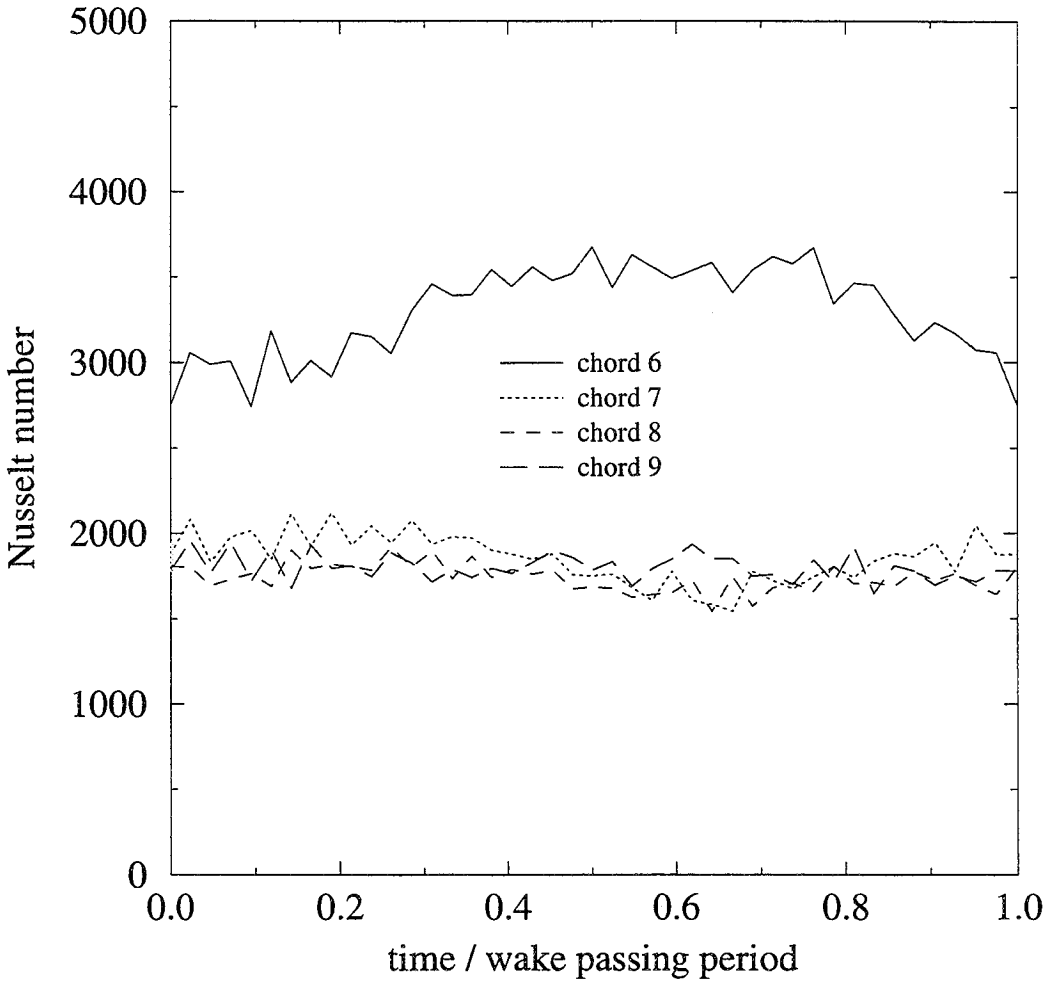

Figure 24: Span–average Nusselt number on pressure surface for St=0.600.

Figures 25 through 36 present the corrected phase-average film effectiveness and Nusselt number plots for Strouhal numbers of 0.500, 0.250, and 0.167. The high frequency fluctuations are higher for these cases because of differences in the 5 kHz low-pass filtering process. The 0.600 Strouhal number data was filtered during data recording, while the lower Strouhal number data was filtered during post-processing. Apparently differences between the two processes removed different levels of noise from the data. In view of the uncertainty in the unsteady data by both filtering processes, it was decided not to re-record the data using a common filtering process. Both filtering processes retain the lower (near wake passing) frequency fluctuations since they only filter frequencies higher than 5 kHz. It is difficult to derive any conclusions from Figures 25 through 36 other than the point that the film effectiveness and Nusselt number distributions are nearly constant within the admittedly high experimental uncertainty. They are presented here for completeness.

It was concluded that the instrumentation as configured is unable to resolve much meaningful unsteady variation in film effectiveness, at least at the frequencies of this study. Whether that is due to the deficiencies of the instrumentation or because the film effectiveness does not exhibit high frequency variations is an open question. Steady results presented later in this chapter show a consistent detrimental effect of wake passing on steady film effectiveness, but it is possible that this effect occurs only in a steady sense, and the film effectiveness does not undergo a large variation with time. This question could be resolved in the future through the use of double-

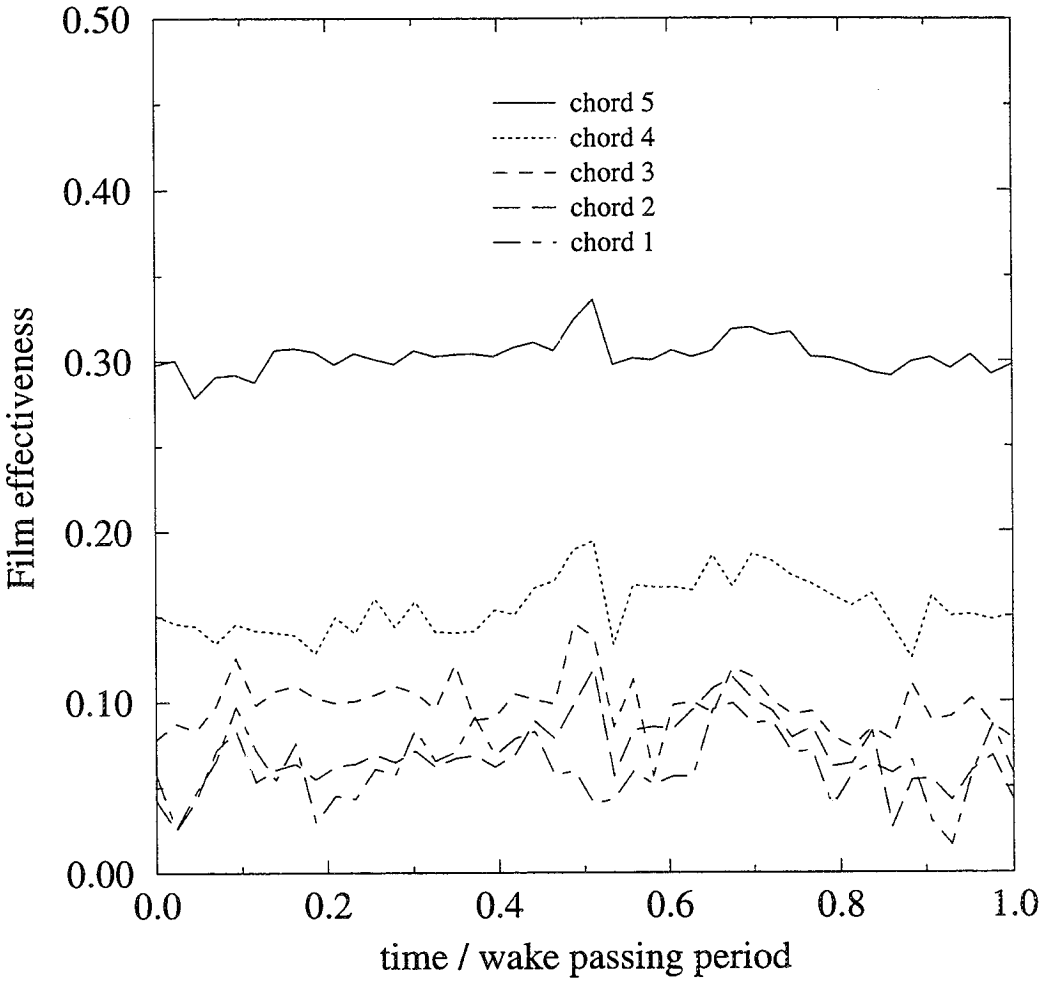

Figure 25: Span–average film effectiveness on suction surface for St=0.500.

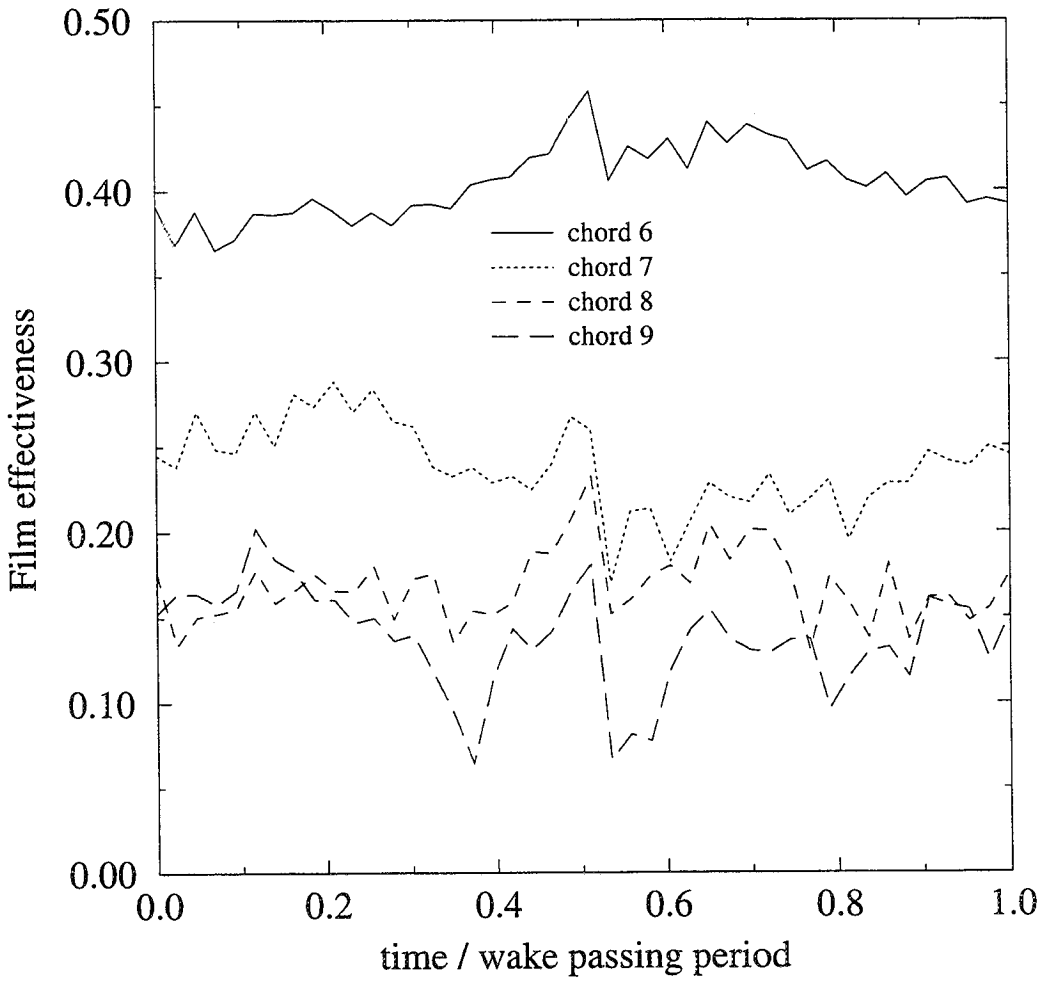

Figure 26: Span–average film effectiveness on pressure surface for St=0.500.

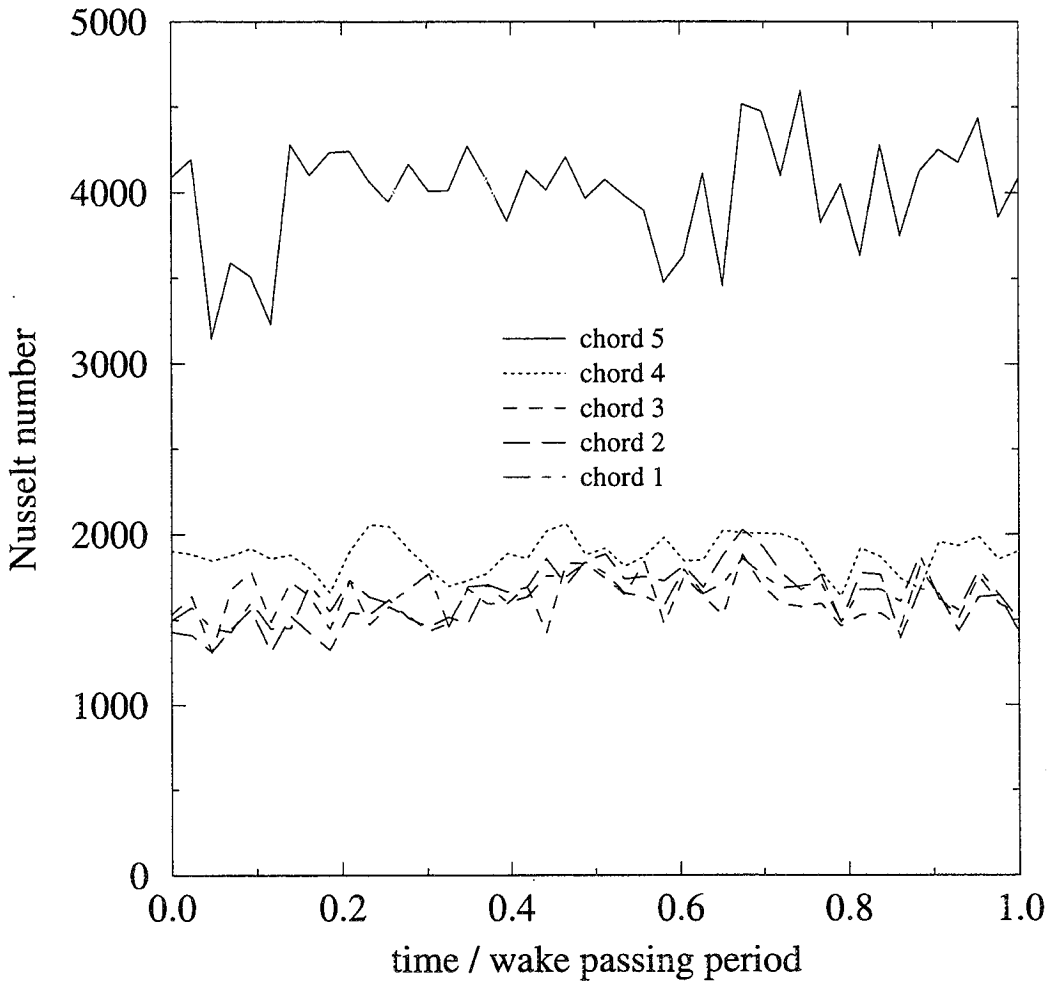

Figure 27: Span–average Nusselt number on suction surface for St=0.500.

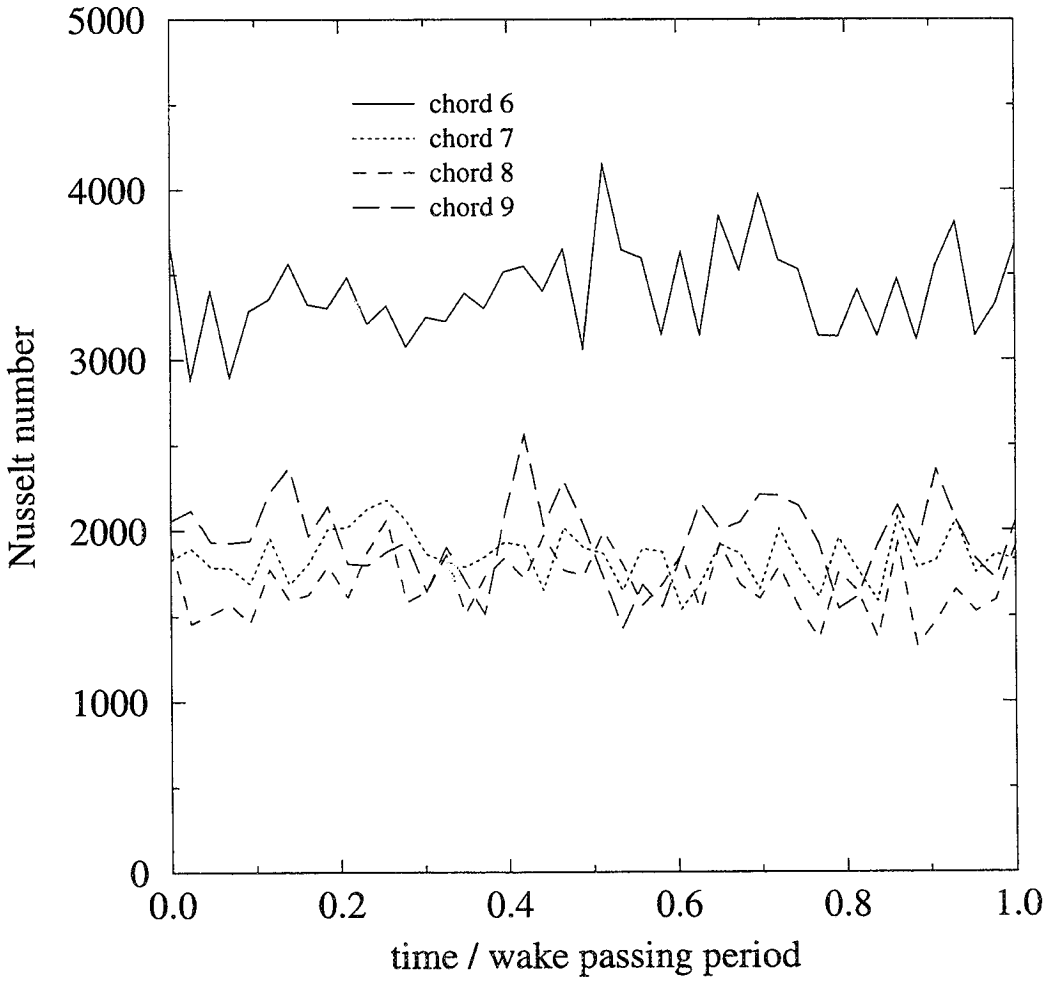

Figure 28: Span–average Nusselt number on pressure surface for St=0.500.

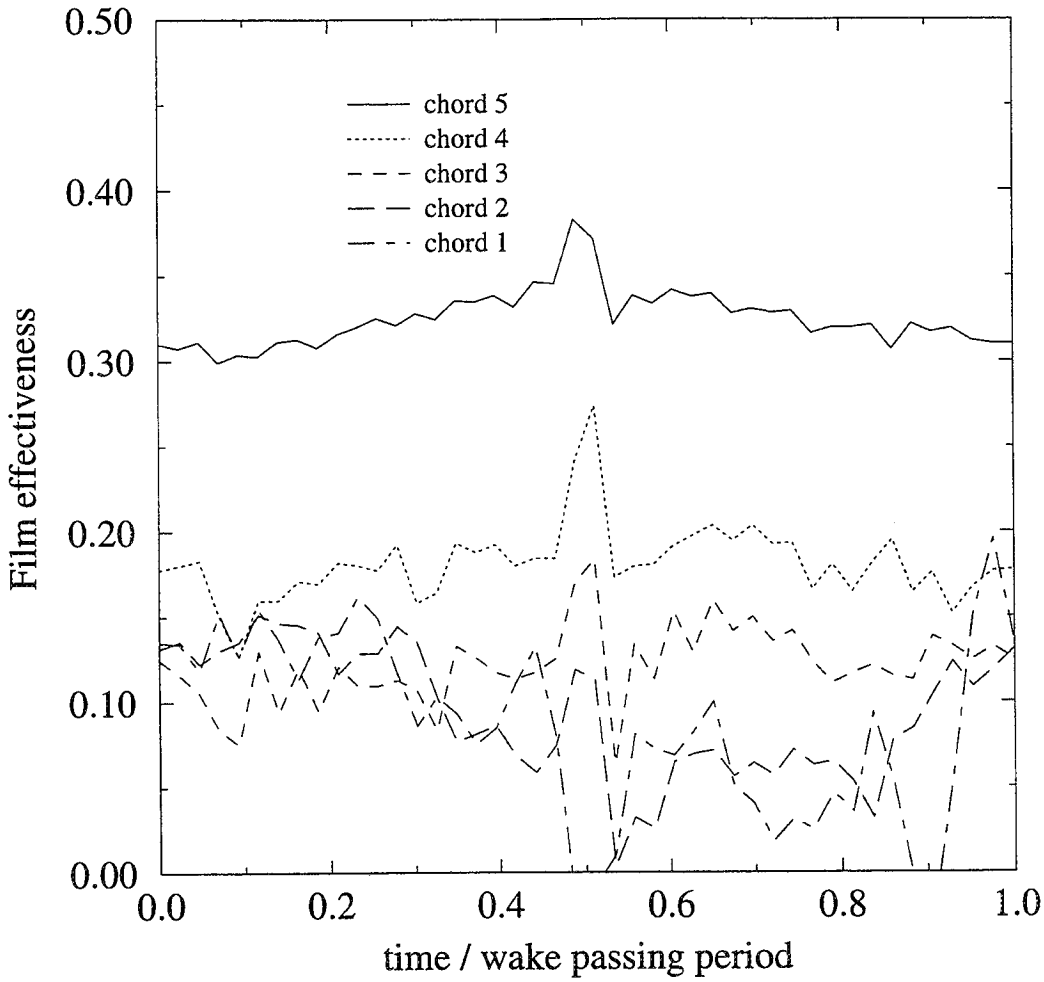

Figure 29: Span–average film effectiveness on suction surface for St=0.250.

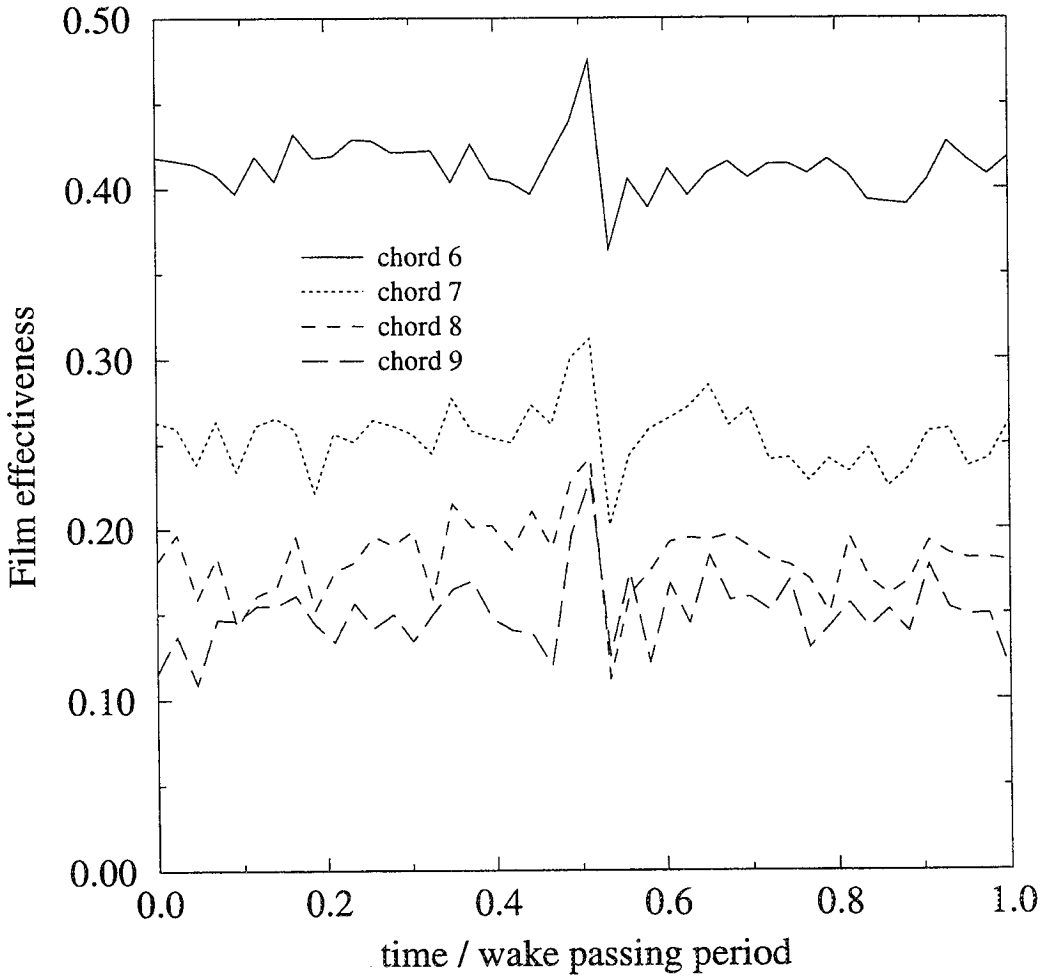

Figure 30: Span–average film effectiveness on pressure surface for St=0.250.

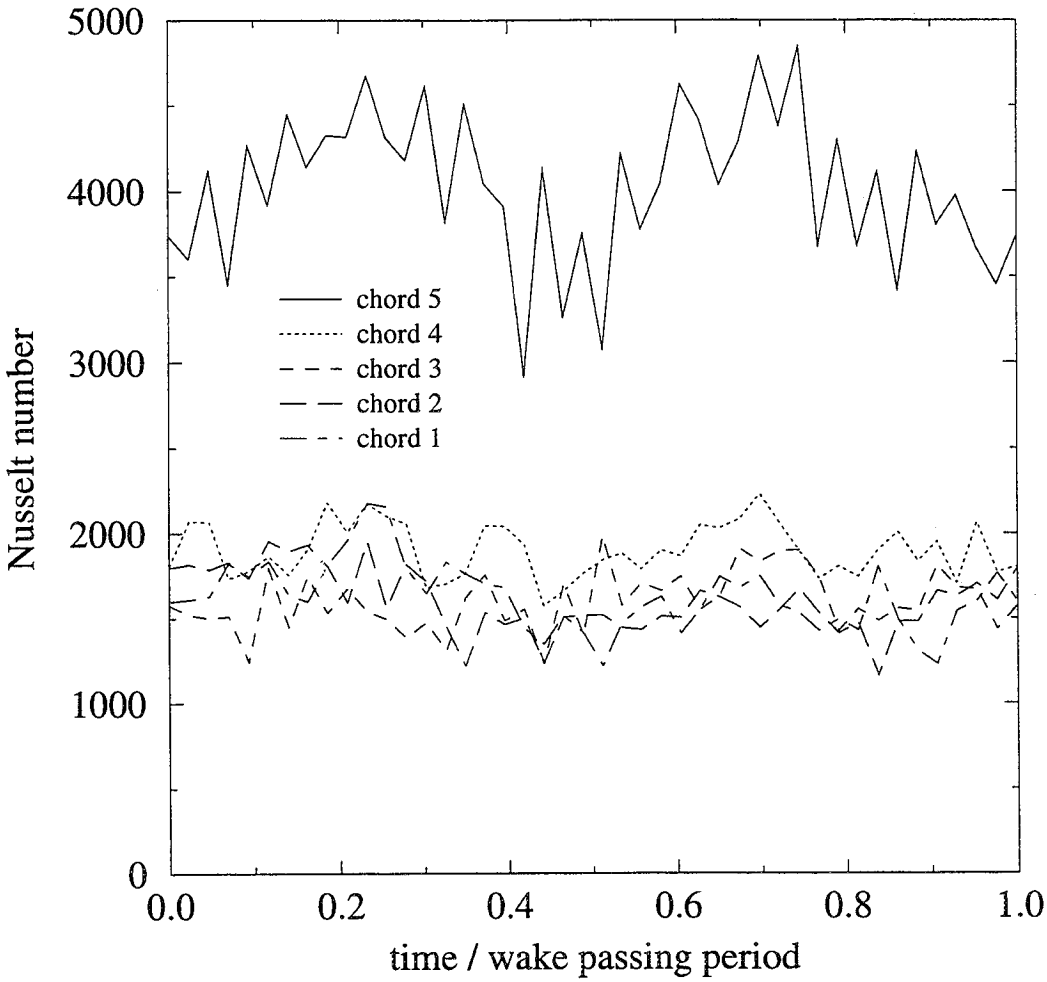

Figure 31: Span–average Nusselt number on suction surface for St=0.250.

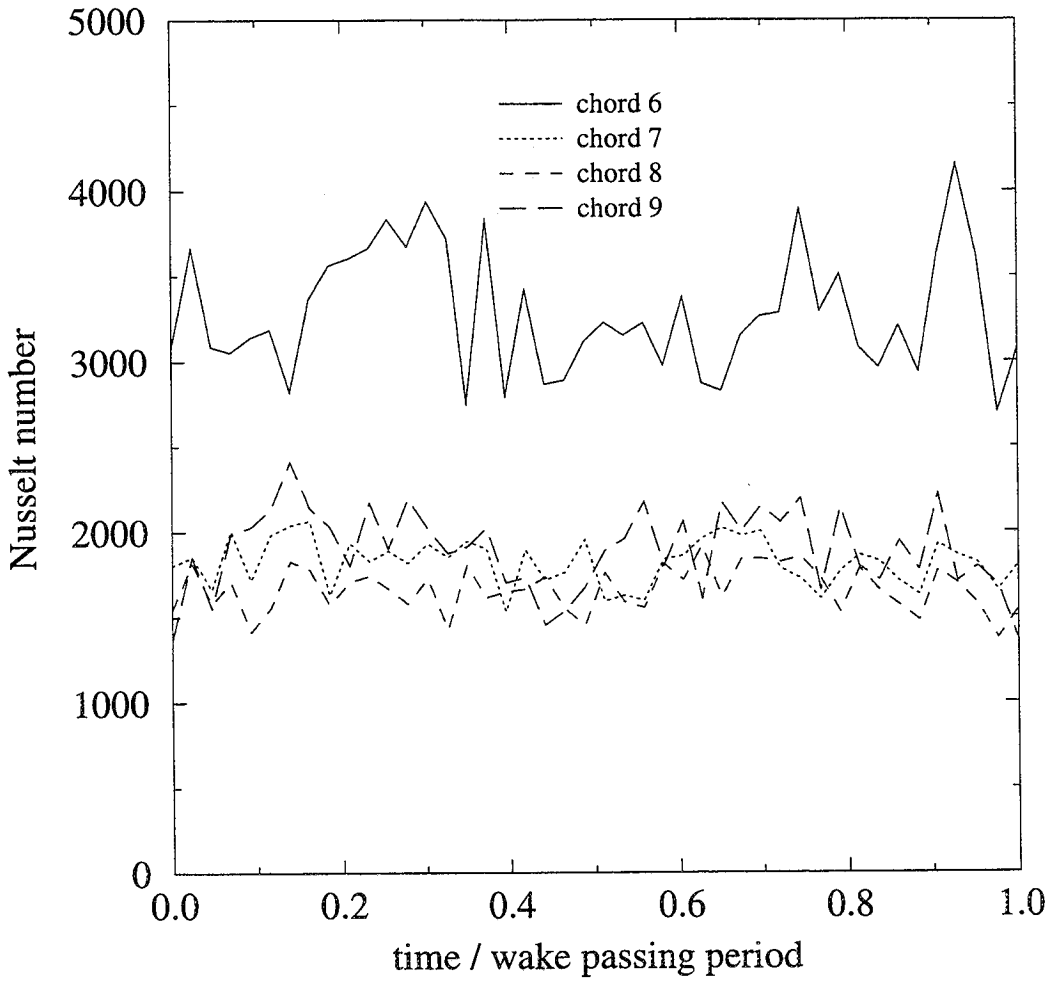

Figure 32: Span–average Nusselt number on pressure surface for St=0.250.

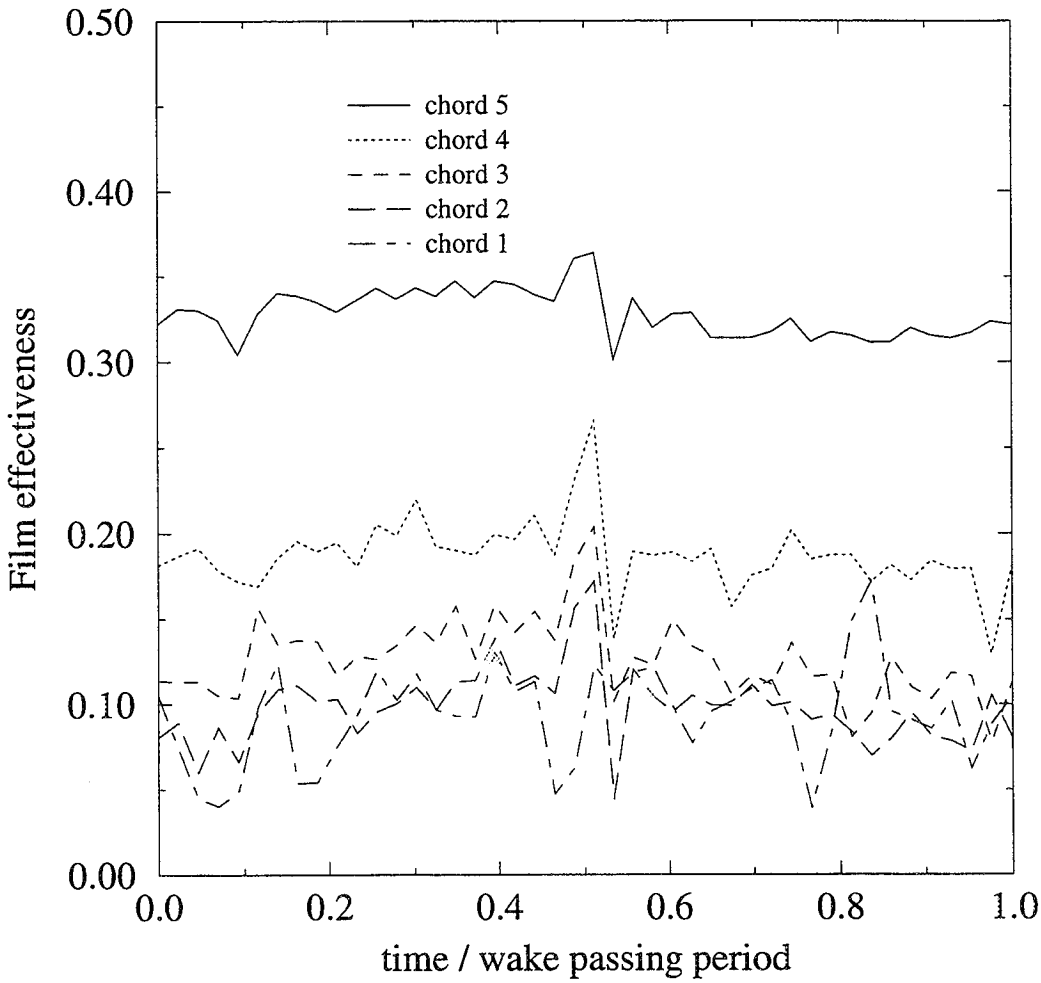

Figure 33: Span–average film effectiveness on suction surface for St=0.167.

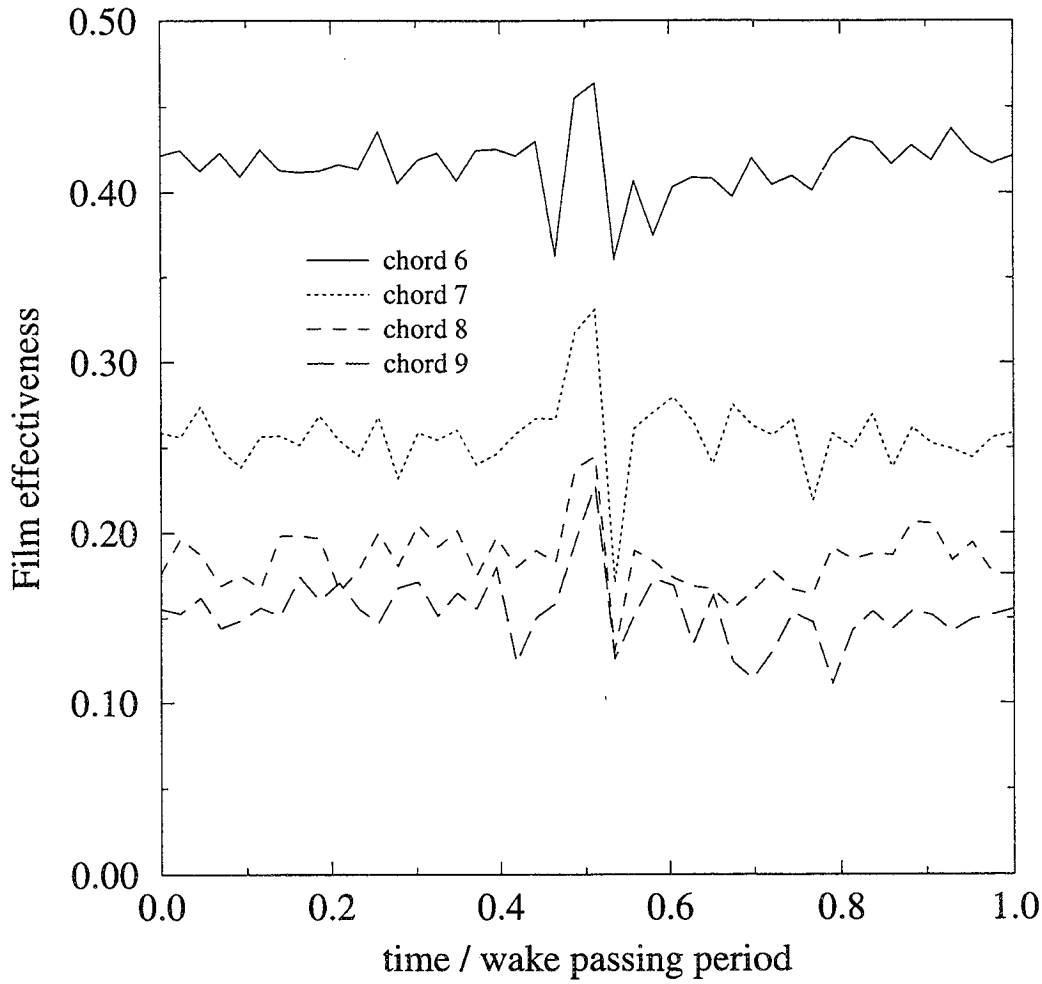

Figure 34: Span–average film effectiveness on pressure surface for St=0.167.

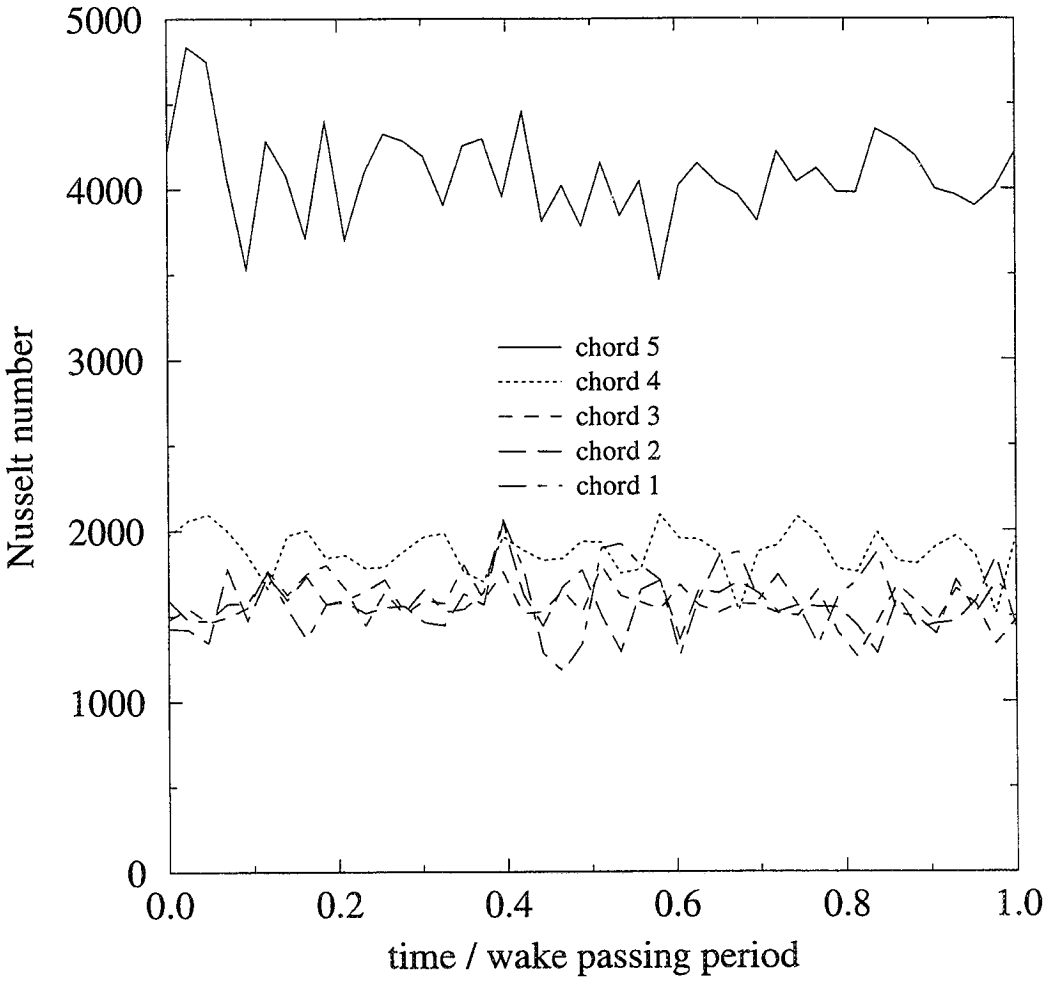

Figure 35: Span–average Nusselt number on suction surface for St=0.167.

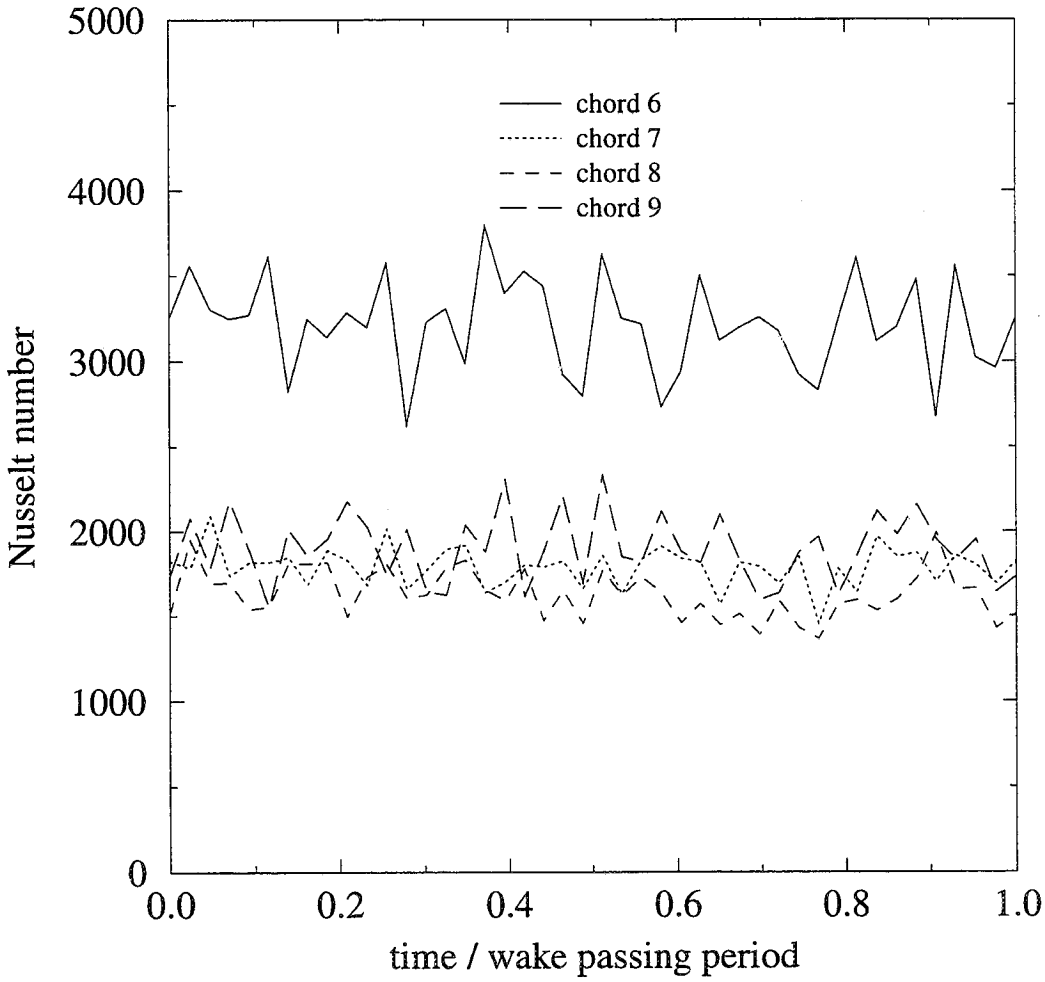

Figure 36: Span–average Nusselt number on pressure surface for St=0.167.

sided gauges, which would be better able to account for the transient conduction in the substrate.

Time-average span-average results

The steady experimental results will be shown in two forms. First, the effect of blowing ratio and injectant species on span-average film effectiveness and Nusselt number will be shown at each wake Strouhal number. Next, the effect of wake Strouhal number on the span-average heat transfer quantities will be presented for each blowing condition. The span-average quantities are plotted as a function of chordwise location. Due to the large amount of data available, representative spanwise plots of local steady heat transfer quantities will be shown. These spanwise plots are preferable to surface contour plots, because the large ratio of chordwise to spanwise spacing of the instrumentation causes two-dimensional contour plots to be misleading due to interpolation problems. The experimental uncertainties as estimated in Appendix I are shown as vertical lines at each data point.

Figures 37 through 40 show the steady span-average film effectiveness versus chordwise location for the four blowing conditions. The thick solid line indicates the case with the rotor removed and no wakes present. The thin solid line is the average of the eight equispaced stationary rotor cases. Although the Strouhal number is thus zero for this case, the effect of the wake is apparent as a reduction in film

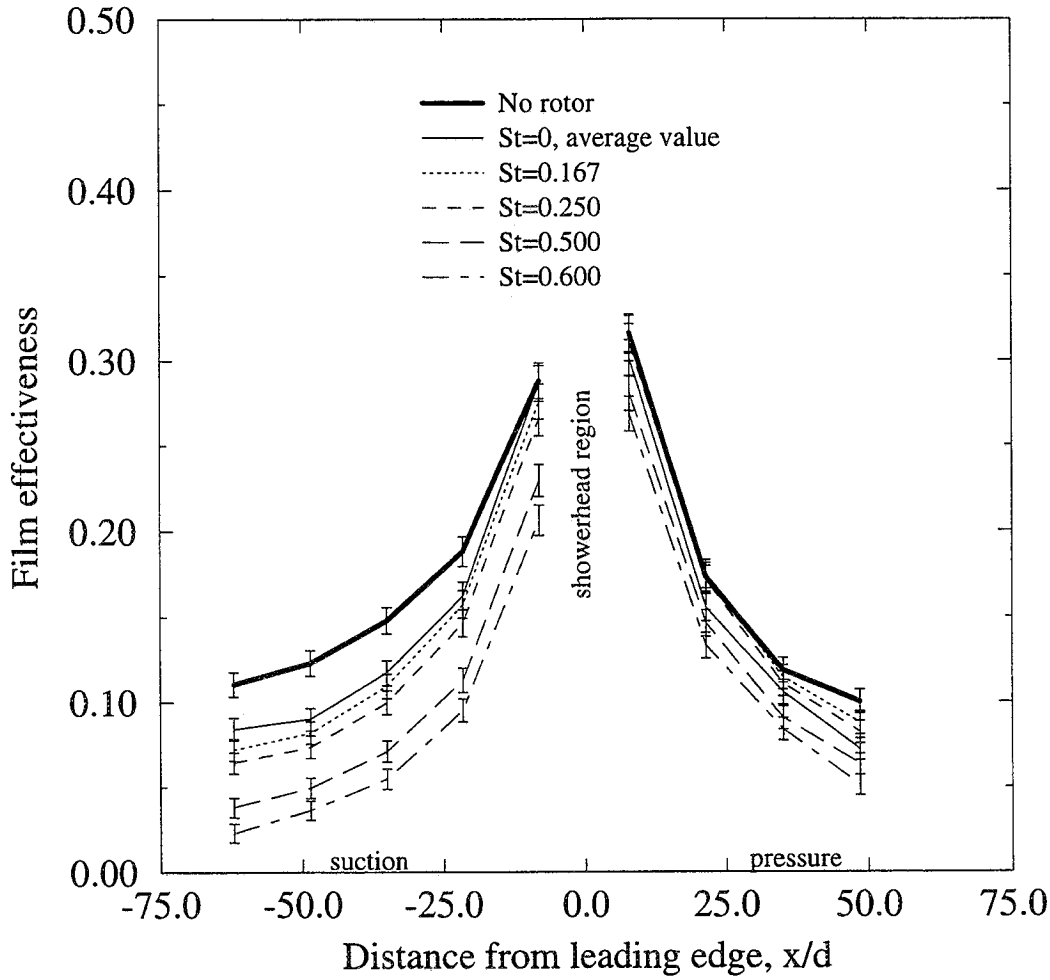

Figure 37: Span–average film effectiveness for air injection at B=0.5.

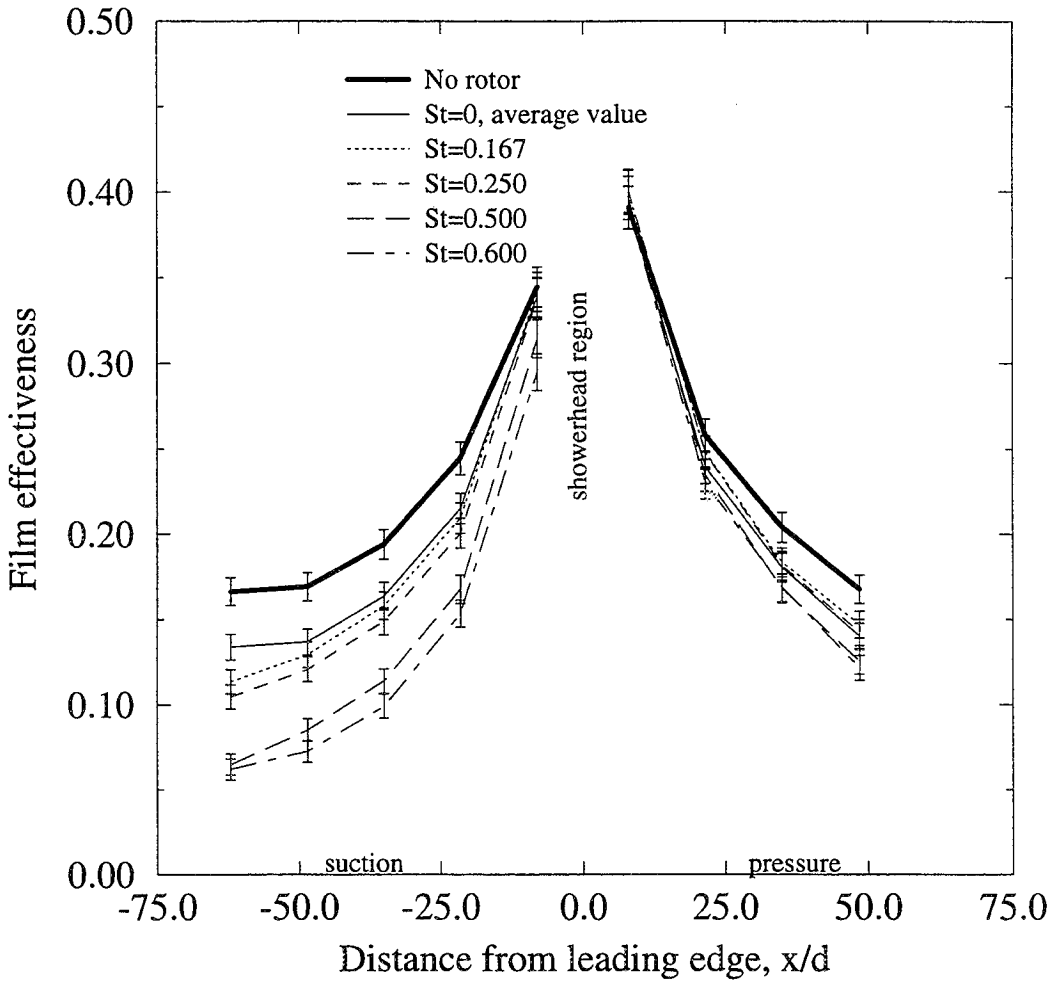

Figure 38: Span–average film effectiveness for air injection at B=1.0.

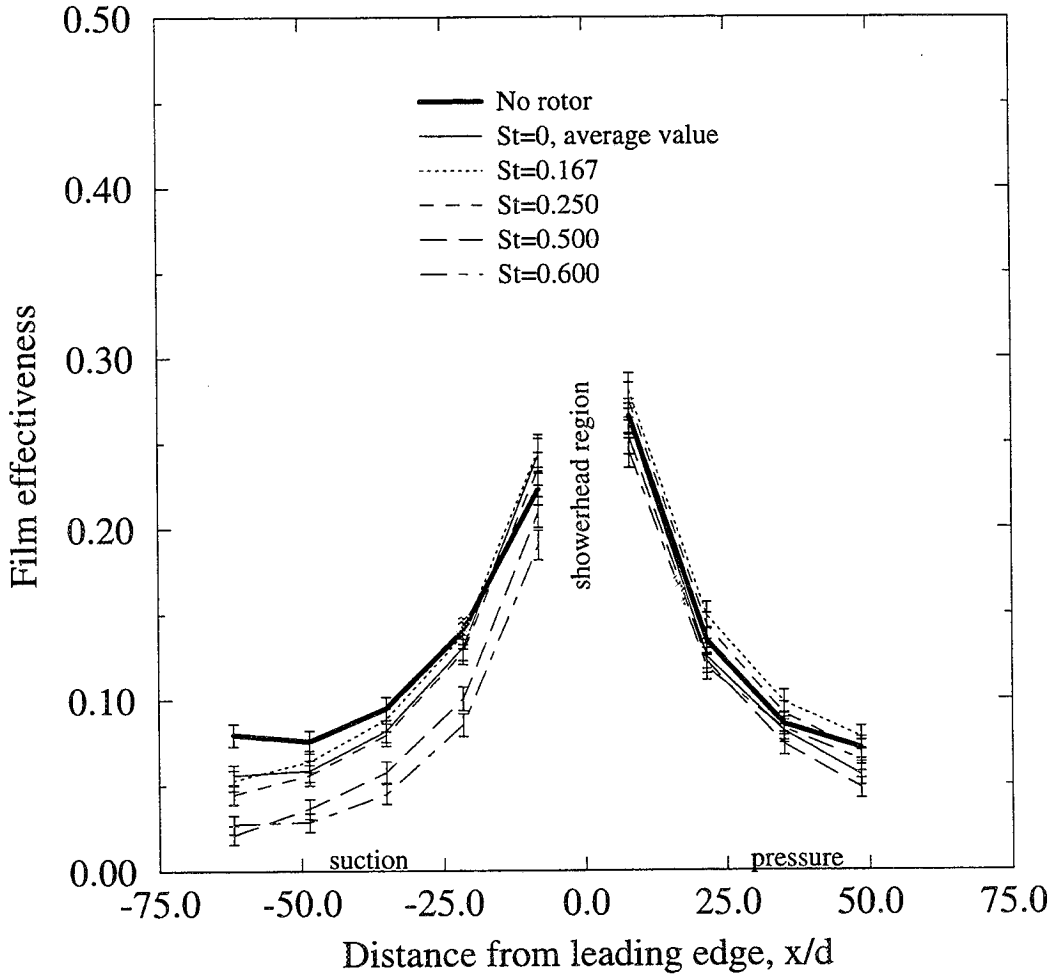

Figure 39: Span–average film effectiveness for CO_2 injection at B=0.5.

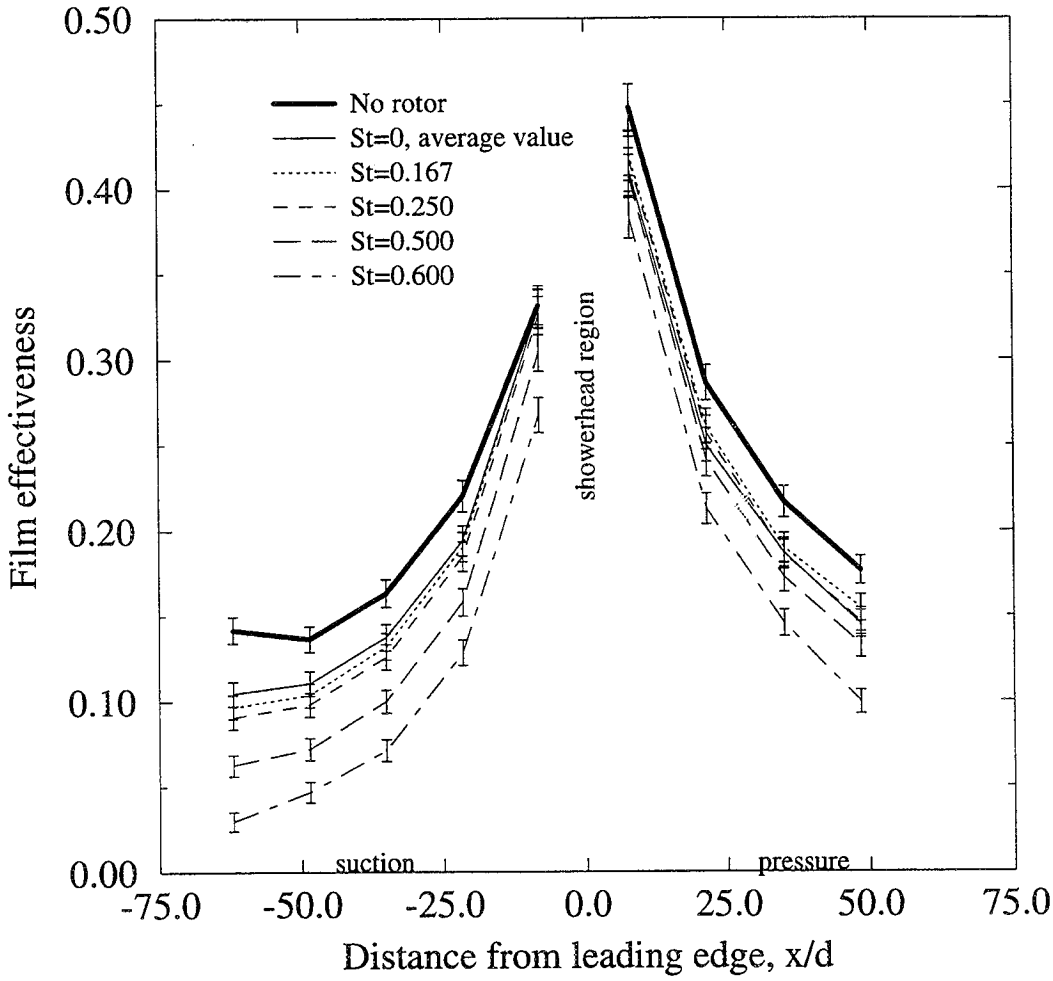

Figure 40: Span–average film effectiveness for CO_2 injection at B=1.0.

effectiveness relative to the no rotor case. This reduction increases with distance from the leading edge, especially on the suction side of the blade, and is due to spanwise mixing processes which will be discussed in the span-resolved data discussion.

All four plots indicate a general reduction in film effectiveness as the level of unsteadiness increases. This reduction is nearly monotonic with increasing Strouhal number. The reductions in film effectiveness are most pronounced on the blade suction surface. This phenomenon is explained by the swirl caused by the rotor. For the no rotor and stationary rotor cases, no swirl is imparted to the flow by the rotor, and the flow enters the cascade with zero swirl. This condition establishes a particular attachment line on the blade, and determines the split of coolant between the suction and pressure sides of the blade. As the Strouhal number increases, the wake-producing pins impart swirl to the free-stream toward the pressure side of the blade (see Figure 4). This moves the attachment line toward the suction side, and skews the coolant flow toward the pressure side of the blade. This in turn increases the film effectiveness on the pressure side compared to the suction side. However, this effect is smaller than the reduction due to increased mixing, so the overall effect of increased Strouhal number is to reduce film effectiveness on both the suction and pressure sides of the blade.

Figures 41 through 44 show the steady span-average Nusselt number versus chordwise location for the four blowing conditions. The results on the suction surface indicate

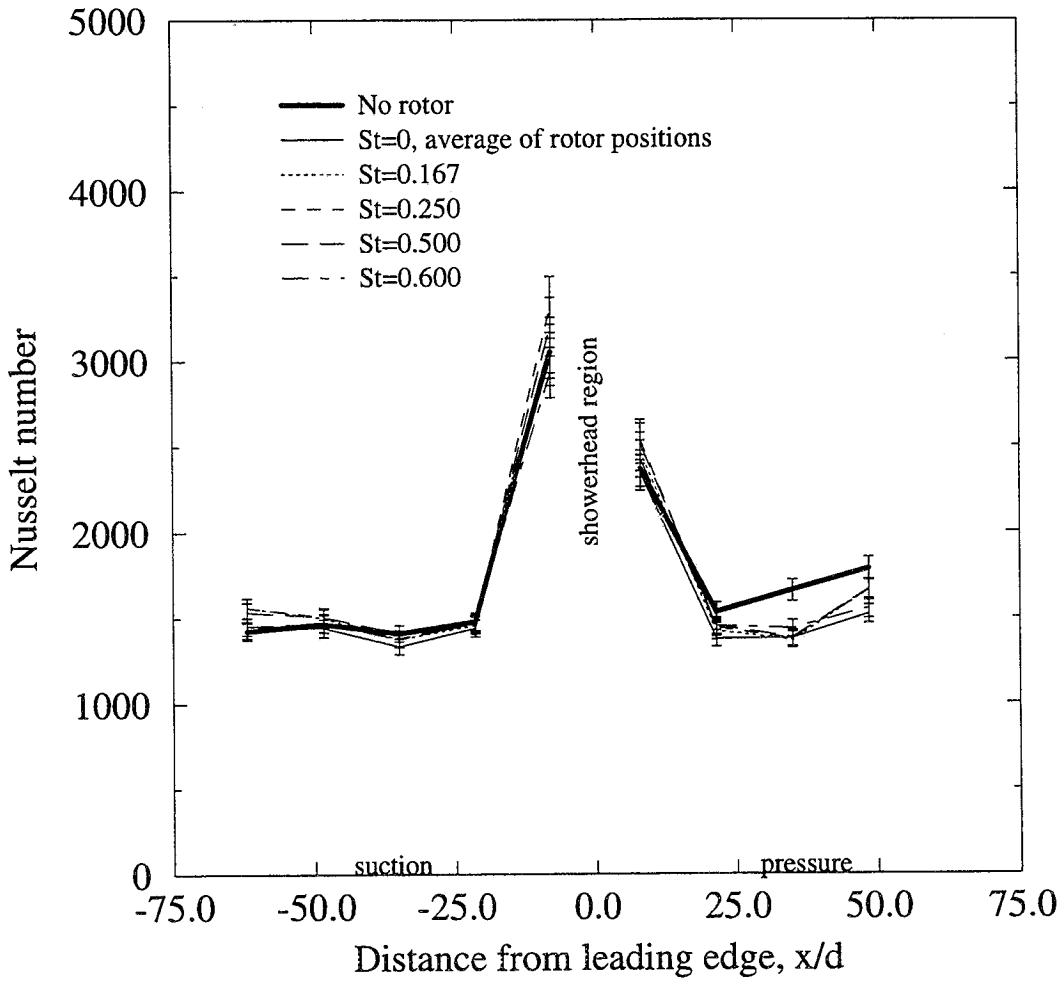

Figure 41: Span–average Nusselt number for air injection at B=0.5.

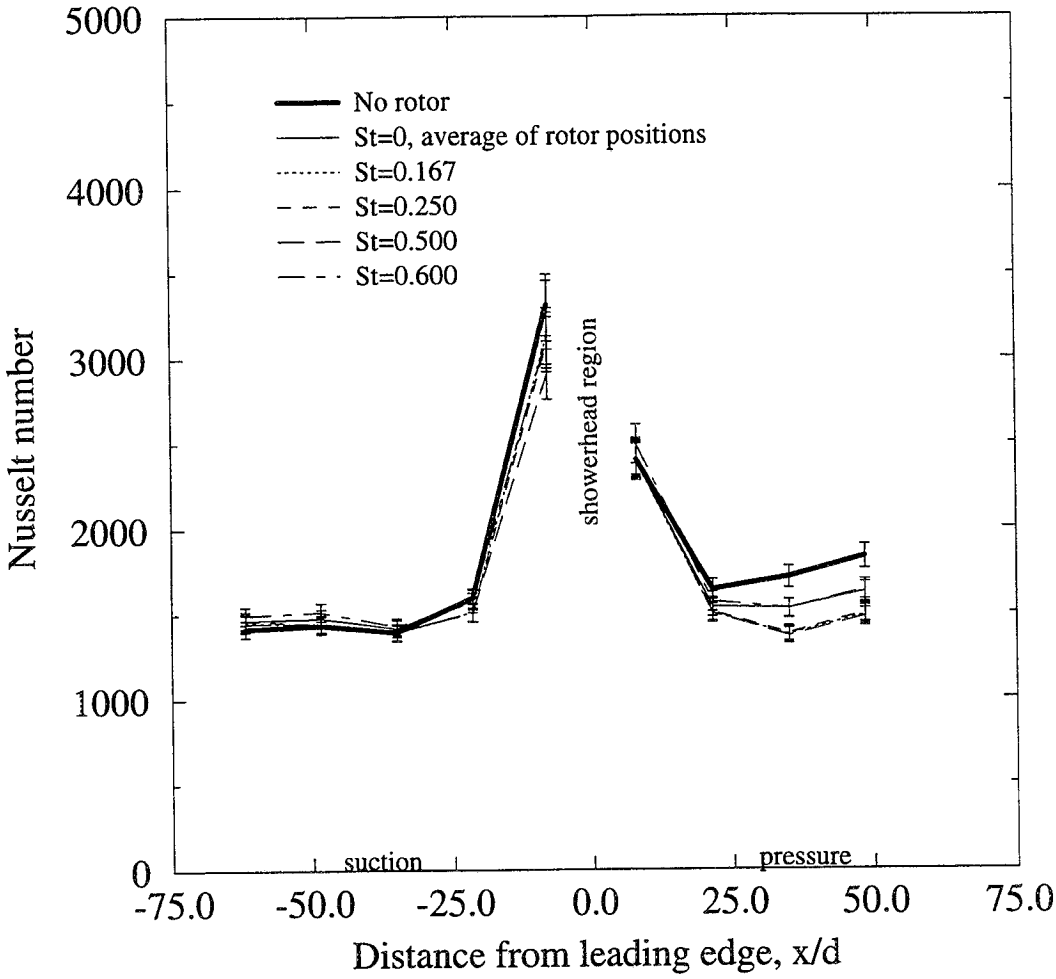

Figure 42: Span–average Nusselt number for air injection at B=1.0.

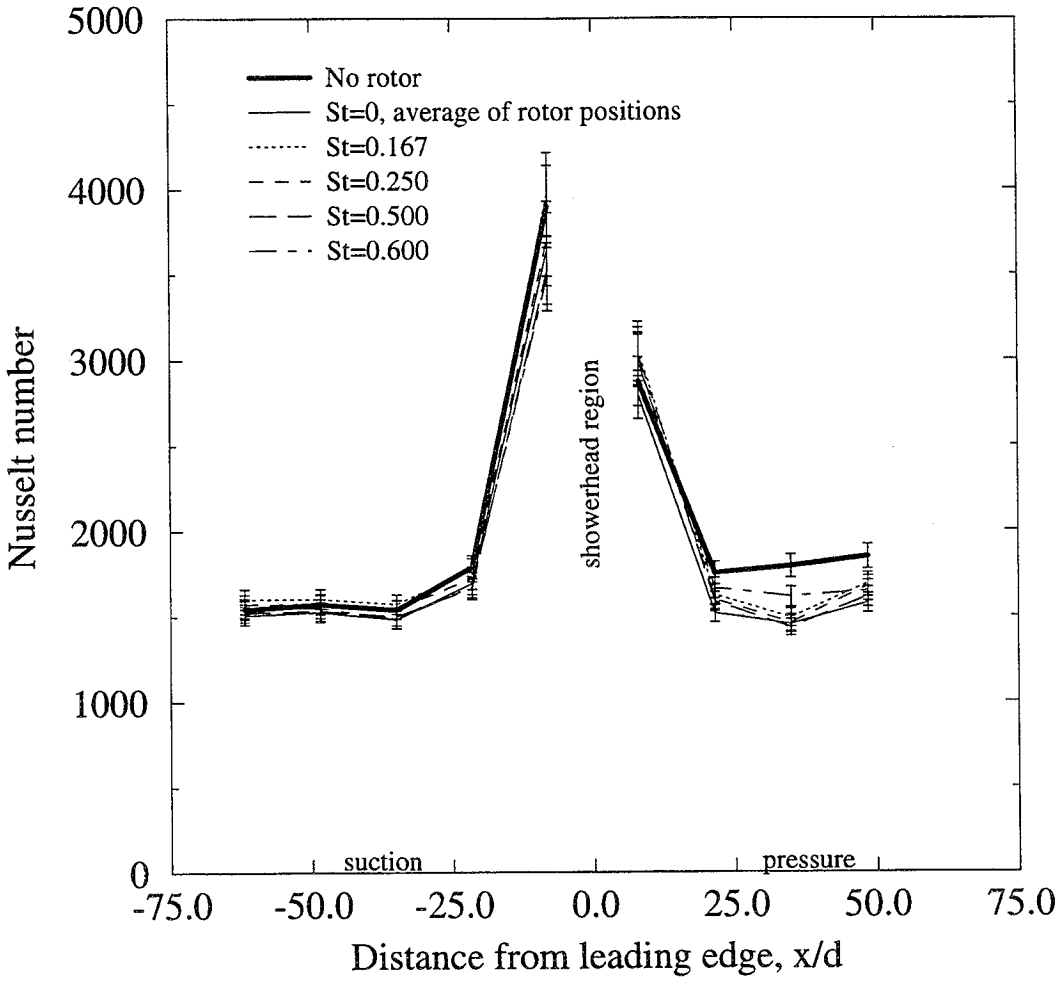

Figure 43: Span–average Nusselt number for CO_2 injection at B=0.5.

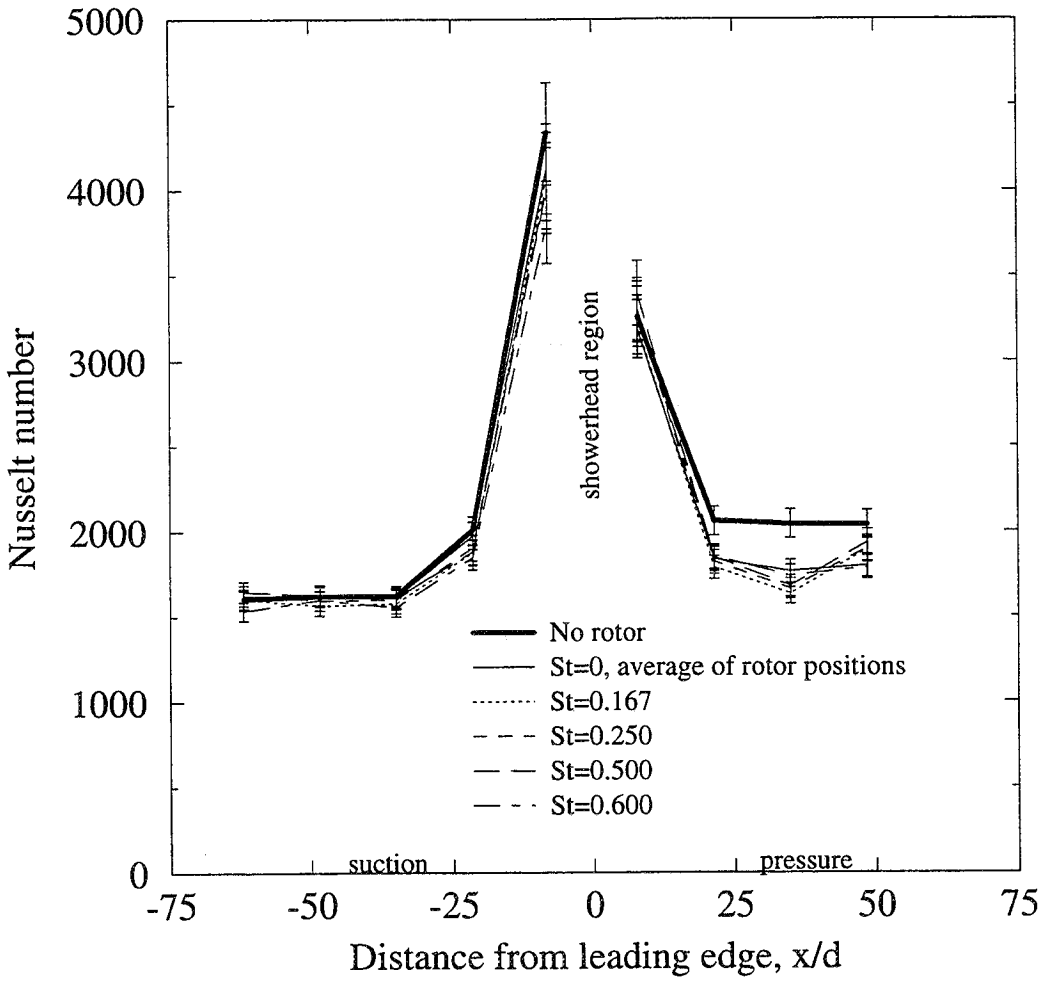

Figure 44: Span–average Nusselt number for CO_2 injection at B=1.0.

little effect of rotational speed or even presence of the rotor for all blowing conditions. The pressure side results near the leading edge are likewise independent of rotational speed. However, the downstream pressure side results show a marked increase in Nusselt number with the rotor removed. This is most likely due to changes in the blade aerodynamic performance, and not changes in the film cooling behavior, although detailed flow measurements would be necessary to confirm this hypothesis. Computations indicated a small separation bubble near the suction side trailing edge with no wakes which was not present with moving wakes. This indicates that the blade exhibits different aerodynamic performance depending on the presence of a passing wake. It is not clear why the data indicate no effect on the suction side.

Figures 41 through 44 show the Nusselt number distribution to be nearly constant downstream of the first chordwise gauge location on both the suction and pressure sides of the blade for all cases with rotor present. This is typical for turbine blades and illustrates the competing effects of increasing free-stream velocity and increasing upstream heating length with increasing distance from the leading edge. For all cases, the highest Nusselt number is found near the suction surface leading edge, consistent with the velocity spike and absence of upstream heating in this region. The pressure side leading edge Nusselt number is also large due to the absence of upstream heating.

Figures 45 through 50 are plots of steady span-average film effectiveness versus

chordwise location for each rotational speed. For all wake conditions, the blowing ratio of 1.0 yields higher film effectiveness values at all chordwise locations than the blowing ratio of 0.5. This indicates that the 1.0 blowing ratio is not sufficiently high to cause lift-off of the film jets from the blade surface, which would be evidenced by a more rapid decay in film effectiveness with chordwise distance. This is not surprising, because of the relatively small angle of injection (30° to the surface), and the very nature of showerhead cooling where the free-stream velocity is nearly normal to the blade surface, which tends to force the injectant to remain attached. Interestingly, the film effectiveness for air injection is generally higher than for carbon dioxide injection for all cases except at the higher blowing ratio on the pressure side, where it is only slightly lower. The specific reason for the better performance of air is difficult to determine, since not only do the two gases have different densities and hence momenta at the same blowing ratio, but are also different species. A possible explanation is that the air, having a lower density and thus a higher velocity, is better able to produce a stable film. However, this seems to contradict the prevailing wisdom that low momentum injectant performs better, although this rule of thumb was developed mainly for non-showerhead cooling. Perhaps some aspect of the CO_2 injection enhances turbulent mixing, although this seems unlikely since the molecular diffusion of CO_2 is expected to be slower than air because of its higher density. In addition, this would require a more rapid decay of film effectiveness with chordwise distance, which is not indicated. A definitive resolution of this question would require a facility capable of producing a large range of injectant temperatures.

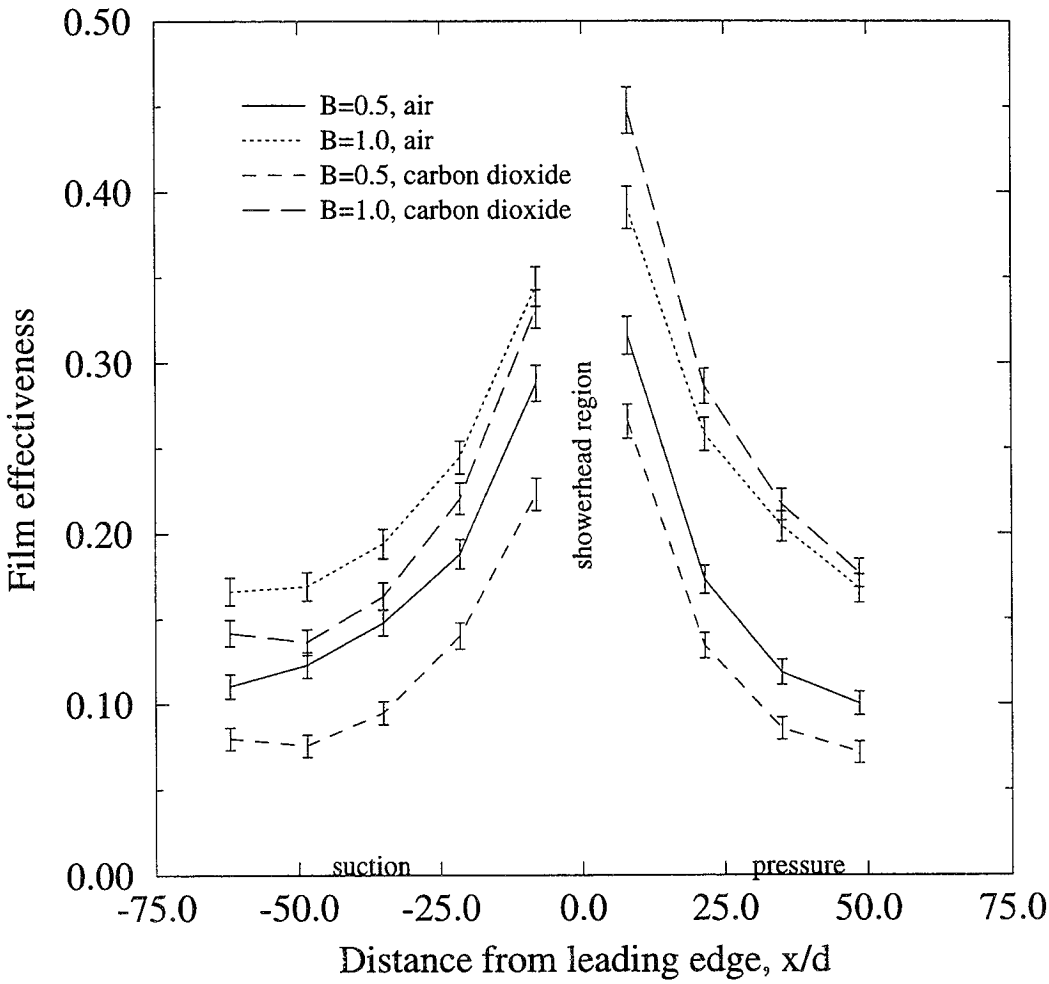

Figure 45: Span–average film effectiveness with no rotor.

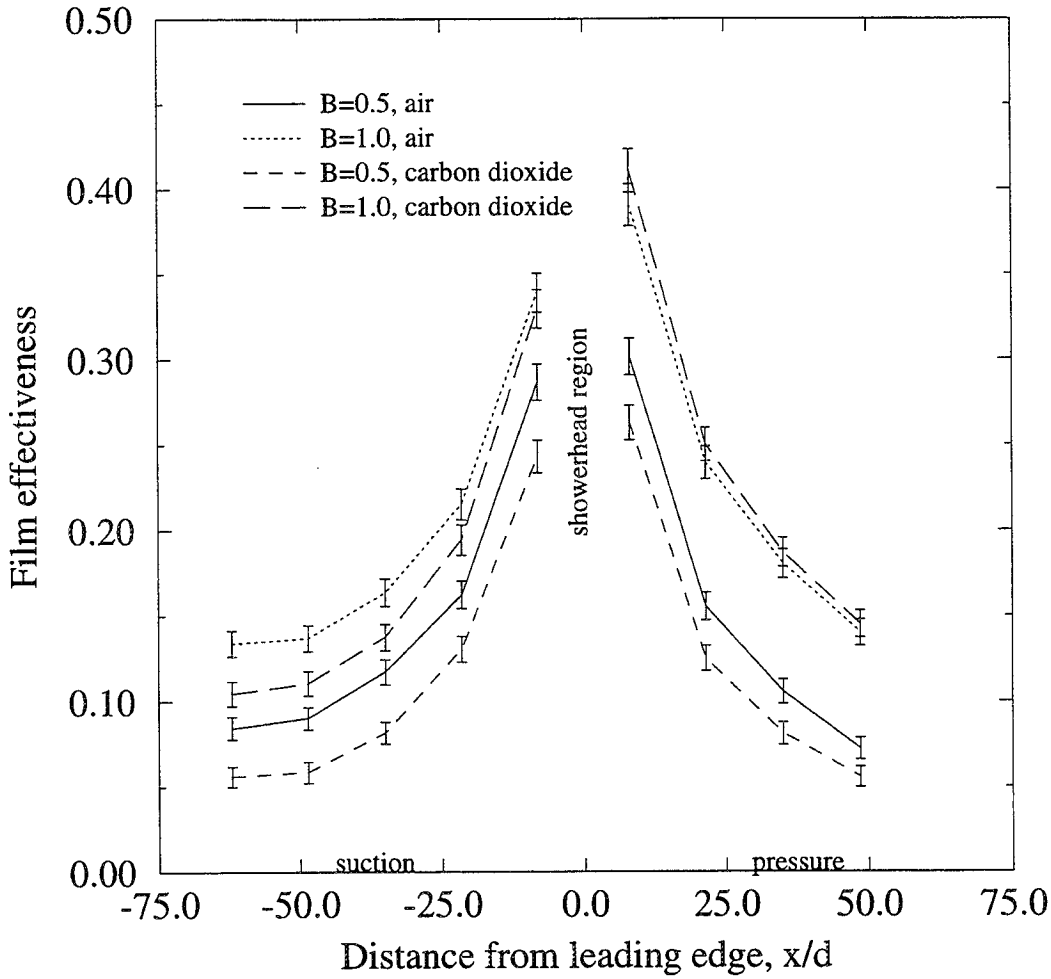

Figure 46: Span–average film effectiveness averaged over stationary rotor positions.

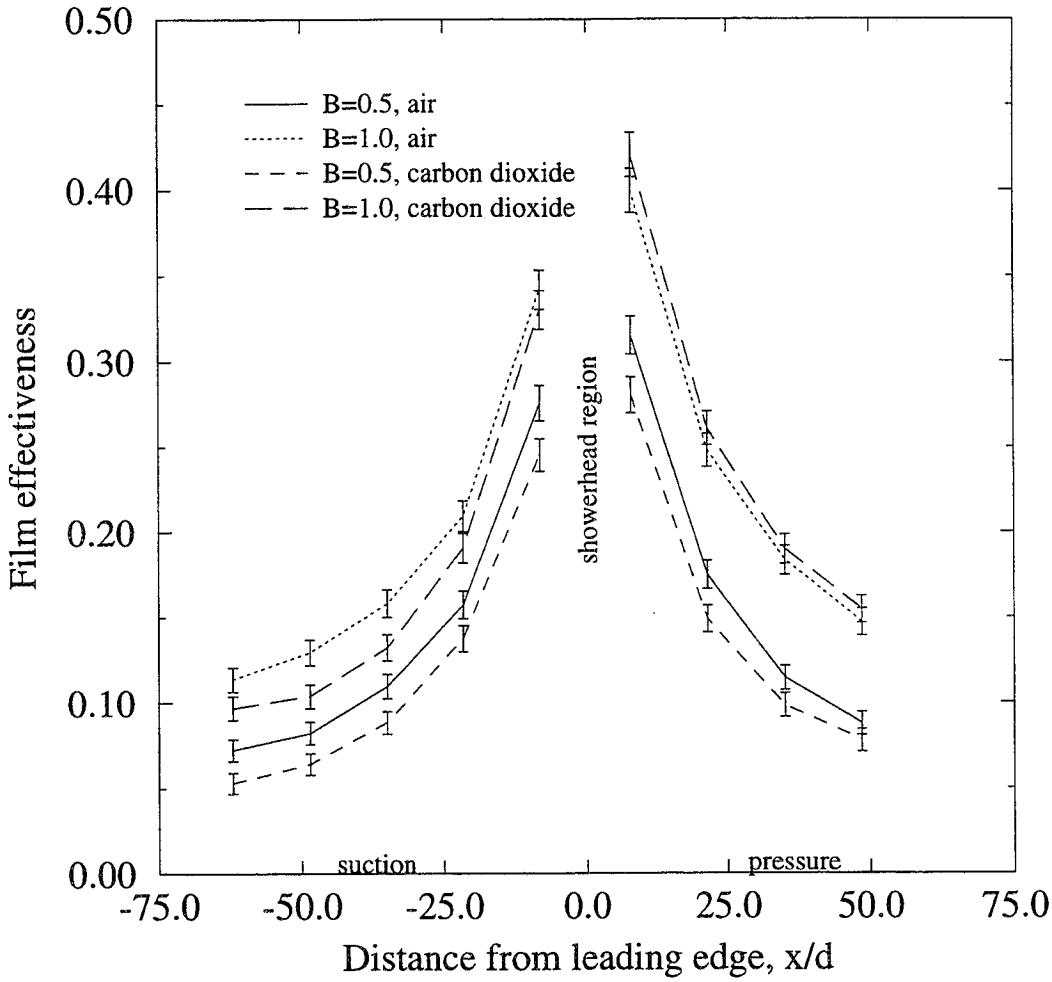

Figure 47: Span–average film effectiveness for St=0.167.

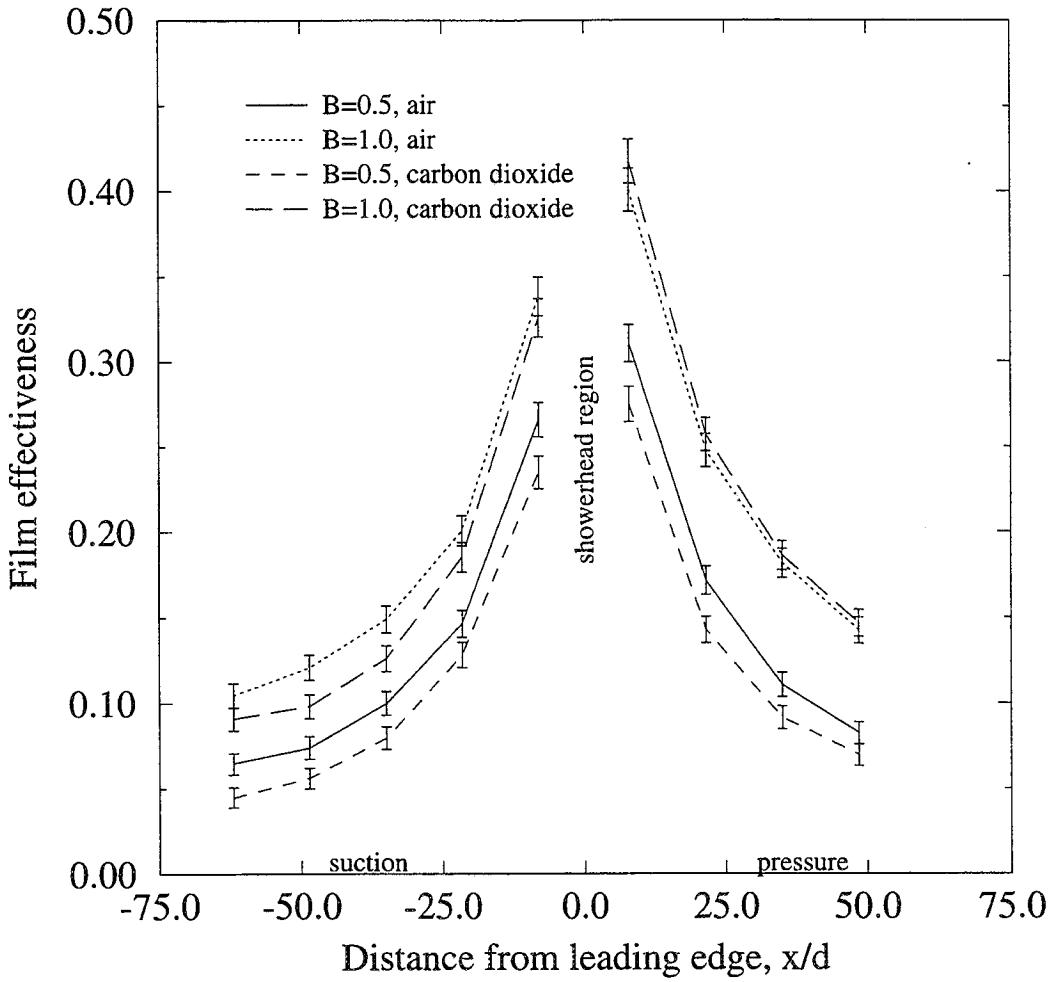

Figure 48: Span–average film effectiveness for St=0.250.

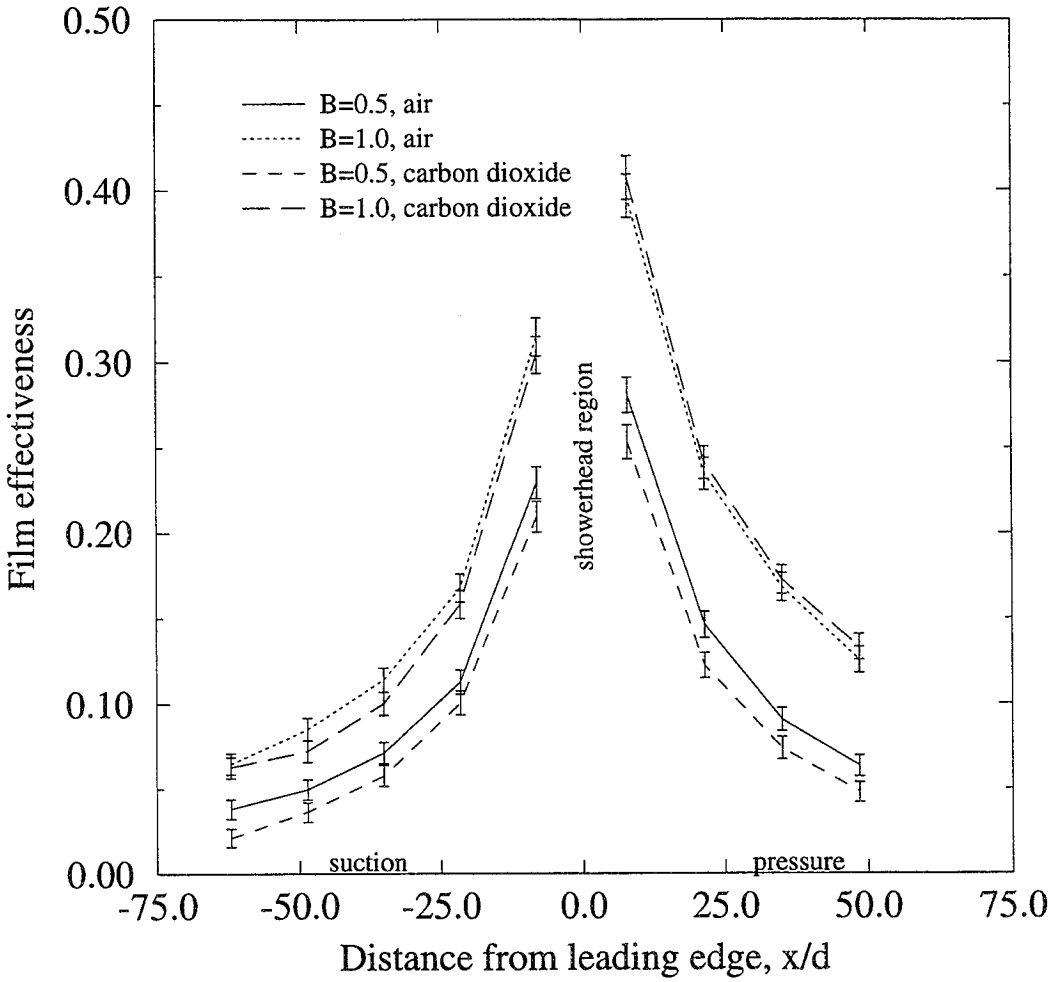

Figure 49: Span–average film effectiveness for St=0.500.

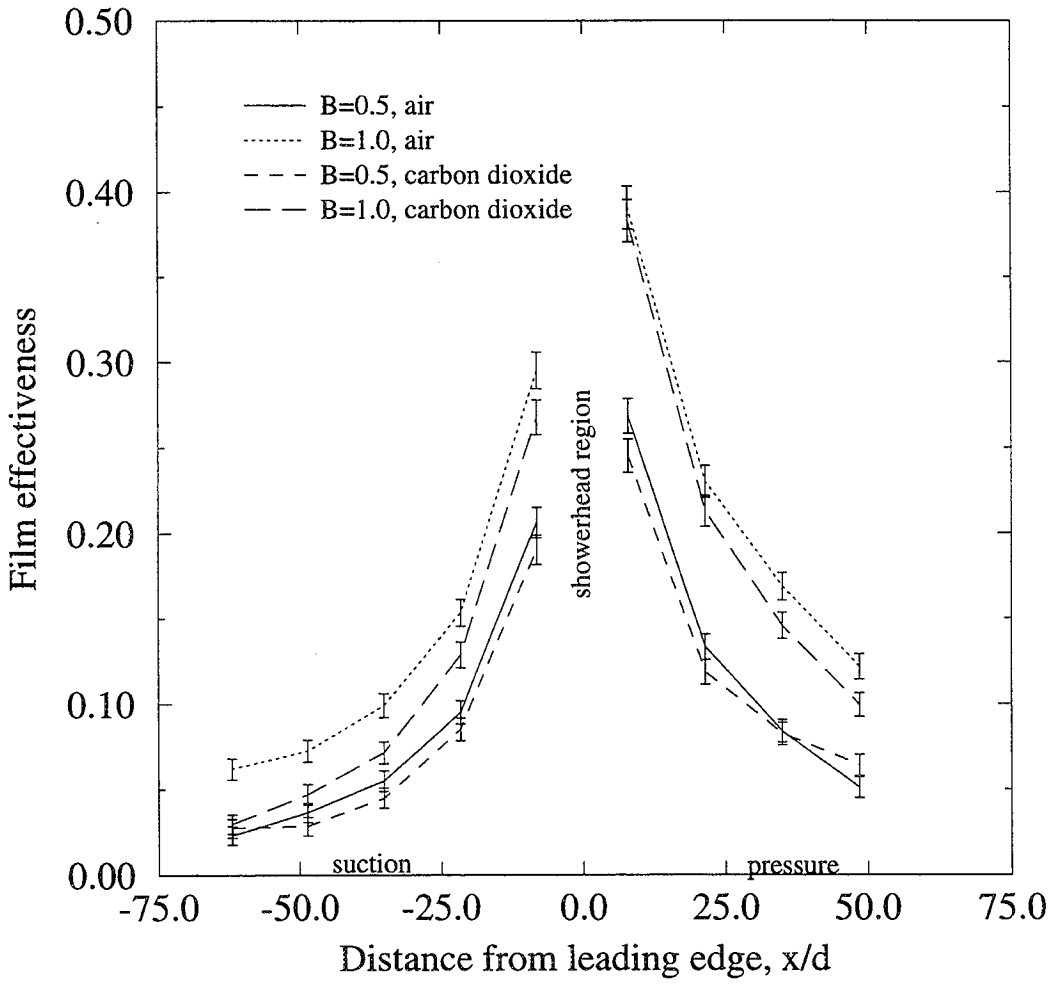

Figure 50: Span–average film effectiveness for St=0.600.

Figures 51 through 56 show the steady span-average Nusselt number distributions for each rotational speed. In general, the presence of injection through the film holes increases the Nusselt number. As expected, the increase is greatest for the higher blowing ratio, since there is more interaction between the injectant and the free-stream and hence more mixing and greater heat transfer. Surprisingly, the carbon dioxide injection even at the lower blowing ratio produces higher Nusselt numbers than air injection at the higher blowing ratio. This phenomenon is consistent with the higher film effectiveness measured for air versus carbon dioxide. In both cases the CO_2 indicates an unexplained increase in mixing relative to air.

Time-average span-resolved results

All experimental results to this point have been in terms of steady span-average film effectiveness and Nusselt number. The next set of graphs show film effectiveness and Nusselt number versus spanwise gauge location at each chordwise location. To limit the results to a manageable level, only the carbon dioxide injection with a blowing ratio of 1.0 results are given. These results are representative of those for the other blowing conditions. For all plots, spanwise gauge location 9 is a periodic point identical to spanwise gauge location 1. A few of the 72 thin-film gauges were lost during the experimental study. A location without a working gauge is indicated by the absence of a symbol at that spanwise location on the plot. Most of the lost gauges were at chord location 9, the suction surface trailing edge.

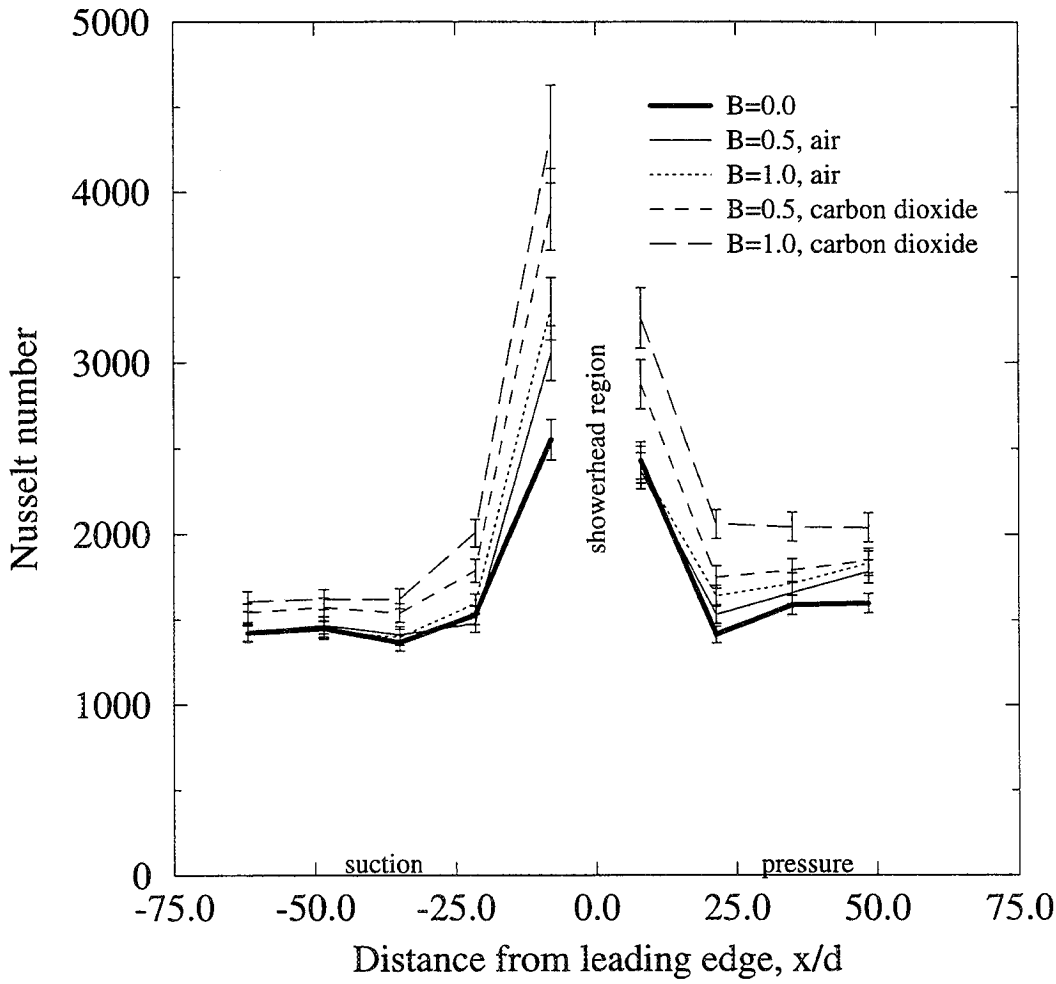

Figure 51: Span–average Nusselt number with no rotor.

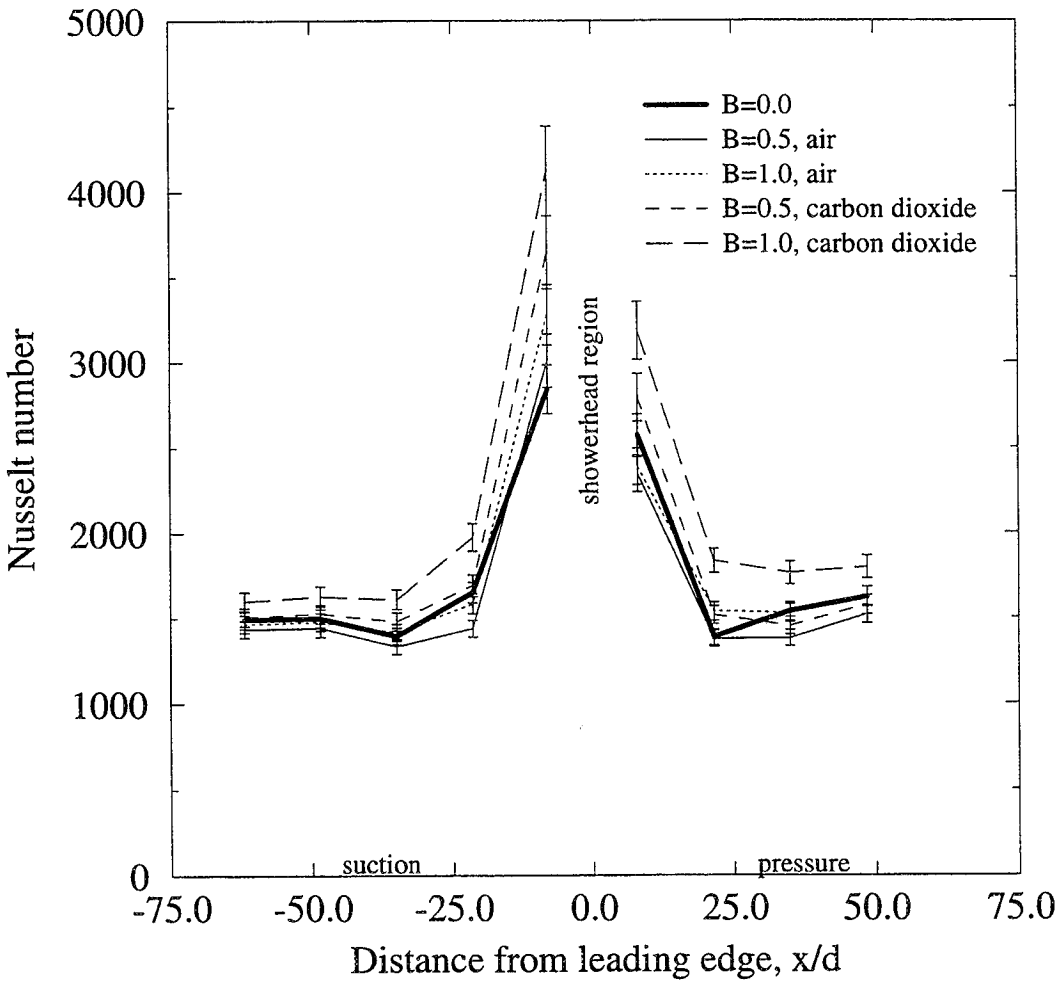

Figure 52: Span–average Nusselt number averaged over stationary rotor positions.

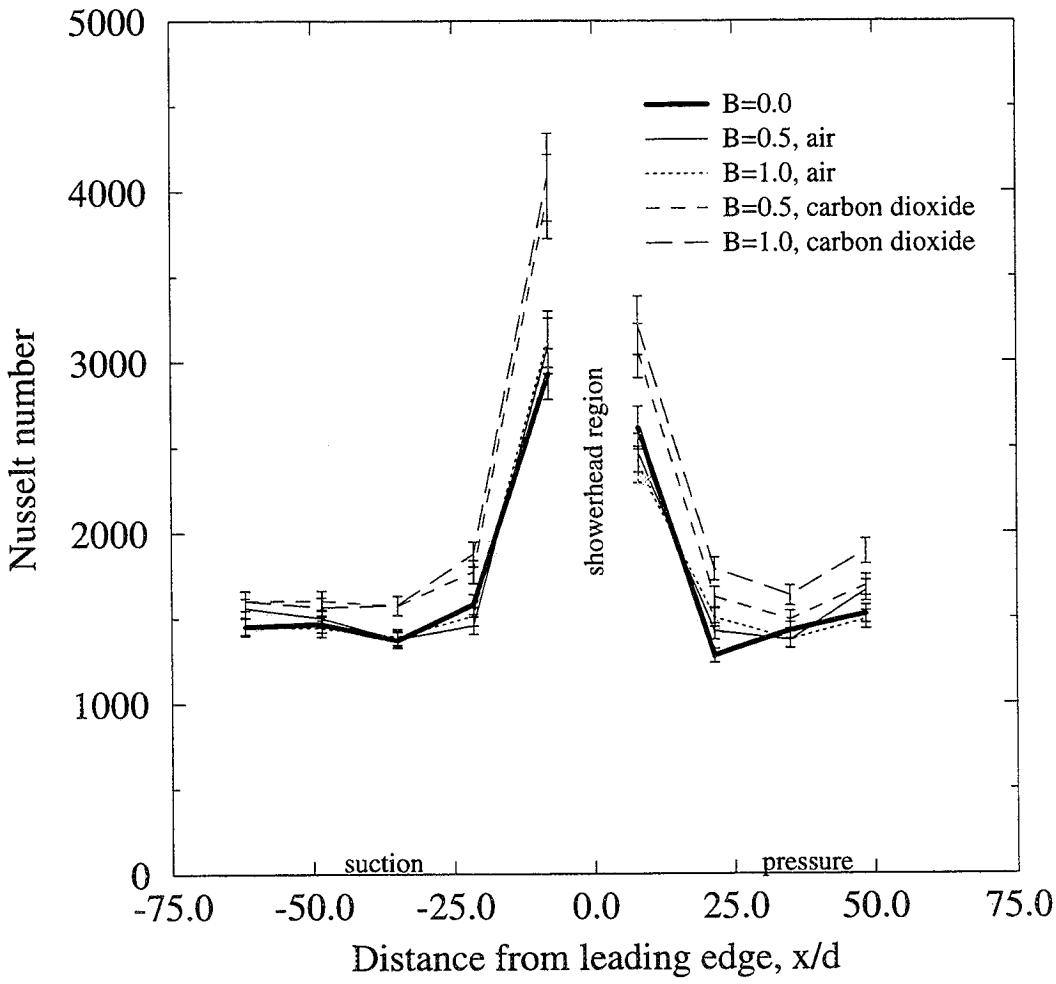

Figure 53: Span–average Nusselt number for St=0.167.

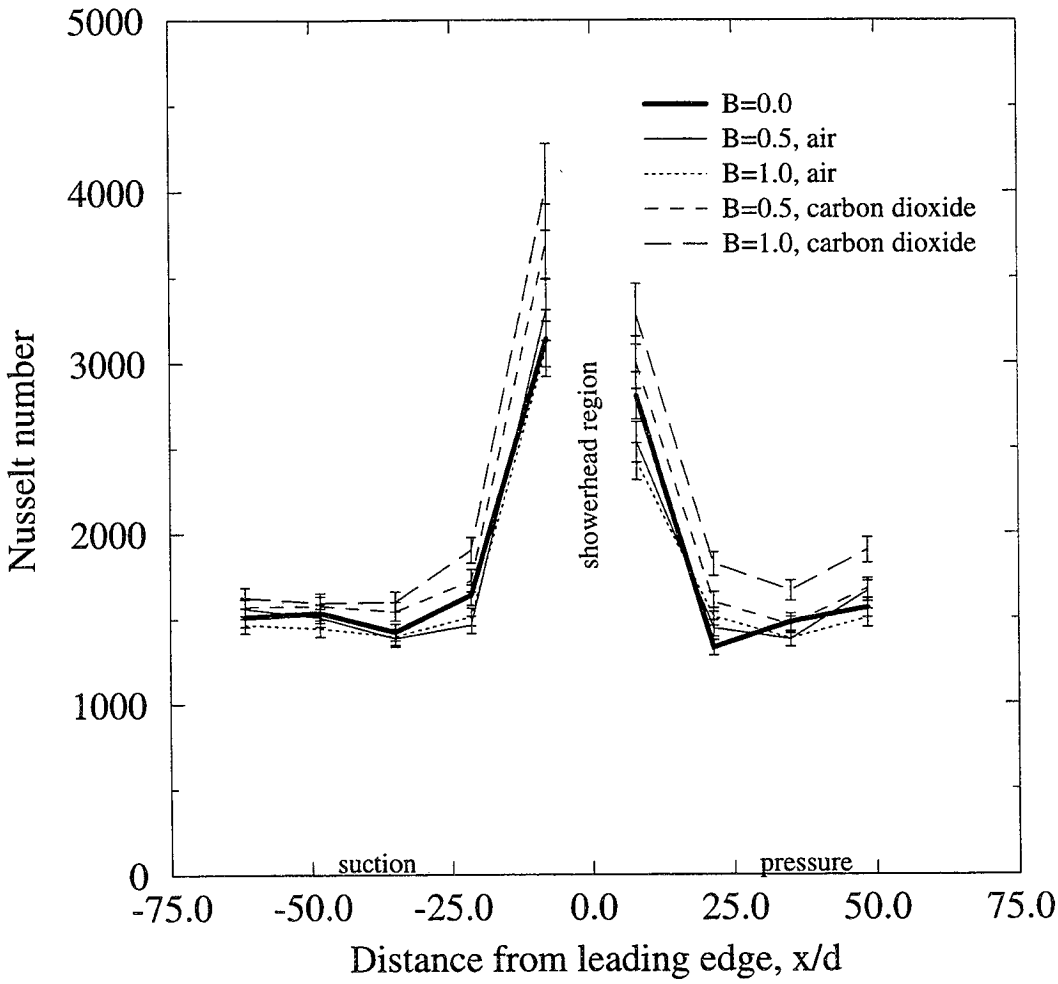

Figure 54: Span–average Nusselt number for St=0.250.

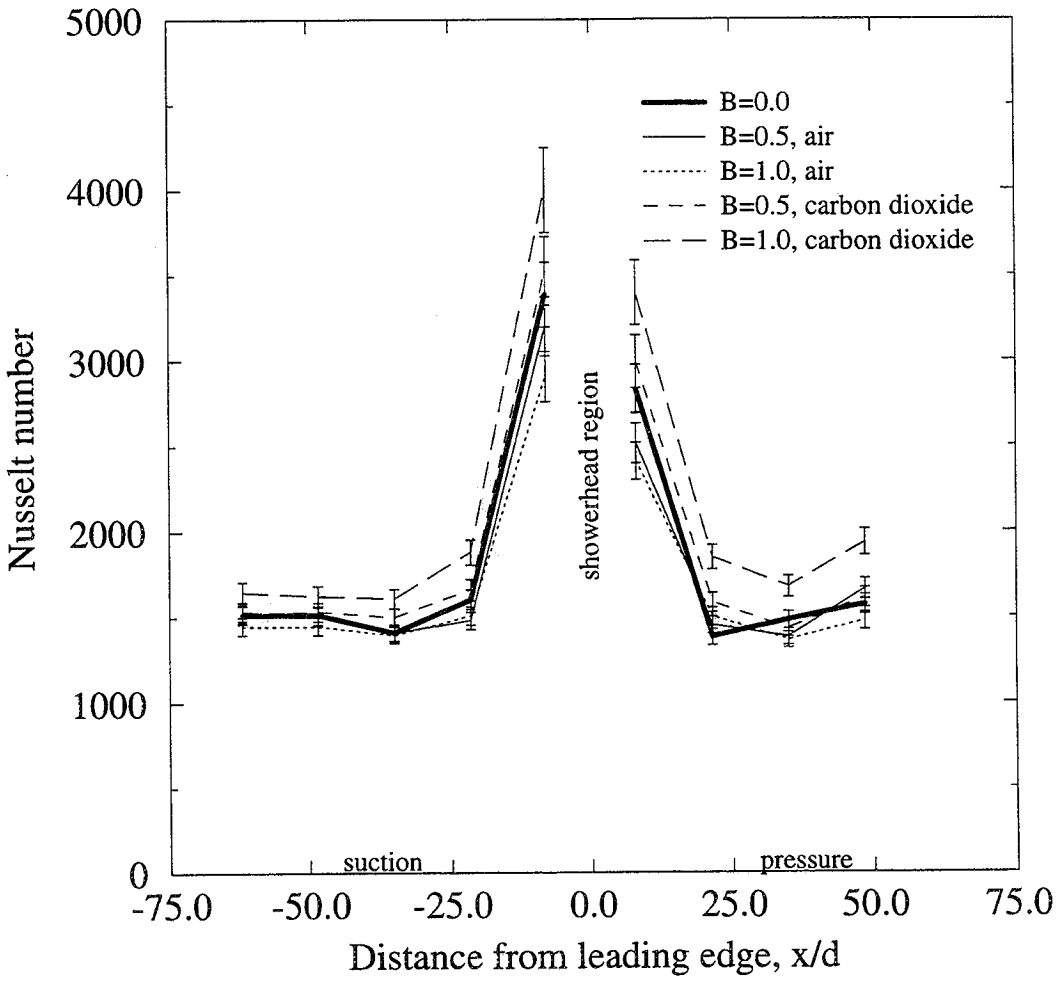

Figure 55: Span–average Nusselt number for St=0.500.

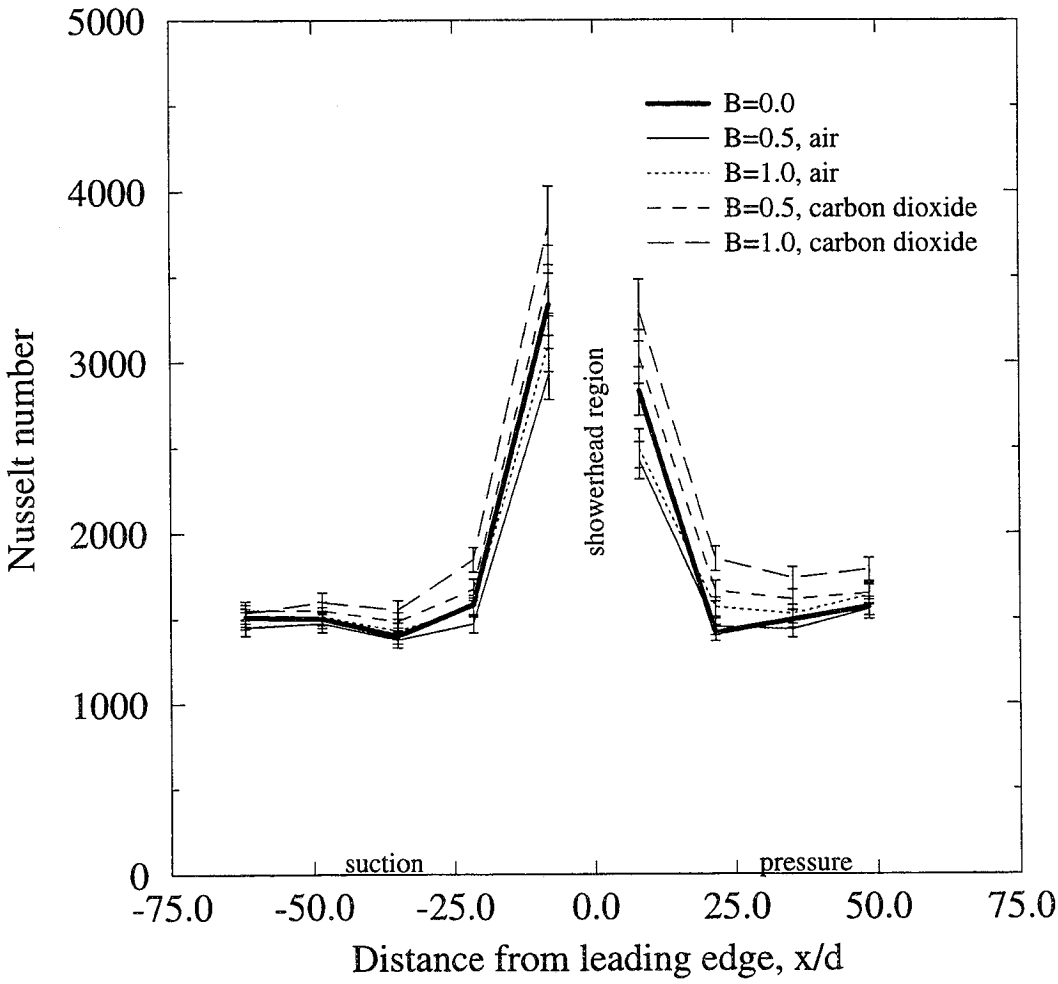

Figure 56: Span–average Nusselt number for St=0.600.

Figures 57 through 65 are the steady spanwise film effectiveness plots for chordwise locations 1 through 9, respectively. Each plot shows the effect of increasing Strouhal number on the spanwise film effectiveness distribution. Except for chord location 5 (x/d=-8.0), and to a lesser extent chord location 6 (x/d=8.0), the film effectiveness distribution is uniform. The only possible exception is for the no rotor case on the downstream suction surface (chords 1, 2, and 3), where there is a slight increase at span locations 4 through 6, possibly indicating a coherent film coolant trajectory. However, the presence of a wake seems to dissipate any non-uniformities at these locations.

On the suction surface near the leading edge (Figure 61), a large spanwise variation in film effectiveness is found. The trends are consistent for all Strouhal number cases, but the differences in magnitude provide some interesting details about the film/wake interaction in this region. The largest spanwise variations occur when the rotor is removed, due to the absence of wake-induced mixing of the film. As the Strouhal number is increased, not only does the span-average film effectiveness decrease, but the spanwise variations decrease as well, indicating that the higher wake passing speeds provide more spanwise mixing of the film. Perhaps the most interesting aspect of Figure 61 is the behavior at spanwise locations 2 and 3. This is the lowest film effectiveness region, and thus corresponds to the gap between two adjacent film jets. It appears that the presence of a rotor wake actually increases the film effectiveness slightly in this region up to a Strouhal number of 0.500. This

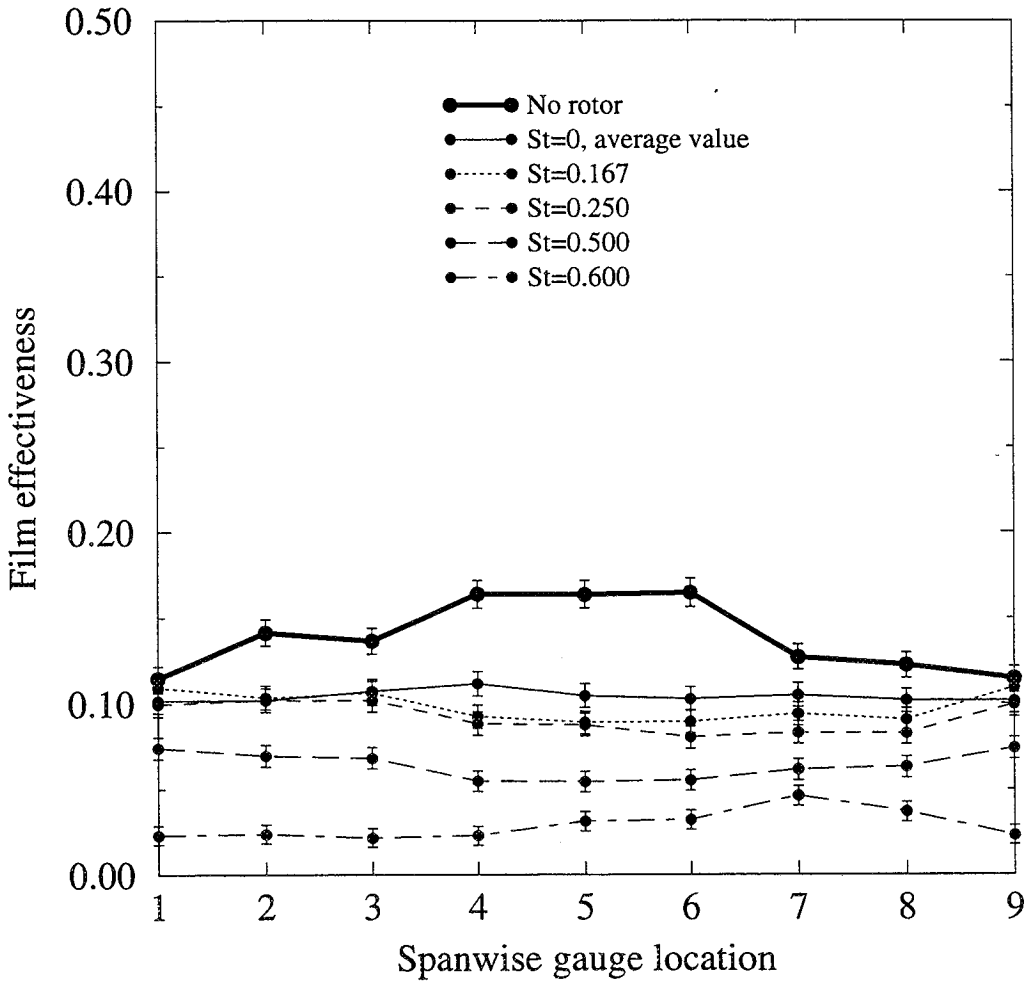

Figure 57: Film effectiveness for CO_2 injection at B=1.0, chord location 1.

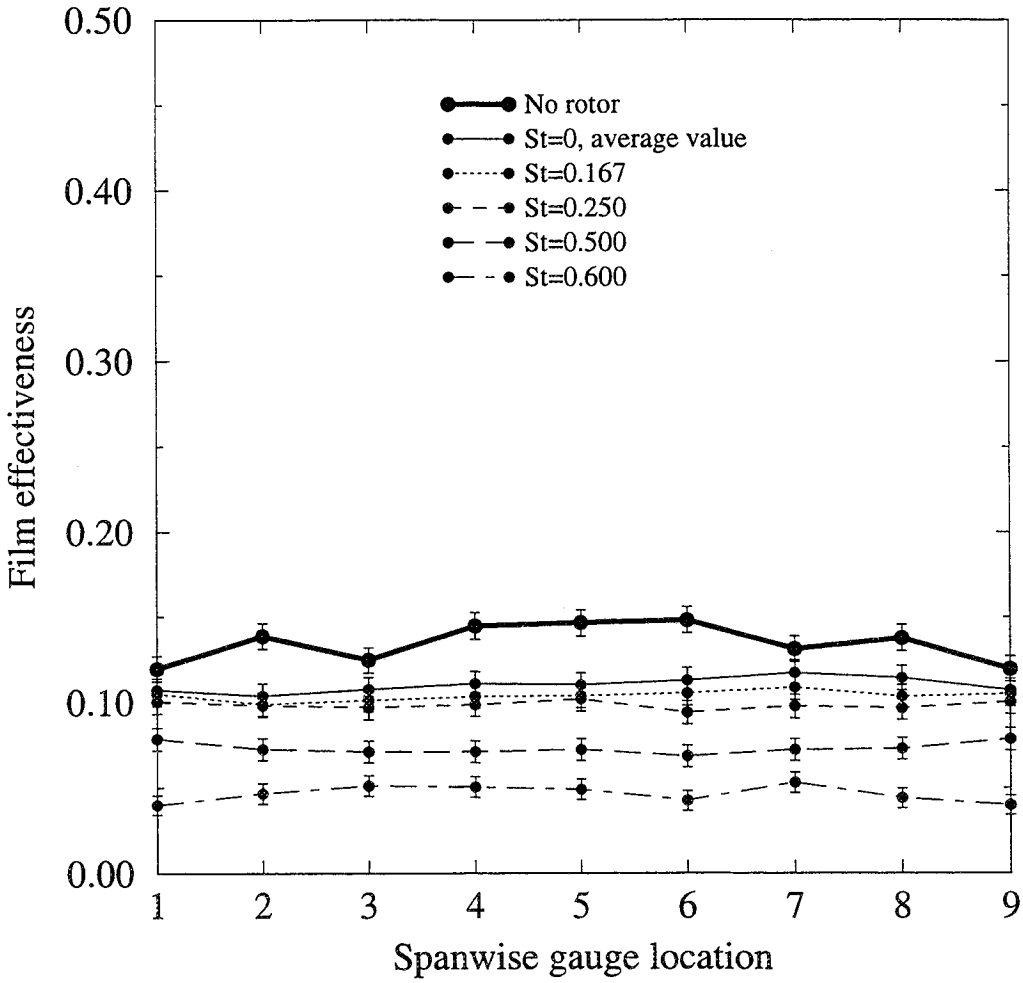

Figure 58: Film effectiveness for CO_2 injection at B=1.0, chord location 2.

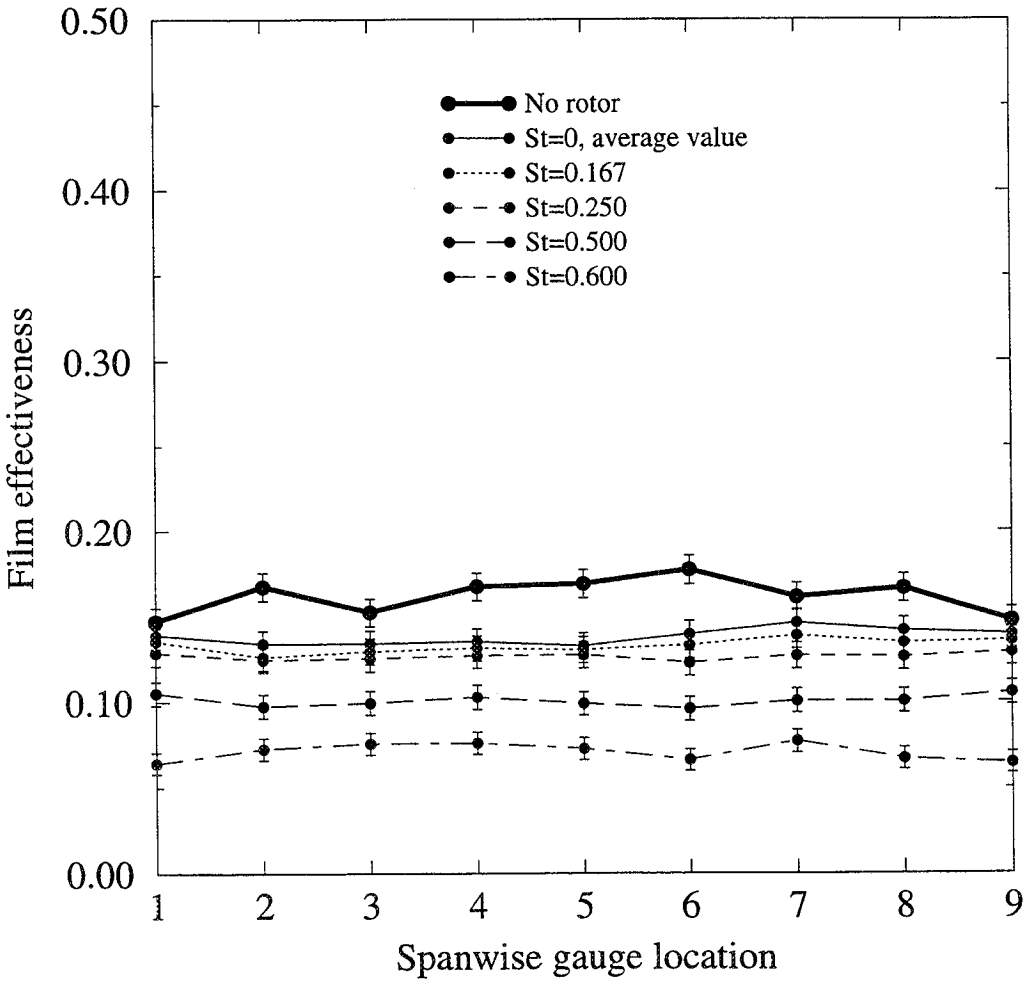

Figure 59: Film effectiveness for CO_2 injection at B=1.0, chord location 3.

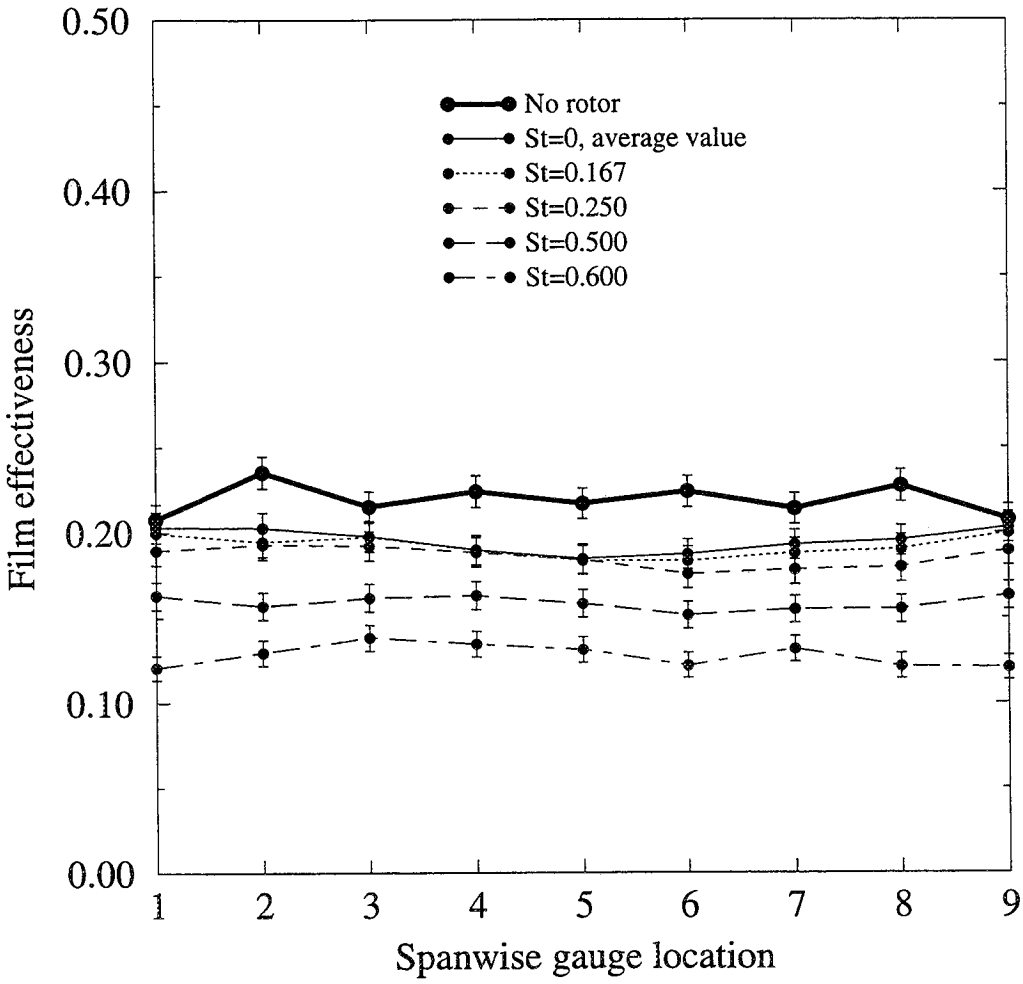

Figure 60: Film effectiveness for CO_2 injection at B=1.0, chord location 4.

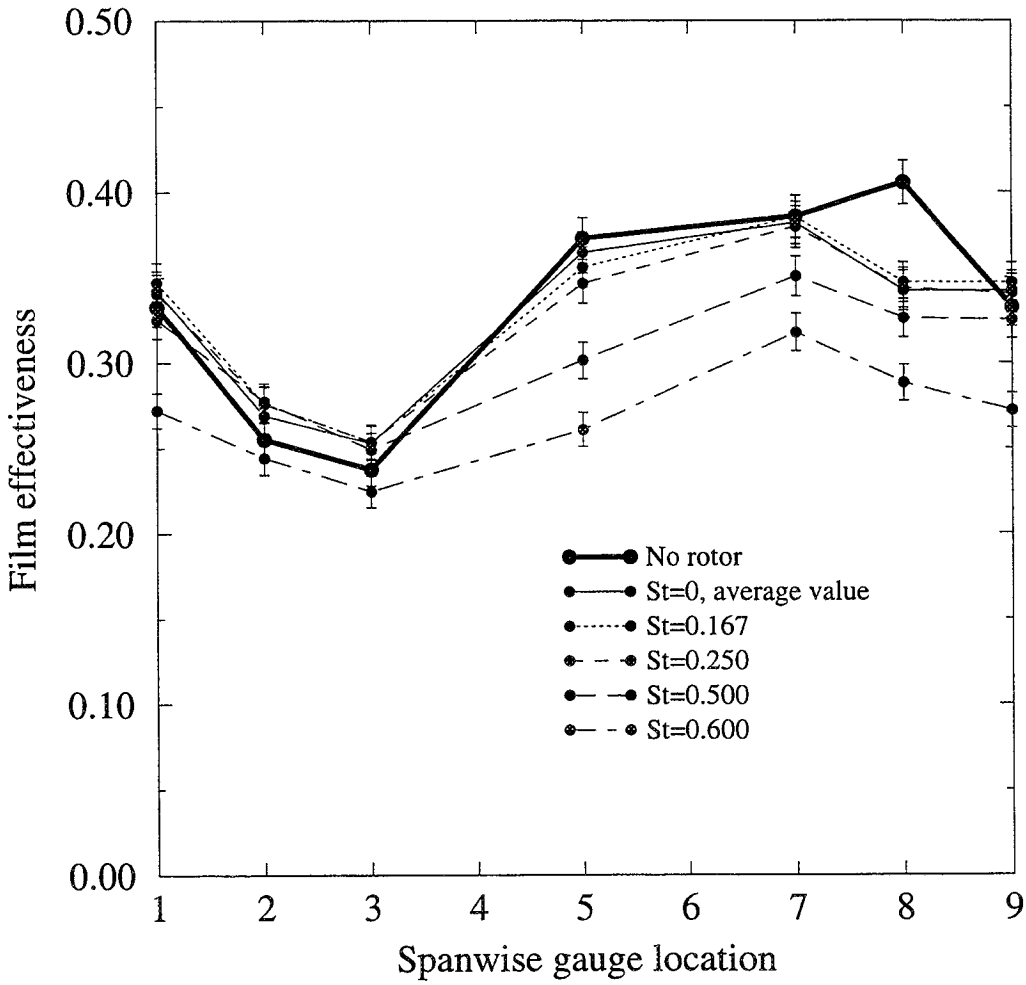

Figure 61: Film effectiveness for CO_2 injection at B=1.0, chord location 5.

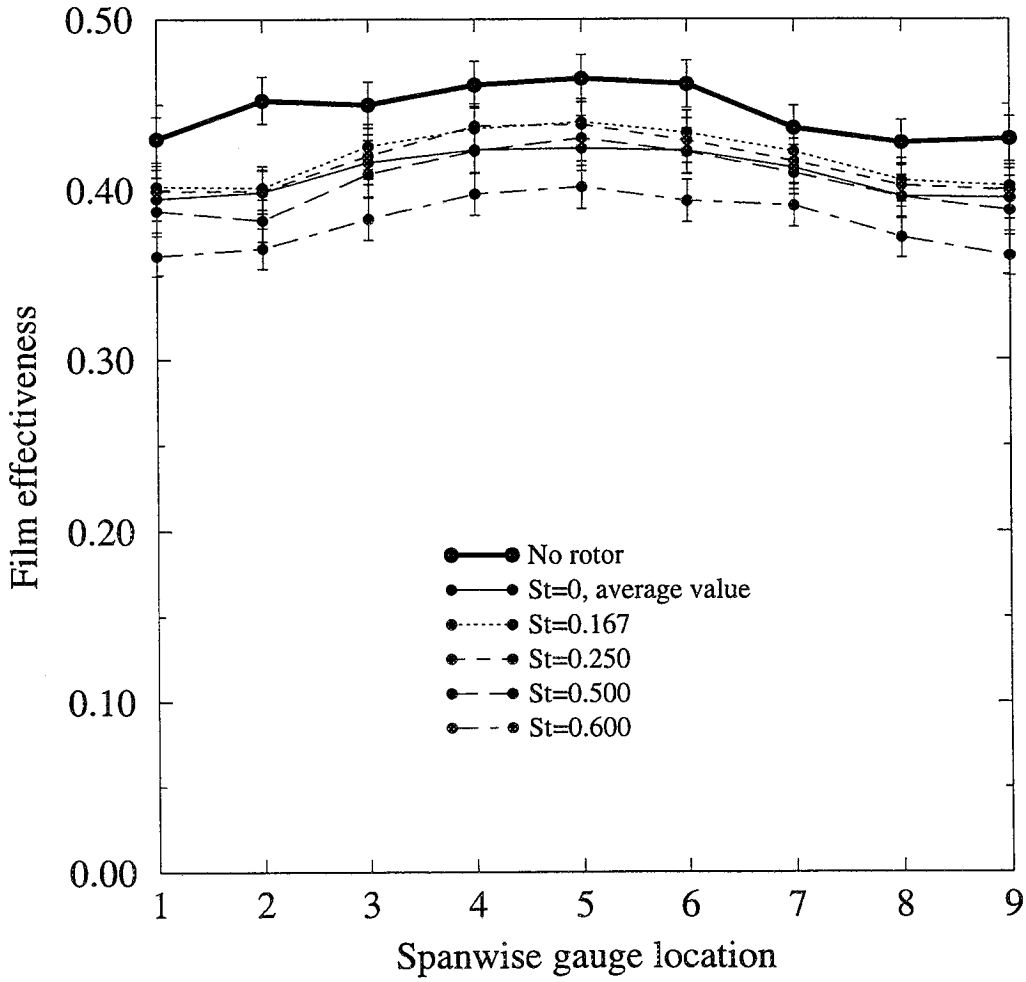

Figure 62: Film effectiveness for CO_2 injection at B=1.0, chord location 6.

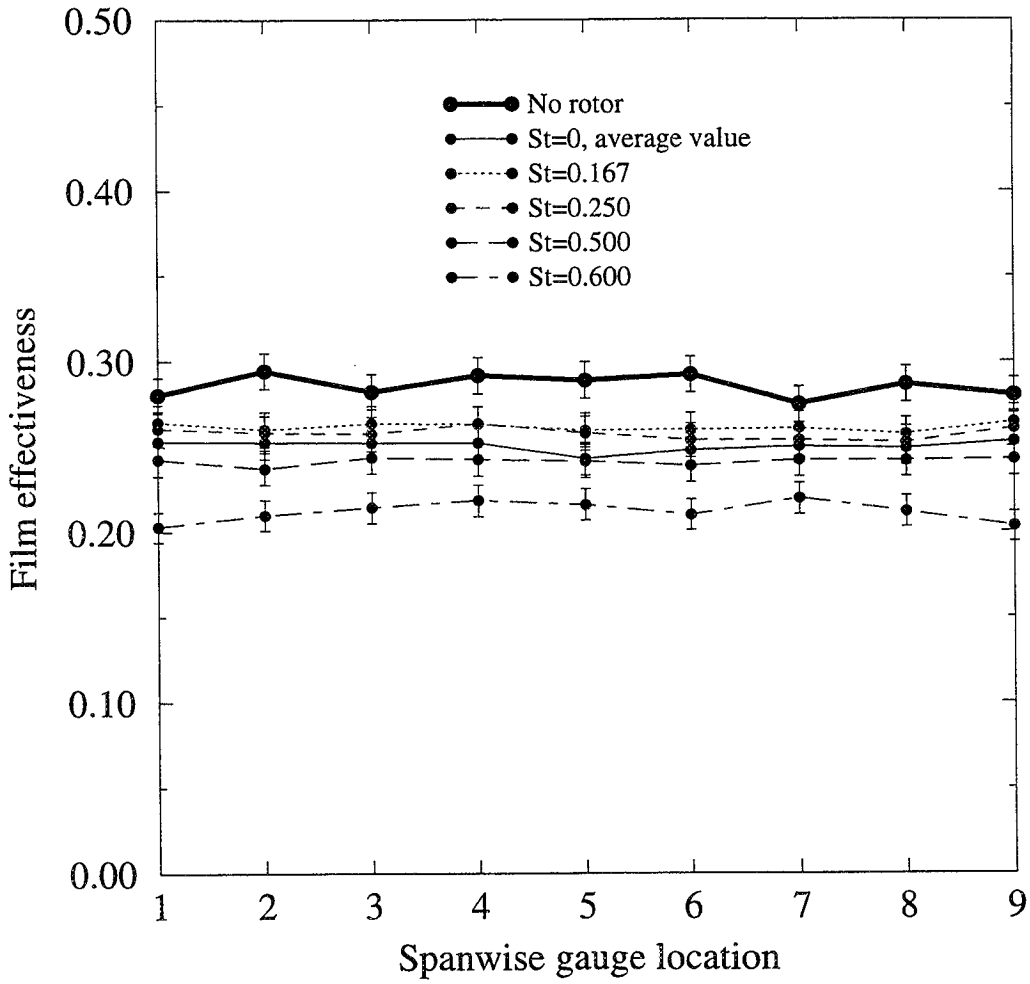

Figure 63: Film effectiveness for CO_2 injection at B=1.0, chord location 7.

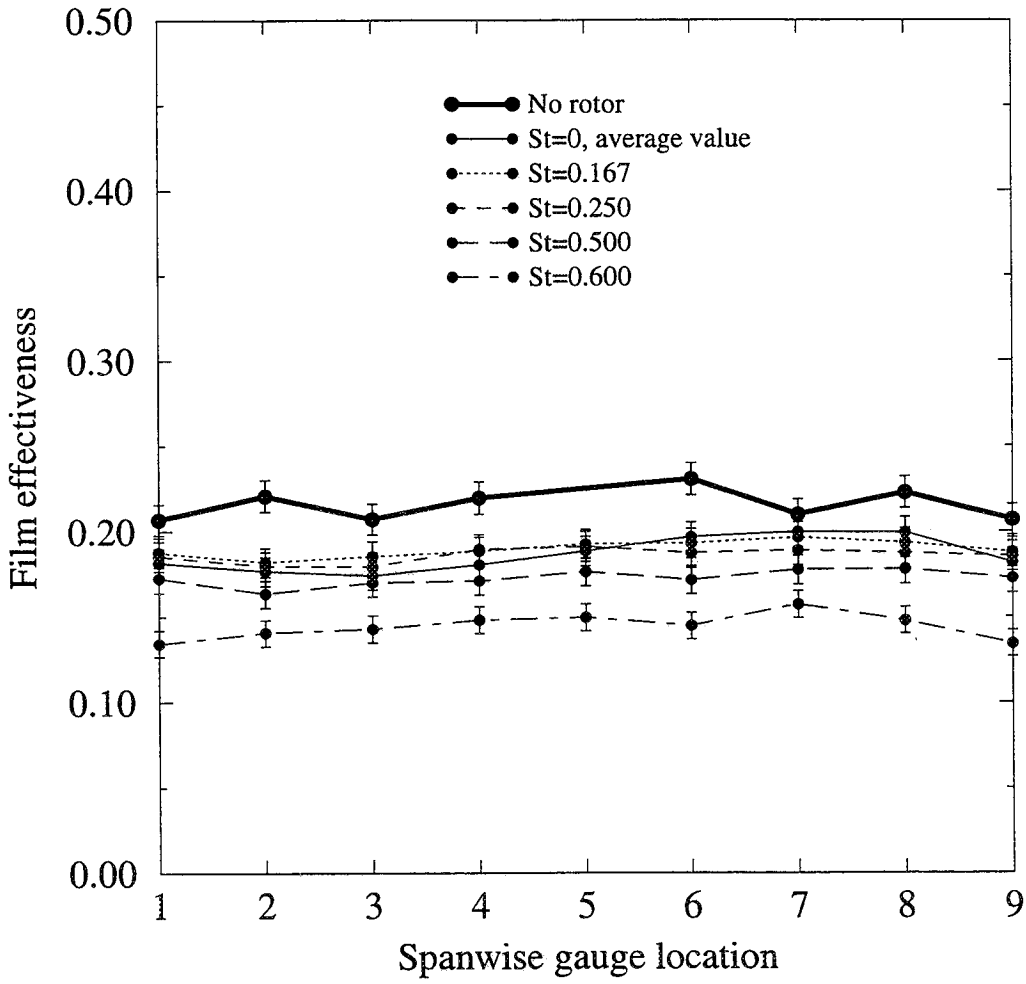

Figure 64: Film effectiveness for CO_2 injection at B=1.0, chord location 8.

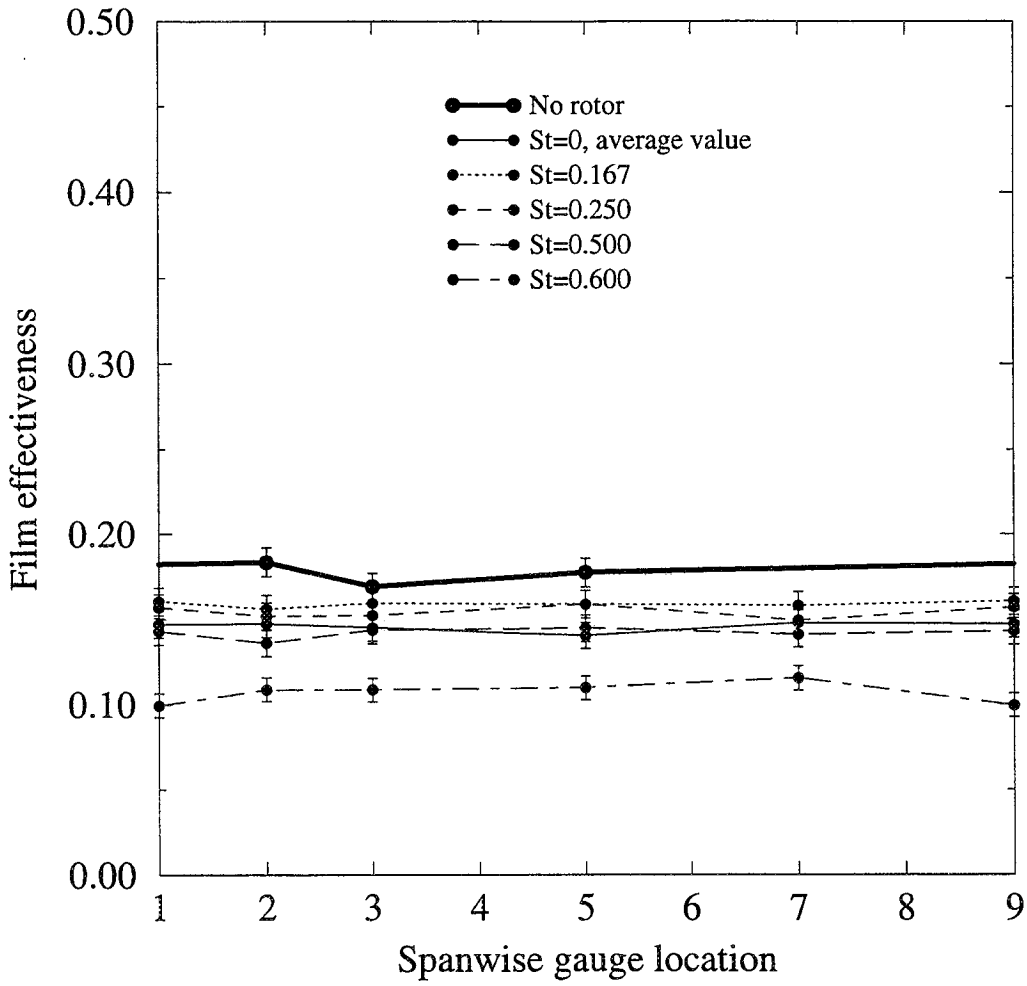

Figure 65: Film effectiveness for CO_2 injection at B=1.0, chord location 9.

increase offsets the decrease in the high film effectiveness region (spanwise locations 5 through 8), so the span-average film effectiveness is not degraded by the presence of a rotor wake or by increasing Strouhal number up to about St=0.250. This helps explain the behavior seen on the suction side in Figures 37 through 40, where the presence of a rotor has a greater effect at larger distances from the film holes. Near the film holes, the wake acts to effectively spread the film jet, reducing spanwise gradients but not the span-average film effectiveness since the gaps between the film jets are filled. Farther downstream, the effect of this spanwise mixing of the jet begins to reduce the span-average film effectiveness since the low film effectiveness gaps are already filled, and no additional benefit results from spanwise mixing.

Near the pressure surface leading edge (Figure 62), there is a small but consistent spanwise variation of film effectiveness. For all wake conditions, the film effectiveness is slightly higher at spanwise locations 3 through 6. However, unlike Figure 61, the reductions in film effectiveness due to increased Strouhal number are constant across the span, much like the downstream suction and pressure surface locations. This indicates that the film jets spread out more quickly on the pressure surface, and any benefit due to increased spreading of the jets by the wake is no longer present at x/d=8.0.

Figures 66 through 74 present the spanwise Nusselt number distributions, again for the case of carbon dioxide injection at a blowing ratio of 1.0. These plots indicate

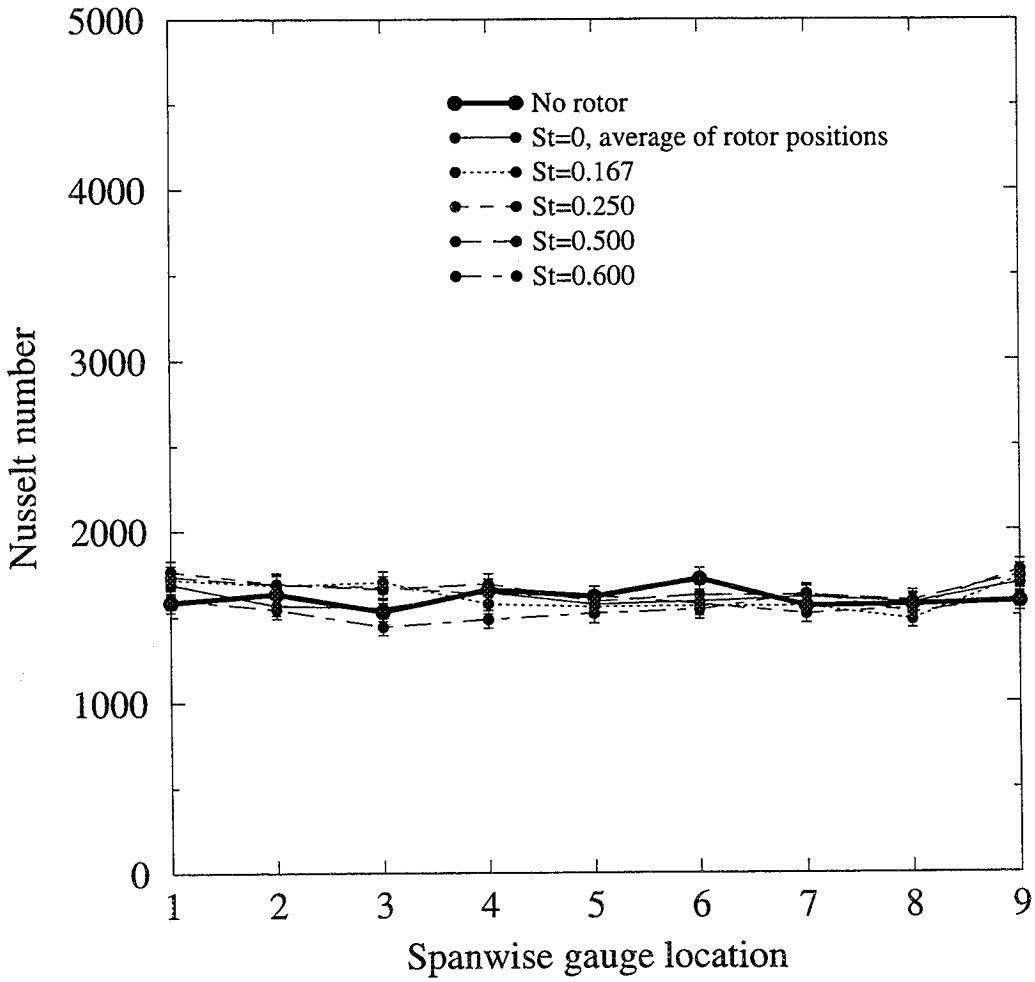

Figure 66: Nusselt number for CO_2 injection at B=1.0, chord location 1.

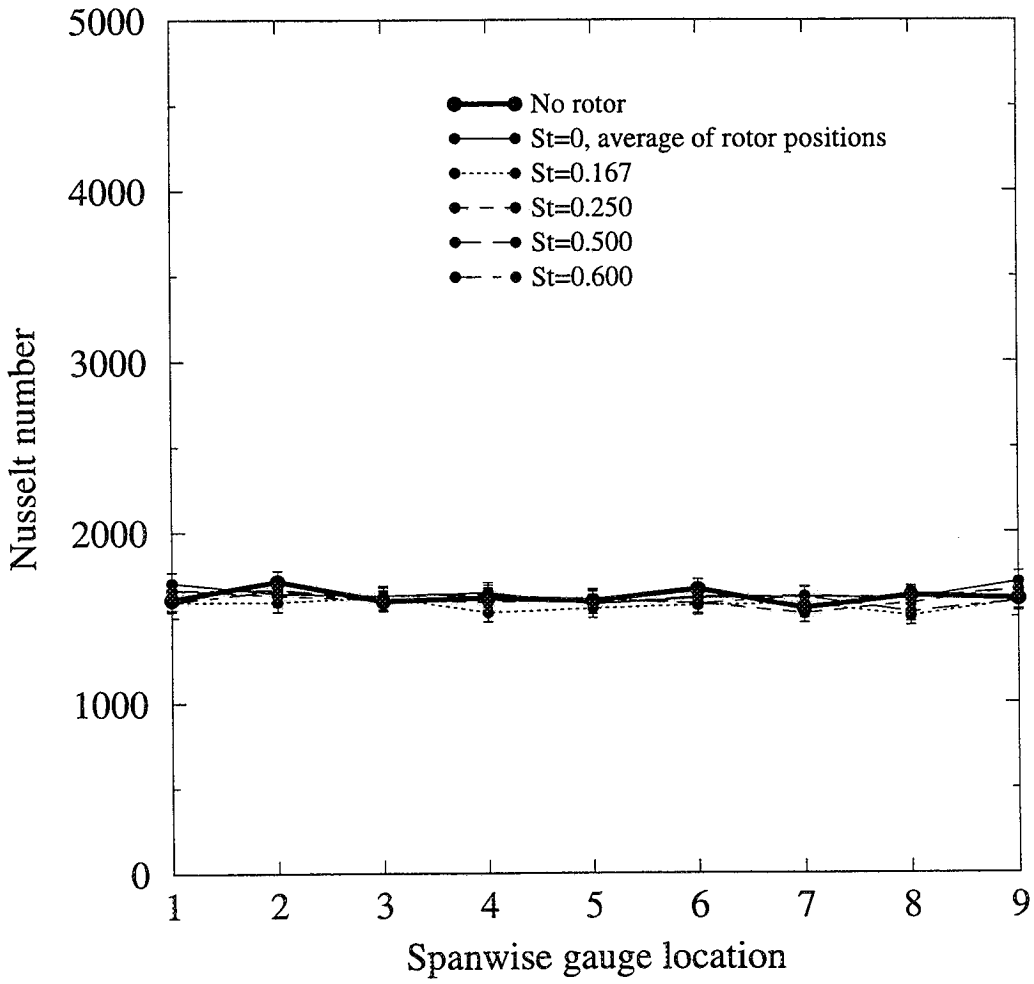

Figure 67: Nusselt number for CO_2 injection at B=1.0, chord location 2.

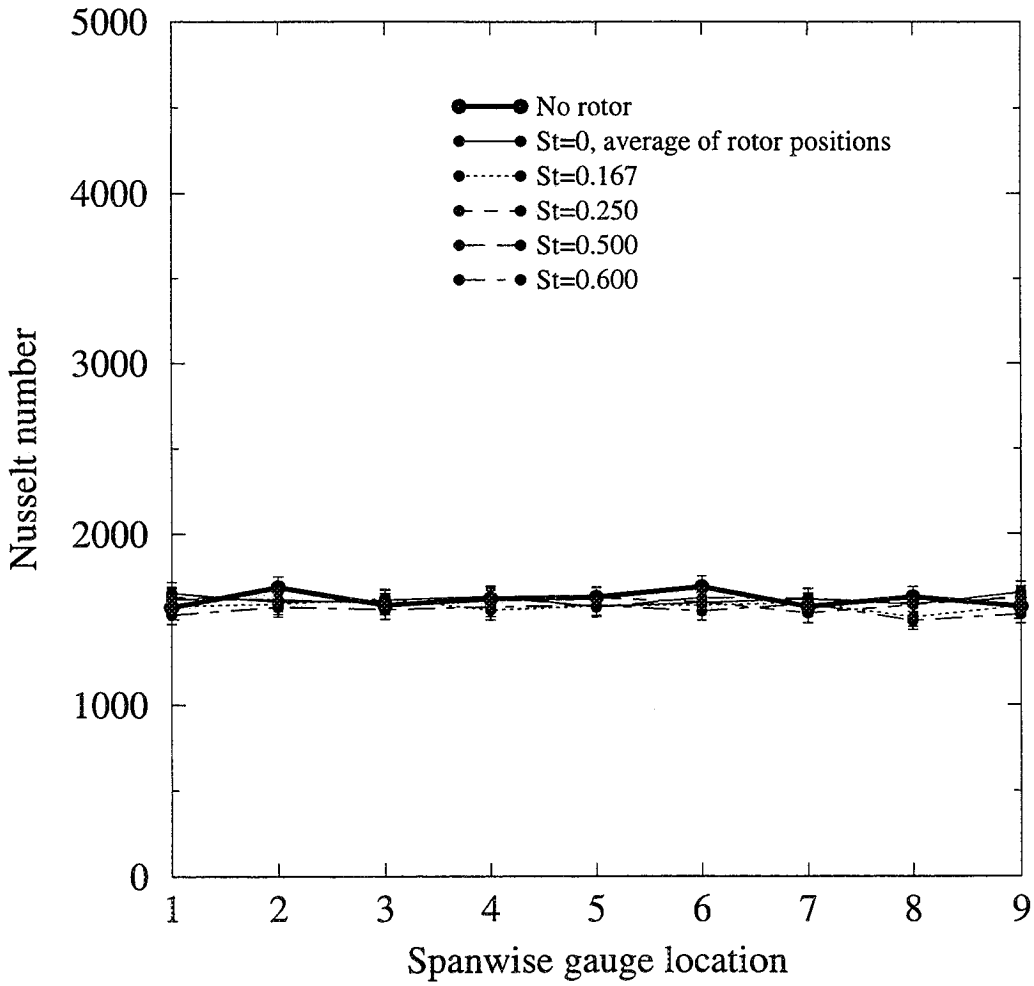

Figure 68: Nusselt number for CO_2 injection at B=1.0, chord location 3.

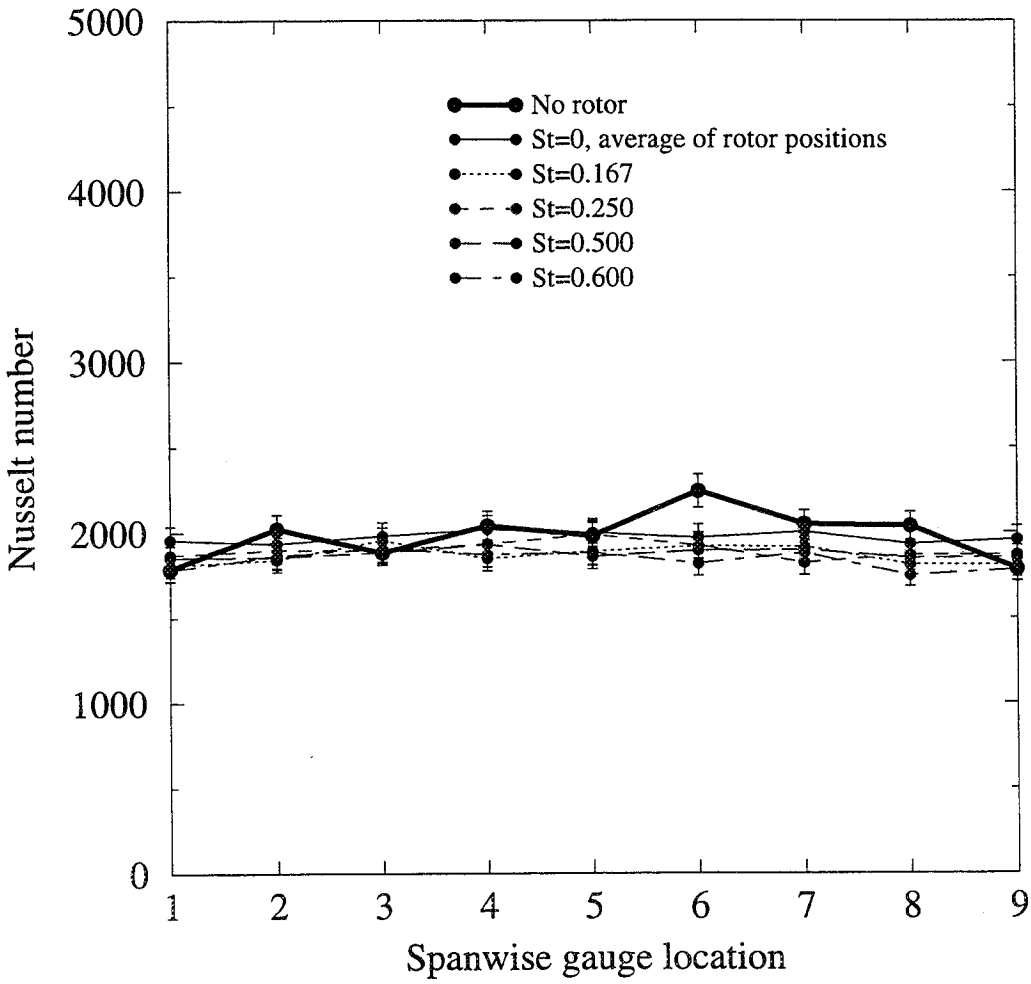

Figure 69: Nusselt number for CO_2 injection at B=1.0, chord location 4.

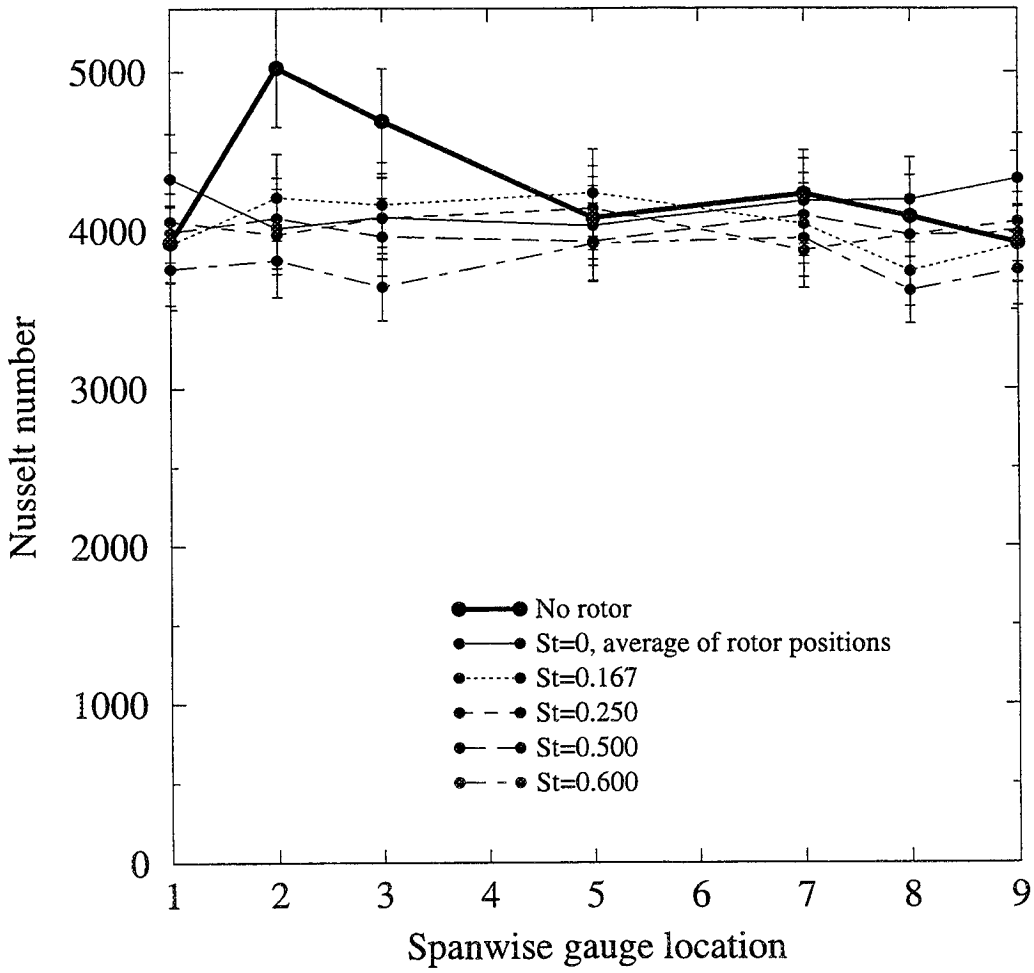

Figure 70: Nusselt number for CO_2 injection at B=1.0, chord location 5.

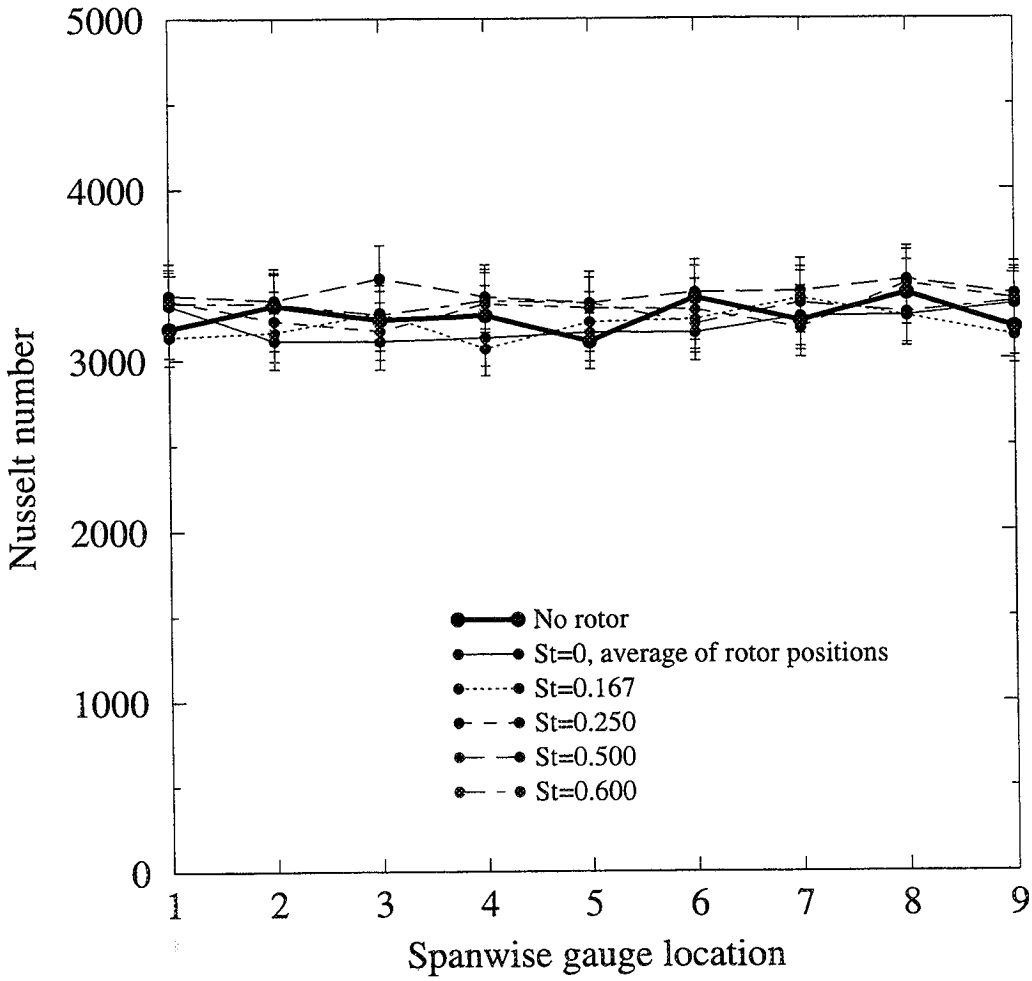

Figure 71: Nusselt number for CO_2 injection at B=1.0, chord location 6.

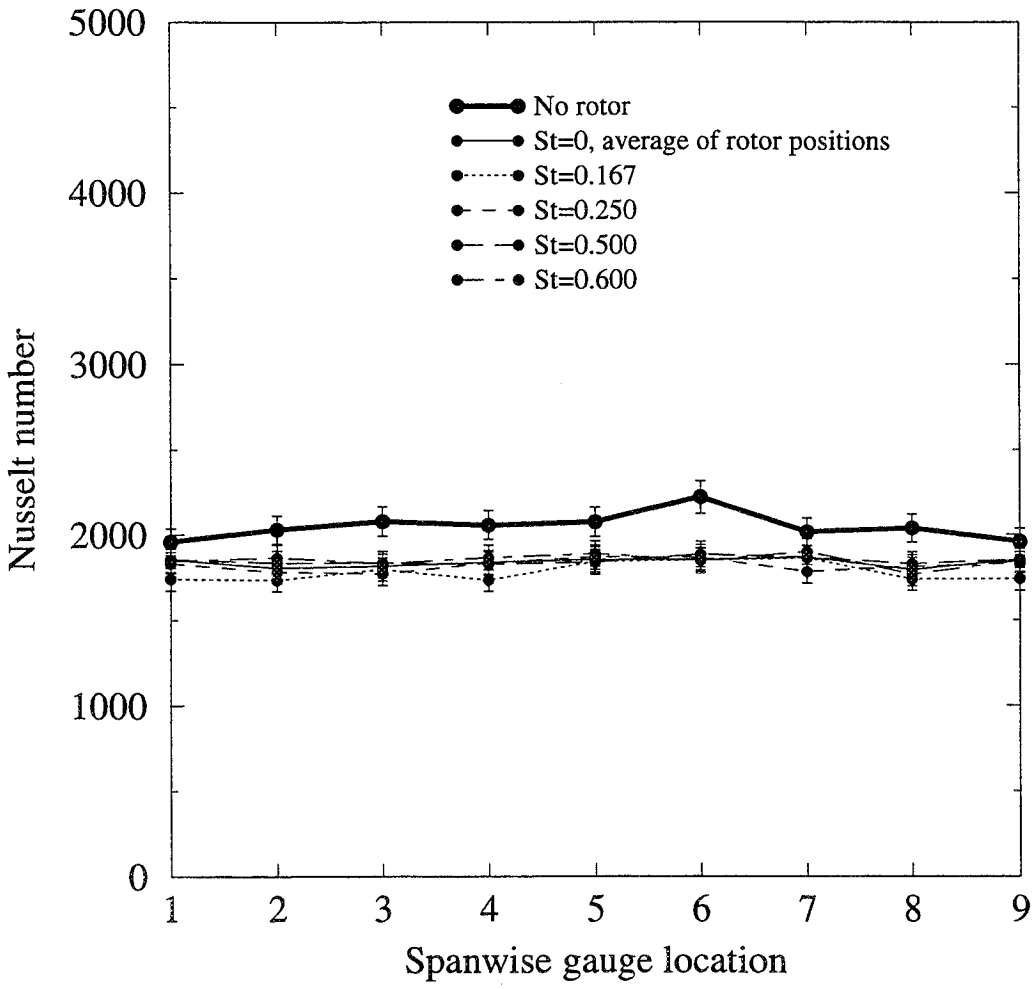

Figure 72: Nusselt number for CO_2 injection at B=1.0, chord location 7.

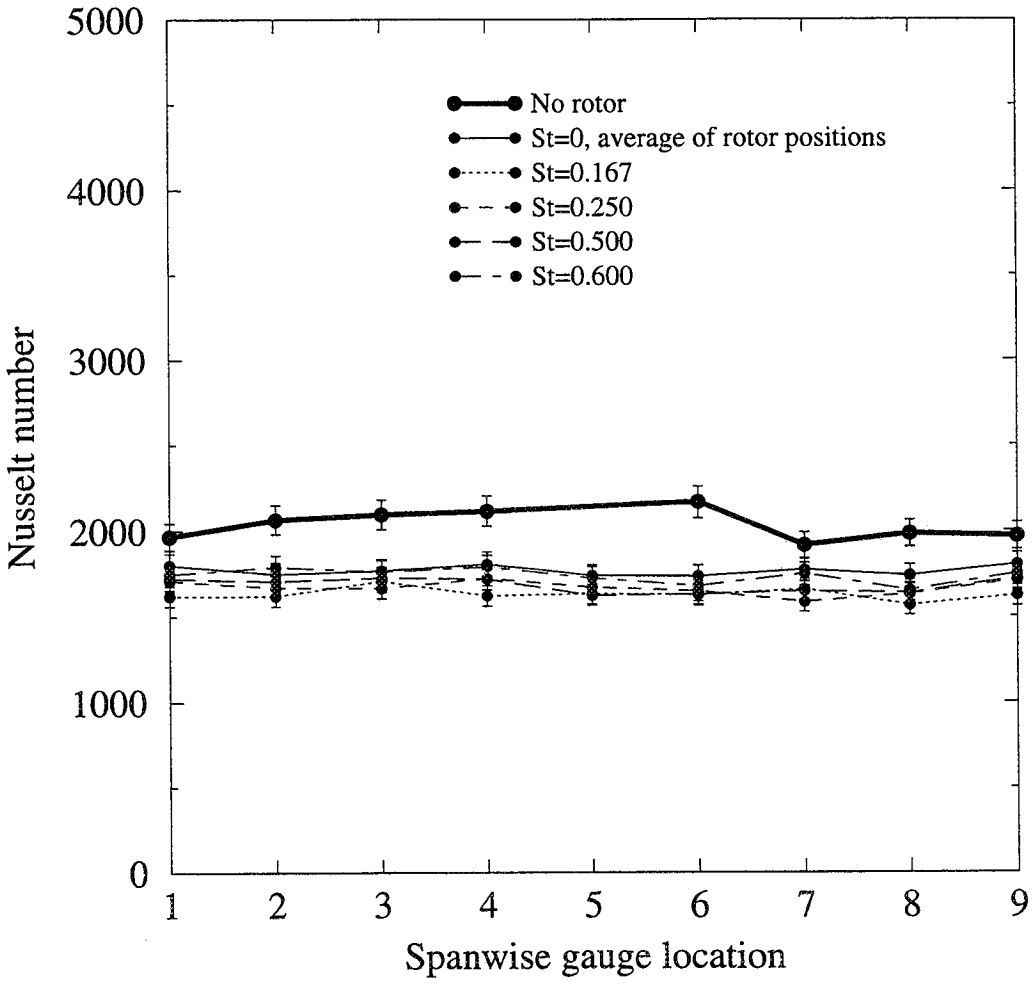

Figure 73: Nusselt number for CO_2 injection at B=1.0, chord location 8.

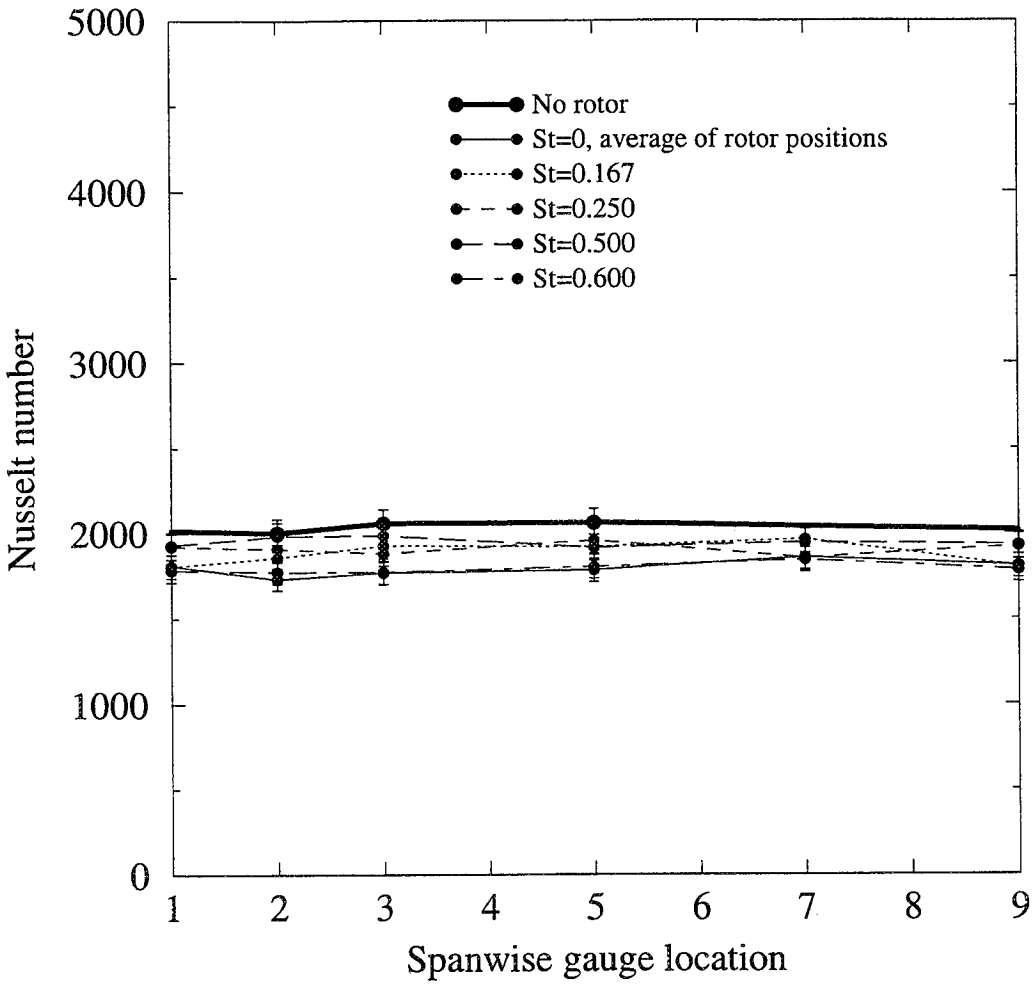

Figure 74: Nusselt number for CO_2 injection at B=1.0, chord location 9.

very little spanwise variation in Nusselt number, even near the leading edge. At chord location 5 (Figure 70), spanwise gauge locations 2 and 3 for the no rotor case seem to indicate an increase in Nusselt number, but the sharp drop to spanwise location 1 and the absence of a similar trend for other Strouhal numbers cast doubt on these points, although a subsequent check of the data showed the gauges to be functioning properly. Except for those data points, there is no indication of meaningful spanwise variation for any chordwise location at any Strouhal number. These plots again show the increase in Nusselt number for the no wake case near the pressure surface trailing edge that was seen in Figures 41 through 44. Except for this increase, there is very little effect of Strouhal number on Nusselt number.

Stationary wake results

Because of the difficulty in obtaining meaningful results from the unsteady temperature readings, it was decided to scrutinize the results from the stationary wake data that was obtained as a limiting case of zero Strouhal number. Figures 75 and 76 show the span-average steady film effectiveness variations with rotor wake location for the suction and pressure surfaces of the blade, respectively. Wake location 5 corresponds to a rotor position such that the wake is aligned with the blade leading edge. Wake location 9 is identical to location 1, and is for the wake at mid-passage. Wake locations 2 through 4 are nearer the suction surface, and wake locations 6 through 8 are nearer the pressure surface. These plots are essentially a limiting case

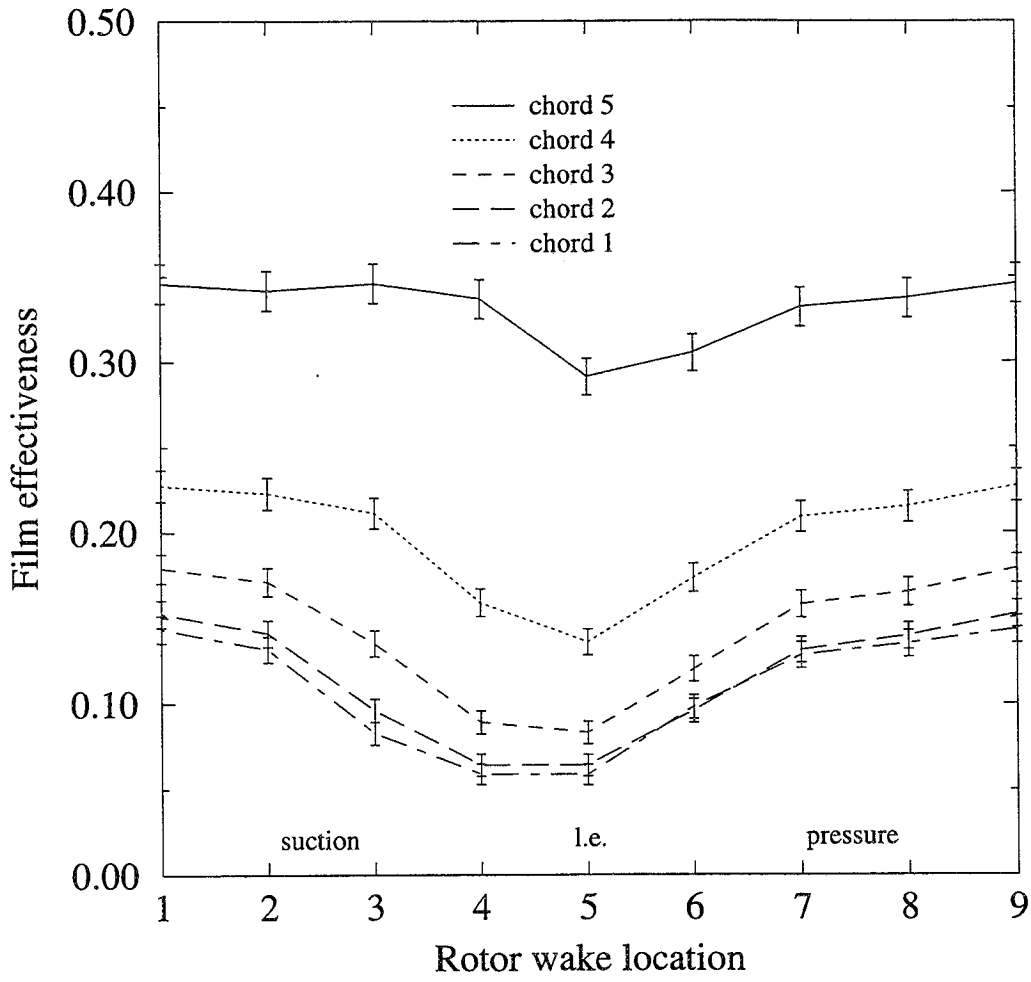

Figure 75: Span–average film effectiveness for CO_2 injection at B=1.0 with stationary rotor, suction surface.

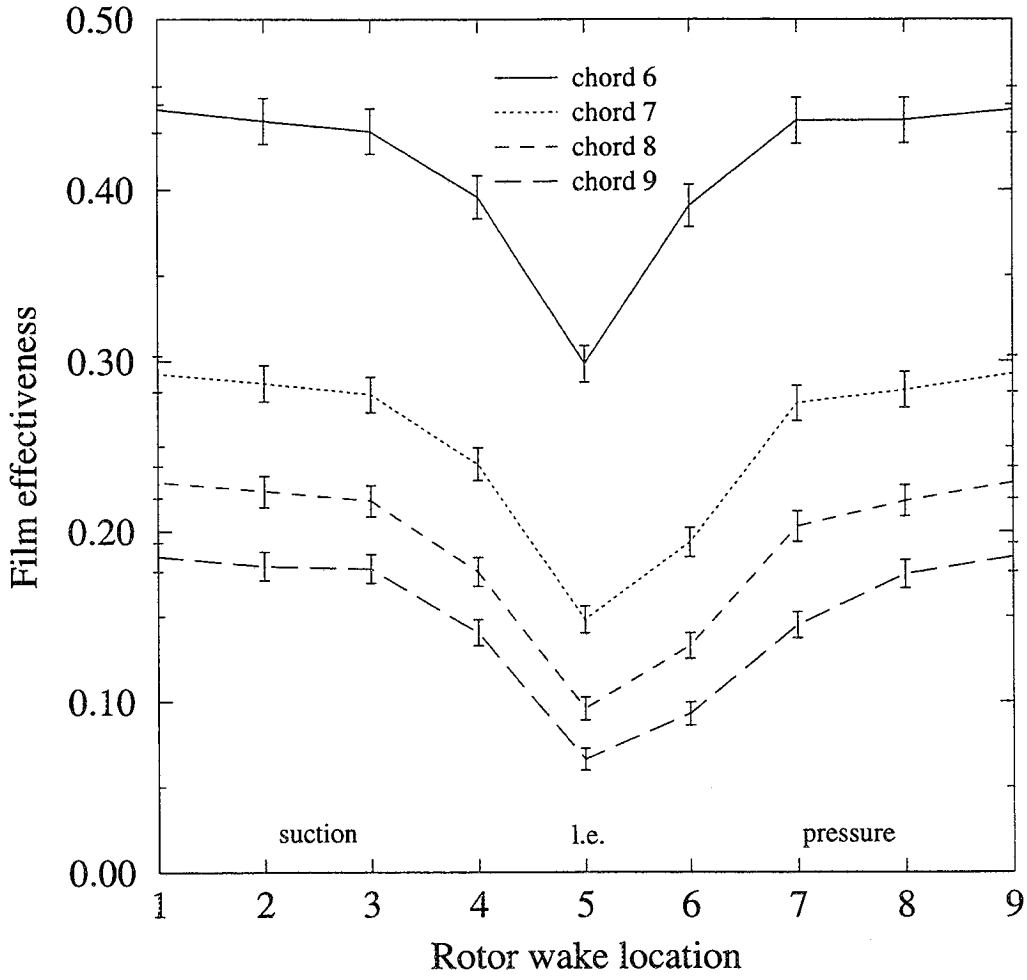

Figure 76: Span–average film effectiveness for CO_2 injection at B=1.0 with stationary rotor, pressure surface.

of what was shown in Figures 21 and 22. Here, however, the rotor speed has been reduced to zero, and instead of plotting as a function of time, the results are plotted as a function of angular wake location.

Figure 75 shows a highly repeatable distribution for all chordwise locations. With the wake impinging on the blade (location 5), the film effectiveness is reduced by about 0.05 at chord 5 and almost 0.10 at the downstream locations. This result is expected due to the enhanced film mixing caused by the increased turbulence in the wake. It is surprising that the absolute reductions in film effectiveness are greater at the downstream locations, because the levels of film effectiveness are lower at these locations. However, this supports the explanation given for the behavior in Figure 61. The impingement of the wake on the leading edge increases spanwise mixing of the film, but this action is actually favorable in the low effectiveness gaps between jets, which at chord 5 partially offsets the detrimental dissipation of the film.

Figure 76 indicates an even greater reduction in film effectiveness due to wake impingement on the pressure surface than on the suction surface. Reductions of about 0.15 at chord 6 and at least 0.10 downstream are noted. Both the suction and pressure surface data show an asymmetry of the film effectiveness profile. For both sides of the blade, the film effectiveness is reduced more for a wake location nearer that side, as expected. Thus the suction surface film effectiveness is reduced more at wake locations 3 and 4 than at wake locations 6 and 7, while the opposite is true on the

pressure surface.

Figures 77 and 78 show the span-average steady Nusselt number variations with rotor wake location for the suction and pressure surfaces of the blade, respectively. The only chordwise location which indicates an effect of wake location is chord 6, which is the pressure surface leading edge. There are two competing mechanisms at work in the wake. First, the wake exhibits an increase in turbulence, which would tend to increase the Nusselt number for the same reason that it tends to decrease film effectiveness - because of enhanced mixing. But the wake also exhibits a velocity defect which would tend to decrease the Nusselt number because of lower velocity gradients at the wall. Apparently, the second effect is predominant on the pressure surface leading edge. A very small but consistent reduction may also be seen for chords 7 through 8 near wake location 5.

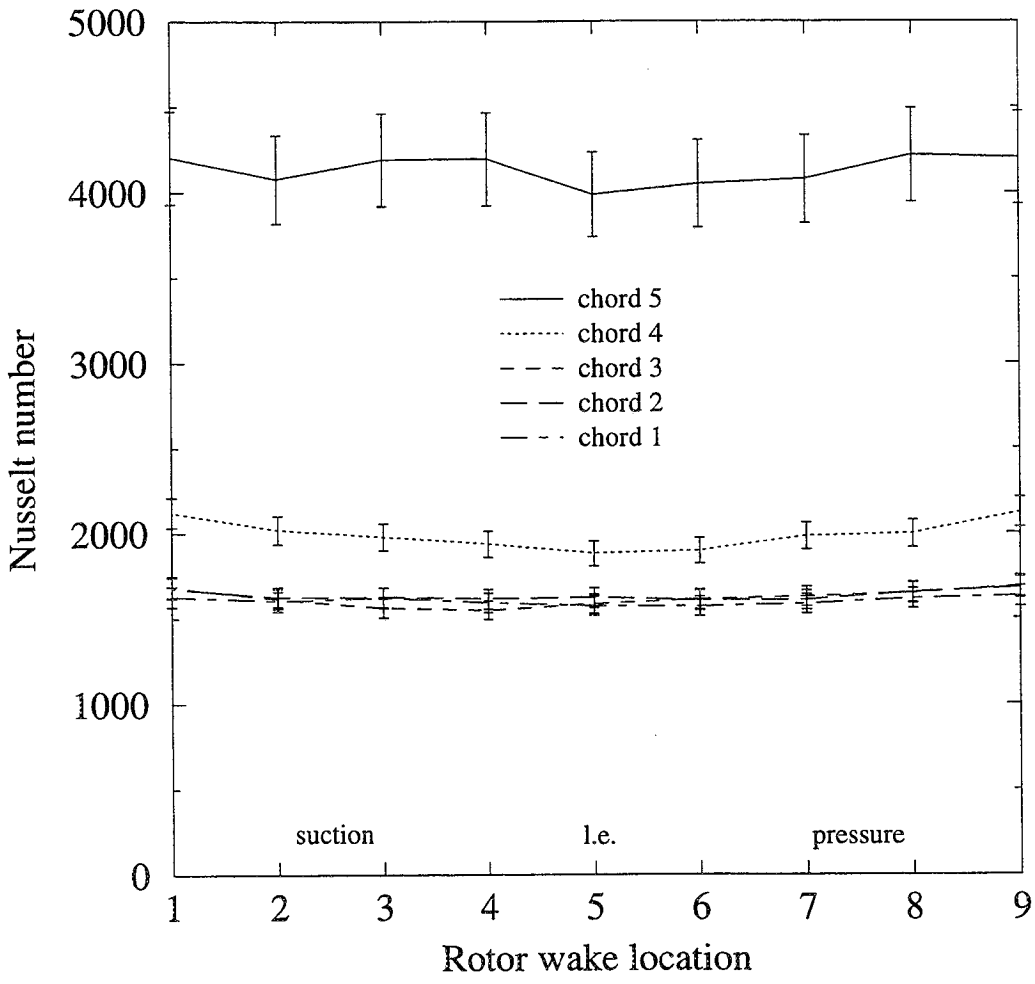

Figure 77: Span–average Nusselt number for CO_2 injection at B=1.0 with stationary rotor, suction surface.

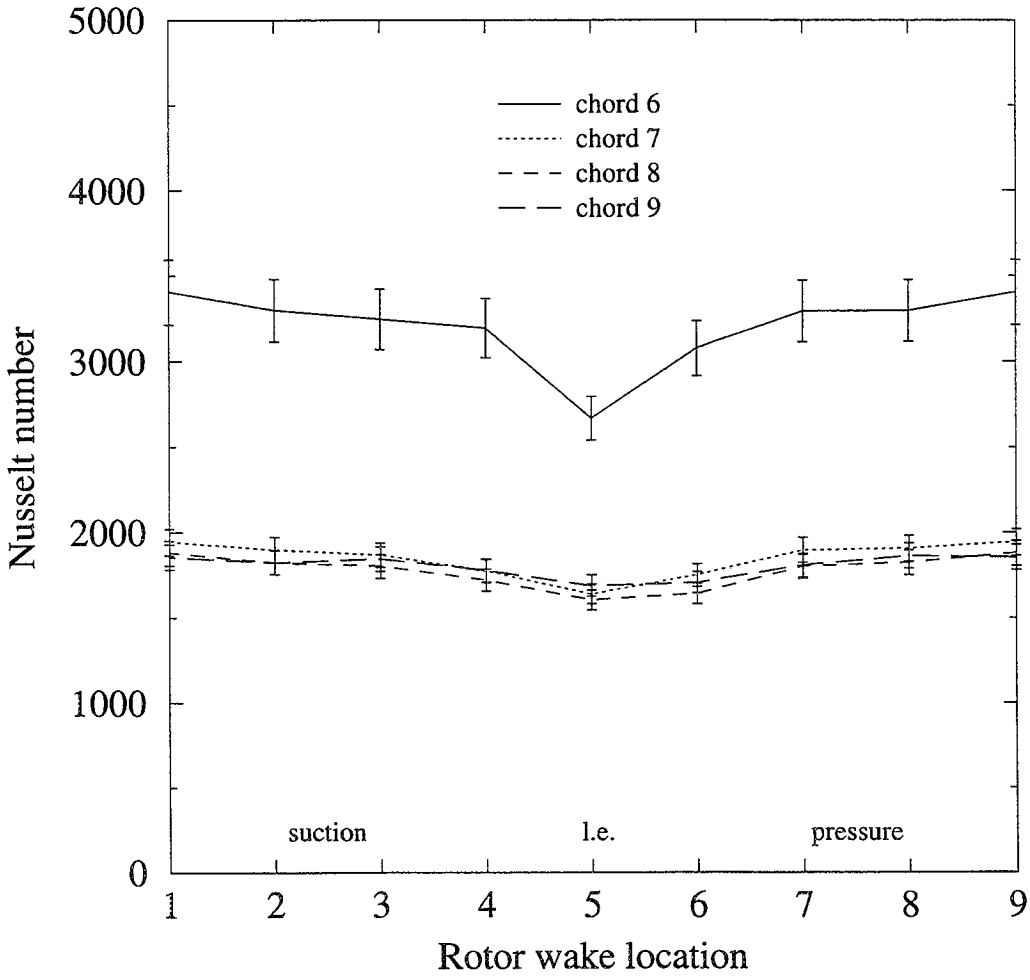

Figure 78: Span–average Nusselt number for CO_2 injection at B=1.0 with stationary rotor, pressure surface.

4. COMPUTATIONAL STUDY

Unsteady computation description

A three-dimensional viscous turbulent calculation was performed for the experimental geometry using the code rvc3d [42]. The code solves the thin-layer Navier-Stokes equations with an explicit finite-difference technique. The Baldwin-Lomax turbulence model was employed [43]. The computation described herein attempts to model the geometry and flow conditions studied in the previously described companion experiment. The calculation models the flowfield as a linear cascade with spanwise periodicity based on a unit cell of the film hole pattern. Although the experiment is not precisely periodic due to the annular geometry and endwall effects, this simplification greatly reduces the number of grid points required to resolve the flow field. This is especially important for unsteady calculations. The blade-to-blade C-grid consists of 305 points tangential to the blade and 90 points normal to the blade (Figure 79), and was generated using the grape code [44]. The large number of grid points in the blade-to-blade direction is required to adequately resolve the wake at the upstream boundary, particularly along the grid line from the upstream corners to the blade. The grid upstream boundary is located at the plane of the rotor. The passing wakes are modeled using a zero axial velocity boundary condition on a patch of the upstream boundary. This patch translates with each iteration based on a design rotor speed of 5800 rpm, and produces a 1:1 ratio of wakes to blades. The experimental

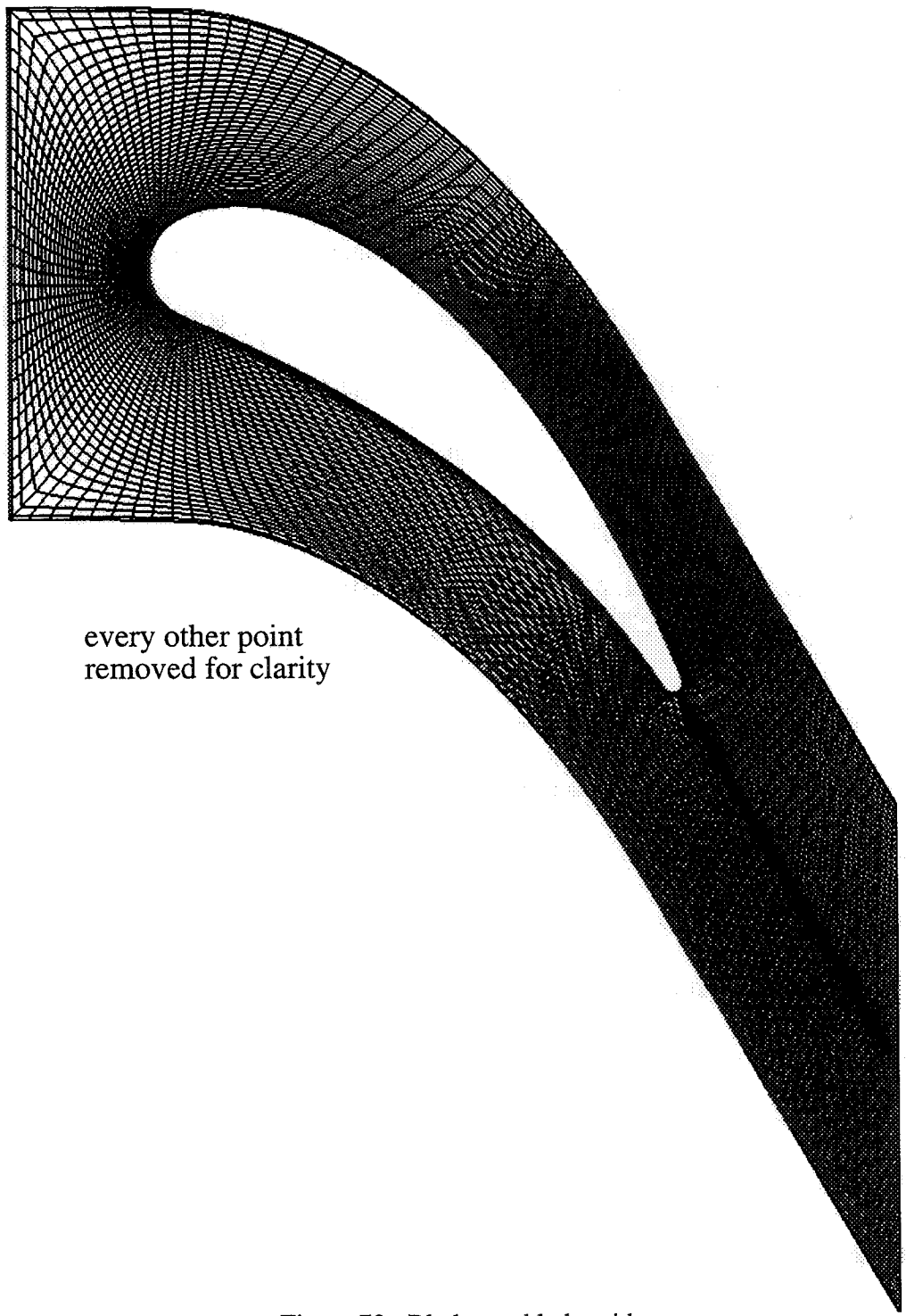

Figure 79: Blade–to–blade grid

ratio is 24:23. The non-wake portion of the upstream boundary is modeled by constant stagnation pressure and purely axial flow. The entire upstream boundary uses extrapolated static pressure.

The three-dimensional grid has 20 grid points in the spanwise direction, and is produced by simply stacking the two-dimensional grid of Figure 79 in the spanwise direction, producing an orthogonal surface grid (Figure 80). The film holes are modeled using 69 grid points per hole. Grid points are packed in the leading edge region to increase the number of grid points in the holes. The blade boundary conditions are modified in the following manner. At each surface grid point, the code determines from geometry whether the grid point is a hole point or a wall point. Wall points are given standard viscous adiabatic wall boundary conditions. Hole points are given inlet stagnation pressure boundary conditions based on fully developed laminar circular duct flow and extrapolated static pressure. The application of a stagnation pressure profile rather than the velocity profile used by most researchers (e.g. Garg and Gaugler [26]) has the advantage of allowing variations in local static pressure to skew the velocity profile. This is especially important for showerhead cooling, since static pressures exhibit large gradients in the showerhead region. A stagnation temperature and centerline stagnation pressure of 0.65 and 1.03 times cascade upstream values, respectively, were assumed for the film coolant plenum. These values were chosen to produce density and blowing ratios approaching those in the experimental portion of this study. The plenum temperature of 0.65

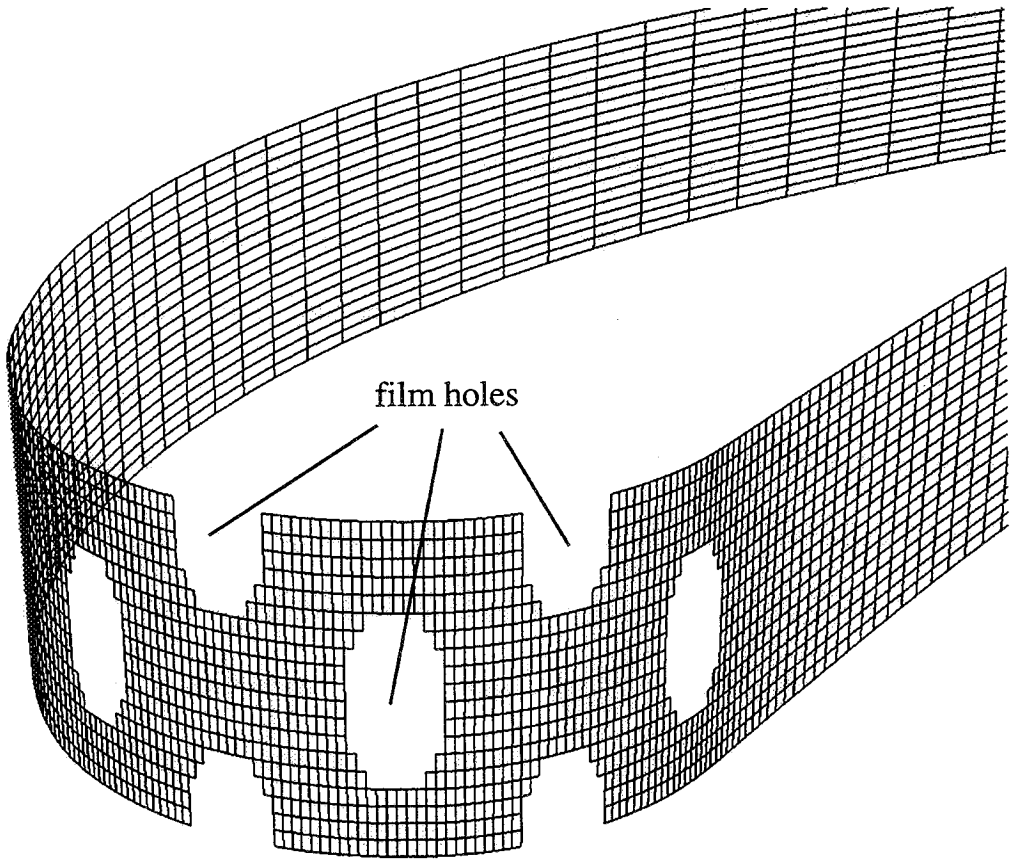

Figure 80: Blade surface grid.

yields a stagnation density ratio equal to that for carbon dioxide injection. The plenum pressure of 1.03 yields a time-average blowing ratio of about 0.824. This was considered an acceptable value to investigate the flow physics since it is in the range typical of showerhead film cooling blowing ratios. Further reductions in the stagnation pressure yielded numerical instabilities which caused the solution to diverge. This divergence could only be avoided by severely underrelaxing the updating of the static pressure at the hole boundary. While this was done for most of the steady computations where time-accuracy is not necessary, it was not done for the unsteady computation. The purpose of the unsteady computation is to understand the flow physics, and this includes the high frequency changes in the hole exit static pressure. The flow angle at hole points was fixed at the geometric angle of the holes themselves, which is a 30° angle to the blade in the spanwise direction. This angle produces a 2:1 aspect ratio ellipse at the blade surface. Figure 80 shows the surface grid with all hole points removed. Because of the discontinuity between wall and hole, wall and hole boundary conditions were smoothly interpolated for points straddling the boundaries. It was determined that this method was preferred over attempting to distort the surface grid to conform to the elliptical holes. Such distortions were found to produce spatial spikes of increased entropy upon close inspection of earlier calculations.

The unsteady calculation was performed on the NASA Lewis Cray Y-MP supercomputer. Implicit residual smoothing was employed using a spatially-varying

coefficient with a maximum value of 0.75, allowing a maximum CFL number of about 7.7. The maximum time step was limited due to stability considerations by the grid spacing at the wall. A dimensionless distance from the wall may be defined as:

$$y^{+} = \frac{y(|\tau_{wall}|/\rho_{wall})^{1/2}}{\nu_{wall}}$$

where y is the dimensional normal distance from the wall, and τ_{wall}, ρ_{wall}, and ν_{wall} are the shear stress, density, and kinematic viscosity at the wall, respectively. For heat transfer calculations, a y^{+} of less that 1 is recommended at the first grid point away from the wall. However, such a spacing would have resulted in unacceptably large run times. Because of the adiabatic wall boundary condition and the resulting lack of temperature gradients at the wall, it was decided to relax y^{+} to less than 10 at the first grid point for all locations. Approximately 2.5 hours of CPU time were required for a single wake passing period. 13 wake passings were required for the solution to converge. Residuals based on density were computed eight times per wake passing by comparing the current solution with the previous wake passing solution at the same phase. The solution was considered converged when the residuals had decreased by at least three orders of magnitude. The residuals were reduced another order of magnitude as a check, and there were no appreciable changes in the solution. The unsteady solution was then averaged with time over one wake passing to allow for meaningful comparison with steady solutions. This average was obtained by time-averaging pressure, temperature, and the three components of velocity at each

grid point.

Steady computation description

In order to isolate the time-average effect of the wake passing on the blade film effectiveness distribution, a companion steady solution was produced using an identical solution procedure to the unsteady case, except the wake boundary condition was removed. The time-average unsteady solution was used as the starting solution for this computation. The steady solution had no wake on the upstream boundary, so it was necessary to apply a steady stagnation pressure and tangential velocity boundary condition. Since a tangentially varying boundary condition would be difficult to estimate for a steady solution a priori, tangentially constant stagnation pressure and tangential velocity were applied. In order to best model the unsteady solution with a steady solution, it is important to match the time-average flow rate of the coolant and the flow split of the coolant between the suction and pressure sides of the blade. If this is not done, any differences between the solutions may simply be due to a different amount of coolant flow on one or both surfaces of the blade. The coolant flow rate and flow split are determined by the local static pressure and stagnation line at the blade surface, which in turn can be controlled in the steady solution by changing the upstream stagnation pressure and the upstream swirl, respectively.

An initial attempt at a matching steady solution employed a zero inlet tangential velocity condition with an inlet stagnation pressure equal to the time- and circumferential-average inlet stagnation pressure from the unsteady solution. The stagnation pressure was computed to be about 0.99 times the unsteady solution non-wake stagnation pressure. This first steady solution was found to predict a greater coolant flow rate than the unsteady solution by several percent. In addition, a greater percentage of the coolant flowed to the suction side of the blade in the steady prediction. These differences indicated that a higher inlet stagnation pressure and a positive inlet swirl (in the wake direction) were necessary to match the time-average coolant flow properties from the unsteady solution. After several iterations, it was found that the desired stagnation line and hence coolant flow split could be produced by requiring a very small amount of swirl in the steady solution, about ten percent of the average inlet swirl in the unsteady solution. It was also determined that the correct showerhead region static pressure and hence film hole flow rate could be achieved by using a stagnation pressure about midway between the unsteady solution time-average and non-wake inlet stagnation pressures.

Additional steady computations were performed for purposes of comparison directly with the experimental data of this study. These computations made use of local time-stepping with a CFL number of 5.0 at all locations. This greatly reduced the time required to achieve a converged solution, and allowed solutions for various grid densities, hole boundary conditions, and heat flux conditions to be found. It also

allowed use of grids with tighter wall spacing. Because of local time-stepping, the y^+ value at the first grid point away from the solid boundaries may be chosen to be arbitrarily small. Solutions were performed using the unsteady solution grid as well as two other grids having wall grid spacings 10 and 100 times smaller than the unsteady solution grid. This produced y^+ values of less than 1 and less than 0.1 for all wall locations, respectively. Of course the wake may not be modeled in such steady solutions.

The reduced run time of solutions produced with local time-stepping also allowed variation of the hole boundary conditions. Solutions were performed with fully-developed laminar (polynomial), fully-developed turbulent (one-seventh power law), and slug flow (constant) stagnation pressure profiles. Solutions were also performed for other hole boundary conditions including a 45° hole exit angle boundary condition, and a hot injectant case with a plenum stagnation temperature of 1.113 times the cascade upstream value to match the temperature ratio from the experiment. Finally, heated wall cases were performed for all cases with a constant heat flux boundary condition matching that of the experiment to allow prediction of Nusselt numbers. Since the local time-stepping results are meant for comparison with experimental results and not with the unsteady computation results which used no underrelaxation, an underrelaxation value of 0.01 for the local static pressure update was applied in conjunction with different plenum stagnation pressure profiles to produce blowing ratios of 1.0 for all cases. This required plenum stagnation pressures for some cases

of less than the upstream stagnation pressure. This was particularly true for the slug flow cases, and resulted in very little or no flow from the center row of holes where the static pressure is near the upstream stagnation pressure. The results of the local time-stepping steady computations are presented in comparison with experimental results in Chapter 5.

Computational results

Figures 81 and 82 show the blade-to-blade entropy for two snapshots in time of the unsteady calculation. Entropy is defined here as:

$$s = c_v \ln(\frac{p}{p_\infty}) - c_p \ln(\frac{\rho}{\rho_\infty})$$

Entropy is higher in the wake because as modeled in the computation, the high loss wake fluid is of lower pressure and density than the free-stream by about the same ratio, but c_p is greater than c_v. These plots are useful for determining the location of the wake with time. The wake can be seen as a region of increased entropy impinging on the leading edge of the blade. The dark region near the blade is the low entropy flow resulting from the film coolant. A slight thickening of the coolant flow layer can be seen on the pressure side of the blade in Figure 82 as the previous wake passes. This indicates that the wake has an effect on the coolant flow on the pressure surface of the blade. Disturbance of the film on the suction side is not as apparent.

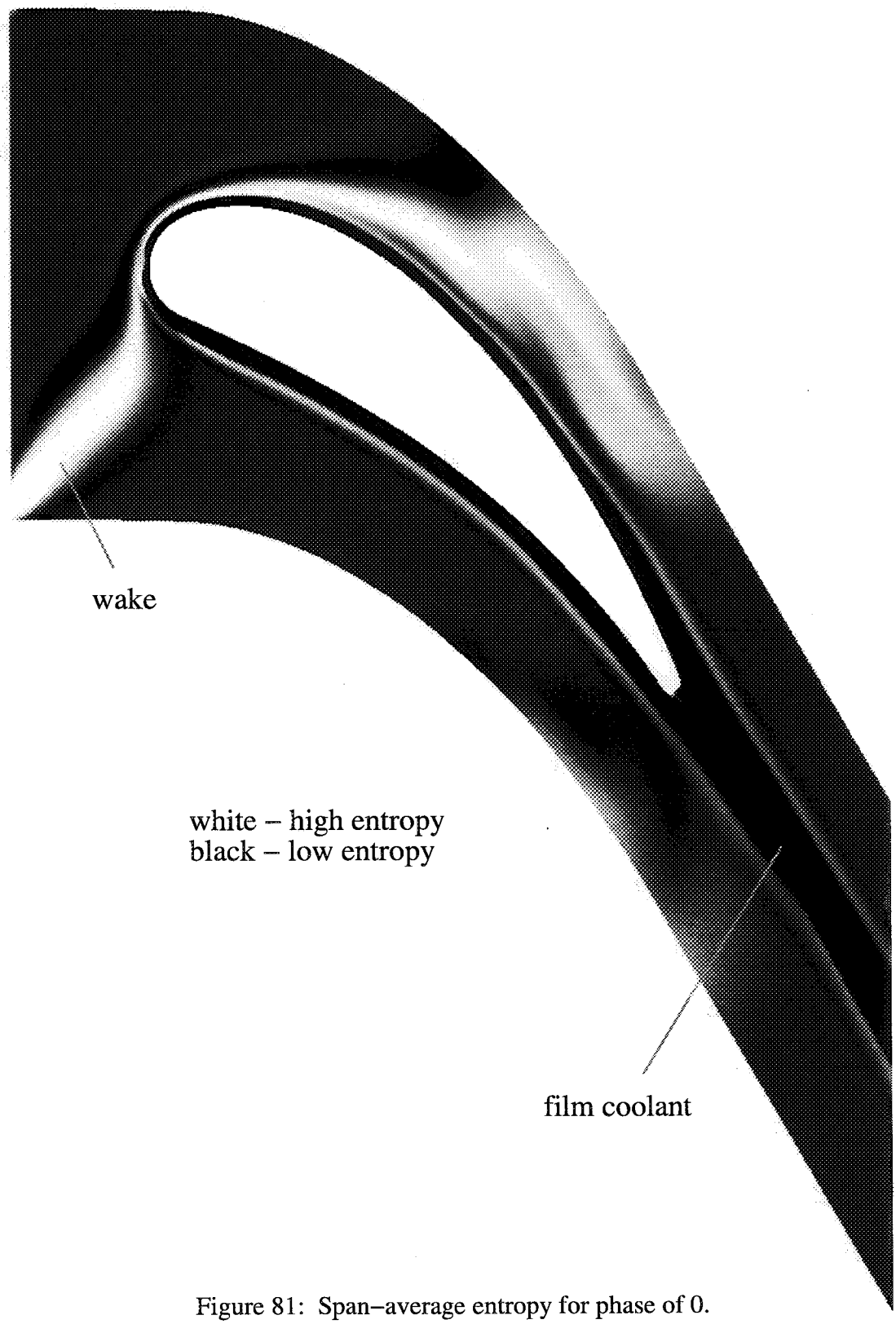

Figure 81: Span–average entropy for phase of 0.

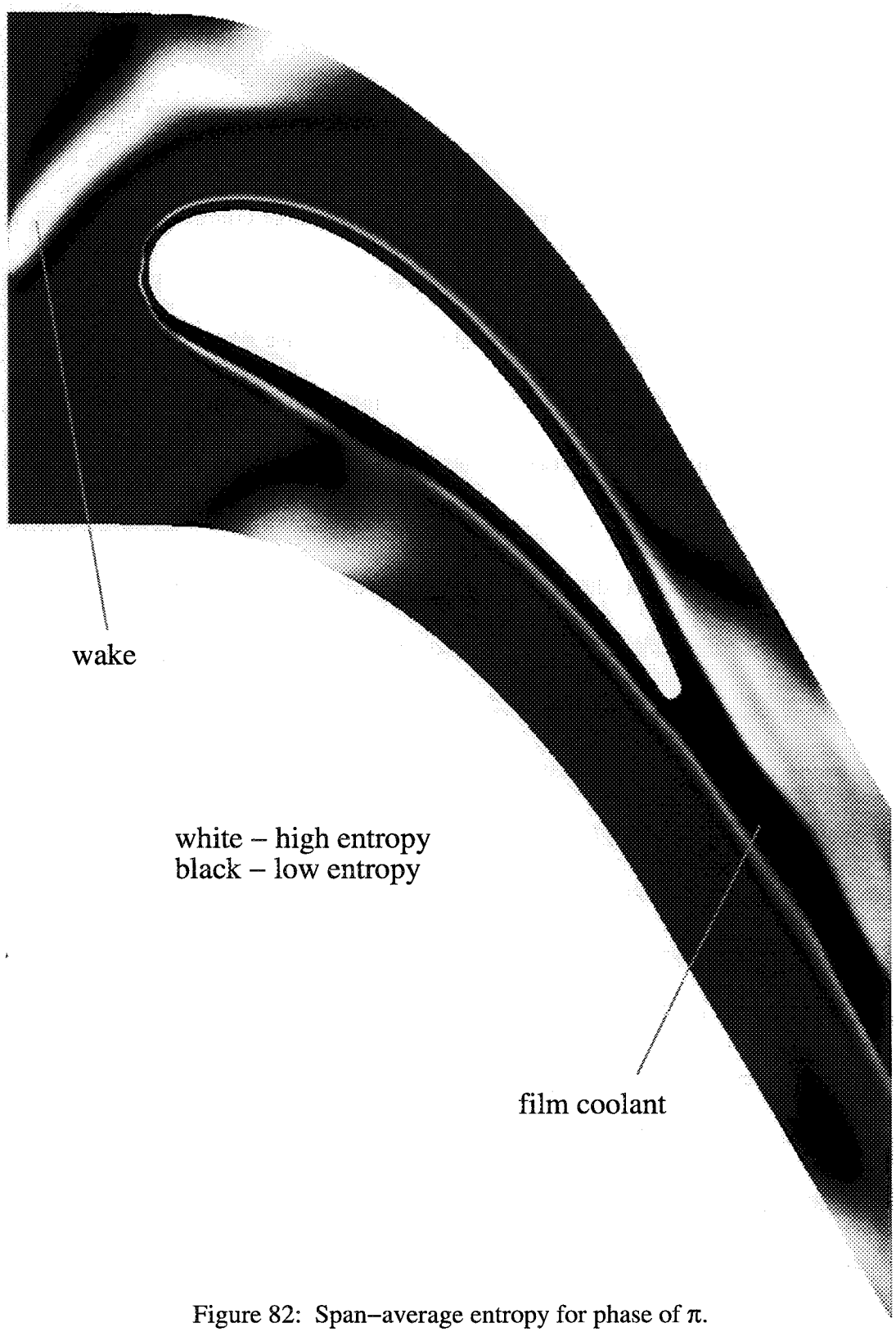

Figure 82: Span–average entropy for phase of π.

These effects will be investigated in more detail in later figures which compare the steady and unsteady solutions.

Figure 83 is a contour plot of time-average adiabatic film effectiveness for the unsteady computation in the showerhead region. The blade contour is shown as an unwrapped flat surface. The computational domain (one unit cell of film hole pattern) is repeated 5 times in the spanwise direction. The spanwise direction of the coolant is upward in the figure. The five rows of film holes can be seen as black ellipses, with streaks of high film effectiveness extending downstream. The locations of these streaks change slightly with time, especially near the holes. Because of the higher free-stream acceleration on the suction side, the coolant flow is turned more quickly to the chordwise direction, while the pressure side coolant flow migrates more in the spanwise direction initially. The lowest film effectiveness (highest temperature) is seen in the region between the two suction side rows of holes, just upstream of the last suction side hole. A similar region exists just upstream of the last pressure side hole. These are regions that are not protected by the coolant, and are exposed directly to the free-stream temperature. Their location is determined by the film hole pattern and the injection angle of the coolant. Since the holes are closely spaced in the spanwise direction, staggered, and angled sharply in the spanwise direction, the coolant from a given hole can be seen to align with that of those downstream. Thus for high angle, closely spaced holes, an aligned or less structured staggered hole pattern may be more effective than this structured staggered hole pattern for reducing

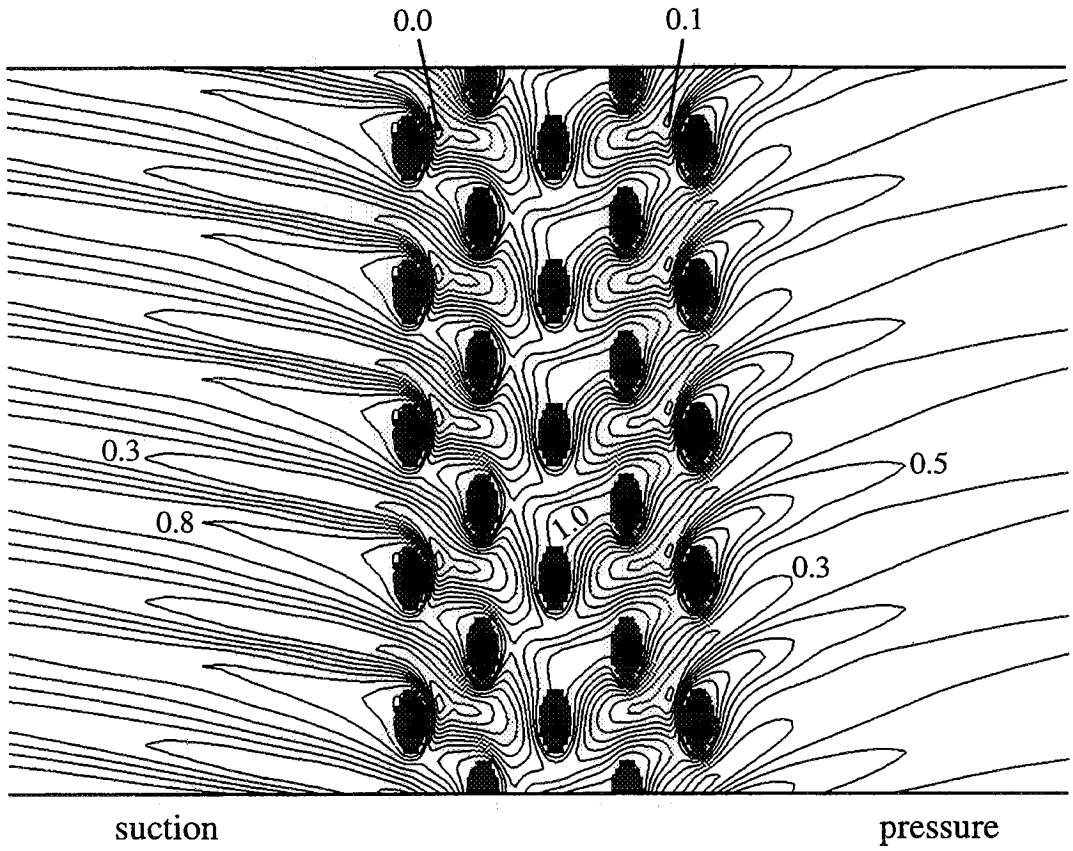

Figure 83: Time–average unsteady film effectiveness in showerhead region.

the maximum blade temperature.

The difference between the adiabatic film effectiveness for the time-average of the unsteady calculation and the final steady solution is shown on the unwrapped showerhead region in Figure 84. It can be seen that the wake passing causes a decrease in film effectiveness over a large portion of the stagnation region, with a maximum decrease of 8 percent between the second and third row of holes. A smaller increase with a maximum value of 3 percent can be seen over an adjacent area. Differences in local film effectiveness can be deceiving, however, because at some locations the film effectiveness distribution is similar between the two solutions and merely shifted spanwise, producing no net change in span-average film effectiveness.

Figure 85 is a plot of span-average film effectiveness versus surface distance for the time-average of the unsteady solution and the two steady solutions. As in the time-averaging process, pressure, temperature, and the three components of velocity were area-averaged in the spanwise direction, with all velocities being zero at the wall. In the showerhead region, only solid-wall grid points were included in the averaging process. It can be seen that in a span-average sense, the final steady solution is in better agreement with the time-average unsteady solution. However, because of the large gradients in the showerhead region, it is difficult to interpret differences between the curves in this region.

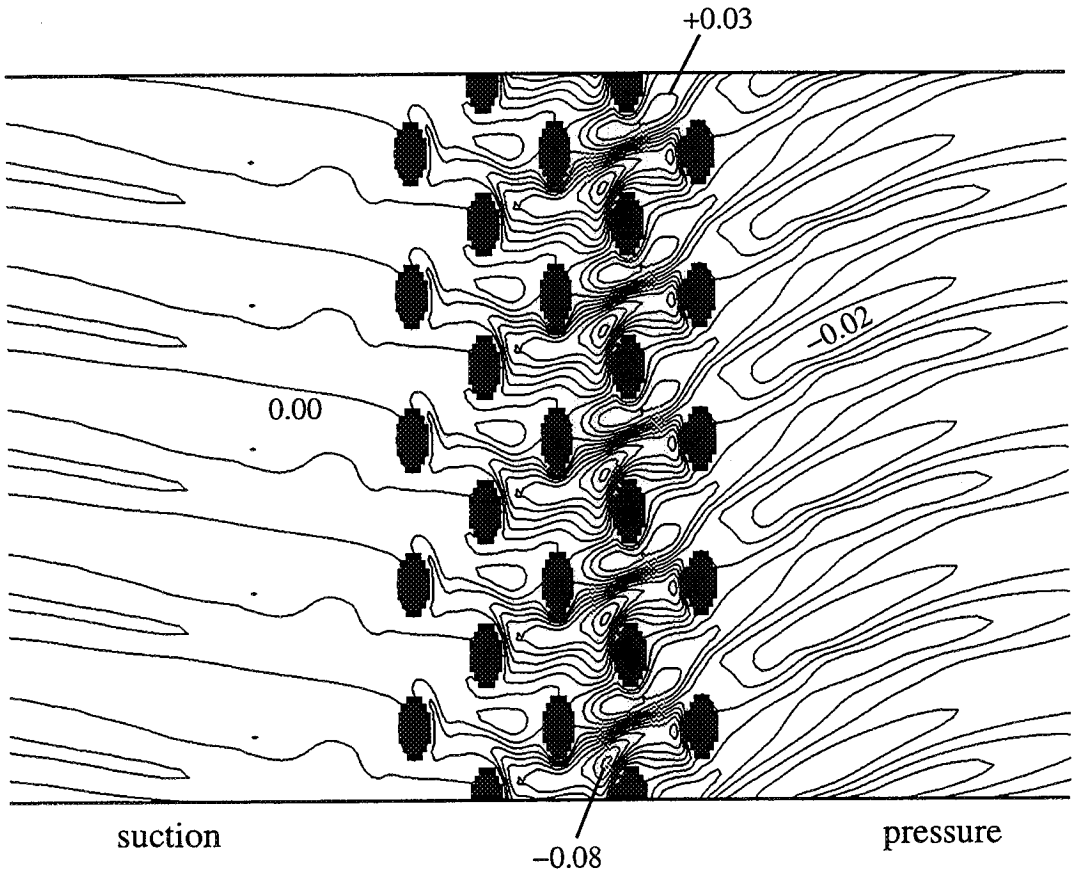

Figure 84: Time–average unsteady minus final steady film effectiveness in showerhead region.

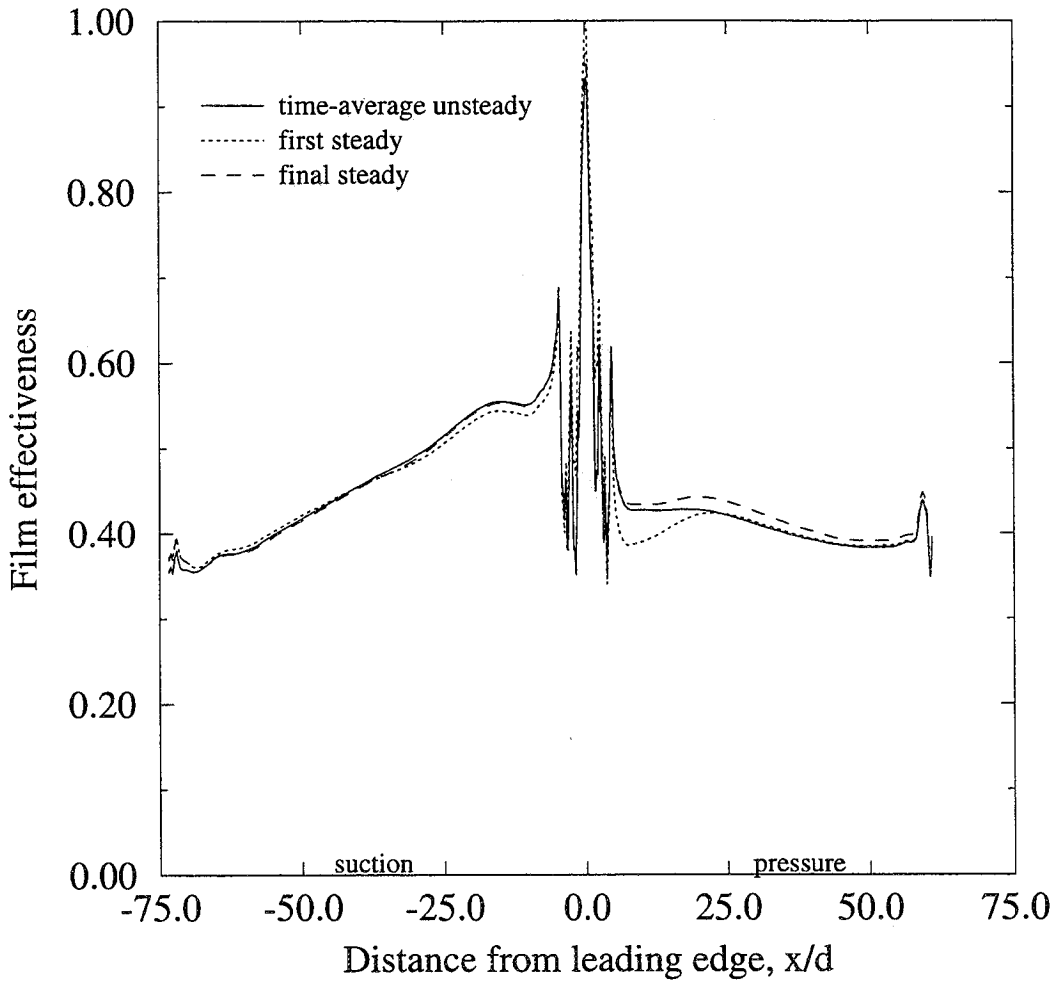

Figure 85: Computed steady and time–average unsteady span–average film effectiveness.

In Figure 86, the difference in span-average film effectiveness between the two steady solutions and the time-average unsteady solution are plotted directly. It is confirmed that the modifications made to the final steady solution improve the film effectiveness prediction, and there are only small differences between the final steady and time-average unsteady film effectiveness span-average values. The most notable differences are the reduction in film effectiveness over most of the pressure surface and the reduction in the showerhead region. There is also a reduction near the trailing edge on the suction surface, which is most likely due to a small unsteady separation bubble induced by the wake passing effect in the unsteady solution. The maximum differences are about 2 to 3 percent of the inlet stagnation temperature. Although small on a relative basis, the difference is significant, as it could translate to a 20 ℃ difference in a high temperature turbine. Local variations as shown in Figure 84 are even greater, up to 8 percent.

Shown in Figure 87 are eight instantaneous plots of the unsteady solution. These snapshots are equally-spaced in time over one wake passing period. The quantity plotted in Figure 87 is the difference between each instantaneous span-average film effectiveness and the time- and span-average unsteady film effectiveness. The large instantaneous fluctuations in span-average film effectiveness of up to 15 percent are reflective of the location of the wake on the blade and its effect on the coolant flow. However the unsteady fluctuations largely cancel each other over time with respect to the steady solution except in the regions previously indicated. The maximum

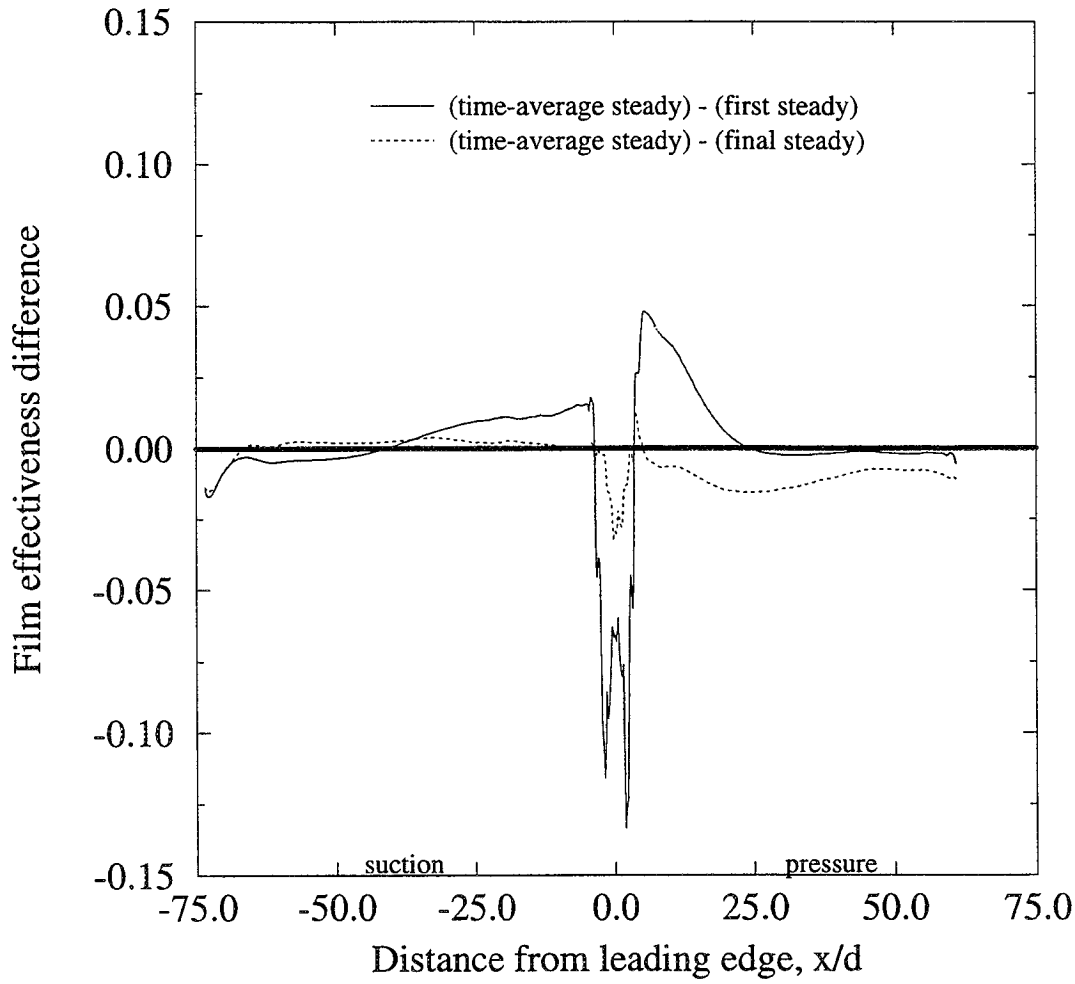

Figure 86: Computed differences in steady and time–average unsteady span–average film effectiveness.

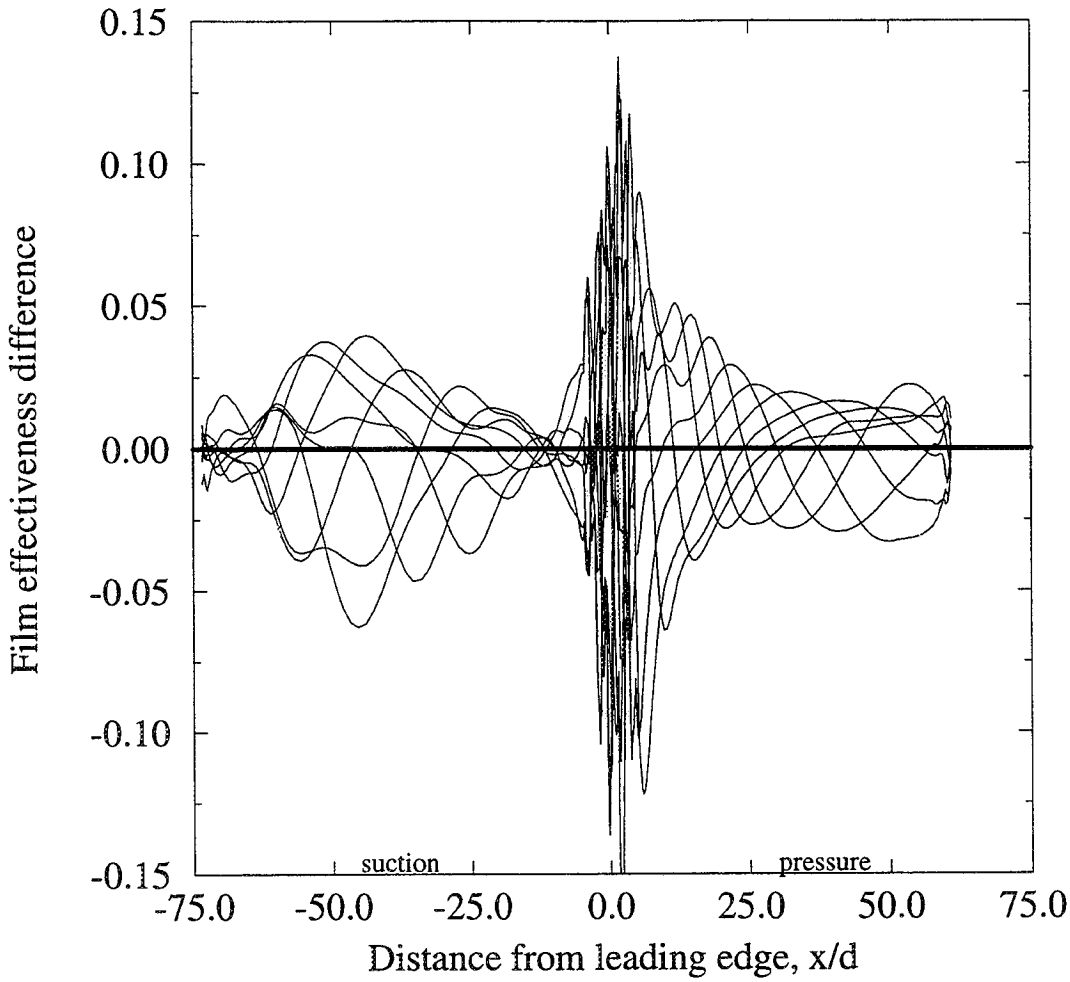

Figure 87: Computed differences in instantaneous and time–average unsteady span–average film effectiveness.

unsteady perturbation is in the showerhead region, as expected. It is interesting that at about 10 to 15 hole diameters on the suction side, the unsteady perturbation is very small. This location coincides with the approximate impingement point of the wake, as indicated by Figures 81 and 82.

Figure 88 highlights the behavior of the film jets as they exit the blade. Stagnation temperature contours at the wall and on three spanwise grid planes normal to the surface for the time-average unsteady calculation are shown. The normal planes are on the near pressure surface of the blade, corresponding to surface distances of about -5.5, -8.5, and -11.5 hole diameters in Figures 85 and 86. The dark oval regions on the normal planes indicate lower stagnation temperature, and correspond to flow from the upstream film coolant holes. Also shown in Figure 88 are time-average particle traces from the film holes. As previously mentioned, the staggered hole arrangement causes flow from holes in adjacent rows to merge, resulting in the appearance of discrete jets at these locations rather than as the preferred smooth buffer layer. Since spanwise variations diminish in the streamwise direction as reflected by Figure 83, different scales are used for the three normal planes in Figure 88 to highlight the coolant jet location.

Because it was established that the coolant flow rate and flow split between pressure and suction sides for the unsteady solution were matched in the final steady solution, the small differences in span-average film effectiveness between the time-average

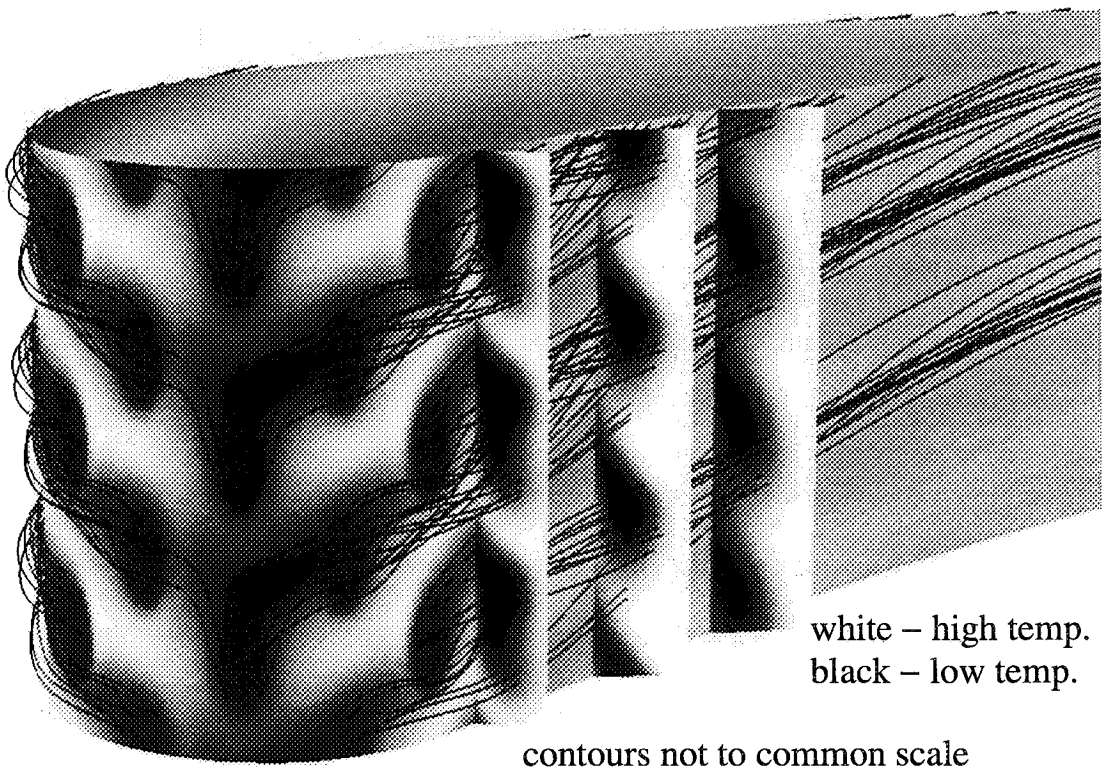

Figure 88: Wall and cross–plane stagnation temperature contours with time–average particle traces.

unsteady and final steady cases is likely due to differences in stagnation temperature distribution normal to the blade surface. For example, although the flow rate and stagnation temperature of coolant on each surface is matched, the coolant may exhibit differences in its rate of diffusion into the free stream or separation characteristics. Normal span-average stagnation temperature distributions are plotted in Figure 89 for two locations of interest. The stagnation temperature is normalized by the inlet stagnation temperature. Referring to the final steady plot in Figure 86, the first is the sharp minimum near the stagnation point. The second is the broader minimum on the pressure side at a surface distance of about -25 hole diameters. At both locations, the unsteady span-average film effectiveness is slightly less than the steady prediction, meaning the unsteady span-average wall temperature exceeds the steady prediction. In Figure 89, it can be seen that although the unsteady wall temperature exceeds the steady wall temperature at both locations, the reverse is true farther away from the wall. This indicates that the coolant has penetrated into the free stream to a greater extent in the unsteady case, and that the differences in film effectiveness exhibited in Figure 86 are indeed due to unsteady effects and not merely caused by changes in coolant flow rate or flow split.

To identify the unsteady mechanism causing the reductions in film effectiveness on the pressure surface, it is helpful to examine Figures 81 and 82. Although the time-average location of the wake is primarily near the suction side of the blade, this is not a good indicator of impact on the film coolant. This is because the wake wraps

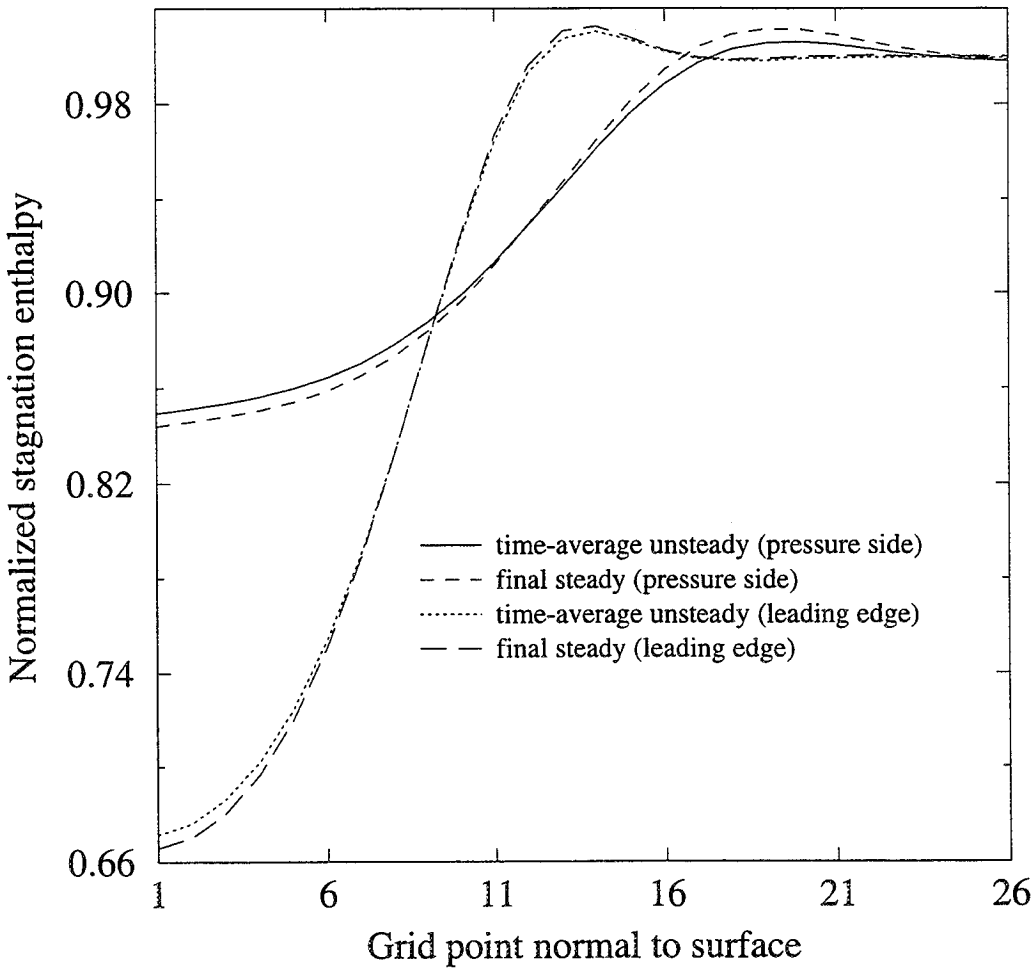

Figure 89: Computed steady and time–average unsteady normalized stagnation enthalpy.

around the suction side, as can be seen in Figure 81, and the effect does not penetrate to the blade surface. On the pressure side, however, the wake sweeps the blade surface normally as indicated by the high entropy region near the pressure surface in Figure 82. This allows the wake disturbance to penetrate the boundary layer and impact the coolant flow properties. Figure 90 shows span-average disturbance velocity vectors near the pressure surface for the same time as Figure 82. The disturbance velocity is defined as the instantaneous velocity minus the final steady velocity. This definition allows direct observation of the unsteady effect relative to steady prediction. It can be seen that the disturbance velocity is away from the blade in the wake due to the velocity defect in the wake. This behavior extends into the coolant flow layer adjacent to the blade. The periodic sweeping of the pressure surface by the wake thus results in a periodic relative lifting of the coolant flow on the pressure surface which likely contributes to the time-average reduction in film effectiveness seen in Figure 86. The increased temperatures predicted in the showerhead region by the unsteady solution can be explained by the effect of the unsteady wake passing. The wake does not allow the film to establish a steady pattern in this region, and the resultant increase in mixing causes hot fluid to be introduced to the surface more effectively.

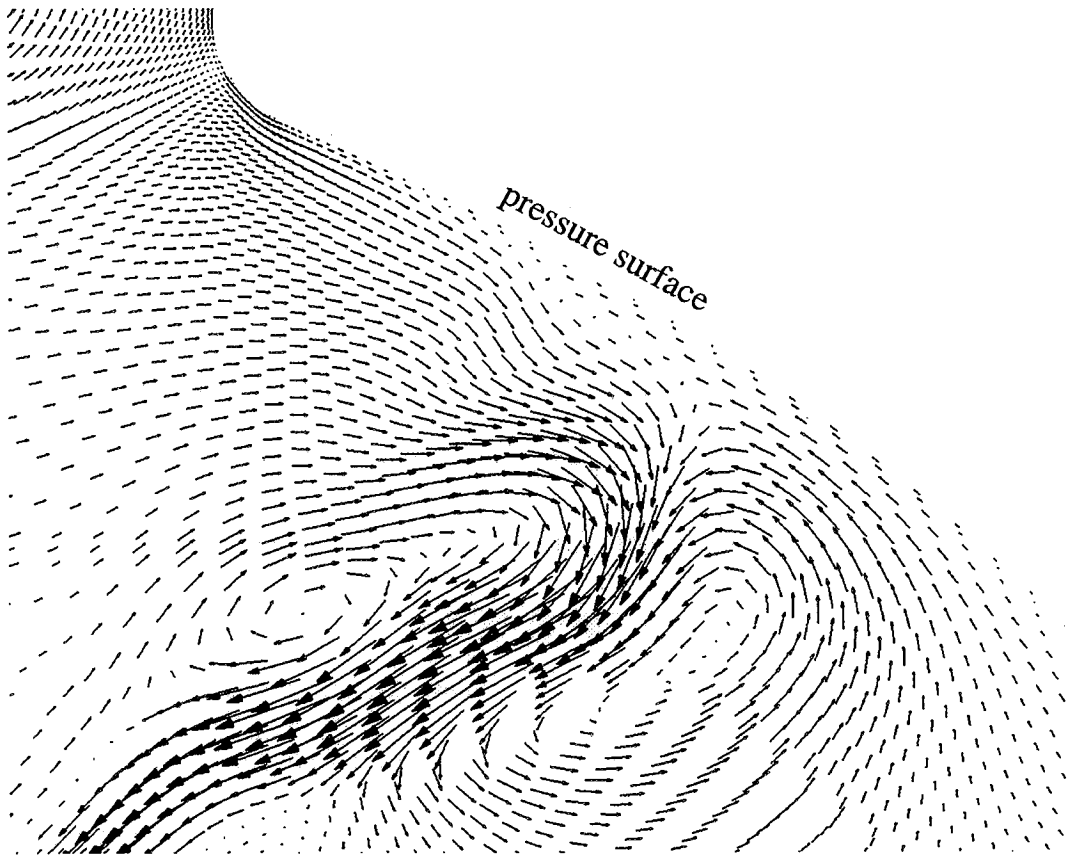

Figure 90: Computed instantaneous disturbance velocity at phase of π.

5. EXPERIMENTAL/COMPUTATIONAL COMPARISON

Fundamental differences

A direct comparison of the experimental and computational results is made more difficult by several inherent differences between them. One difference is the linearity of the computational geometry versus the annular geometry of the cascade. To precisely model the cascade geometry computationally would require removing the periodic boundary condition from the analysis and computing over the entire span of the blade. As previously indicated, this would require a vast number of grid points if detailed resolution of each film hole were desired. The assumption of periodicity in the computation has several implications. The most obvious is the fact that a cascade blade has a radius change along its span, and a corresponding change in pitch between adjacent blades. The computational model assumes no pitch change between blades. However, this effect is not considered severe since the blades are two-dimensional in design, the turning is moderate, and the inlet flow angle is nominally 0°. In addition, the instrumentation is located near the midspan of the blade, where endwall effects are minimized. The more pronounced effect caused by the periodicity assumption relates to the spanwise angle of the film injection. For a truly periodic blade, the heat transfer at a particular downstream location is in theory affected by the coolant from film holes at an infinite number of spanwise locations. For a cascade blade, only the holes which actually exist on the blade have an effect. Even if the

cascade were linear, this second effect would be present, since periodicity would not precisely hold on the scale of the hole pattern.

Another difference between the experiment and the computation is the conditions in the coolant plenum. In the experiment, the plenum is actually a circular flow channel 6.3 mm in diameter. Since the velocity in the plenum is not negligible, there are momentum effects on the behavior of the coolant flow. The computation assumes a stagnation pressure profile at the film hole exit which is symmetric about the hole centerline, and an injection angle of the coolant which is constant for all holes. Assumptions of this type are necessary unless the flow inside the film holes and plenum is computed. Such a computation was considered beyond the scope of this study, but others, namely Leylek and Zerkle [10], and He et al. [15] have focused on this aspect of the problem.

A third difference between the experiment and the computation was the use of cold air injection in the computation. This was done to match the density ratio between CO_2 and air since the code is not able to solve for non-homogeneous mixtures of gases. Thus the computation models aspects of both injection gases, but does not fully model either.

Span-average results

Figure 91 shows a comparison between the span-average film effectiveness predicted from the steady computations with the experimental values for both air and CO_2 at a blowing ratio of 1.0. The three computational plots shown are for 3 different wall grid spacings: a coarse spacing with y^+ less than 10.0 at all locations, a medium spacing with y^+ less than 1.0 at all locations, and a fine spacing with y^+ less than 0.1 at all locations. The coarse spacing corresponds to the spacing used for the unsteady computation. The computations used a film temperature of 0.65 times the inlet stagnation pressure to model the density of CO_2, a constant stagnation pressure hole profile, and a 30° injection angle. The experimental plots are for the no rotor case. It can be seen that the computations overpredict the film effectiveness at all locations. The medium and fine wall grid spacings show an improvement over the coarse grid on the suction surface. The computations predict a film effectiveness at least as high on the suction surface as on the pressure surface, while the experiments show higher values on the pressure surface. This may be due to minor differences in the location of the attachment line. The decay rate on the suction surface is predicted well, as the computations exceed the experimental values by a nearly constant value of about 0.15. The decay rate on the pressure surface is underpredicted, perhaps due to the spanwise injection and the presence of endwalls. Indeed, Figure 83 shows a greater spanwise migration of injectant on the pressure surface than on the suction surface, which would indicate a greater susceptibility to this effect. In any case, the computation is

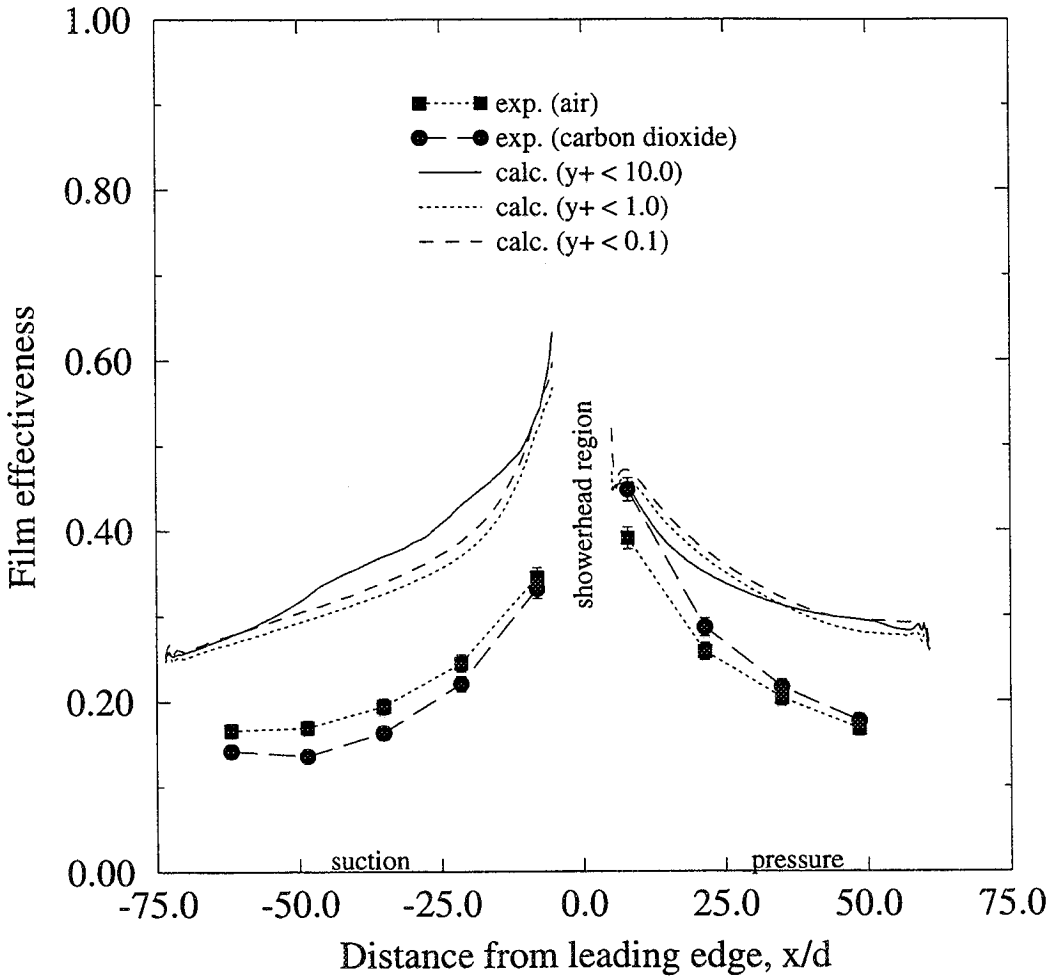

Figure 91: Computed and experimental span–average film effectiveness for B=1.0, various grid wall spacings.

in good agreement with the experimental data on the pressure surface near the showerhead region.

Figure 92 shows a comparison of predicted and experimental Nusselt number values for the same conditions as in Figure 91. Here it becomes clear that the coarse grid spacing is not able to resolve the near-wall flow physics, in agreement with the standard rule-of-thumb to limit the first grid point from the wall to a y^+ value of 1.0 or less. The medium and fine wall spacings are in good agreement with the experimental data, especially considering the typical difficulty in predicting Nusselt numbers computationally. This may be fortuitous, since no special effort was made to modify the turbulence model or other heat transfer criteria, although the quadratic temperature extrapolation at the wall was a simple modification which improved the solutions. Still, the results show that the computation generally captures the heat transfer physics with sufficiently fine wall spacing. The very high gradients near the showerhead region are attributable to the collocation of the first Nusselt number point on each side of the showerhead region with the start of the heat flux boundary condition. Thus the showerhead region acts as an unheated starting length, with the Nusselt numbers undefined in this region. This matches the experimental conditions.

The decision not to attempt Nusselt number predictions with the unsteady computation is justified, since the Nusselt number predictions with the coarse grid in Figure 92 suffer more from grid dependency than the film effectiveness predictions in Figure 91.

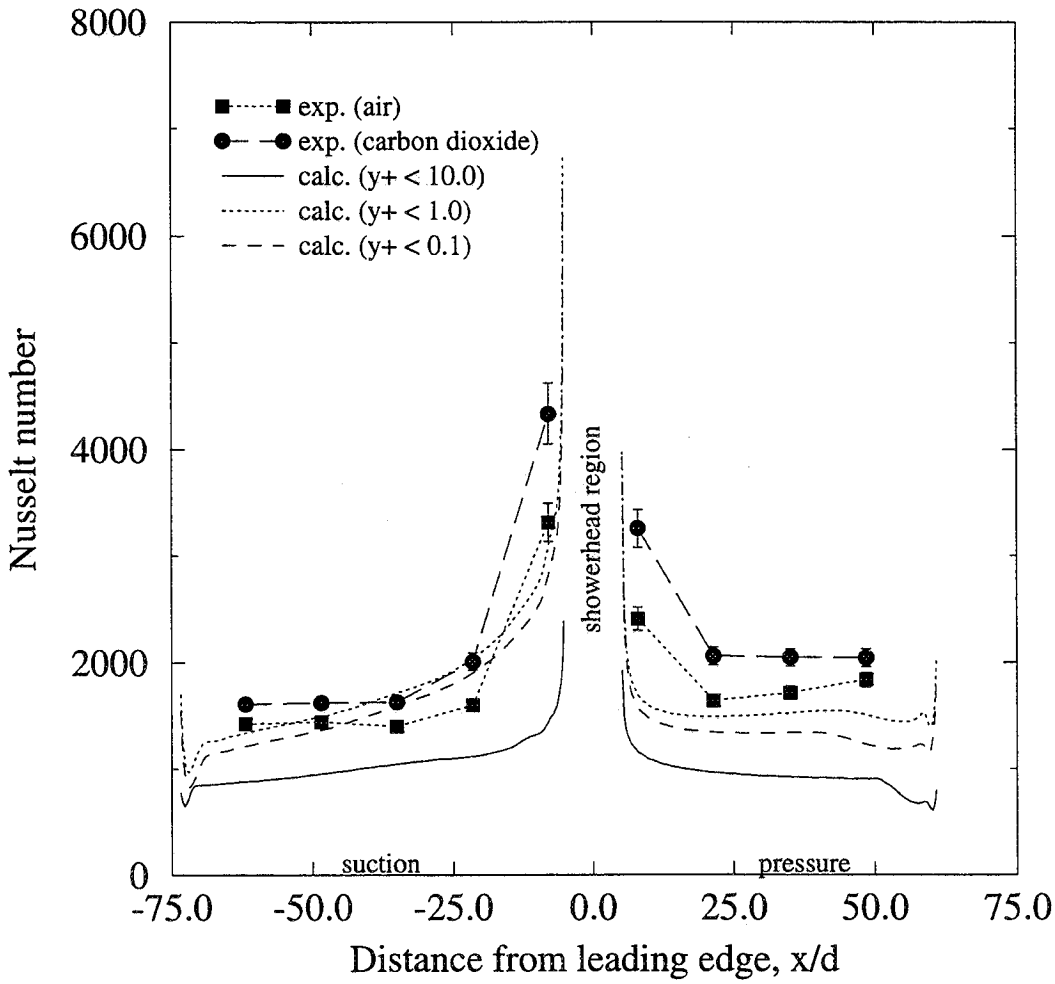

Figure 92: Computed and experimental span–average Nusselt number for B=1.0, various grid wall spacings.

This is because Nusselt number predictions involve the introduction of temperature gradients at the wall which cannot be accurately predicted with coarse spacing, while film effectiveness values do not. Figure 92 also indicates that the medium wall grid spacing ($y^+ < 1.0$) is sufficiently fine to have nearly achieved grid independence. For this reason, the comparisons for different hole boundary conditions will use the medium wall grid spacing. The conditions used in Figures 91 and 92 (CO_2 injection at 30° angle with slug flow profile) will define the baseline conditions for these comparisons.

Figure 93 presents the same experimental film effectiveness plots in comparison with calculations using three different injectant conditions: the baseline case of CO_2 injection at an angle of 30 degrees, CO_2 injection at 45 degrees, and air injection at 30 degrees. The CO_2 cases were performed as before with an injection temperature of 0.65 times the inlet stagnation temperature to match density ratio. The air case was performed with the nominal experimental temperature ratio of 1.113. All cases are again for a blowing ratio of 1.0. The temperature ratio has a moderate effect on the film effectiveness. Increasing the temperature ratio to that of air increases the film effectiveness on the pressure surface and decreases it on the near suction surface. This is in contrast to the trend exhibited by the experimental data, where the air performs better on the suction surface but worse on the pressure surface. This may again be due to species differences which the computer code is unable to model.

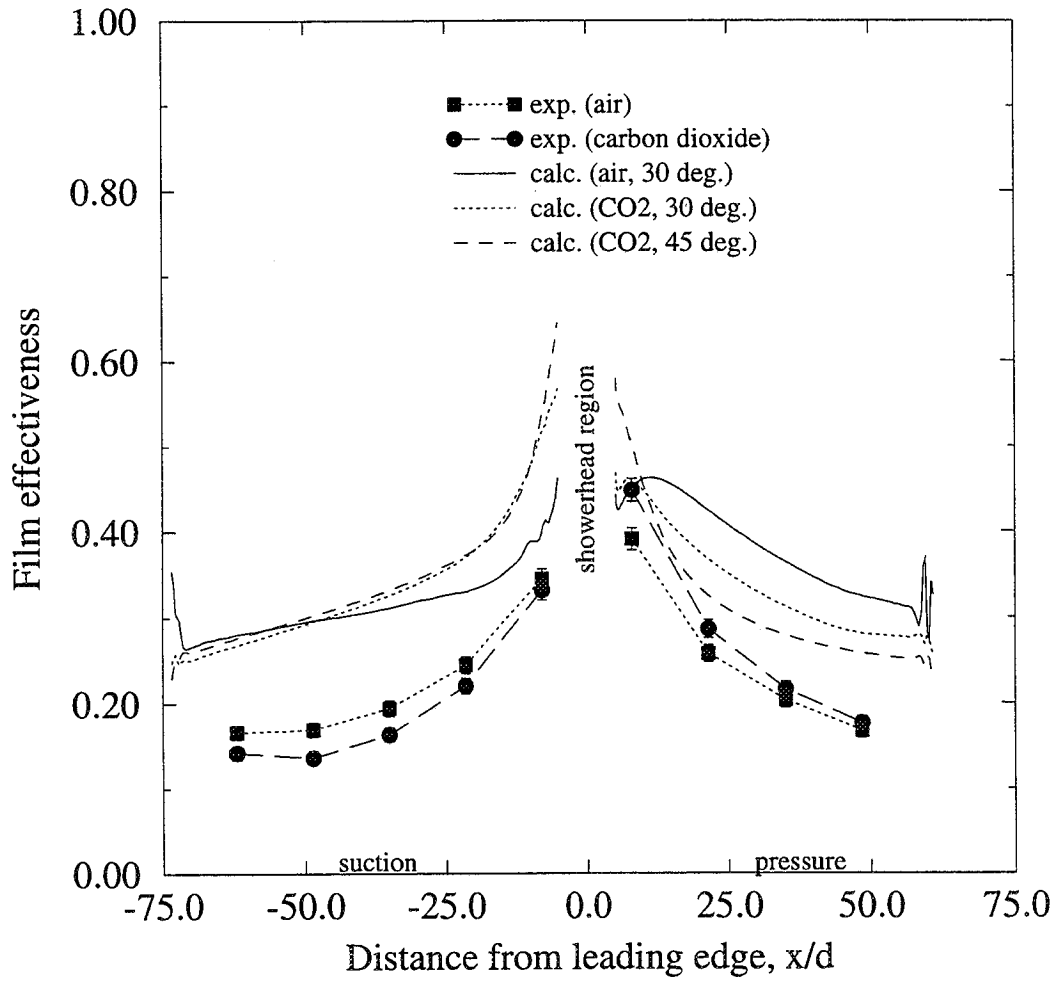

Figure 93: Computed and experimental span–average film effectiveness for B=1.0, various injectant conditions.

Since all computational cases to this point have used a hole exit angle of 30°, a solution was performed with a different hole exit angle to determine the effect. This is particularly important because there is evidence from He et al. [15] and others that have computed the flow inside the film holes that the hole exit flow angle can vary greatly from the geometric angle of the hole itself. Figure 93 shows the effect of increasing the injection angle from 30° to 45° to be negligible on the suction surface and to cause a slight decrease in film effectiveness on the pressure surface. However, very near the showerhead region the more normal injection performs markedly better. On the pressure surface, the 45° injection provides a better film to an x/d value of about 10, at which point the enhanced mixing caused by the more normal injection predominates and lowers the effectiveness.

Figure 94 shows the Nusselt number distributions for the same conditions as the previous figure. The effect of changing the hole angle is small, while CO_2 injection produces higher Nusselt numbers than air injection by a nearly constant offset of about 350. This trend is remarkably consistent with the experimental data, which also shows increased Nusselt numbers for CO_2 injection. This strengthens the argument that these increases are due to density ratio differences, and are not a result of species differences, since the code cannot model species differences.

Figure 95 presents film effectiveness values for three different film hole exit stagnation pressure profiles in comparison with the experimental data. As before, all

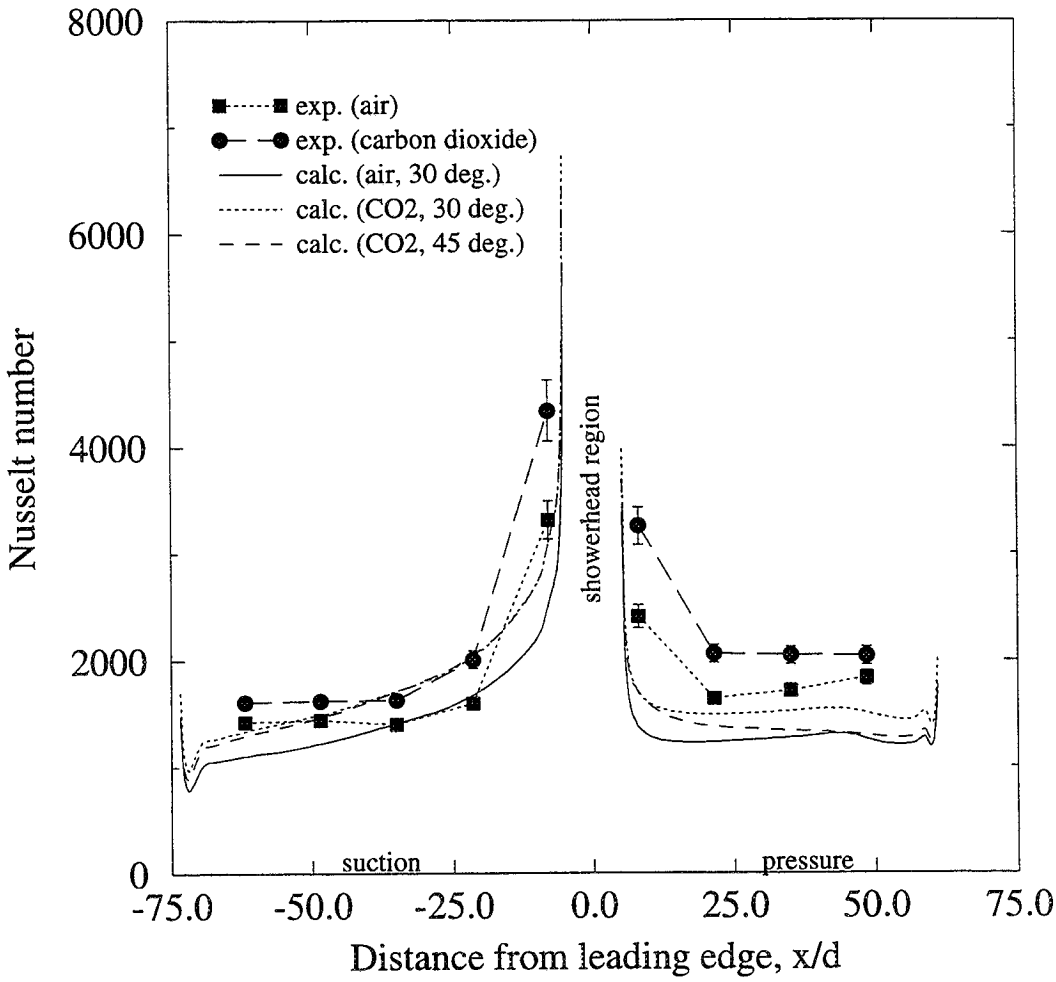

Figure 94: Computed and experimental span–average Nusselt number for B=1.0, various injectant conditions.

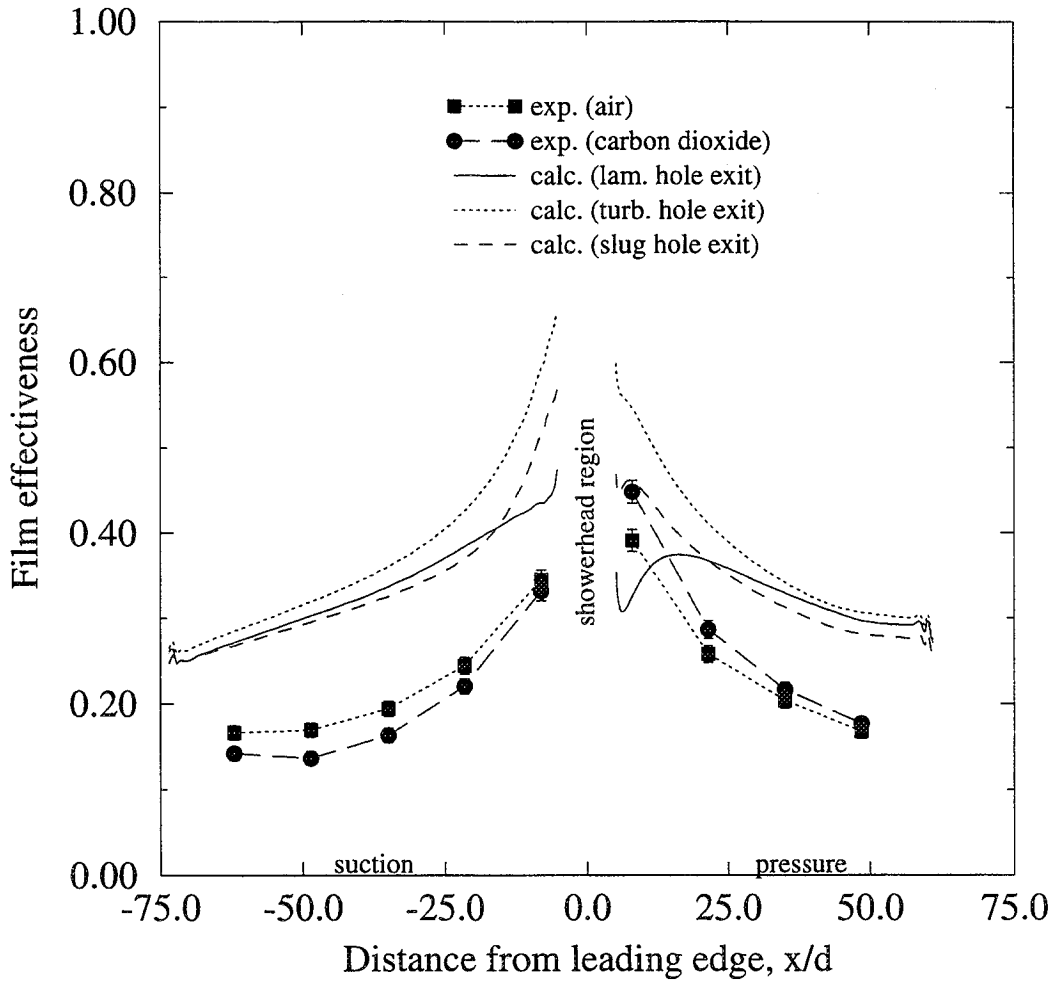

Figure 95: Computed and experimental span–average film effectiveness for B=1.0, various hole exit profiles.

plots are at a blowing ratio of 1.0, and the slug flow profile is the baseline case. Interestingly, there is not a monotonic progression of film effectiveness from laminar to turbulent to slug cases, even though the profiles become flatter in that order. One reason is that the situation for multiple rows of holes is much more complex than for a single hole or a single row of holes. Changing the hole stagnation pressure profile while fixing the overall blowing ratio necessitates changing the hole centerline stagnation pressure between cases. This in turn changes the percentage of total injectant flow which issues from each row of holes. For laminar profiles, a higher centerline stagnation pressure is required to maintain the blowing ratio. This results in a more equally distributed injectant split between rows than the slug case, where the center row is nearly blocked. The turbulent and slug cases exhibit similar behavior, with the turbulent profile producing higher film effectiveness values, perhaps due to the smoother transition from injectant to free-stream velocity and the attendant reduction in film jet shear. These two cases have nearly equal centerline stagnation pressures and flow splits between rows due to their similar nature. Perhaps the smooth transition in the turbulent profile case is just enough to improve film effectiveness while not changing the overall coolant behavior. The laminar profile case shows a large reduction in film effectiveness on the near pressure surface and a smaller one on the near suction surface, but approaches the other solutions far downstream. As indicated, the laminar profile requires a greater percentage of the injectant to exit from the center row of holes, and to a lesser extent from the 2nd and 4th rows. This flow is relatively ineffective, since it is pushed away from the wall

by the downstream rows as shown in Chapter 4. Thus the film effectiveness is not as high immediately downstream of the showerhead region. However, the film does not fully separate from the wall as it might for suction or pressure surface (non-showerhead) cooling, so it contributes to the film effectiveness farther downstream. In fact, the relative insensitivity of downstream film effectiveness to hole exit boundary conditions indicates that the downstream film performance is mainly driven by overall film cooling quantities such as blowing ratio and momentum ratio. Comparison with the experimental data confirms that the hole exit profiles are more properly modeled as either fully-developed turbulent or slug flow. Based on the short hole L/d of 3.5, slug flow is probably the best model, and so is used as the baseline profile. The slug flow film effectiveness values are closer to the experimental data, although this may be fortuitous.

Figure 96 shows the Nusselt number distributions for the different hole exit profiles in comparison with the experimental data. The turbulent and slug flow profiles produce virtually identical Nusselt number distributions, while the laminar results are slightly lower. The smoother and more even distribution of injectant in the laminar case is probably less disruptive to the free-stream, which lowers the heat transfer rate. The similarity of the turbulent and slug profiles yields identical heat transfer rates, indicating that the Nusselt number is rather insensitive to minor changes in the film cooling profile. The turbulent and slug profiles are in slightly better agreement with the experimental data for carbon dioxide injection. Again, this may be fortuitous

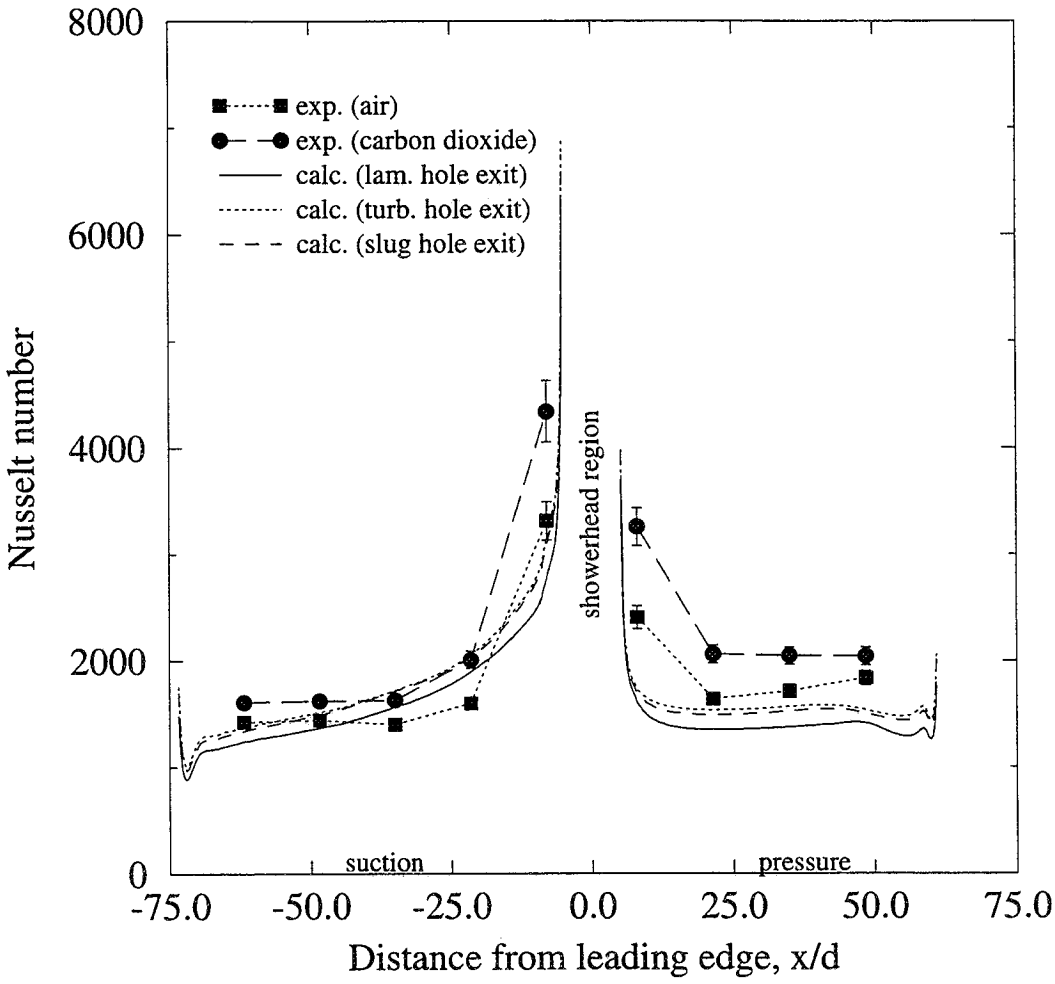

Figure 96: Computed and experimental span–average Nusselt number for B=1.0, various hole exit profiles.

since other factors may be involved.

Span-resolved results

The next series of figures compare the experimental and computational film effectiveness and Nusselt number variations in the spanwise direction. The experimental data are for carbon dioxide injection at a blowing ratio of 1.0. The computational results are for the baseline steady case: slug flow profile, temperature ratio of 0.65, and medium grid spacing. Figures 97 through 105 show the spanwise distribution of film effectiveness at chordwise locations 1 through 9, respectively. Although the film effectiveness levels are different as discussed in the preceding paragraphs, the amount and spanwise location of the spanwise film effectiveness variations are in good agreement for the suction surface locations (chords 1 through 5). Chord 5 is especially interesting as the calculation matches the phase of the spanwise variations precisely and only underpredicts their magnitude slightly. This indicates that the calculation predicts the trajectory of the suction surface film jets well. However, the pressure surface computational results indicate much greater spanwise variations, especially at chords 6 and 7. The experimental data shows almost no spanwise variation on the pressure surface, although the span-average value is in better agreement than on the suction surface. Figure 101 indicates that the instrumentation is able to resolve spanwise gradients if they are present, so the experiment must have a mechanism for spanwise mixing on the pressure surface for

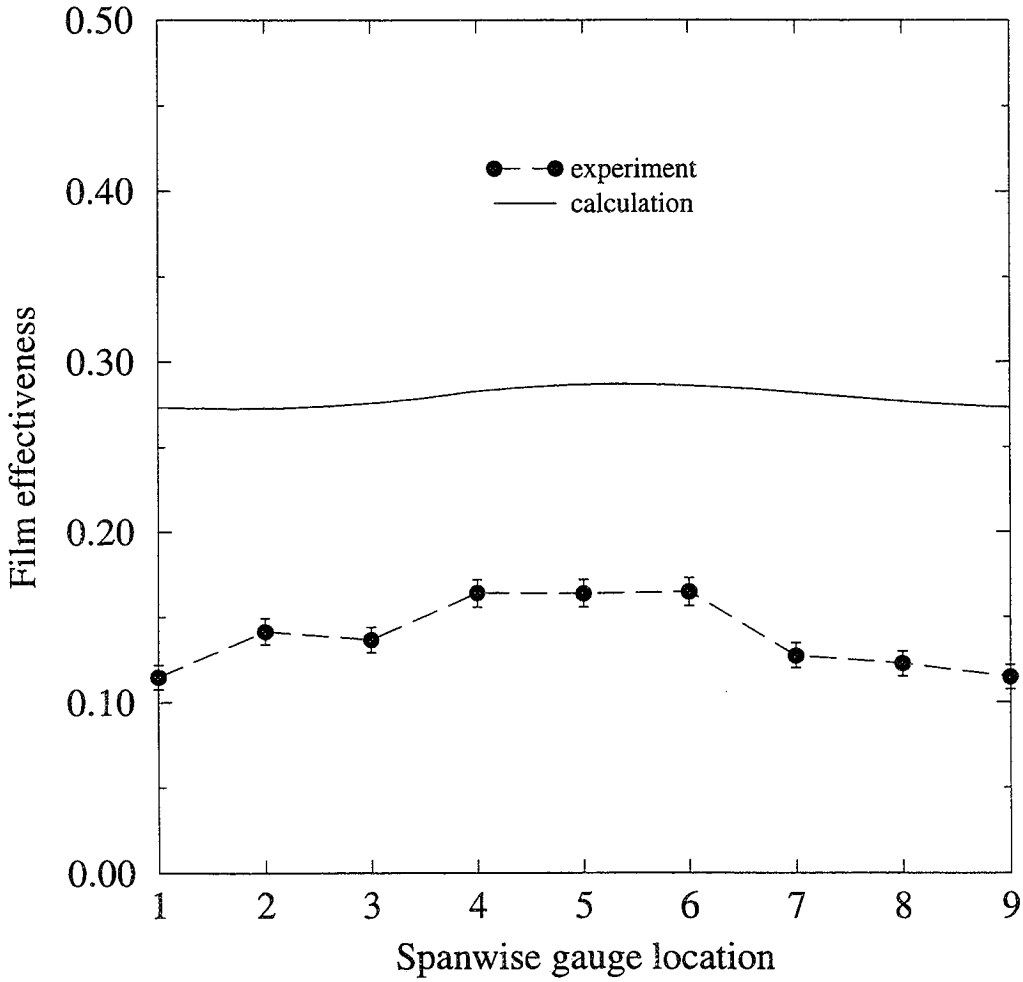

Figure 97: Computed and experimental film effectiveness for CO_2 injection at B=1.0, chord location 1.

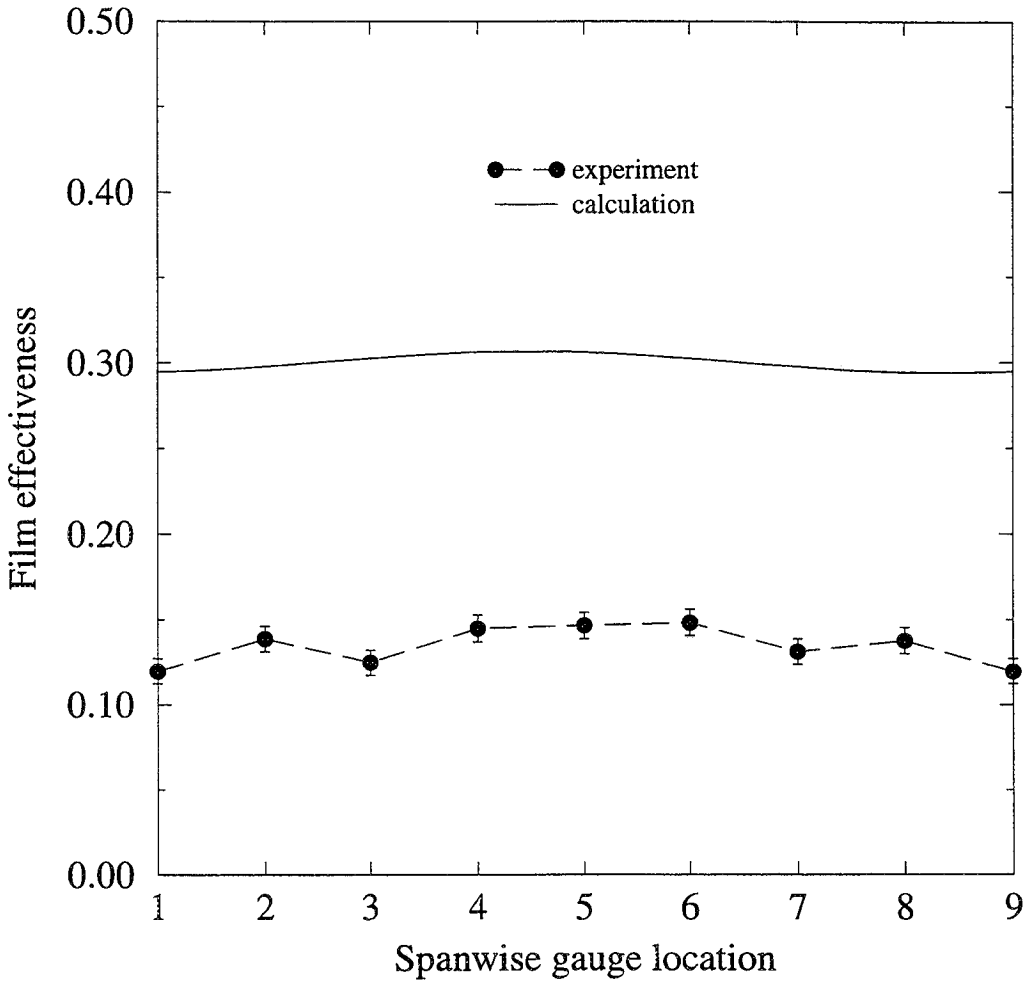

Figure 98: Computed and experimental film effectiveness for CO_2 injection at B=1.0, chord location 2.

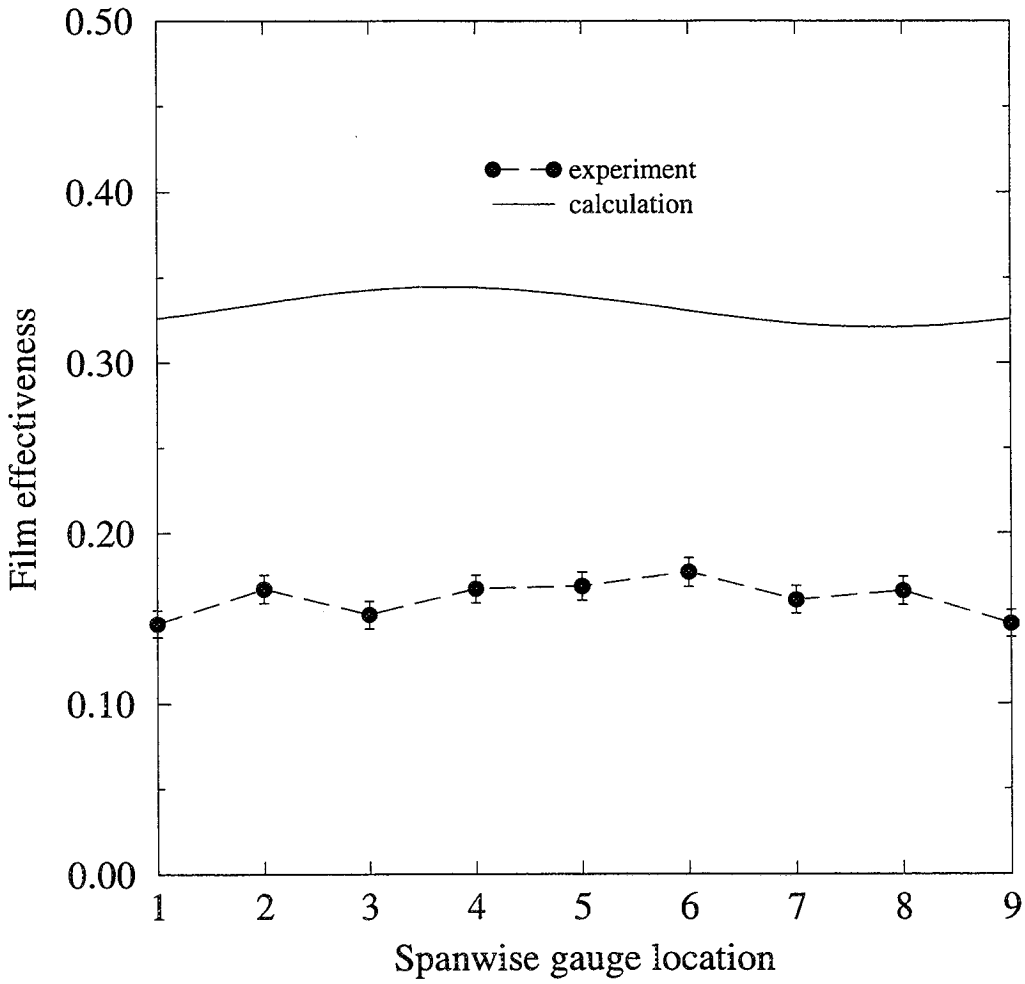

Figure 99: Computed and experimental film effectiveness for CO_2 injection at B=1.0, chord location 3.

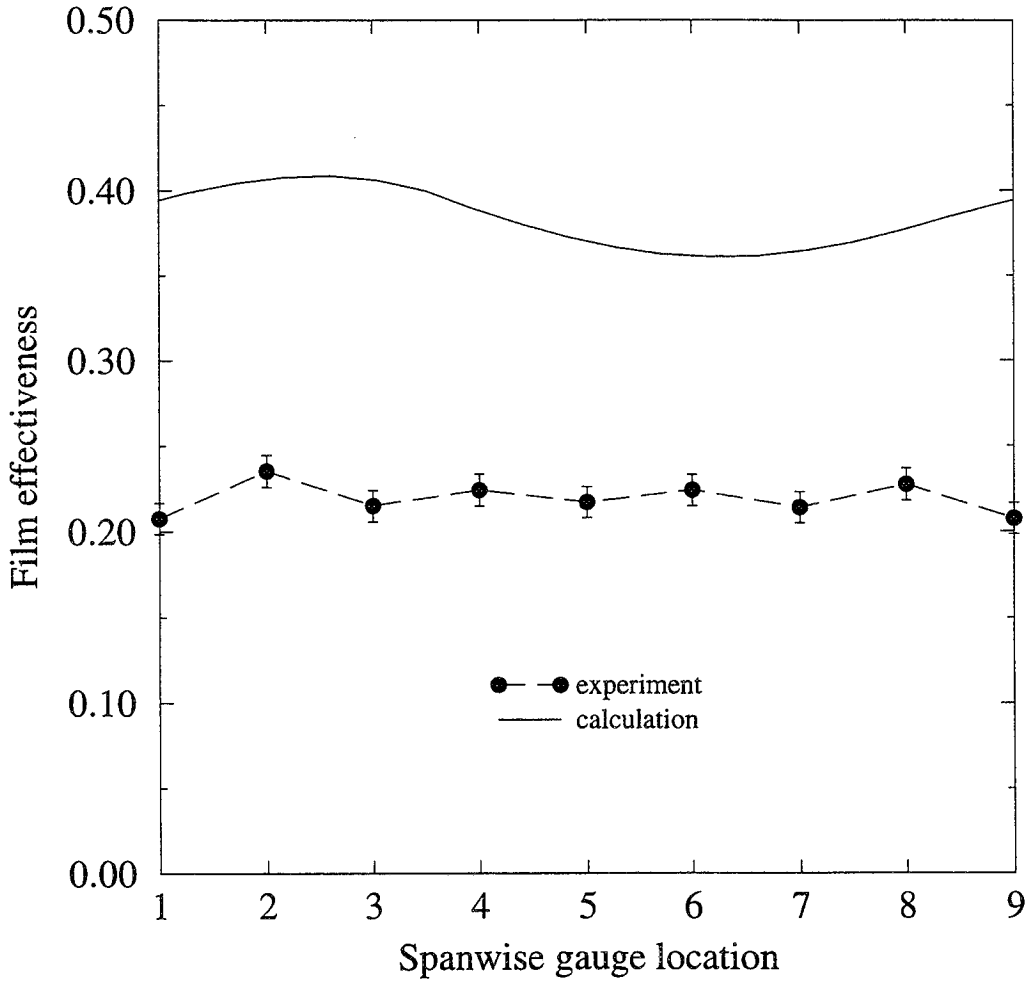

Figure 100: Computed and experimental film effectiveness for CO_2 injection at B=1.0, chord location 4.

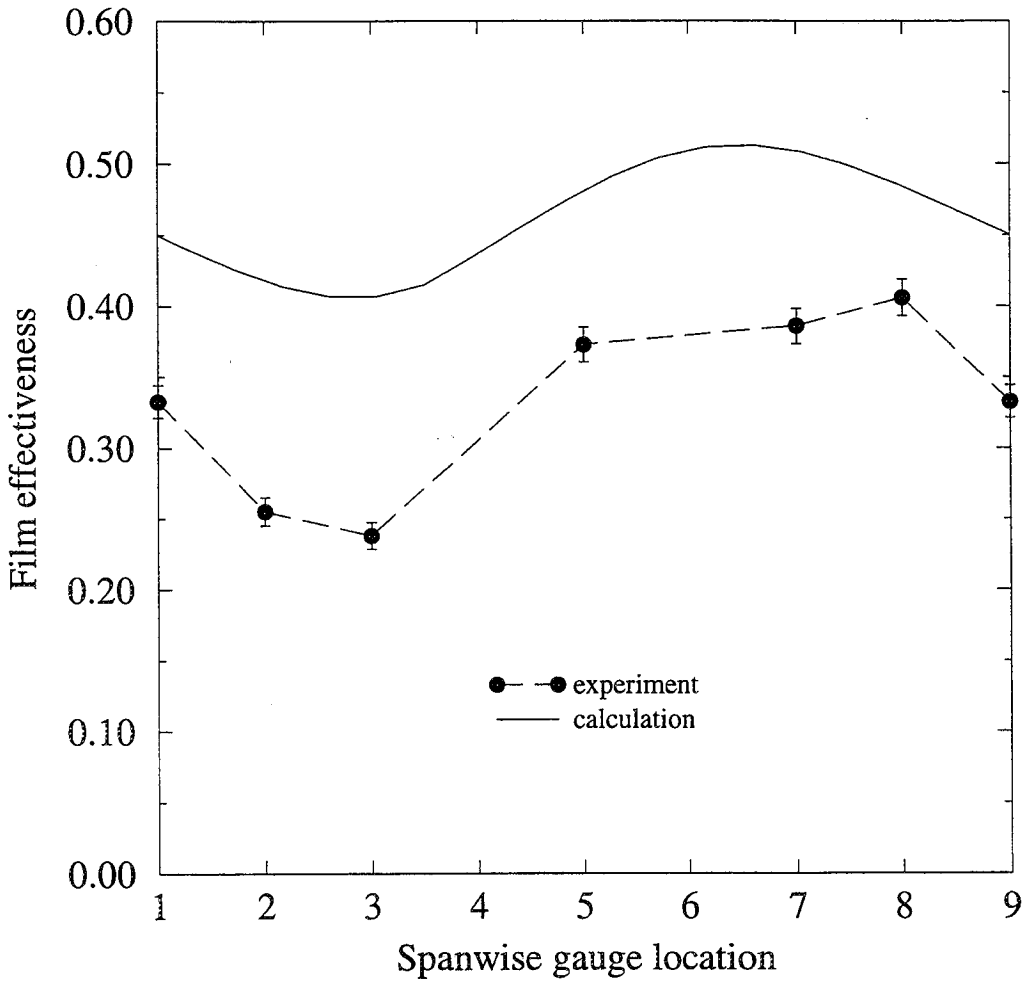

Figure 101: Computed and experimental film effectiveness for CO_2 injection at B=1.0, chord location 5.

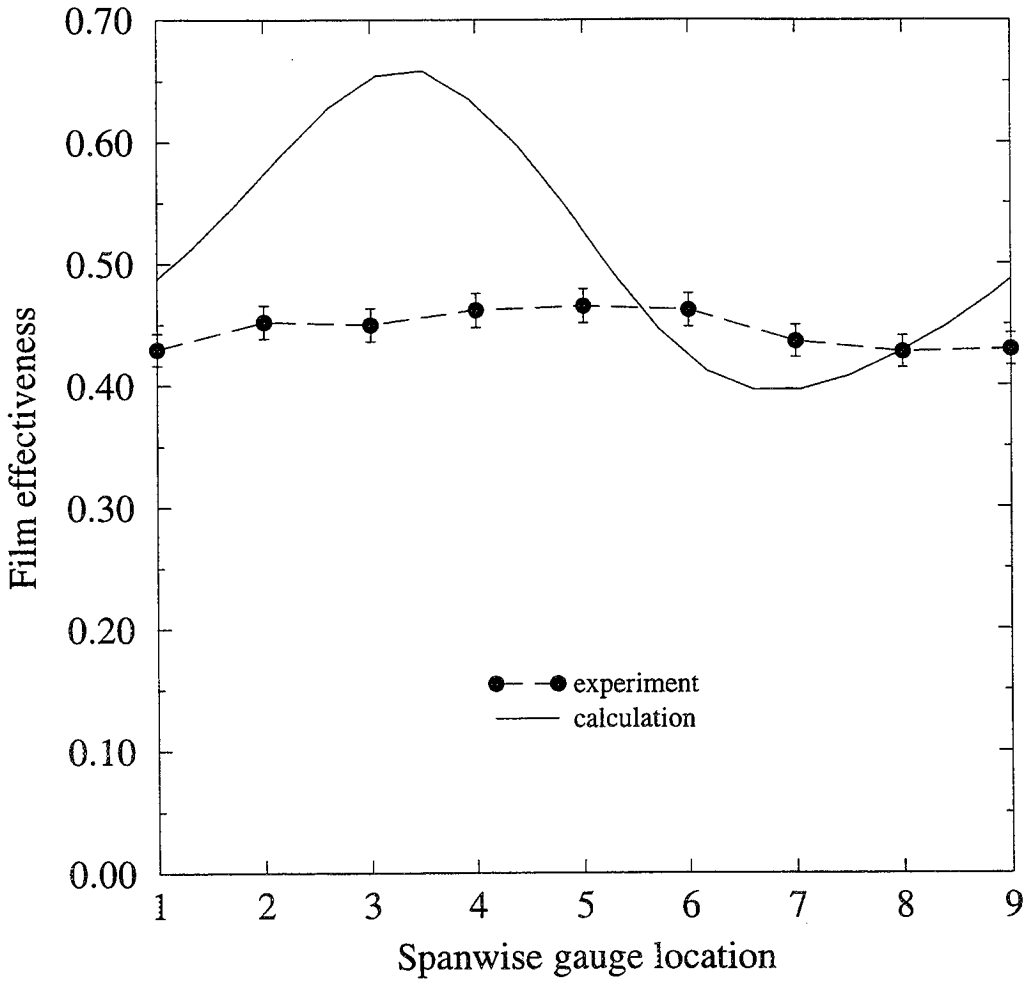

Figure 102: Computed and experimental film effectiveness for CO_2 injection at B=1.0, chord location 6.

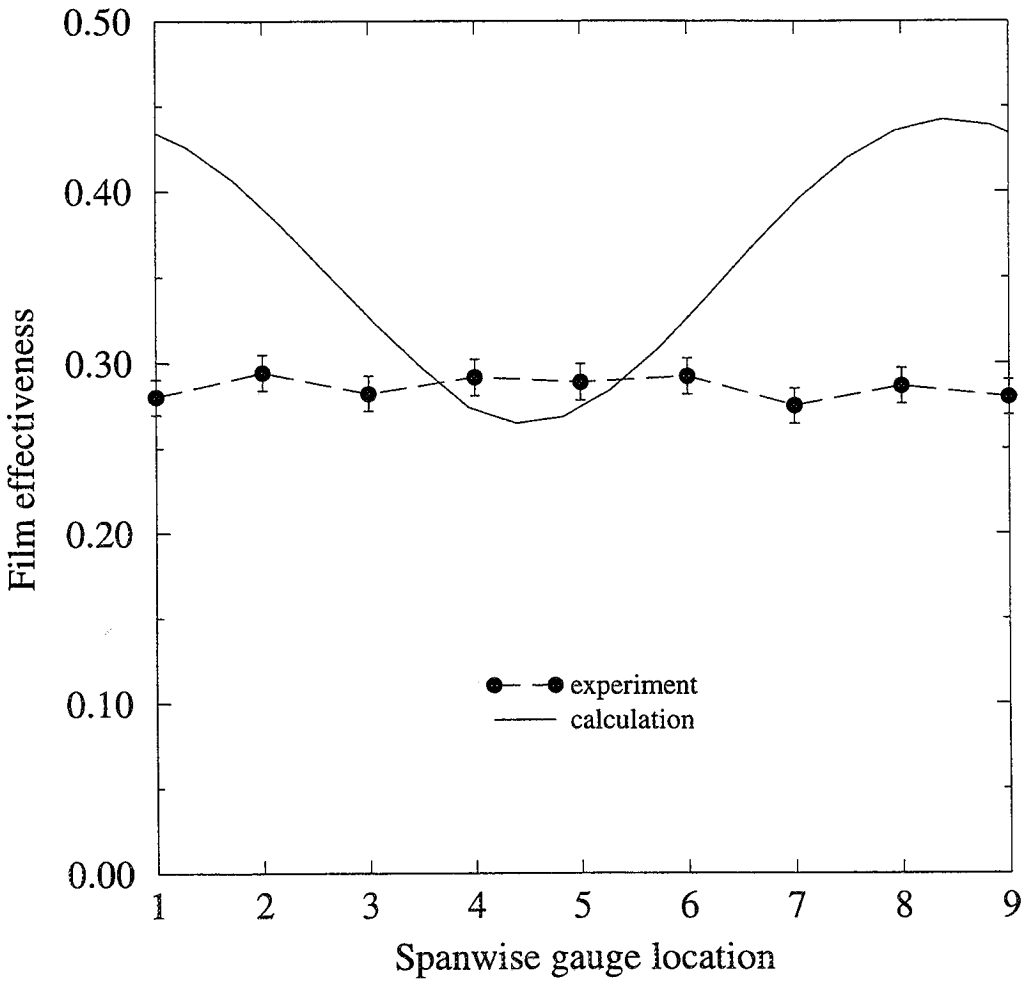

Figure 103: Computed and experimental film effectiveness for CO_2 injection at B=1.0, chord location 7.

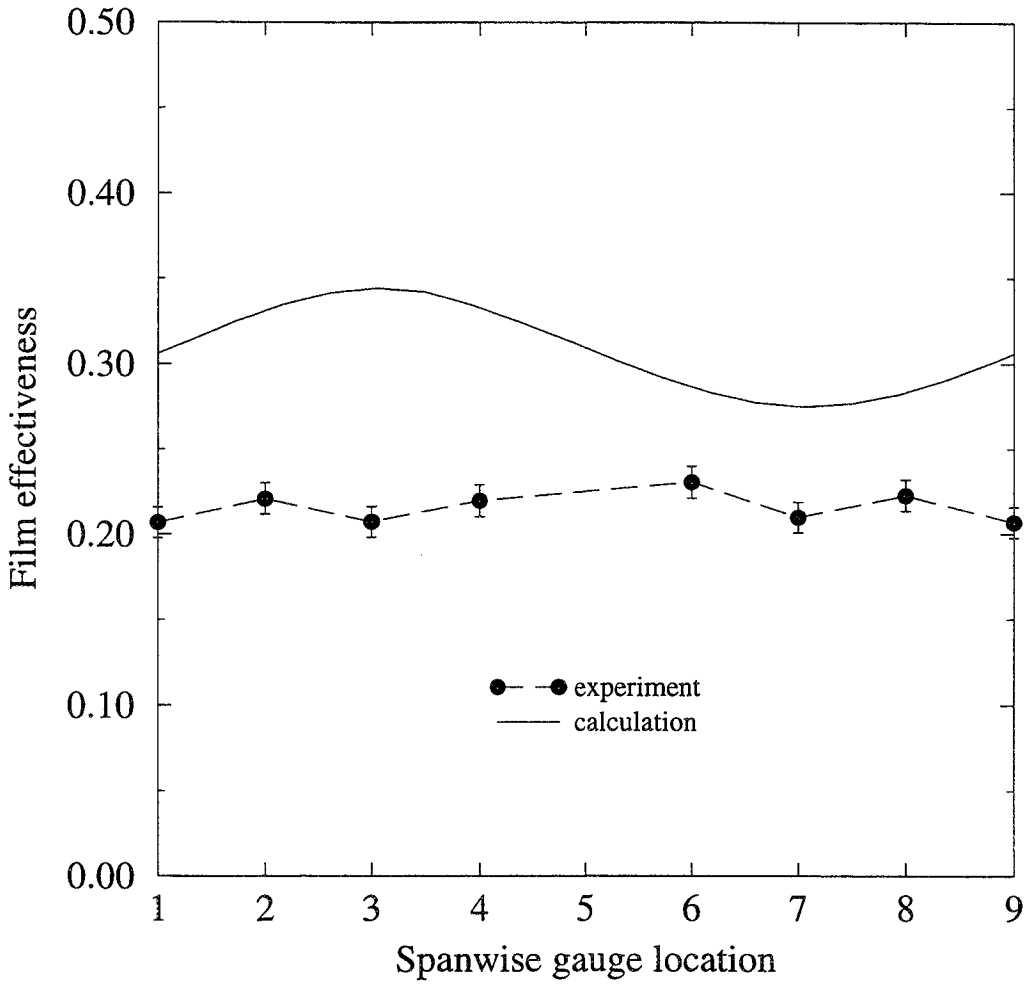

Figure 104: Computed and experimental film effectiveness for CO_2 injection at B=1.0, chord location 8.

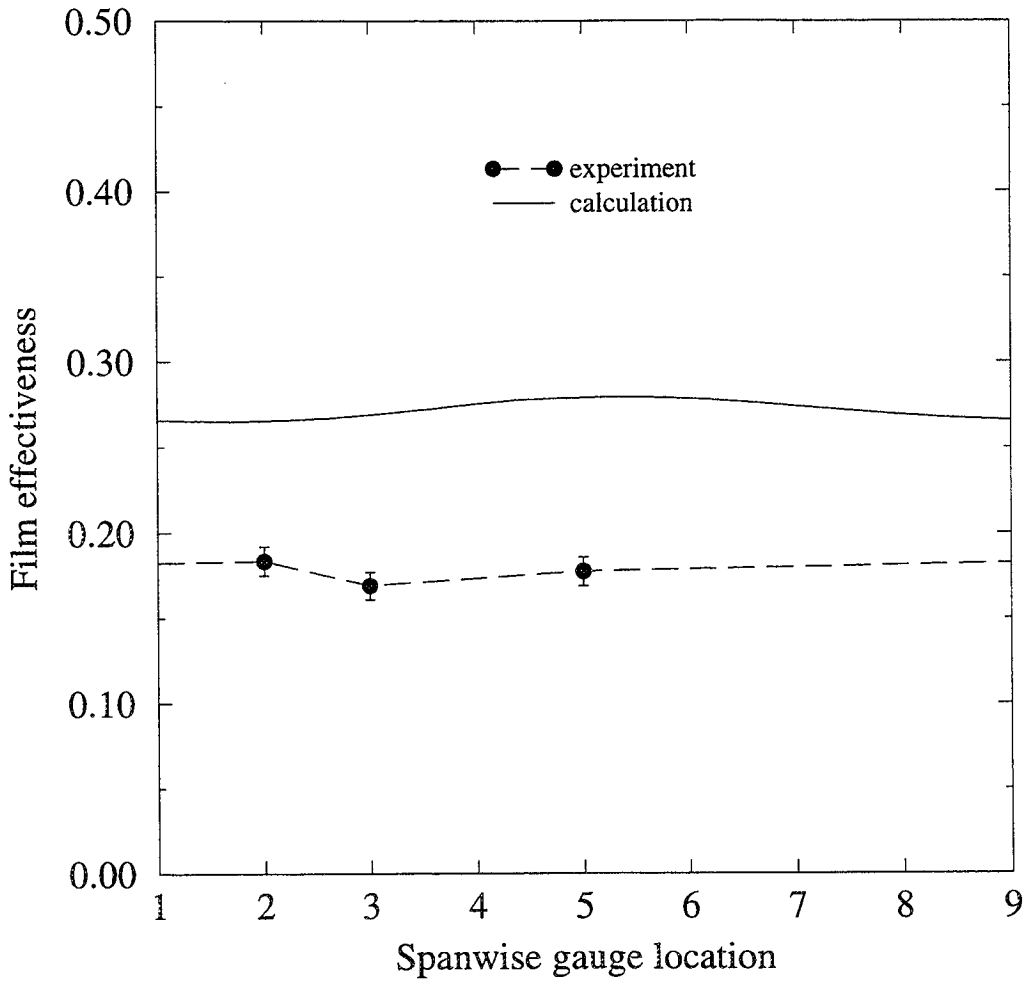

Figure 105: Computed and experimental film effectiveness for CO_2 injection at B=1.0, chord location 9.

which the computation is unable to account.

Figures 106 through 114 present experimental and computational spanwise Nusselt number distributions for chord locations 1 through 9, respectively. Focusing on spanwise trends, both the computation and experiment indicate very little spanwise variation in the Nusselt number. The only exception is at the first gauge location on each side of the blade (chords 5 and 6). Here the computation predicts a mild spanwise variation, again greater on the pressure surface. The experimental data seems to indicate some spanwise variation at chord 5, although the sharp rise from spanwise location 1 to 2 is unusual. It is interesting to note that the spanwise variations of film effectiveness and Nusselt number predicted by the calculation at chords 5 and 6 are out of phase. This means that the Nusselt number is predicted to be lower in the path of the film jet.

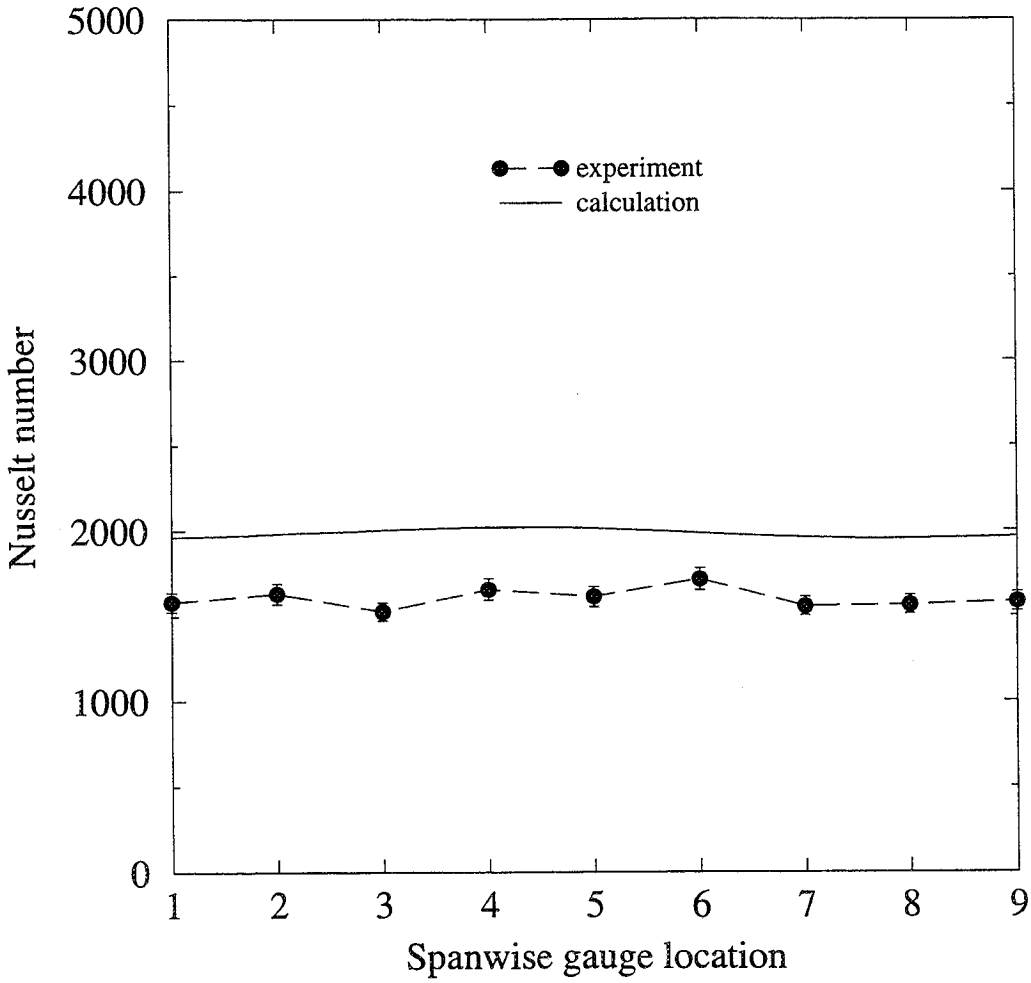

Figure 106: Computed and experimental Nusselt number for CO_2 injection at B=1.0, chord location 1.

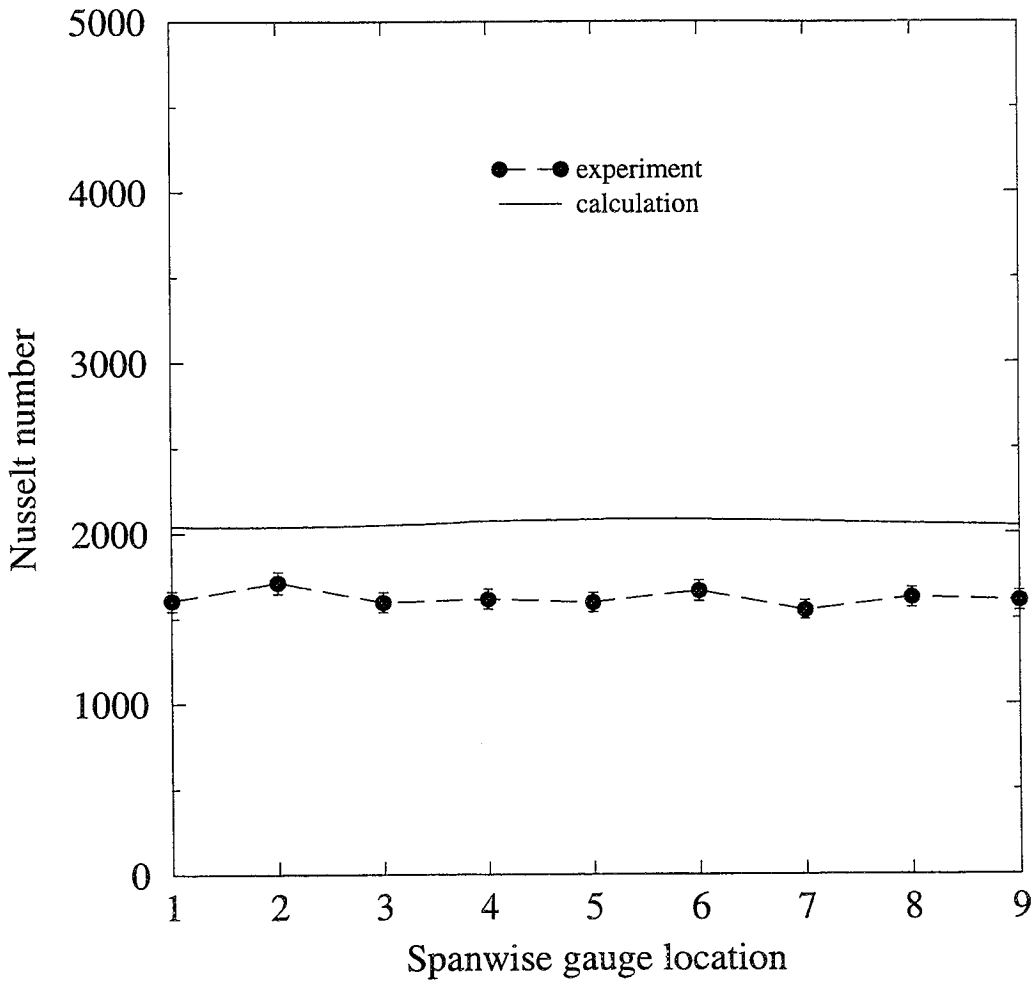

Figure 107: Computed and experimental Nusselt number for CO_2 injection at B=1.0, chord location 2.

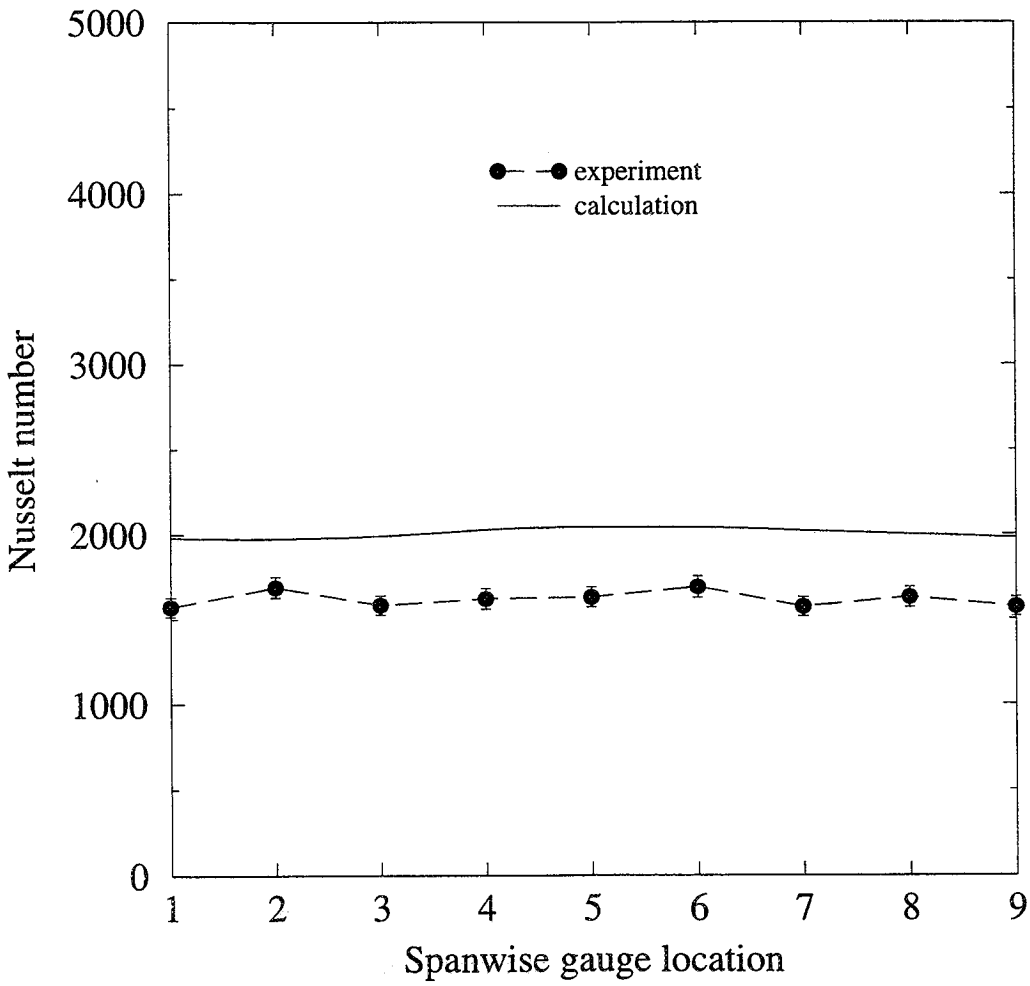

Figure 108: Computed and experimental Nusselt number for CO_2 injection at B=1.0, chord location 3.

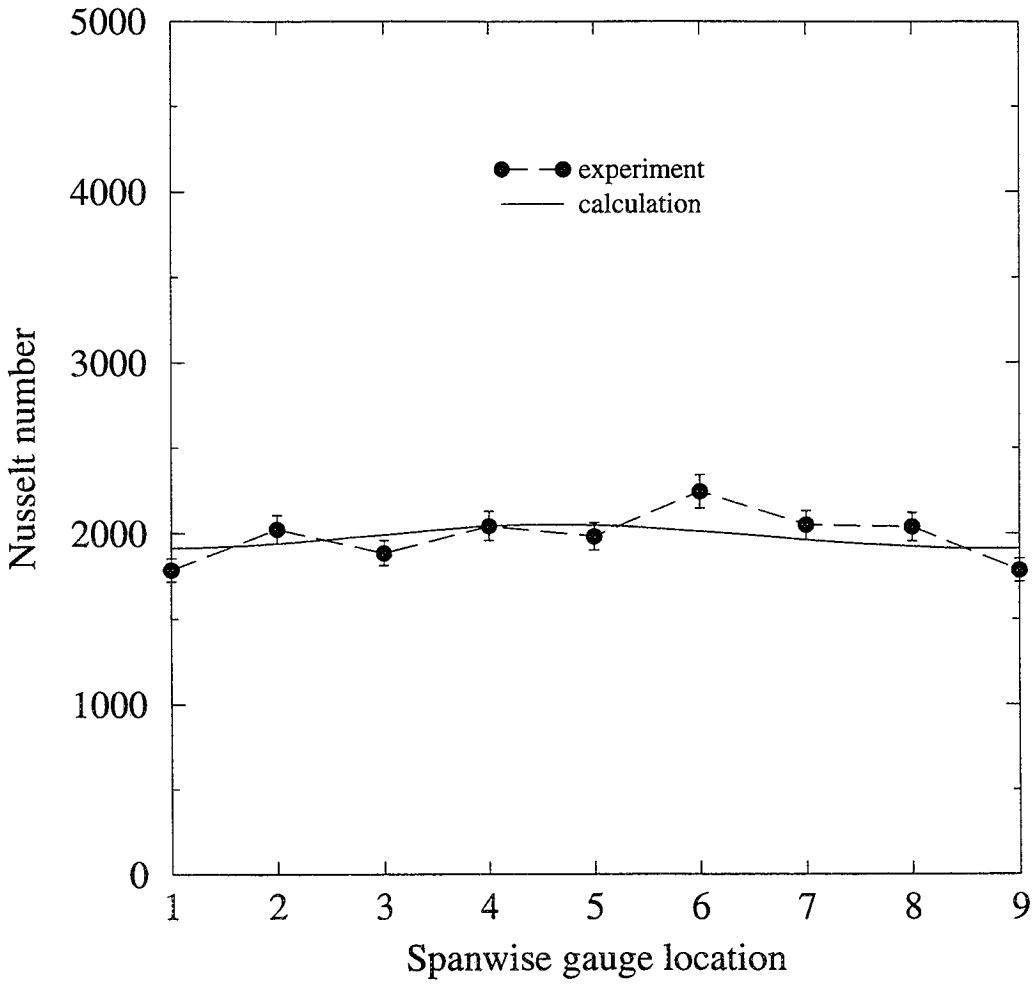

Figure 109: Computed and experimental Nusselt number for CO_2 injection at B=1.0, chord location 4.

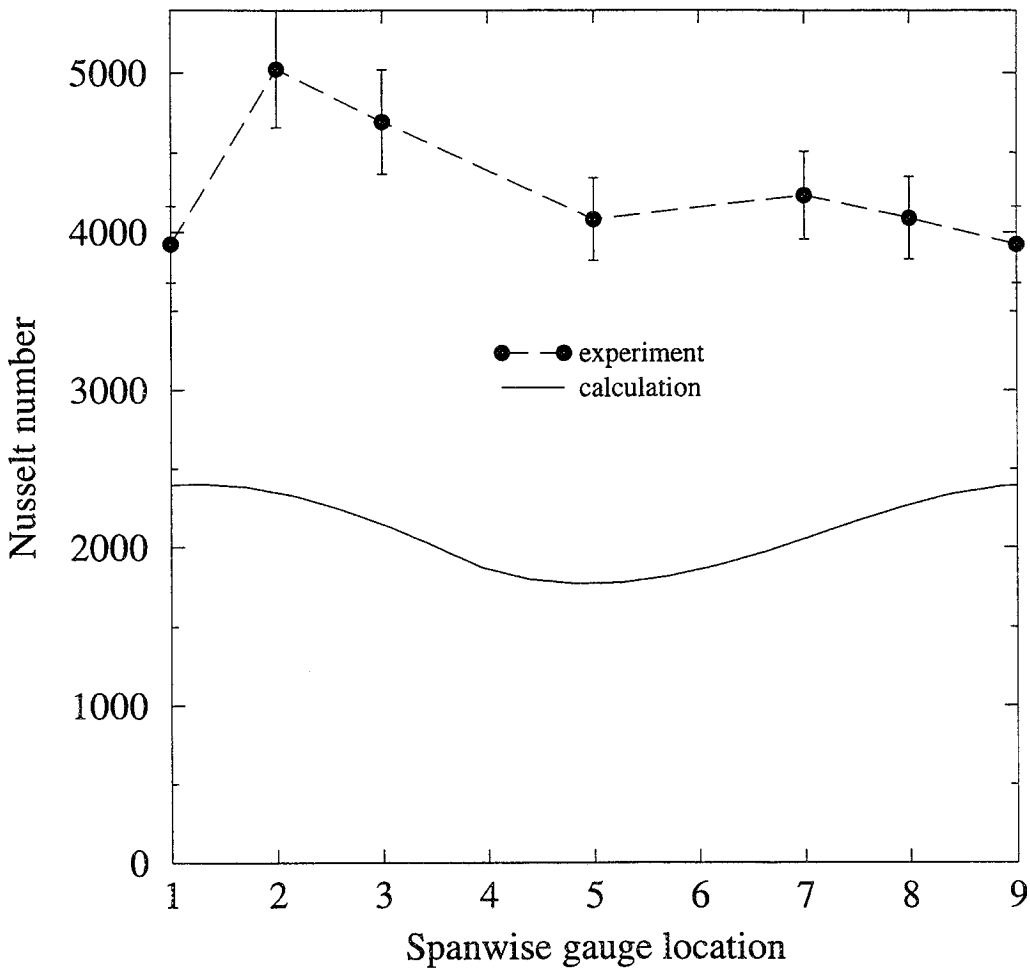

Figure 110: Computed and experimental Nusselt number for CO_2 injection at B=1.0, chord location 5.

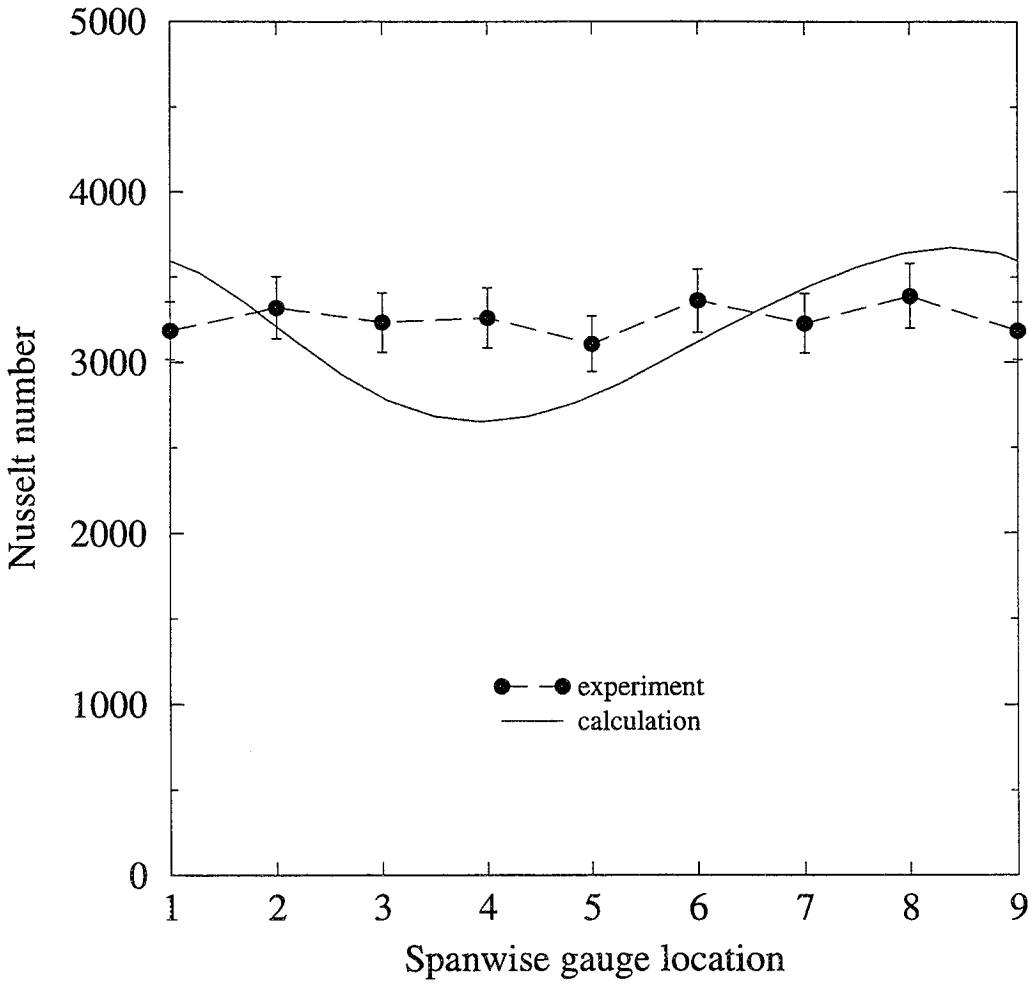

Figure 111: Computed and experimental Nusselt number for CO_2 injection at B=1.0, chord location 6.

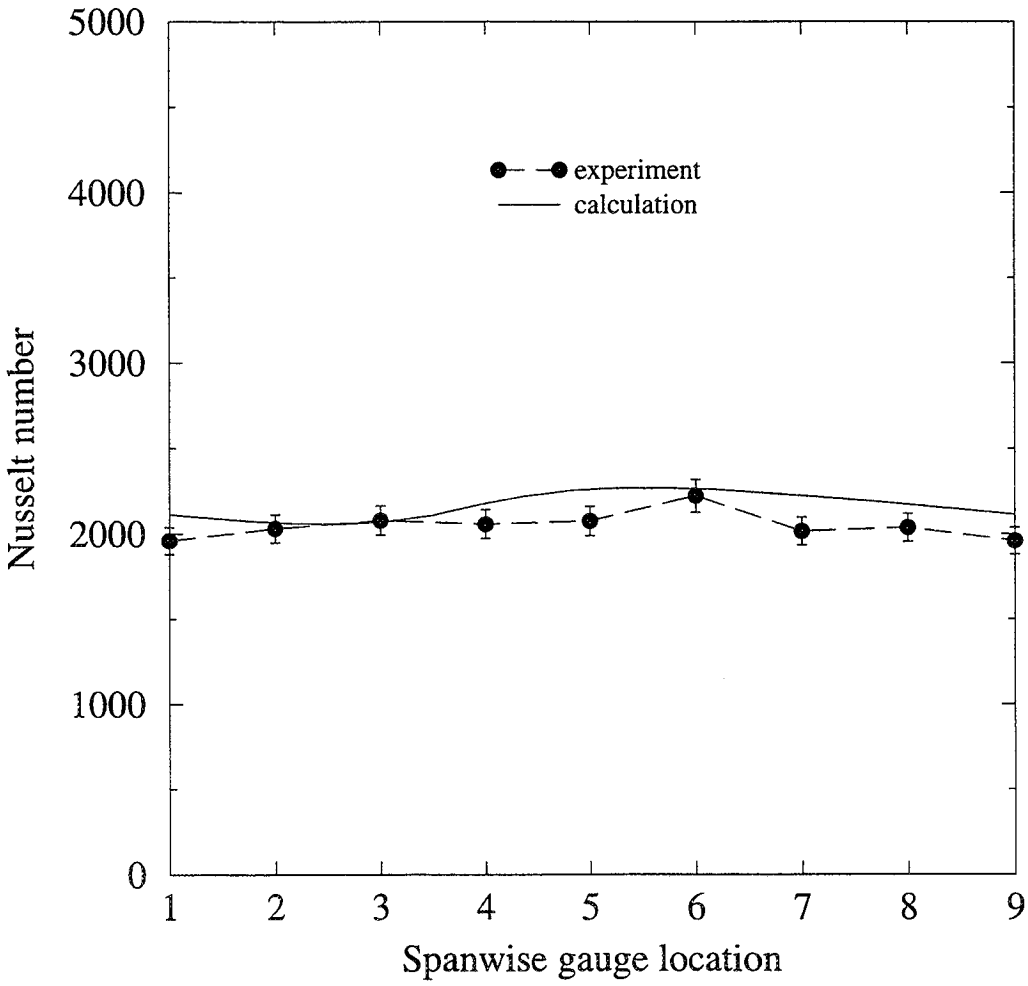

Figure 112: Computed and experimental Nusselt number for CO_2 injection at B=1.0, chord location 7.

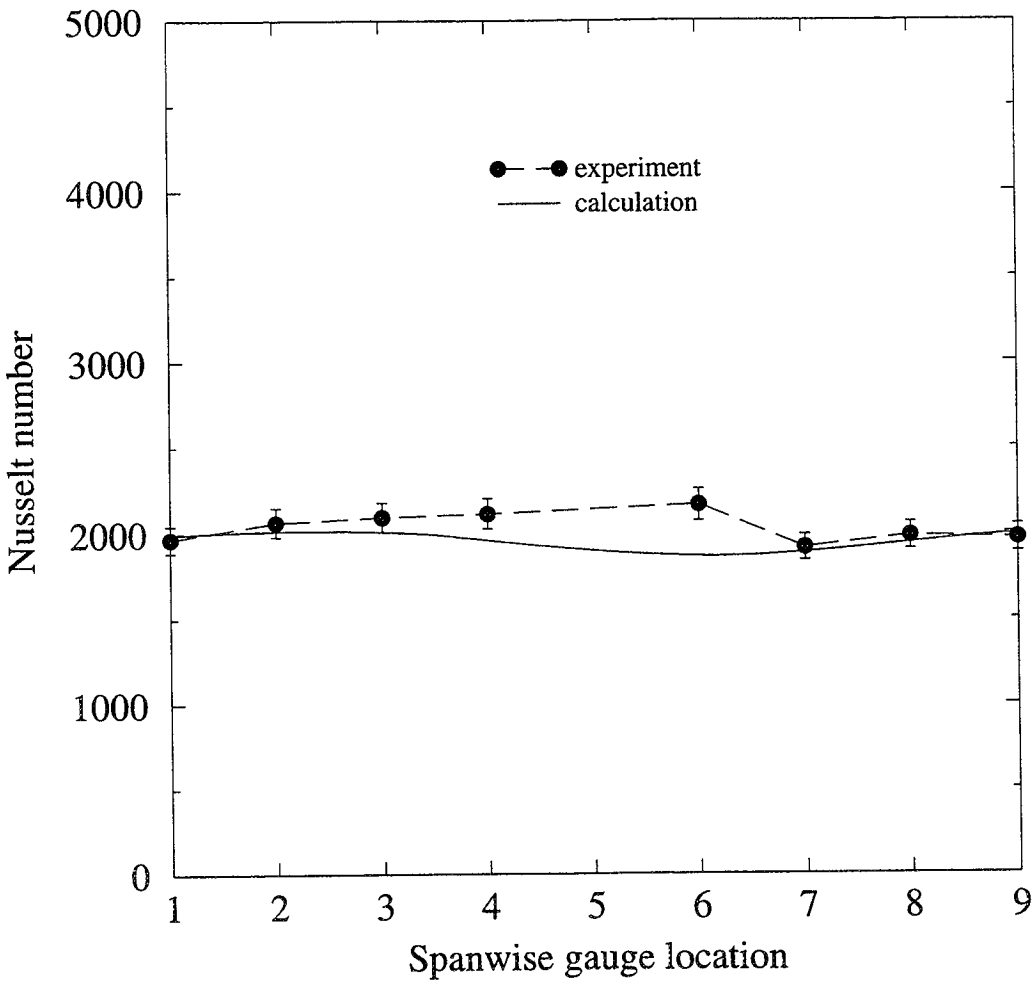

Figure 113: Computed and experimental Nusselt number for CO_2 injection at B=1.0, chord location 8.

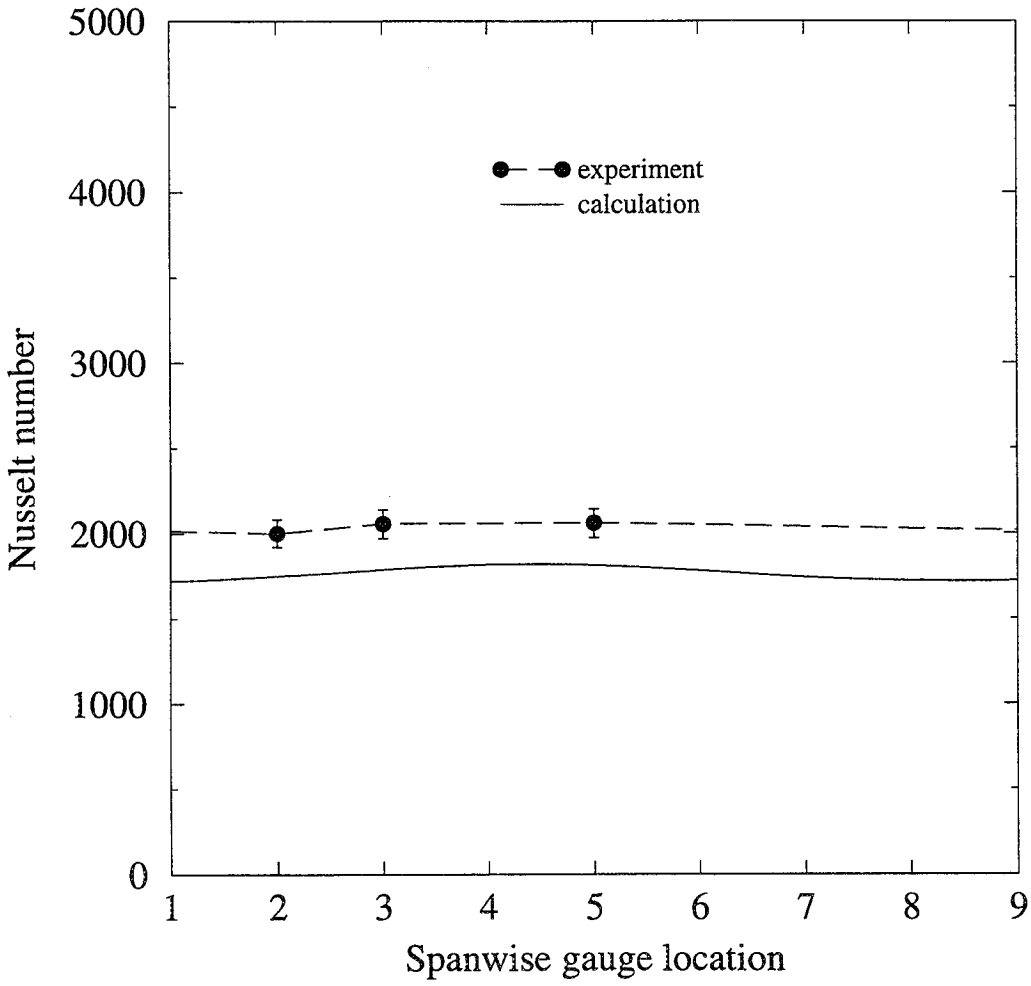

Figure 114: Computed and experimental Nusselt number for CO_2 injection at B=1.0, chord location 9.

6. UNSTEADY FILM COOLING MODEL

Motivation

In the present turbomachinery design environment, unsteady effects on film cooling effectiveness are not accounted for explicitly. They are taken into account only through the fact that all film-cooled turbine blades in operation exist in an unsteady environment, and empirical studies of this environment have yielded certain design rules for film cooling. This methodology has proven useful, and has led to very good current film cooling designs. However, these empirical design rules have not accounted for variabilities in the unsteady turbine environment such as wake passing frequency, wake thickness, and wake speed. This is to be expected, since it is impossible to change most parameters relating to wake behavior for a given machine without changing the design point of the machine.

As future gas turbine engines require higher turbine inlet temperatures and lower coolant bleed flow rates to improve performance, it is becoming increasingly necessary to account for unsteady effects early in the turbomachinery design process. This allows the freedom to change parameters such as the wake speed or the ratio of the number of stator blades to rotor blades while other design parameters are still flexible. Such a process can result in a design that utilizes the unsteadiness by means of minimizing its detrimental effects or even capitalizing on its benefits. This is

already being done for unsteady effects on aerodynamic performance [2], and it is still unclear if inherent unsteadiness can in some way be harnessed to have a positive aerodynamic effect.

In order for turbine designers to account for the effect of wake unsteadiness on film cooling early in the design procedure, it is necessary to give them a clear indication of the effect that the various wake parameters have on the film cooling. This would ideally be in the form of an equation which could predict film cooling performance for the widest possible range of parameters. The following discussion describes the rationale and procedure used to develop such an equation.

Basis for film cooling model

A full description of film cooling performance involves inclusion of both film effectiveness and Nusselt number. However, combining their effects into one value, such as the Nusselt number as defined by Abhari [19], reduces the generality of the information, since only cases having the same wall-to-coolant temperature ratio may then be compared directly. This was the rationale for determining both parameters separately in the present experiment. It is clear from Figures 37 through 44 that the effect of unsteadiness on film effectiveness is more pronounced and consistent than on Nusselt number, especially when the no rotor case is not considered. On this basis, it is useful to focus attention on the behavior of film effectiveness under

changes in wake parameters. The no rotor case is not considered in the film effectiveness model because it does not represent a true zero rotational speed limiting case, and thus would not be expected to be correlated by the same expression used to describe the rotational cases. Similarly, the average of the stationary rotor cases was not included in the model because only an average over a very large number of rotor positions would yield data of as high a confidence as the rotational cases. Indeed, attempts to include either of these two cases in the model met with a lack of success, as expected from inspection of Figures 37 through 40.

The form of the equation used to model the film effectiveness data was developed by a combination of theoretical and empirical methods, while attempting to maintain similarity to traditional film effectiveness correlations. The first practical correlations are summarized by Goldstein [9], and are applicable to slot injection. These are typically of the form:

$$\eta = \frac{C_1}{1.0 + C_2(\frac{x}{BS})^{C_3}}$$

where C_1, C_2, and C_3 are constants, x is the streamwise distance from the slot, B is the blowing ratio, and S is the slot width. The form of this equation derives from mass and energy balances in the boundary layer. The values of the coefficients depend on the assumed velocity profile. Theoretically, C_1 should have a value of 1.0, since the film effectiveness is defined to be 1.0 at the slot (x=0). However, in some

empirical correlations C_1 differs from 1.0 to achieve better correlation far from the slot.

For three-dimensional film cooling on a blade with discrete holes instead of a flat plate with a slot, an analytical description of the temperature profile in the boundary layer is usually not available. In addition, the large number of additional parameters (blade geometry, hole size, shape, and location, spanwise and streamwise hole pitch, hole angle, etc.) make generalized correlations impossible. For this case, empirical correlations are often used, although their applicability is limited to the geometry and conditions from which they were derived. Using the basic form given for slot injection, others have produced correlations of experimental data. For example, Takeishi et al. [20] give the following empirical correlation for film effectiveness on a low aspect ratio turbine nozzle with suction- and pressure-side circular hole film cooling:

Suction surface:

$$\eta = \frac{C}{2.8 + 0.027(\frac{x}{BS})}$$

where

$$C = \frac{1.5}{B^{0.3}} \qquad B<1$$

$$C = \frac{1.5}{B^{0.8}} \qquad B\geq 1$$

Pressure surface:

$$\eta = \frac{1}{1.67 + 0.00456(\frac{x}{BS})^{1.6}}$$

where S is now the effective slot width, or the width of a slot having the same flow area as the hole pattern. For n rows of circular holes, $S=n\pi d^2/4p$, where p is the hole pitch.

The variables which are available to be correlated in this experiment are x, the surface distance downstream of the holes, B, the blowing ratio, St, the Strouhal number for wake passing, and the species of the injected gas - air or carbon dioxide. In addition, it is necessary to distinguish between the suction and pressure surfaces as done by Takeishi et al. [20] because the curvature differences affect the film cooling behavior. As discussed in the experimental results, the pressure and suction surfaces also differ due to changes in attachment line with Strouhal number. This effect must be addressed by the correlation. Because differences between the air and carbon dioxide injection results may be due to density differences and/or species differences, it was decided to derive separate correlations for each injectant. Preliminary attempts to

include density ratio in a global correlation were unsuccessful, and even if a global correlation were achieved, doubt would remain concerning whether the density ratio effect had truly been correlated, or if species differences were important. A low temperature air or high temperature carbon dioxide case could help resolve this issue.

The form of the correlation which proved to provide the best agreement with the experimental data is:

$$\eta = \frac{C_1}{1.0 + \left(\frac{C_2 x}{BS(1.0 \pm C_3 B \pm C_4 St)}\right)^{C_5 \pm C_6}} - C_7 St$$

The positive signs are taken for the pressure surface, and the negative for the suction surface. On the basis of computational predictions which showed a nearly equal injectant split between suction and pressure surfaces, S is taken to be half of the effective slot width for all rows of holes. It can be seen that the basic form of the equation follows that of the previous correlations, but supplements it with additional terms to account specifically for suction/pressure surface and Strouhal number differences. The rationale for these differences will now be discussed.

The primary effect of the wake unsteadiness on the film effectiveness is to reduce it as the rotational speed or Strouhal number increases. This is evident in Figures 37 through 40. In addition, the change in film effectiveness for a given change in

Strouhal number seems to be fairly constant with downstream distance x on either the suction or pressure surface. Obviously this behavior could not continue for very large downstream distances, since the zero Strouhal number film effectiveness will approach zero very far downstream, and the correlation will predict negative values. Thus an attempt was made to correlate the Strouhal number effect through the exponent in the correlation (C_5). This would allow an increased Strouhal number to enhance the decay rate of the film effectiveness with x, while causing the film effectiveness to correctly approach zero for all Strouhal number cases at large x. However, this causes the Strouhal number effect to approach zero for small x, which does not agree with the data. Although more sophisticated models were considered to correct this, additional coefficients were required, and it was decided that for simplicity, the $-C_7St$ term would be used. This term does provide excellent agreement over the range of experimental data. In addition, the simplicity of this term allows for ease of interpretation. C_7 is simply the slope of the film effectiveness versus Strouhal number trend.

As alluded to previously, the Strouhal number effect, although nearly constant with x, differs on the suction and pressure surfaces. The reason for this as discussed in Chapter 3 is that the increased rotational speed of the rotor causes a shifting of the attachment line on the blade. Because of the showerhead location of the film holes, this changes the injectant split between the suction and pressure surfaces of the blade. Increased rotational speeds shift the attachment line toward the suction surface,

causing more injectant to flow toward the pressure surface, offsetting part of the reduction in film effectiveness caused by the wakes. The reduction of injectant on the suction surface has the opposite effect. This phenomenon is addressed in the correlation through the C_4St term. This term arises from an assumption that the changes in injectant split are linear with Strouhal number. Previous correlations such as those summarized by Goldstein [9] use the x/BS term to correlate data at different blowing ratios. The quantity BS is an effective flow rate and is modified in the correlation to be $BS(1.0 \pm C_3B \pm C_4St)$, where the pressure side flow rate is increased and the suction side flow rate is decreased. This modification maintains the total flow rate on both sides of the blade at 2BS.

The term C_3B arises from the observation that the difference between the pressure and suction surface film effectiveness is greater for B=1.0 than for B=0.5 for both air and carbon dioxide injection. A preliminary attempt to correlate the data using a correction of $(1.0 \pm C_3 \pm C_4St)$ resulted in overprediction of the film effectiveness on the suction surface and underprediction on the pressure surface at B=1.0. The opposite result was found for B=0.5. The introduction of the C_3B term corrected these mispredictions quite well. The physical interpretation of the C_3B term is that the injectant split depends upon the blowing ratio. At low blowing ratios, the momentum of the injectant is low, and the split between pressure and suction surfaces depends primarily on the geometric location of the film holes. At high blowing ratios, the injectant penetrates more deeply into the free-stream, and the split may be

influenced by the angle of injection and free-stream flow behavior. For the present experiment, the pressure surface is favored for higher blowing ratios, but this may be due to geometric considerations unique to this configuration.

It is obvious from the data that the limiting film effectiveness as x approaches zero has different values on the suction and pressure surfaces. The pressure surface data not only has a larger value at x/d=8.5 than at x/d=-8.5, but the decay rate is also higher, indicating a higher x=0 limit. Of course this limit is only theoretical, since x=0 is within the hole pattern and no data is available there, but the correlation should reflect these different limits to best fit the available data. The constant C_1 is the x=0, St=0 film effectiveness limit, and accounts for the different limits. Although the film effectiveness may not exceed 1.0 in practice, non-unity values of C_1 allow greater flexibility in correlating the data, and present no problems for the x/BS values typical of experiments such as this. Indeed, Takeishi et al. [20] have previously found non-unity limiting values to provide improved correlation with experimental data.

The $(C_5 \pm C_6)$ exponent represents the decay rate of the film effectiveness with x. For large values of this exponent the decay is rapid, and for smaller values it is more gradual. For example, an exponent of zero would yield a constant film effectiveness or no decay. Typical values of the exponent are near 1.0. The C_6 term represents the fact that the pressure surface data was found to decay more rapidly in the streamwise direction than the suction surface data. This finding agrees with the analysis of Ito

et al. [16], which predicts better film cooling performance on a convex wall than on a concave wall for momentum flux ratios less than 1.0. All conditions for the present experiment were performed for momentum ratios less than or equal to 1.0. The values vary from 0.167 for carbon dioxide at B=0.5 to 1.00 for air at B=1.0, which would seem to call for different wall curvature effects for the different cases, which is not reflected in the data. However, the analysis of Ito et al. [16] is for tangential injection in the streamwise direction. For the showerhead cooling of the present experiment, the injectant exits the hole with zero streamwise momentum, since the fluid is injected in the spanwise direction. Replacing the streamwise momentum in the analysis with the zero streamwise momentum of showerhead cooling results in an effective streamwise momentum ratio of zero for all cases. Thus the convex (suction) surface should perform better than the concave (pressure) surface to the same degree for all blowing cases. The experimental data agrees with this prediction. It should be noted that the preceding discussion relates only to the decay rate of the film effectiveness, and not to the x=0 limiting value. The limiting value may differ on the two sides of the blade due to effects such as the relative mass flow rate of injectant on each side. The analysis of Ito et al. [16] pertains to the performance of a fluid element once it has established a trajectory on either side of the blade. Because of this the C_6 term is thought to be independent of blowing ratio, and is incorporated as such in the exponent. For showerhead cooling on a blade of different geometry (i.e. different curvature), the magnitude of C_6 will change, and should approach zero for a flat plate. Its sign should remain positive at all times, meaning that the film

effectiveness on the pressure surface should always decay more rapidly than on the suction surface. Of course C_5 will also change with geometry as well as with other parameters such as free-stream turbulence level, which would tend to enhance mixing and increase C_5.

Correlation with data

As is apparent from the preceding discussion, the determination of the optimum correlation equation form and optimum coefficients for that equation were not independent processes. It was necessary to solve for best-fit coefficients for many different equation forms to examine potential candidates and verify theory. The form of these correlating equations is generally not amenable to an exact least-squares solution for the coefficients, so a computer program was written for this project to converge to a minimum least-squares error for a given equation form. The program perturbs each coefficient successively to search for the zero-slope location of the least-squares error function. The magnitude of the perturbation of each coefficient proceeds from large positive and negative values to progressively smaller values by a factor of 0.5 until a new coefficient is found which produces a smaller error than the previous minimum error. The solution is considered converged when even minimum finite machine-accuracy perturbations in each coefficient produce no or positive change in the error.

The application of the computer program produced the following coefficients for the film effectiveness correlation equation:

	air	CO_2
C_1	0.761	0.948
C_2	0.054	0.094
C_3	0.139	0.241
C_4	0.286	0.144
C_5	0.792	0.762
C_6	0.033	0.014
C_7	0.093	0.095

The root mean square average of the error in film effectiveness using these coefficients is about 0.0068 for air and 0.0074 for carbon dioxide.

Some conclusions may be drawn from the two sets of coefficients for the two injectants. In terms of their effect on the film effectiveness, C_5 and C_7 remain fairly constant between injectants. In particular, the magnitude of the Strouhal number effect (C_7) is almost the same for both injectants, having an average value near 0.094 for both air and carbon dioxide. This may indicate a relative insensitivity of wake passing effects to injectant density ratio. The previous argument against drawing conclusions based on inter-species data still applies, but may be somewhat weakened due to the fact that the previous argument was for absolute levels of film

effectiveness, and the present discussion concerns changes in film effectiveness with Strouhal number. That is, given a baseline film effectiveness profile for carbon dioxide injection at a fixed Strouhal number, the effect of Strouhal number variations on film effectiveness may be influenced more by primary fluid properties such as density than by species differences. The agreement between C_5 for air (0.792) and carbon dioxide (0.762) indicates that the film effectiveness decay rate is similar for both cases. The fact that the values are below 1.0 implies a more gradual decay of film effectiveness with downstream distance than for the cases of Takeishi et al. [20], which gave values of 1.0 and 1.6. This is to be expected for showerhead cooling, since the injectant has less opportunity to separate from the blade than does the suction and pressure surface injection of Takeishi et al. [20].

The larger value of C_1 found for carbon dioxide (0.948) versus air (0.761) indicates a higher x=0 limit for carbon dioxide. This value is highly sensitive to the slope of the data between the first two data points on each side of the blade, and is thus subject to a fair amount of variability due to experimental uncertainty. The magnitude of these two values of C_1 is reassuring, however, since slot injection would be expected to yield a value of 1.0, and it could be argued that discrete hole injection should produce a value marginally less than 1.0 since the span-average film effectiveness is less than 1.0 in the showerhead region. Differences between C_2 for air (0.054) and carbon dioxide (0.094) are primarily a result of the C_1 differences. A larger value of C_2 is required to offset a larger value of C_1 if downstream values of

film effectiveness are comparable between species.

C_3, C_4, and C_6 are the three coefficients associated with differences between suction and pressure surface film effectiveness values. All of these coefficients have the same sign for air and carbon dioxide, which indicates that the trend between suction and pressure surface data is consistent for the two injectants. The magnitudes of these coefficients differ, however. C_3 has a value of 0.139 for air and 0.241 for CO_2. This reflects the greater tendency in the carbon dioxide injection case for changes in blowing ratio to cause differences between the suction and pressure surface film effectiveness. C_4 has a value of 0.286 for air and 0.144 for CO_2. This indicates that air injection has about twice the sensitivity of Strouhal number on the difference between suction and pressure surface film effectiveness. This is best visualized in Figures 37 through 40. Figures 37 and 38 (air injection) show a much greater spread of film effectiveness values over the four Strouhal number conditions on the suction surface than on the pressure surface. This is not as clear for carbon dioxide injection. C_6 has a value of 0.033 for air and 0.014 for CO_2. This reflects that although the pressure surface film effectiveness decays more rapidly than the suction surface data for all cases, this difference is more pronounced with air injection.

Figures 115 through 118 show comparisons between the experimental data and correlations for air at blowing ratios of 0.5 and 1.0 and carbon dioxide at blowing ratios of 0.5 and 1.0, respectively. Unlike previous plots, the data are shown by

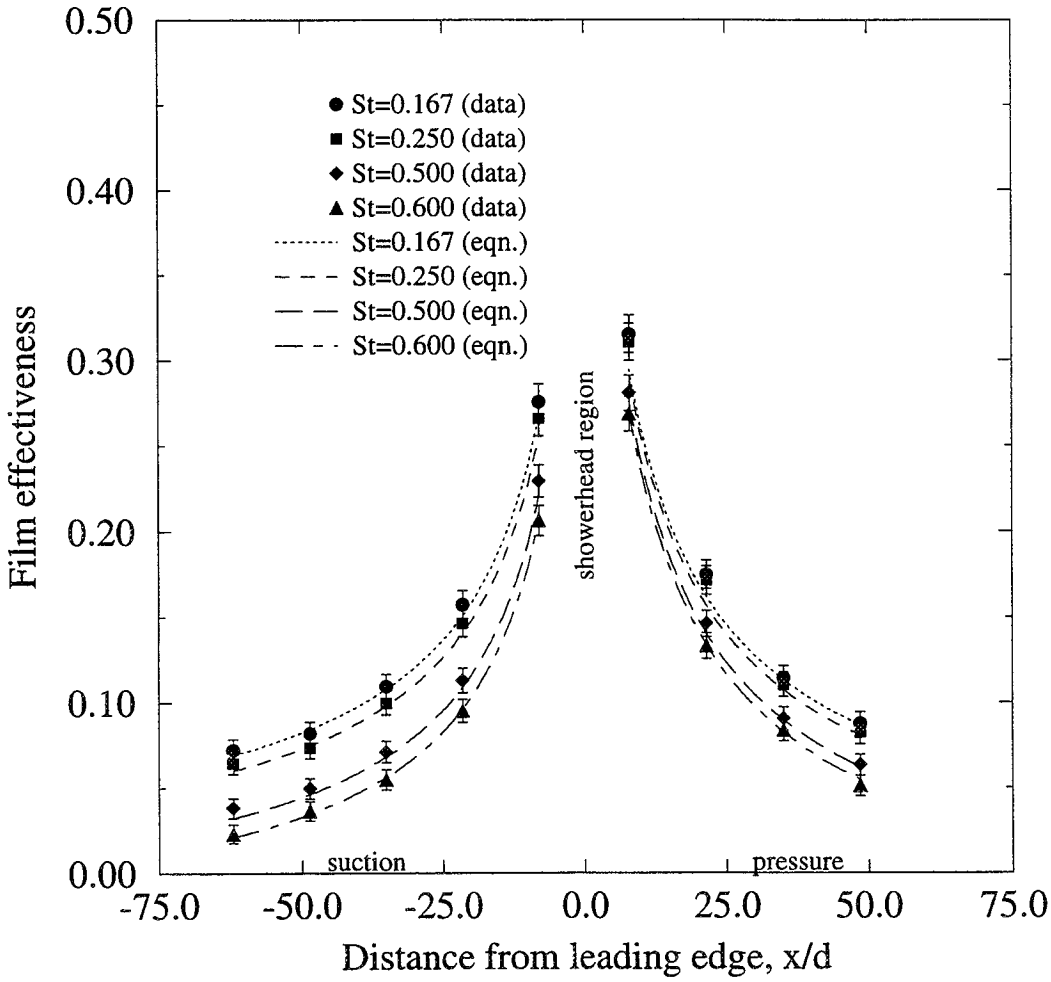

Figure 115: Correlated experimental span–average film effectiveness for air injection at B=0.5.

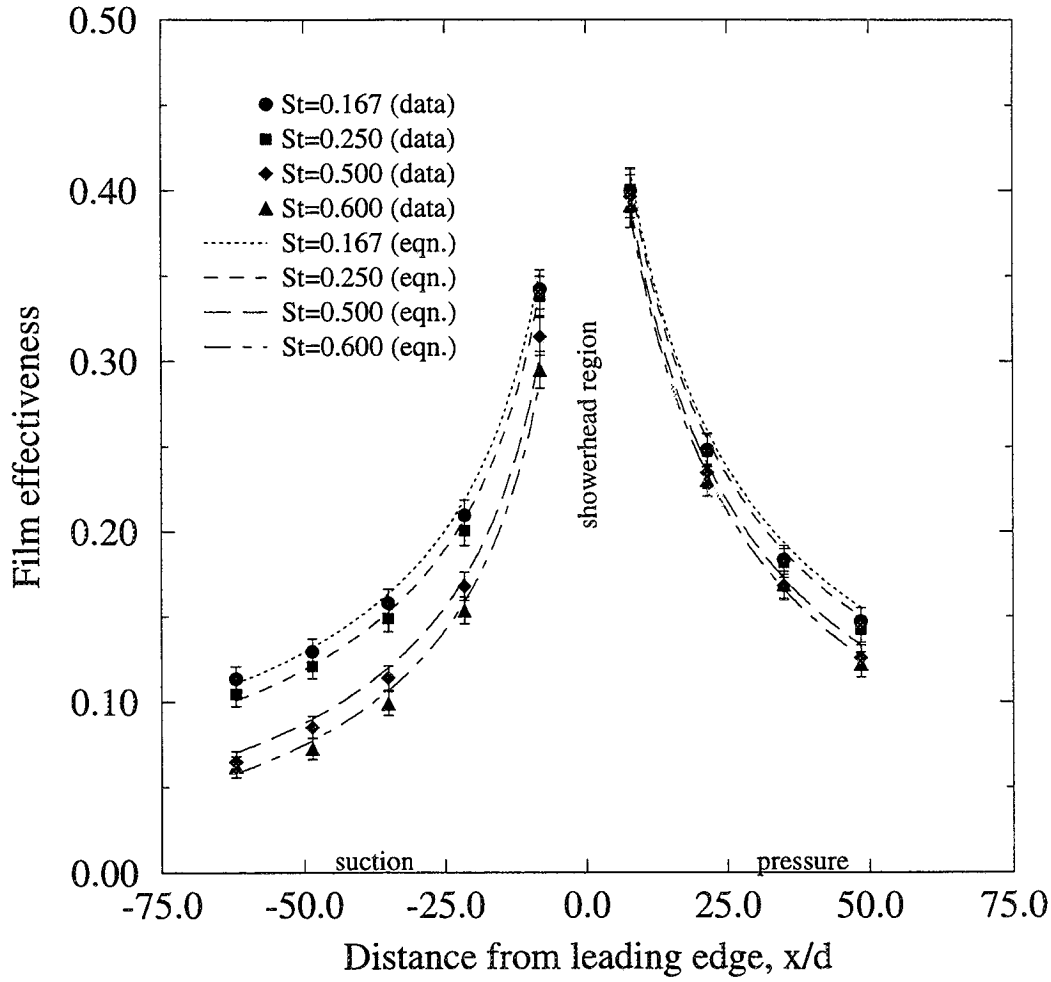

Figure 116: Correlated experimental span–average film effectiveness for air injection at B=1.0.

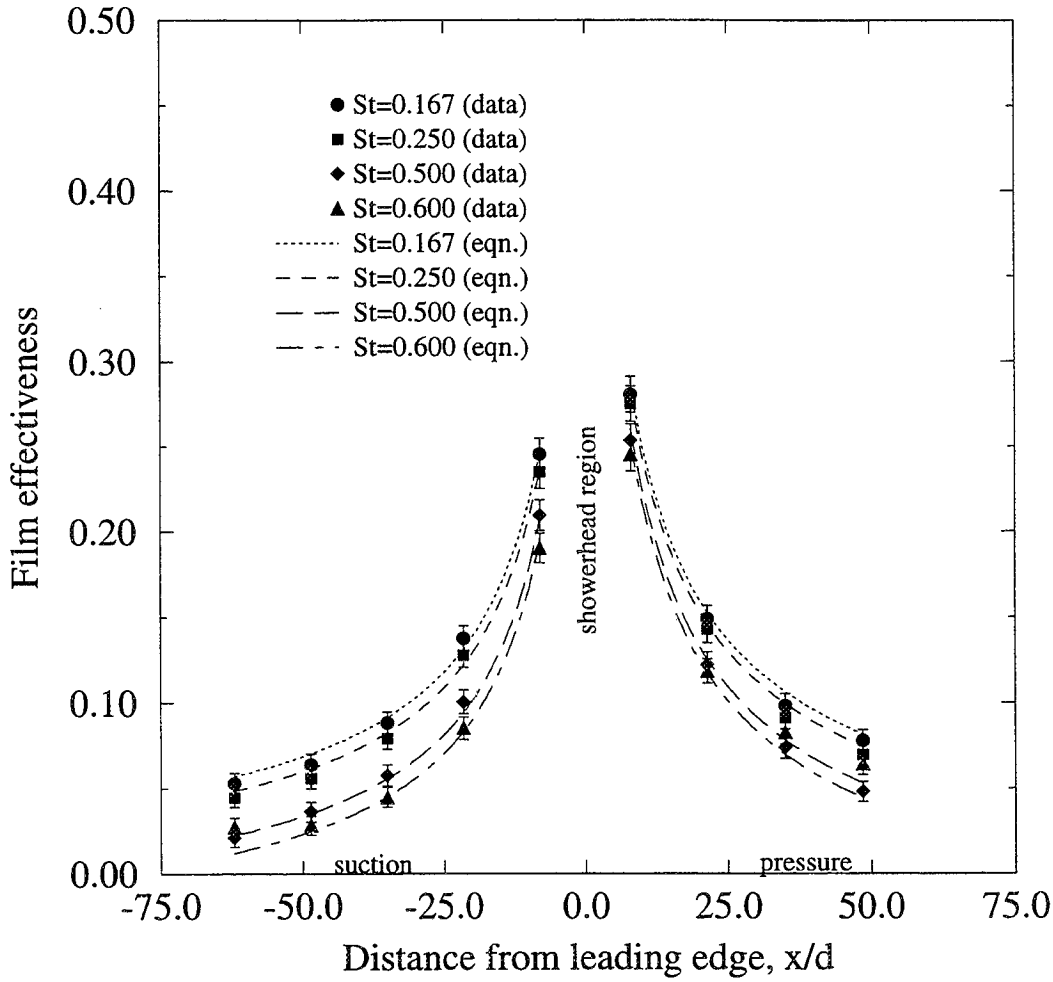

Figure 117: Correlated experimental span–average film effectiveness for CO_2 injection at B=0.5.

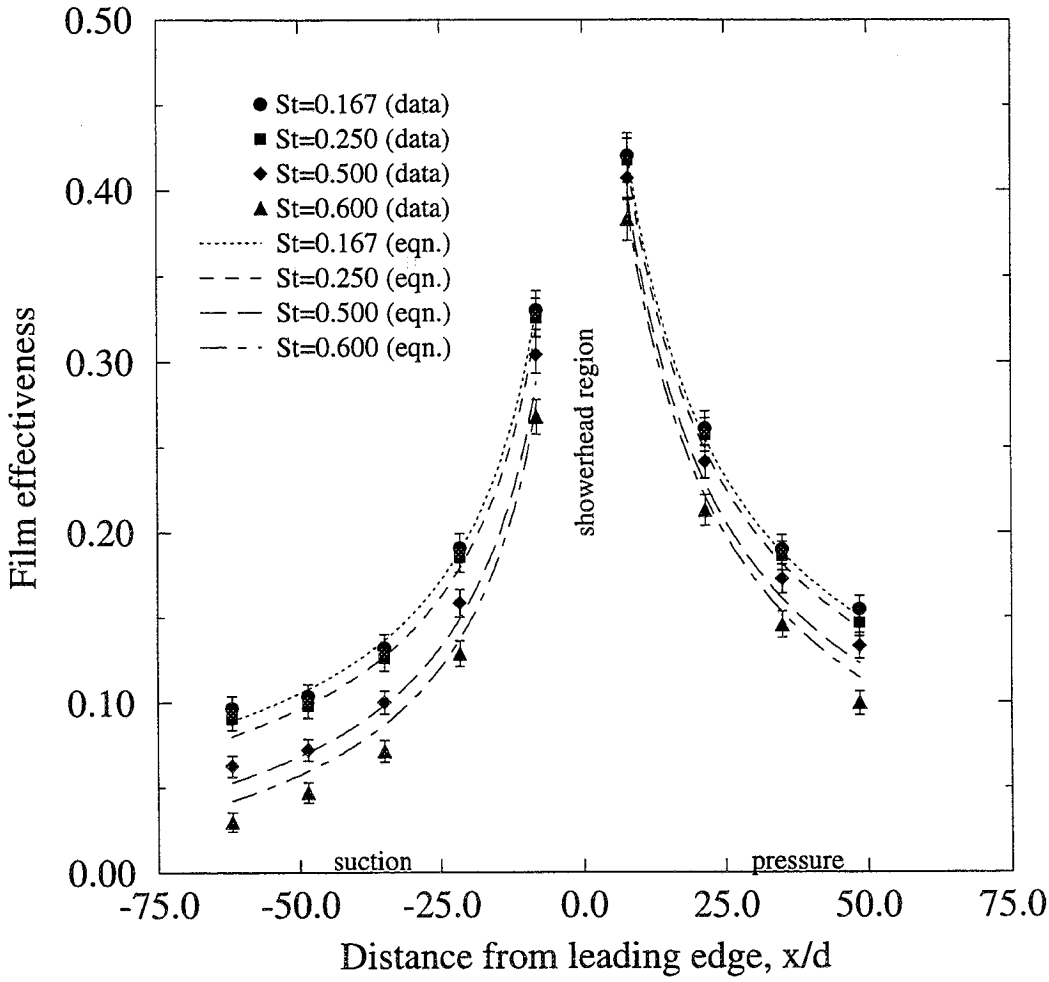

Figure 118: Correlated experimental span–average film effectiveness for CO_2 injection at B=1.0.

symbols and the correlations by continuous lines. It can be seen from Figures 115 and 116 that the correlation is in excellent agreement with the experimental data for air injection at both blowing ratios. While there is some offset at the blowing ratio of 1.0 on the suction surface, the change in film effectiveness with increasing Strouhal number is captured quite well. This indicates that the assumption of linear decay of film effectiveness with Strouhal number is proper. Other measures of wake unsteadiness would not necessarily produce such a linear effect. For example, the flow coefficient, which is defined as the ratio of throughflow velocity to rotor velocity, is inversely proportional to the Strouhal number. Over the range of rotor speeds tested, the flow coefficient versus film effectiveness relationship is not linear.

Figures 117 and 118 show the correlation and data for carbon dioxide injection. In general, the correlation agrees well with the data. The magnitude of the Strouhal number effect is underpredicted for a blowing ratio of 1.0, particularly on the suction surface, and is overpredicted for a blowing ratio of 0.5, particularly on the pressure surface. This indicates that the correlation might properly require a blowing ratio influence on the C_7St term. However, in view of the excellent correlation achieved for air injection with the relatively simple correlation equation, and the additional complexity which would be required to further collapse the carbon dioxide data, the recommended correlation stands. The purpose of the correlation is not to precisely match the data point-by-point, but to capture the main trends in a fairly simple equation which can be used to help elucidate the flow physics.

Comparison with existing data

There is limited experimental data in the literature for span-average film effectiveness with variable wake Strouhal number. The two most appropriate data sets for comparison are Mehendale et al. [29] and Funazaki et al. [45]. Both studies include experimental data for B=0.4, 0.8, and 1.2. Funazaki et al. [45] measured span-average film effectiveness values on a blunt body with a cylindrical leading edge and a showerhead film cooling arrangement very similar to the one in the present study. However, the blade leading edge diameter is used as the length scale in the Strouhal number definition. When converted to the wake-producing bar diameter definition, the variation in Strouhal number is small - about 0.05 from the highest to lowest rotor speeds. As a result, the variations in film effectiveness are small and difficult to scale from the plots.

The Mehendale et al. [29] data set has a larger Strouhal number range of 0.20, and thus is more amenable to comparison. The Mehendale et al. [29] experiment was conducted for a more highly-loaded turbine blade and consists of suction and pressure surface cooling in addition to the showerhead cooling of the present study, so direct comparisons are difficult. However, the Strouhal number effect is nearly constant in the chordwise direction as in the present study. The mean film effectiveness decrement predicted by the current model for a Strouhal number increase of 0.2 is 0.019. The Mehendale et al. [29] data set shows a decrement ranging from 0.025 at

B=0.8 to slightly negative (enhancement) at B=0.4 on the pressure surface, with a mean value of about 0.013. The model predicts a smaller film effectiveness decrement on the pressure surface due to attachment line variations at higher Strouhal numbers. This effect is present, particularly at B=0.4 and B=1.2, although it is smaller than in the present study, presumably due to the presence of suction and pressure surface (non-showerhead) cooling, which is unaffected by attachment line variations.

Scope of Model

In an actual film-cooled gas turbine engine, unsteadiness may result from not only wake passing, but also from three-dimensional flows, shock waves, free-stream turbulence, and other sources. In addition, the film cooling may be on a moving blade itself, resulting in buoyancy and Coriolis forces. Effects such as these make direct application of the correlation impossible. Even if all these effects were considered (which would make for a very complicated study), the use of a specific blade shape and film cooling scheme limits the applicability of the correlation to very similar if not identical geometries. Thus the proper use of this correlation is not in blindly using it to predict film effectiveness values for various cases, but in deriving insight from the trends it predicts, and extrapolating them to the particular case of interest. For example, a turbine designer may need an estimate of the reduction in film effectiveness resulting from a particular wake passing frequency. By calculating

the wake passing Strouhal number using the trailing edge thickness of the upstream blade row, the model will give an estimate for this decrement. Engineering knowledge of the situation is still required, since for example the free-stream turbulence in the design may be high which would lessen the effect of the wake passing. But the model would at least establish an upper bound for the decrement, which is useful to the designer.

The user of this correlation should be mindful of the geometry and conditions under which it was developed. The geometry and conditions were intentionally chosen to be relatively general. The blade design allows it to be viewed as either a stator or rotor cascade. The cooling scheme although specific in the type of cooling (showerhead), is typical of modern showerhead cooling designs. The flow regime (high subsonic) is in the range of modern gas turbine engines without reaching transonic conditions, which would reduce its generality. Finally, the unsteadiness, while again specific in its form (wake-induced), is the most general since all embedded turbomachinery is subject to wake passing effects. The rotating rod arrangement extends this generality by allowing different rotating speeds at nearly the same design incidence angle. These features allow the conclusions of this study to be applied to a wide range of turbomachinery flow physics.

7. CONCLUSIONS AND RECOMMENDATIONS

A model has been developed which accounts for the primary effects of wake passing unsteadiness on film cooling effectiveness for a showerhead-cooled stationary turbine blade. The experimental film effectiveness as correlated by the model is seen to be reduced by wake passing unsteadiness for all cases by a nominal value of 0.094 times the wake passing Strouhal number. This value may be of importance to designers in allowing an estimate of the reduction in film effectiveness for various rotor speeds. The model is most applicable near midspan, where wake passing is the primary mode of unsteadiness.

The ability to correlate the data well with a fairly simple model speaks to the veracity of the time-average values of the unsteady experimental data. The trends shown in the steady data are consistent and reasonable. Besides the quantification of the Strouhal number effect, there are several other important conclusions to be drawn from the steady data. First, the Strouhal number has a measurable effect on the flow split between the suction and pressure surfaces for showerhead cooling. This effect is due to the variation of the blade attachment line with Strouhal number. A higher Strouhal number moves the attachment line toward the suction surface and skews the coolant flow toward the pressure surface, producing better cooling on the pressure surface and worse on the suction surface. This effect is quantified by the model through the coefficient C_4. Secondly, the higher blowing ratio of 1.0 yields higher

film effectiveness values than the 0.5 blowing ratio case in accordance with the traditional (x/BS) method of correlating non-detaching cooling jets. This indicates that for the typical showerhead cooling arrangement of this study, a blowing ratio of 1.0 is not sufficient to cause jet lift-off of the nature seen for suction and pressure surface cooling. Finally, Nusselt numbers were found to remain fairly constant with changing Strouhal number, but to increase with injection blowing ratio due to the enhanced mixing caused by injection.

The unsteady experimental data proved difficult to execute and interpret. Substrate conduction effects led to the development of the correction technique presented in Appendix II which in theory should account for these effects. However, the experimental noise is amplified by the differential nature of the technique, which increased the experimental uncertainty. It is recommended that future experiments which aim to measure high frequency temperature fluctuations use double-sided gauges similar to those used by Abhari and Epstein [33]. These gauges limit error by measuring two high frequency temperatures separated by a very thin substrate of known properties.

Despite the difficulty in obtaining unsteady temperatures, several important mechanisms of wake passing were isolated by other methods. Perhaps the most interesting were those found through the use of stationary wake experiments. A clear and consistent reduction in film effectiveness was found for stationary wake locations

near the blade leading edge. Reductions of up to 0.10 and 0.15 were exhibited on the suction and pressure surfaces, respectively. Nusselt numbers were more constant, although slight reductions were found near the leading edge with the wake impinging on the blade. These results show a substantial quasi-unsteady effect and may set an upper bound on the unsteady effect. Based on the success of these data, stationary wake experiments are recommended in the absence of advanced instrumentation capable of resolving high frequency data. In addition, the averaging of these data more properly represent a limiting case for wake passing experiments than the more traditional no wake condition. Another unsteady mechanism identified by the steady experiments is the spanwise variation in film effectiveness at chord 5 for various Strouhal numbers. The reduction in span-average film effectiveness is found to be primarily due to reductions near the peak film effectiveness value. This indicates that the wake passing influences the film jets by enhancing their spanwise mixing.

The Nusselt numbers are predicted fairly well by the steady computation when adequate grid resolution is employed. The traditional $y^+ < 1$ criterion for heat transfer computations is confirmed by grid resolution studies. Film effectiveness prediction is not as successful. The computation predicts higher film effectiveness values and greater spanwise gradients than the experiments, both of which indicate an underprediction of film mixing. This is thought to be primarily due to not resolving the flow inside the film holes, as well as the absence of reliable turbulence models for film cooling.

The unsteady computation showed that there are essentially two effects of wake passing on film cooling: changes in the coolant flow characteristics at the hole exit and changes in the coolant boundary layer. These two effects were separated by matching the time-average hole exit properties through judicious selection of free-stream inlet boundary conditions, leaving only the effect of unsteadiness on the boundary layer. The unsteady analysis indicated that if the correct coolant flow rate and flow split can be matched, the presence of unsteady wakes (as modeled in this study) has a small effect on the heat transfer behavior of showerhead film cooling. The span-average adiabatic film effectiveness is reduced by 2 to 3 percent in the showerhead region and on the pressure surface compared to the steady prediction. Local reductions of up to 8 percent are found in the showerhead region. These reductions are likely due to the periodic relative lifting of the coolant boundary layer from the pressure surface as the wake passes, and enhanced mixing in the showerhead region. The computational reductions in film effectiveness due to wake passing are in general smaller than the experimental reductions. One reason is because the computation models the cylindrical rods as flat plates with no thickness in the streamwise direction. A recommended future computational project would account for the circular geometry of the rods, perhaps through a full multi-grid technique which was beyond the scope of this study.

Although the present study represents only one film cooling geometry, it was noted from the computations that film hole placement and angle is of great importance in

achieving a smooth, spanwise uniform coolant film. For the staggered film hole arrangement of this report, the coolant jets tend to "line up" and merge together, leaving portions of the blade practically uncooled. This is especially important in the showerhead region, since this region is exposed to the highest temperatures. The designer should consider these three-dimensional effects to avoid local hot spots, perhaps employing an aligned or less structured film hole pattern in the showerhead region. This will depend on the hole spacing and angle as well, but is true for both steady and unsteady environments.

Many effects related to unsteady coolant flow interactions remain to be explained. As expressed in [19], modeling of the interaction between the turbulent wake and the blade boundary layer has not included the process of turbulent energy entrainment by the boundary layer, and the interaction of free-stream turbulence with the boundary layer. An adequate understanding of the film coolant flow structure is still being obtained under a variety of test conditions. Such an understanding is necessary to provide the basis for needed turbulence models which are applicable for film cooling situations. It is hoped that the results of this study represent a step in this direction, and will lead to other research in the field.

APPENDIX I - UNCERTAINTY ANALYSIS

The method of Kline and McClintock [46] was used to determine the magnitude of experimental errors associated with the calculation of film effectiveness and Nusselt number from the raw experimental data. As described by Kline and McClintock [46], if the quantity R can be expressed as an independent function of n variables x_1, x_2, x_3, ... , x_n, then w_R, the uncertainty in R, can be estimated from:

$$w_R = \left[\sum_{i=1}^{n} \left(\frac{\partial R}{\partial x_i} w_i\right)^2\right]^{\frac{1}{2}}$$

where w_i is the uncertainty in x_i.

The film effectiveness η is given by:

$$\eta = \frac{T_f - T_r}{T_c - T_r}$$

where T_f is the film temperature, T_r is the recovery temperature, and T_c is the coolant stagnation temperature. Further, the film and recovery temperatures are determined from quadratic calibration equations of the gauge current I and voltage V:

$$T = a\left(\frac{V}{I}\right)^2 + b\left(\frac{V}{I}\right) + c$$

where a, b, and c are the calibration coefficients.

The uncertainty in T_f and T_r results primarily from calibration uncertainty. The calibration uncertainty has a value of about 1.0 °C. This uncertainty results from the fundamental uncertainty in the calibration process, which was estimated from repeated readings, and the use of a quadratic relation to fit the calibration data. This is primarily a systematic uncertainty, since repeated measurements with the same gauge would tend to produce repeatable measurements to within about 0.1 °C. The systematic uncertainties cancel in the numerator of the film effectiveness definition, so the effective uncertainty in the numerator terms is the random error of 0.1 °C. The uncertainties in electrical current and voltage are about 10^{-7} Amperes and 10^{-7} Volts, respectively. These uncertainties are less than 0.1% of the absolute voltage and current values, and so have very little effect compared to the calibration uncertainty. Applying the uncertainty relation, an uncertainty in the numerator values of T_f and T_r of 0.1 °C is estimated.

T_c is measured using a standard type-E thermocouple, and has uncertainties resulting from thermocouple uncertainty. The thermocouple uncertainty can again be separated into random and systematic uncertainty. The systematic uncertainty of about 1.0 °C is present for all cases and results in an offset error to the film effectiveness. The random thermocouple error is estimated to be about 0.1 °C. Since the denominator of the film effectiveness relation uses the difference of two dissimilar gauges, the

systematic uncertainties of 1.0 °C are included in the overall uncertainty estimate. Applying the uncertainty relation, an uncertainty in the values of T_c of 1.0 °C is estimated. Using the estimated errors for all temperatures in the film effectiveness relation, a maximum value of $(T_f - T_r)$ of 14 °C, and a value of $(T_c - T_r)$ of 33 °C, the uncertainty relation gives a maximum estimated uncertainty in the experimental film effectiveness of 0.013. This uncertainty varies based on the local film effectiveness, reaching a value of 0.005 as the film effectiveness approaches zero.

The experimental Nusselt numbers are calculated from the relation:

$$Nu = \frac{hc}{k}$$

where h is found from:

$$h = \frac{q''}{T_w - T_f}$$

The uncertainties in the measured temperatures are again the 0.1 °C random errors as determined in the film effectiveness analysis, since both T_w and T_f incur the larger systematic errors sympathetically, and these cancel in the difference. q" is determined from:

$$q'' = \frac{V_h I_h}{L_h W_h}$$

where V_h and I_h are the voltage and current across the foil heater, respectively, and L_h and W_h are the length and width of the foil heater. The uncertainty in V_h results primarily from uncertainties in the voltage drop from the copper busbars to the foil itself, as well as from non-uniformities in the foil voltage distribution. These are estimated to have a value of about 0.01 Volts. The uncertainty in I_h results mainly from uncertainties in the foil thickness and data recording error which are quite small. This is estimated to be about 0.01 Amps. The length and width of the heater are known to within 0.2 mm, and the width is measured as the distance between weld lines. Using the uncertainty relation with nominal voltage and current values of 1.1 Volts and 36.0 Amps, respectively, and a heater length and width of 76.2 mm and 127 mm, respectively, an uncertainty of 39.3 W/m^2 was calculated for q". The majority of this error arises from uncertainty in the voltage reading. For comparison, a nominal heat flux of 4090 W/m^2 is produced by the heater, so the uncertainty is less than 1.0% of the absolute value.

The uncertainty in h may now be estimated from the definition of h and the uncertainty relation. Such an estimate results in an uncertainty in h of 24 W/m^2K, which is about 2.9 percent of the nominal value of 820 W/m^2K. This value is representative for the majority of the blade surface. Very near the showerhead region, high heat transfer coefficient values drive the temperature difference $(T_w - T_f)$ to smaller values, and the percentage error increases to about 5.7 percent based on an uncertainty of 94 W/m^2K and a nominal heat transfer coefficient of 1640 W/m^2K.

The primary cause of this uncertainty is the random temperature error.

The uncertainty in Nusselt number follows directly from the heat transfer coefficient uncertainty. The uncertainty in the blade chord c is 0.2 mm, and the uncertainty in k for air is 0.0007 W/m·K, which results from the assumption of constant fluid properties for a temperature of 300 K. The uncertainty in the pure CO_2 thermal conductivity is likewise 0.0007 W/m·K, since the slopes of the air and CO_2 thermal conductivity versus temperature relations at 300 K are nearly equal. However, the CO_2 experimental cases are based on a mixture of the two gases as shown in Chapter 2. Thus the CO_2/air mixture thermal conductivity has the additional error based on the uncertainty in the mole fraction of each species. From the mixture relation:

$$k_{mix} = 0.0263 \cdot \left(\frac{1 + 0.258\eta - 0.045\eta^2}{1 + 0.774\eta + 0.150\eta^2}\right) \frac{W}{m \cdot K}$$

Using the estimated uncertainty in the value of η of 0.01, and assuming that the film effectiveness is a reliable measure of mole fraction as argued in Chapter 2, the uncertainty in the thermal conductivity of the mixture due to errors in η is estimated to be 0.0001 W/m·K. Thus, surprisingly, the uncertainty due to constant temperature assumption is much greater than that due to species mole fraction error. This is because the thermal conductivities for the two gases are reasonably close, and one species (air) has a much higher mole fraction than the other (CO_2). Using these

values in the Nusselt number definition, an uncertainty of 81 is estimated for the Nusselt number value, based on a nominal Nusselt number of 2000, for a percentage error of 4.0% this error is nearly equally divided between heat transfer coefficient error and thermal conductivity error. For the higher Nusselt number values near the showerhead region, an uncertainty in the Nusselt number of 250 with a nominal value of 4000 is estimated. This yields an uncertainty of 6.3%, with the heat transfer coefficient uncertainty becoming the primary source of uncertainty in this region.

APPENDIX II - 1-D PERIODIC HEAT CONDUCTION ANALYSIS

The adiabatic film effectiveness is defined in terms of the fluid temperature adjacent to the adiabatic wall, i.e., the film temperature, T_f. For the time-average experimental data, this is equivalent to the time-average temperature measured on the blade surface by the thin-film gauges, assuming no net flow of heat to or from the blade. However, the situation is more complicated for the time-resolved experimental data. Even with no net heat flow to or from the blade, the instantaneous heat flux at the surface is non-zero in general, due to one-dimensional transient conduction in the substrate. Thus the instantaneous temperature measured by a gauge on the solid surface is not in general equal to the film temperature. Assuming zero net heat flux over one period of temperature fluctuation, the surface gauges will indicate a temperature having the same mean value as the film temperature, but the amplitude of the variations will be reduced due to conduction. The following derivation describes a method for determining the unsteady film temperature from the known unsteady surface temperature and thermophysical properties of the substrate material.

The idealized problem under consideration is shown in Figure 119. A solid slab which is infinite in the y and z directions has a finite thickness of 2L in the x direction. Because it is desired to have an adiabatic boundary condition at x=0, the domain is extended from x=-L to x=L. Under the application of identical boundary conditions at the surfaces, this will produce the desired adiabatic condition at x=0 due

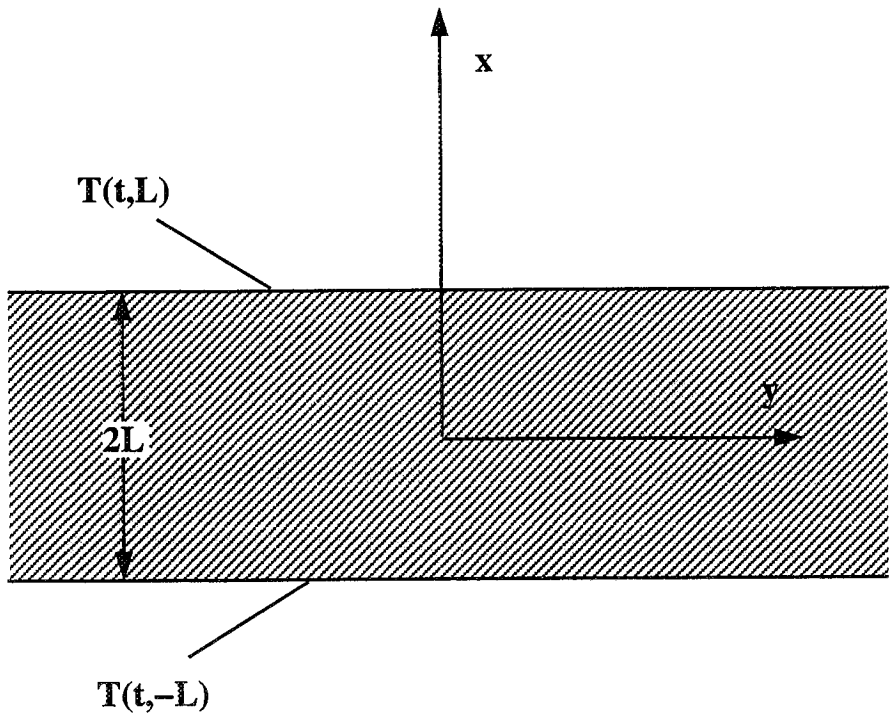

Figure 119: Idealized periodic heat conduction model.

to symmetry. The x=0 and x=L locations correspond to the bottom and exposed surfaces of the substrate, respectively. The partial differential equation for this problem is:

$$\frac{\partial T(t,x)}{\partial t} = \alpha \frac{\partial^2 T(t,x)}{\partial x^2}$$

Two boundary conditions in space and one in time are required. The first boundary condition in space is the known periodic surface temperature. It is assumed that this can be represented as a Fourier series:

$$T(t,L) = \sum_{n=1}^{n_{max}} a_n \sin \frac{2\pi nt}{t_o}$$

where t_o is the period of the wake passing. This expression requires that the periodic temperature have a mean value of zero. This is easily obtained by establishing a datum temperature equal to the time-mean temperature. As indicated, the second boundary condition in space which requires that the heat flux at the bottom of the substrate be zero can be achieved by applying the same periodic temperature at x=-L. Thus:

$$T(t,-L) = \sum_{n=1}^{n_{max}} a_n \sin \frac{2\pi nt}{t_o}$$

For the boundary condition in time, it is sufficient to require that the solution be

periodic for all x. This assumes that any initial transients have fully dissipated.

Carslaw and Jaeger [47] have given the solution to this problem as:

$$T = \sum_{n=1}^{n_{max}} a_n A_n \sin\left(\frac{2\pi n t}{t_o} + \phi_n\right)$$

where

$$A_n = \sqrt{\frac{\cosh 2b_n x + \cos 2b_n x}{\cosh 2b_n L + \cos 2b_n L}}$$

$$\phi_n = arg\left(\frac{\cosh b_n x(1+i)}{\cosh b_n L(1+i)}\right)$$

$$b_n = \sqrt{\frac{n\pi}{\alpha t_o}} = \sqrt{\frac{n\pi \rho c_p}{k t_o}}$$

ϕ_n can also be given as a real number for $-\pi/2 < \phi_n < \pi/2$:

$$\phi_n = \tan^{-1}\left(\frac{\sinh(b_n x)\sin(b_n x)\cosh(b_n L)\cos(b_n L) + \cosh(b_n x)\cos(b_n x)\sinh(b_n L)\sin(b_n L)}{\sinh(b_n x)\sin(b_n x)\sinh(b_n L)\sin(b_n L) + \cosh(b_n x)\cos(b_n x)\cosh(b_n L)\cos(b_n L)}\right)$$

Using hyperbolic trigonometric identities and rearranging,

$$\phi_n = -\tan^{-1}\left(\frac{\sinh(b_n(L+x))\sin(b_n(L-x)) + \sinh(b_n(L-x))\sin(b_n(L+x))}{\cosh(b_n(L+x))\cos(b_n(L-x)) + \cosh(b_n(L-x))\cos(b_n(L+x))}\right)$$

For the generalized case where the heat flux at x=0 is a non-zero constant, the partial differential equation may be separated into two problems, the solutions of which are superposed. The first problem is the one for which the solution has been given, and the second is for the same differential equation with different boundary conditions. The new boundary conditions are zero temperature at x=L, and the constant heat flux boundary condition at x=0:

$$-k\left(\frac{\partial T(t,x)}{\partial x}\right)\Big|_{x=0} = q''$$

It can be seen that the superposition of the boundary conditions for the two new problems yields those for the generalized problem. The solution of the second problem is trivial and is easily shown to be:

$$T = \frac{q''}{k}(L-x)$$

Superposition of the two solutions yields the solution to the unsteady surface temperature problem with non-zero heat flux at x=0:

$$T(x,t) = \frac{q''}{k}(L-x) + \sum_{n=1}^{n_{max}} a_n A_n \sin\left(\frac{2\pi nt}{t_o} + \phi_n\right)$$

In order to determine the temperature the wall would reach if it were a perfect

insulator, it is necessary to apply a boundary condition for convection. Now,

$$-k(\frac{\partial T}{\partial x})|_{x=L} = h(t)(T(t,L)-T_{aw}(t))$$

where $T_{aw}(t)$ is the adiabatic wall temperature. In addition,

$$q'' = h(t)(T_{iw}(t)-T_{aw}(t))$$

where $T_{iw}(t)$ is the unsteady ideal wall temperature, or the temperature which the wall would reach if the substrate were a perfect insulator with the heat flux q" applied at the surface. Combining these two conditions yields:

$$-k(\frac{\partial T}{\partial x})|_{x=L} - q'' = h(t)(T(t,L)-T_{iw}(t))$$

or

$$T_{iw}(t) = T(t,L) + \frac{k(\frac{\partial T}{\partial x})|_{x=L} + q''}{h(t)}$$

Taking the derivative of the temperature solution and setting x=L:

$$\frac{\partial T}{\partial x}|_{x=L} = -\frac{q''}{k} + \sum_{n=1}^{n_{max}} a_n[(\frac{\partial \phi_n}{\partial x}|_{x=L})\cos(\frac{2\pi nt}{t_o})+(\frac{\partial A_n}{\partial x}|_{x=L})\sin(\frac{2\pi nt}{t_o})]$$

since $A_n(L)=1$ and $\phi_n(L)=0$.

Next, taking the derivatives of ϕ_n and A_n:

$$\frac{\partial \phi_n}{\partial x} = b_n \frac{\sinh(2b_n x)+\sin(2b_n x)}{\cosh(2b_n x)+\cos(2b_n x)}$$

$$\frac{\partial A_n}{\partial x} = b_n \frac{\sinh(2b_n x)-\sin(2b_n x)}{\sqrt{(\cosh(2b_n L)+\cos(2b_n L))(\cosh(2b_n x)+\cos(2b_n x))}}$$

Setting x equal to L for these derivatives yields:

$$\frac{\partial \phi_n}{\partial x}\Big|_{x=L} = b_n \frac{\sinh(2b_n L)+\sin(2b_n L)}{\cosh(2b_n L)+\cos(2b_n L)}$$

$$\frac{\partial A_n}{\partial x}\Big|_{x=L} = b_n \frac{\sinh(2b_n L)-\sin(2b_n L)}{\cosh(2b_n L)+\cos(2b_n L)}$$

Substituting back into the temperature derivative expression:

$$\frac{\partial T}{\partial x}\Big|_{x=L} = -\frac{q''}{k} + \sum_{n=1}^{n_{max}} [a_n b_n \frac{\sinh(2b_n L)+\sin(2b_n L)}{\cosh(2b_n L)+\cos(2b_n L)} \cos(\frac{2\pi nt}{t_o}) + \frac{\sinh(2b_n L)-\sin(2b_n L)}{\cosh(2b_n L)+\cos(2b_n L)} \sin(\frac{2\pi nt}{t_o})]$$

For the conditions of this experiment ($t_o \leq 0.001286$ s, $\alpha = 7.75 \times 10^{-8}$ m^2/s, and L=6.35 x 10^{-5} m), $2b_nL$ has a value of at least 22.5. For values this large,

$$\frac{\sinh(2b_nL) \pm \sin(2b_nL)}{\cosh(2b_nL) + \cos(2b_nL)} \approx 1.0$$

so that:

$$\frac{\partial T}{\partial x}\Big|_{x=L} = -\frac{q''}{k} + \sum_{n=1}^{n_{max}} a_n b_n [\cos(\frac{2\pi nt}{t_o}) + \sin(\frac{2\pi nt}{t_o})]$$

Applying the convection boundary condition:

$$-k \sum_{n=1}^{n_{max}} a_n b_n [\cos(\frac{2\pi nt}{t_o}) + \sin(\frac{2\pi nt}{t_o})] = h(t)(T(t,L) - T_{iw}(t))$$

Rearranging and using the definition of b_n:

$$T_{iw}(t) = T(t,L) + \frac{1}{h(t)}\sqrt{\frac{\pi \rho c_p k}{t_o}} \sum_{n=1}^{n_{max}} \sqrt{n} a_n [\cos(\frac{2\pi nt}{t_o}) + \sin(\frac{2\pi nt}{t_o})]$$

At this point, there are two unknowns: $T_{iw}(t)$ and h(t). However, if two experimental cases are performed with all conditions held constant except for a different value of q", and it is assumed that h(t) does not depend on q", then two equations can be

written:

$$T_{1,iw}(t) = T_1(t,L) + \frac{1}{h(t)}\sqrt{\frac{\pi \rho c_p k}{t_o}} \sum_{n_1=1}^{n_{1,max}} \sqrt{n_1} a_{n_1} \left[\cos\left(\frac{2\pi n_1 t}{t_o}\right) + \sin\left(\frac{2\pi n_1 t}{t_o}\right)\right]$$

$$T_{2,iw}(t) = T_2(t,L) + \frac{1}{h(t)}\sqrt{\frac{\pi \rho c_p k}{t_o}} \sum_{n_2=1}^{n_{2,max}} \sqrt{n_2} a_{n_2} \left[\cos\left(\frac{2\pi n_2 t}{t_o}\right) + \sin\left(\frac{2\pi n_2 t}{t_o}\right)\right]$$

Without loss of generality, let q"=0 for case 1 and let q">0 for case 2. Then:

$$h(t) = \frac{q''}{T_{2,iw}(t) - T_{1,iw}(t)}$$

Substituting into the two previous equations,

$$T_{1,iw}(t) = T_1(t,L) + \frac{(T_{2,iw}(t) - T_{1,iw}(t))}{q''}\sqrt{\frac{\pi \rho c_p k}{t_o}} \sum_{n_1=1}^{n_{1,max}} \sqrt{n_1} a_{n_1} \left[\cos\left(\frac{2\pi n_1 t}{t_o}\right) + \sin\left(\frac{2\pi n_1 t}{t_o}\right)\right]$$

$$T_{2,iw}(t) = T_2(t,L) + \frac{(T_{2,iw}(t) - T_{1,iw}(t))}{q''}\sqrt{\frac{\pi \rho c_p k}{t_o}} \sum_{n_2=1}^{n_{2,max}} \sqrt{n_2} a_{n_2} \left[\cos\left(\frac{2\pi n_2 t}{t_o}\right) + \sin\left(\frac{2\pi n_2 t}{t_o}\right)\right]$$

The two equations now include only two unknowns, $T_{1,iw}(t)$ and $T_{2,iw}(t)$. For clarity, let

$$B_1(t) = \frac{1}{q''}\sqrt{\frac{\pi \rho c_p k}{t_o}} \sum_{n_1=1}^{n_{1,max}} \sqrt{n_1} a_{n_1} \left[\cos\left(\frac{2\pi n_1 t}{t_o}\right) + \sin\left(\frac{2\pi n_1 t}{t_o}\right)\right]$$

$$B_2(t) = \frac{1}{q''}\sqrt{\frac{\pi \rho c_p k}{t_o}} \sum_{n_2=1}^{n_{2,max}} \sqrt{n_2} a_{n_2} \left[\cos\left(\frac{2\pi n_2 t}{t_o}\right) + \sin\left(\frac{2\pi n_2 t}{t_o}\right)\right]$$

Then solving for $T_{1,iw}(t)$ and $T_{2,iw}(t)$ gives:

$$T_{1,iw}(t) = \frac{(1 - B_2(t))T_1(t,L) + B_1(t)T_2(t,L)}{1 + B_1(t) - B_2(t)}$$

$$T_{2,iw}(t) = \frac{(1 + B_1(t))T_2(t,L) - B_2(t)T_1(t,L)}{1 + B_1(t) - B_2(t)}$$

Finally, applying the definition of h(t):

$$h(t) = \frac{q'' (1 + B_1(t) - B_2(t))}{T_2(t,L) - T_1(t,L)}$$

This procedure may be followed to solve for $T_{1,iw}(t)$ for both the case with blowing and without. If $T_{1,iw,b}(t)$ and $T_{1,iw,nb}(t)$ indicate the unheated ideal wall temperature with and without blowing, respectively, then:

$$\eta(t) = \frac{T_{1,iw,b}(t) - T_{1,iw,nb}(t)}{T_c - T_{1,iw,nb}(t)}$$

LITERATURE CITED

1. Adamczyk, J. J., "Model Equation for Simulating Flows in Multistage Turbomachinery", NASA TM-86869, Nov. 1984.

2. Sharma, O. P., Pickett, G. F., and Ni, R. H., "Assessment of Unsteady Flows in Turbines", ASME Paper 90-GT-150, June 1990.

3. Mayle, R. E., "The Role of Laminar-Turbulent Transition in Gas Turbine Engines", Journal of Turbomachinery, Vol. 113, pp. 509-537, Oct. 1991.

4. Ashworth, D. A., LaGraff, J. E., Schultz, D. L., and Grindrod, K. J., "Unsteady Aerodynamic and Heat Transfer Processes in a Transonic Turbine Stage", Journal of Engineering for Gas Turbines and Power, Vol. 107, pp. 1022-1030, Oct. 1985.

5. O' Brien, J. E., "Effects of Wake Passing on Stagnation Region Heat Transfer", Journal of Turbomachinery, Vol. 112, pp. 522-530, July 1990.

6. Bagby, C. L. and Anderson, W. L., "Effect of Turbofan Cycle Variables on Aircraft Cruise Performance", Journal of Aircraft, Vol. 3, pp. 385-389, Sept.-Oct. 1966.

7. Hennecke, "Turbine Blade Cooling in Aeroengines, VKI Lecture Series,1982-02, Feb. 1982.

8. United Technologies Pratt & Whitney, "The Aircraft Gas Turbine Engine and Its Operation", P&W Oper. Instr. 200, 1988.

9. Goldstein, R. J., "Film Cooling", Advances in Heat Transfer, Vol. 7, pp. 321-379, 1971.

10. Leylek, J. H. and Zerkle, R. D., "Discrete-Jet Film Cooling: A Comparison of Computational Results With Experiments", Journal of Turbomachinery, Vol. 116, pp. 358-368, July 1994.

11. Mick, W. J. and Mayle, R. E., "Stagnation Film Cooling and Heat Transfer, Including Its Effect Within the Hole Pattern", Journal of Turbomachinery, Vol. 110, pp.66-72, Jan. 1988.

12. Mehendale, A. B. and Han, J. C., "Influence of High Mainstream Turbulence on Leading Edge Film Cooling Heat Transfer", Journal of Turbomachinery, Vol.114, pp. 707-715, Oct. 1992.

National Aeronautics and
Space Administration

Lewis Research Center
21000 Brookpark Rd.
Cleveland, OH 44135-3191

24. Abuaf, N., Bunker, R., and Lee C. P., "Heat Transfer and Film Cooling Effectiveness in a Linear Cascade", ASME Paper 95-GT-3, June 1995.

25. Garg, V. K. and Gaugler, R. E., "Heat Transfer in Film-Cooled Turbine Blades", ASME Paper 93-GT-81, May 1993.

26. Garg, V. K. and Gaugler, R. E., "Effect of Velocity and Temperature Distribution at the Hole Exit on Film Cooling of Turbine Blades", ASME Paper 95-GT-2, June 1995.

27. Garg, V. K. and Gaugler, R. E., "Leading Edge Film Cooling Effects on Turbine Blade Heat Transfer", ASME Paper 95-GT-275, June 1995.

28. Ou, S., Han, J.-C., Mehendale, A. B., and Lee, C. P., "Unsteady Wake Over a Linear Turbine Blade Cascade With Air and CO_2 Film Injection: Part I - Effect on Heat Transfer Coefficients", Journal of Turbomachinery, Vol. 116, pp. 721-729, Oct. 1994.

29. Mehendale, A. B., Han, J.-C., Ou, S., and Lee, C. P., "Unsteady Wake Over a Linear Turbine Blade Cascade With Air and CO_2 Film Injection: Part II - Effect on Film Effectiveness and Heat Transfer Distributions", Journal of Turbomachinery, Vol. 116, pp. 730-737, Oct. 1994.

30. Funazaki, K., Yokota, M., and Yamawaki, S., "The Effect of Periodic Wake Passing on Film Effectiveness of Discrete Cooling Holes Around the Leading Edge of a Blunt Body", ASME Paper 95-GT-183, June 1995.

31. Dring, R. P., Blair, M. F., and Joslyn, H. D., "An Experimental Investigation of Film Cooling on a Turbine Rotor Blade", Journal of Engineering for Power, Vol. 102, pp. 81-87, Jan. 1980.

32. Takeishi, K., Aoki, S., Sato, T., and Tsukagoshi, K., "Film Cooling on a Gas Turbine Rotor Blade", Journal of Turbomachinery, Vol. 114, pp. 828-834, Oct. 1992.

33. Abhari, R. S. and Epstein, A. H., "An Experimental Study of Film Cooling in a Rotating Transonic Turbine", ASME Paper 92-GT-201, June 1992.

34. Dorney, D. J., et al., "Investigation of Hot Streak Migration and Film Cooling Effects on Heat Transfer in Rotor/Stator Interacting Flows", N00140-88-C-0677 - Report 1, UTRC Report 91-29, Apr. 1992.

35. Eckert, E. R. G., Goldstein, R. J., Patankar, S. V., and Simon, T. W., "Studies of Gas Turbine Heat Transfer: Airfoil Surfaces and End-Wall Cooling Effects", Air Force Office of Scientific Research, Report N92-19097, Sept. 1991.

36. Henderson, G. H., "Forcing Function and Steady Loading Effects on Unsteady Aerodynamic Gust Response", Ph.D.Thesis, Purdue University, Aug. 1991.

37. O' Brien, J. E. and Capp, S. P., "Two-Component Phase-Averaged Turbulence Statistics Downstream of a Rotating Spoked-Wheel Wake Generator", Journal of Turbomachinery, Vol. 111, pp. 475-482, Oct. 1989.

38. Simoneau, R. J., Morehouse, K. A., VanFossen, G. J., and Behning, F. P., "Effect of a Rotor Wake on Heat Transfer From a Circular Cylinder", NASA TM-83613, 1984.

39. Hippensteele, S. A., Russell, L. M., and Stepka, F. S., "Evaluation of a Method for Heat Transfer Measurements and Thermal Visualization Using a Composite of a Heater Element and Liquid Crystals", NASA TM-81639, 1981.

40. Incropera, F. P., and DeWitt, D. P., Fundamentals of Heat Transfer, John Wiley & Sons, 1981

41. Bird, R. B., Stewart, W. E., and Lightfoot, E. N., Transport Phenomena, John Wiley & Sons, 1960

42. Chima, R. V. and Yokota, J. W., "Numerical Analysis of Three-Dimensional Viscous Flows in Turbomachinery", AIAA J., Vol. 28, No. 5, pp. 798-806, May 1990.

43. Baldwin, B. S. and Lomax, H., "Thin-Layer Approximation and Algebraic Model for Separated Turbulent Flows", AIAA Paper 78-257, Jan. 1978.

44. Sorenson, R. L., "A Computer Program to Generate Two-Dimensional Grids About Airfoils and Other Shapes by Use of Poisson's Equation", NASA TM-81198, 1980.

45. Funazaki, K., Koyabu, E., and Yamawaki, S., "Effect of Periodic Wake Passing on Film Effectiveness of Inclined Discrete Cooling Holes Around the Leading Edge of a Blunt Body", ASME Paper 96-GT-207, June 1996.

46. Kline, S. J. and McClintock, "Describing Uncertainties in Single-Sample Experiments", Mechanical Engineering, pp. 3-8, 1953.

47. Carslaw, H. S. and Jaeger, J. C., Conduction of Heat in Solids, 2nd edition, Oxford University Press, 1959.

REPORT DOCUMENTATION PAGE

Form Approved
OMB No. 0704-0188

AGENCY USE ONLY (*Leave blank*)	2. REPORT DATE	3. REPORT TYPE AND DATES COVERED
	December 1996	Technical Memorandum

TITLE AND SUBTITLE

The Effect of Wake Passing on Turbine Blade Film Cooling

5. FUNDING NUMBERS

WU–523–26–13

AUTHOR(S)

James David Heidmann

. PERFORMING ORGANIZATION NAME(S) AND ADDRESS(ES)

National Aeronautics and Space Administration
Lewis Research Center
Cleveland, Ohio 44135–3191

8. PERFORMING ORGANIZATION REPORT NUMBER

E–10568

9. SPONSORING/MONITORING AGENCY NAME(S) AND ADDRESS(ES)

National Aeronautics and Space Administration
Washington, DC 20546–0001

10. SPONSORING/MONITORING AGENCY REPORT NUMBER

NASA TM–107380

11. SUPPLEMENTARY NOTES

This report was submitted as a dissertation in partial fulfillment of the requirements for the degree of Doctor of Philosophy in Mechanical Engineering to Case Western Reserve University, Cleveland, Ohio, January 1997 (Thesis Advisor: Dr. Eli Reshotko). Responsible person, James D. Heidmann, organization code 5820, (216) 433–3604.

12a. DISTRIBUTION/AVAILABILITY STATEMENT

Unclassified - Unlimited
Subject Categories 02, 07, and 34

This publication is available from the NASA Center for AeroSpace Information, (301) 621–0390.

12b. DISTRIBUTION CODE

13. ABSTRACT ***(Maximum 200 words)***

The effect of upstream blade row wake passing on the showerhead film cooling performance of a downstream turbine blade has been investigated through a combination of experimental and computational studies. The experiments were performed in a steady-flow annular turbine cascade facility equipped with an upstream rotating row of cylindrical rods to produce a periodic wake field similar to that found in an actual turbine. Spanwise, chordwise, and temporal resolution of the blade surface temperature were achieved through the use of an array of nickel thin-film surface gauges covering one unit cell of showerhead film hole pattern. Film effectiveness and Nusselt number values were determined for a test matrix of various injectants, injectant blowing ratios, and wake Strouhal numbers. Results indicated a demonstrable reduction in film effectiveness with increasing Strouhal number, as well as the expected increase in film effectiveness with blowing ratio. An equation was developed to correlate the span-average film effectiveness data. The primary effect of wake unsteadiness was found to be correlated well by a chordwise-constant decrement of 0.094·St. Measurable spanwise film effectiveness variations were found near the showerhead region, but meaningful unsteady variations and downstream spanwise variations were not found. Nusselt numbers were less sensitive to wake and injection changes. Computations were performed using a three-dimensional turbulent Navier-Stokes code which was modified to model wake passing and film cooling. Unsteady computations were found to agree well with steady computations provided the proper time-average blowing ratio and pressure/suction surface flow split are matched. The remaining differences were isolated to be due to the enhanced mixing in the unsteady solution caused by the wake sweeping normally on the pressure surface. Steady computations were found to be in excellent agreement with experimental Nusselt numbers, but to overpredict experimental film effectiveness values. This is likely due to the inability to match actual hole exit velocity profiles and the absence of a credible turbulence model for film cooling.

14. SUBJECT TERMS	15. NUMBER OF PAGES
Turbine; Film cooling; Wake	266
	16. PRICE CODE: A12

17. SECURITY CLASSIFICATION OF REPORT	18. SECURITY CLASSIFICATION OF THIS PAGE	19. SECURITY CLASSIFICATION OF ABSTRACT	20. LIMITATION OF ABSTRACT
Unclassified	Unclassified	Unclassified	

National Aeronautics and
Space Administration

Lewis Research Center
21000 Brookpark Rd.
Cleveland, OH 44135-3191